NASA Contractor Report 189113

P. 313

Numerical, Analytical, Experimental Study of Fluid Dynamic Forces in Seals

Interim Report No. 1

Wilbur Shapiro, Antonio Artiles,
and Bharat Aggarwal
Mechanical Technology Incorporated
Latham, New York

Jed Walowit
Jed A. Walowit, Inc.
Clifton Park, New York

Mahesh M. Athavale and Andrzej J. Przekwas
Computational Fluid Dynamics Research Corporation
Huntsville, Alabama

April 1992

NASA
National Aeronautics and
Space Administration

TABLE OF CONTENTS

ACKNOWLEDGEMENTS

Executive Summary

NASA/ Lewis Research Center is sponsoring a program for providing computer codes for analyzing and designing turbomachinery seals for future aerospace and engine systems. The program is made up of three principal components: 1) the development of advanced 3-D Computational Fluid dynamics codes 2) The production of simpler 2-D industrial codes and 3) the development of a Knowledge Based System(KBS) that contains an expert system to assist in seal selection and design.

The 3-D code is being produced by a major subcontractor, Computational Fluid Dynamics Research Corporation (CFDRC) of Huntsville ,AL., who are enhancing an existing CFD code, REFLEQS. The first task of CFDRC has been to concentrate on cylindrical geometries with straight, tapered and stepped bores. Improvements have been made by adoption of a colocated grid formulation, incorporation of higher-order, time-accurate schemes for transient analysis and high-order discretization schemes for spatial derivatives. This report describes the mathematical formulations and presents a variety of 2-D results, including labyrinth and brush seal flows. Extensions to 3-D are presently in progress.

Three industrial codes have been produced which are capable of being run on a PC.

- SPIRALG predicts performance characteristics of gas-lubricated, spiral-groove cylindrical and face seals including eccentricity and misalignment (four degrees of freedom which consist of two orthogonal displacements and two orthogonal angular misalignments), which represent extensions to the present state of the art. The code produces seal loads and moments, minimum film thickness, axial flow, power loss and up to thirty two frequency dependent cross-coupled spring and damping coefficients. Arbitrary placement of grooving and the dam region is permitted as well as user selection of the spiral-groove pumping direction. The code is coupled to an optimization code that will allow for determination of optimum groove geometry on the bases of stiffness , pumping capacity and flow. A code option is the use of a

Romberg extrapolation procedure for producing rapid and accurate results. Included in this report is a comprehensive theoretical development of the code, several sample cases and validation information.

- The industrial code ICYL is intended for use in analyzing cylindrical seals operating with incompressible fluids. The code includes film turbulence, and inertia effects at inlet and exit and at boundaries where sharp clearance discontinuities result, such as hydrostatic recesses. Configurations include plain circular, hydrostatic, multi-lobe, tapered and Rayleigh Step geometries. An important feature of the code is the incorporation of roughness on the seal housing or rotating shaft. It thus permits analysis of damping seals which are finding favor in advanced cryogenic turbomachines. The code produces seal loads, and righting moments, flows, power loss, clearance and pressure distributions, up to thirty two cross-coupled dynamic spring and damping coefficients as well as critical mass and frequency. This report describes the theoretical development, includes examples of code usage and validation against other codes and information in the literature.

- The industrial code GCYL analyzes cylindrical gas seal configurations. Configurations include plain circular, hydrostatic, multi-lobe, tapered and Rayleigh Step geometries. The code produces seal loads, and righting moments, flows, power loss, clearance and pressure distributions, and up to thirty two frequency dependent, cross-coupled dynamic spring and damping coefficients. This report describes the theoretical development, includes examples of code usage and validation against other codes and information in the literature.

The functions of the Knowledge Based system are 1) to integrate the scientific and industrial codes 2) to provide a user friendly graphical user interface and 3) to include an expert system for seal selection, analysis and design. A significant requirement is portability between a PC and UNIX based workstation. The two operating systems selected are OS/2 with the Presentation Manager interface for the PC and UNIX with OSF/MOTIF for a workstation. A two track development effort is being pursued. The scientific codes are being developed under UNIX and

the industrial codes are being developed using the OS/2 operating system. The user interfaces are being developed using object oriented tools and C++ which are portable between OS/2 and UNIX. The initial development platform will be OS/2 and porting to UNIX will be accomplished by recompilation. This report discusses development plans and presents some OS/2 graphical user interfaces accomplished with the industrial codes.

In addition to code and interface development, the project requires technology transfer to both government and non-government facilities. A peer panel has been established, whose function is to guide program development, and annual workshops are held to transfer information. The first workshop was held on March 26, 1991.

LIST OF FIGURES

LIST OF TABLES

1.0 INTRODUCTION

NASA's advanced engine programs are aimed at progressively higher efficiencies, greater reliability, and longer life. Turbomachinery for future aerospace engine systems will require advanced seal configurations to control leakage, control lubricant and coolant flow, prevent entrance of contamination, inhibit the mixture of incompatible fluids, and assist in the control of rotor response.

A seven year program has been devised with the objective of providing to NASA and the U.S. Aerospace Industry, three dimensional scientific codes and simpler industrial codes for analyzing and designing optimized advanced seals with minimal development time.

The program provides three interdependent parallel paths:

1. The development of scientific Computational Fluid Dynamics (CFD) codes capable of producing full three-dimensional flow field information to enhance understanding of flow phenomena and mechanisms, to contribute design guidance for complex situations, and to furnish accuracy standards for less sophisticated analyses. All tasks involving three-dimensional code development will be accomplished by a major subcontractor to MTI, CFD Research Corporation (CFDRC)

2. The development of industrial codes for expeditious analysis, design and optimization of turbomachinery seals. The industrial codes will consist of a series of separate, stand-alone codes that will be integrated by a Knowledge Based System (KBS).

3. The development of expert systems to assist users to select an appropriate seal type for their application, provide design guidance, and assist in interpreting data from the analysis programs.

The analysis codes and the expert systems developed by the three activities will be integrated into a unified system by the KBS which will provide access to and link all the various components. The key features of the KBS include the following:

- Access to all analysis codes and expert systems
- An easy- to- use, consistent user interface for all KBS components
- Utility functions such as printing and browsing output files
- Plotting of output data from analysis programs
- Database of analytical models and other supporting information
- Portability between PC and Workstation environments

An important aspect of the contract is technology transfer to the industrial, government and academic communities. This is being accomplished through annual workshops, reports, and code distribution through NASA. The first workshop was convened on March 26, 1991 with over 65 attendees. A Peer Review Panel has also been established consisting of seal experts and cognizant representatives from industry, government and the academia. The Peer Panel provides technical guidance to the program.

This report covers the effort completed during the first year of the program which included the following:
- The development of advanced algorithms and validation of the CFD codes with emphasis on cylindrical geometries.
- Delivery of three industrial codes to NASA for Beta testing
  - A gas lubricated spiral groove code SPIRALG for analyzing spiral groove cylindrical and face seals.
  - A cylindrical incompressible seal code ICYL for analyzing a wide variety of cylindrical geometries including roughened surface seals.
  - A cylindrical compressible seal code GCYL for analyzing a wide variety of cylindrical gas seal geometries.
- The establishment of a detailed plan for the implementation of the Knowledge Based System using the PC and OS/2 as the principal up front interface and operating system respectively. Several industrial codes were implemented and information is presented in this report. As a result of the first workshop, a need for a UNIX operating system was expressed by the attendees and the members of the Peer Panel. Resolution is presently being accomplished by KBS software that will be portable to both operating

systems and will be operable utilizing PC's or Workstations. The PC can only act as an interface for the scientific codes that must reside on a mainframe or workstation. The industrial codes can be self contained in a PC environment. The universal approach to the KBS will be presented at the next workshop and described in the next annual report.

2.0 COMPUTATIONAL FLUID-DYNAMICS DEVELOPMENTS

2.1. Introduction

2.1.1 Development of the cylindrical seals CFD code

The objective of Task I is to develop a three-dimensional CFD code for analysis of flows in straight, tapered and stepped cylindrical seal configurations. This code will be capable of solving three-dimensional Navier-Stokes equations in generalized, body-fitted coordinates with provisions for polar and cylindrical systems. The features which are relevant to the seals program include:

1. Stationary and rotating coordinate systems;
2. Steady-state and time-accurate solution capability;
3. Advanced turbulence models for high shear rotating flows;
4. Incompressible and compressible flow solutions;
5. Variable physical properties (viscosity, density, specific heat , *etc.*);
6. Cavitation effects;
7. Provision for stepped surfaces and injection ports;
8. Inclusion of viscous dissipation and phase changes in energy equation;
9. Treatment of sources due to external fields, *e.g.* electromagnetic and electrostatic;
10. Variable surface roughness treatment;
11. Provision for effects of pre-swirl and upstream effects; and
12. Customized input and output features for cylindrical seals.

The code will utilize solution procedures and schemes that are accurate, efficient and robust to include all these characteristics for high-aspect ratio computational cells typically encountered in seal geometries.

2.1.2 Focus of Work for the First Year

During the past year the focus of work has been to develop, implement and test several new concepts in the basic code REFLEQS. The two-dimensional version of REFLEQS was selected as the starting point for all the development work. Two-dimensional problems are sufficiently general, so that once proven, the concepts can be extended to three dimensions in a straightforward manner; at the same time the complexity of the coding is sufficiently low so that rapid development and incorporation of these concepts in the 2-D code are possible. Following are the modifications and improvements which were made in the basic REFLEQS code.

1. Adaptation of a colocated grid formulation in which the velocity components as well as the scalars are stored at the computational cell center as against the earlier staggered grid formulation where the velocity components are stored on the cell faces;

2. Use of Cartesian velocity components as the primary velocity variables in place of the velocity projections which were used before;

3. Incorporation of high-order time-accurate schemes for transient flow analyses which include a) PISO algorithm, b) Crank-Nicholson method, and c) three-point second-order backward time-differencing method; and

4. High-order discretization schemes for spatial derivatives. These include, in addition to central differencing, third-order upwind-biased scheme, Osher-Chakravarty scheme, and minimod limiter scheme.

Some of the items described above merit further attention at this point, and the merits of these and the reasons for implementation are discussed below.

2.1.2.1 Colocated grid formulation with Cartesian Components. Figure 2.1 illustrates the velocity-pressure location arrangement for staggered and colocated grid configurations.
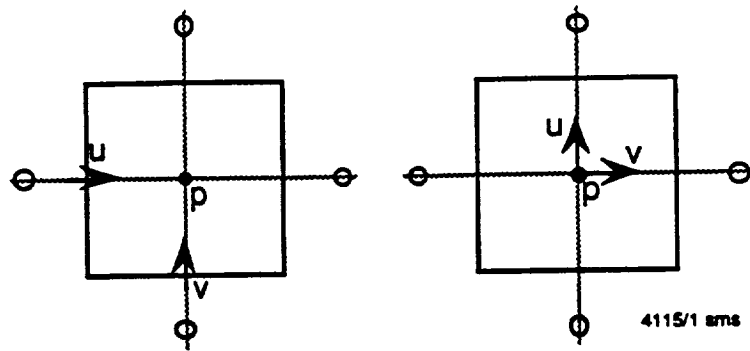
Figure 2.1 Examples of Staggered and Colocated Grids

A number of CFD codes currently in use are based on the **staggered** grid approach. These codes use finite volume methods with segregated or coupled equation solution methods. The chief reason for the use of staggered grid approach is to avoid the phenomenon of the odd-even decoupling of pressure when solving ·incompressible flows. By locating the velocity nodes on the cell faces instead of the cell centers, these velocities now can be linked directly to the pressures at the two nearest cell-centers. This provides a strong coupling between the velocities and the pressures and avoids the checkerboard pressure pattern. In recent years, however, interest in **colocated** grid formulation has been renewed[1-3]. Coupled with this approach is also the use of Cartesian components as the primary velocity components. This combination offers a number of advantages which are listed below.

1. A common control volume for mass, momentum and energy conservation eliminates many calculations which are repeated for the various control volumes in the staggered grid, *e.g.* evaluation of the link coefficients that are needed to set up the discretized form of the flow equations except the mass equation;

2. In a single grid cell, the number of interpolations required to calculate the velocity components at the cell faces is minimized;

3. In a staggered grid, the boundary condition implementation is more involved due to the physically displaced control volumes. In a single grid

2-3

cell the boundaries are the same for all variables, and the treatment is uniform;

4. The use of Cartesian components ensures that the treatment of body-fitted coordinate (BFC) and complex grids is relatively simple and easy to understand and implement. Use of Cartesian components also simplifies the procedure of velocity interpolation to cell faces. Use of any other primary velocity variable can make the interpolation procedure very cumbersome in a complex geometry, since the local angle relations must be taken into account; and

5. Implementation of higher-order spatial discretization schemes is simpler with the single cell approach.

The main drawback of the colocated grid formulation is that the coupling between the pressure and velocities cannot be maintained as easily as in the staggered approach. Recently, however, several methods have been proposed and used successfully to overcome the problem of odd-even decoupling of pressure. The particular formulation used in the present work is discussed in detail in a later section.

2.1.2.2   PISO Algorithm. The earlier formulation in REFLEQS for transient flow calculations involved several iterations of the overall solution procedure for each time step. The solution procedure thus could become expensive since, in effect, each time-step solution involved the solution of the corresponding steady-state solution. The PISO algorithm is designed to calculate transient flows with a non-iterative scheme. The algorithm consists of a predictor step where an intermediate solution is calculated, followed by a series (typically 2 or 3) of corrector steps which improve the accuracy of the predicted solution. Several of the steps in the overall scheme are implicit, so that the algorithm is much more stable with respect to the time step size as compared to an explicit time-marching scheme. Due to the non-iterative nature of the PISO algorithm the overall computational costs for this method can be substantially smaller than the iterative methods. The algorithm can

also be set up to achieve higher order time-accuracy. For these reasons, the development of PISO algorithm for transient analyses was considered.

2.2   Mathematical Formulation

In this section a discussion of the theoretical details of the various procedures implemented in the 2-D code is given. The basic differential and finite difference equations for the fluid flow are shown. A discussion of the mass interpolation procedure used in the code follows next, and finally the solution steps needed in the two basic algorithms: SIMPLEC and PISO are given.

2.2.1 Flow Equations and Discretization

In the Cartesian tensor form the fluid flow equations can be written as

Continuity
$$\frac{\partial \rho}{\partial t} + \frac{\partial (\rho u_i)}{\partial x_i} = 0 \tag{2.1}$$

momentum
$$\frac{\partial (\rho u_i)}{\partial t} + \frac{\partial}{\partial x_j}(\rho u_i u_j) = -\frac{\partial}{\partial x_i}\left(p + \frac{2}{3}K\right) + \frac{\partial}{\partial x_j}\left[\mu\left(\frac{\partial u_j}{\partial x_i} + \frac{\partial u_i}{\partial x_j}\right)\right] + B_i \tag{2.2}$$

or, alternatively, the general transport equation for any flow property, ϕ, is

$$\frac{\partial (\rho \phi)}{\partial t} + \frac{\partial}{\partial x_i}(\rho u_i \phi) = \frac{\partial}{\partial x_j}\left[\Gamma \frac{\partial \phi}{\partial x_j}\right] + S^\phi \tag{2.3}$$

where B_i is the body force, Γ is the diffusion coefficient, and S^ϕ is the source term associated with the variable ϕ. This source term, then, would contain the pressure terms and other body force terms for the momentum equations.

The flow equations are next transformed to a generalized, Body-Fitted Coordinate (BFC) system which allows the grid to conform to the problem geometry. The switch to the BFC system (ξ, η) is done using the transformation

$$\xi = \xi(x,y)$$
$$\eta = \eta(x,y) \tag{2.4}$$

The partial derivatives can then be transformed as:

$$\frac{\partial}{\partial y} = \xi_x \frac{\partial}{\partial \xi} + \eta_x \frac{\partial}{\partial \eta}$$

$$\frac{\partial}{\partial y} = \xi_y \frac{\partial}{\partial \xi} + \eta_y \frac{\partial}{\partial \eta} \tag{2.5}$$

The two-dimensional general transport equation for ϕ then becomes

$$\frac{\partial(\rho J \phi)}{\partial t} + \frac{\partial(\rho U \phi)}{\partial \xi} + \frac{\partial(\rho V \phi)}{\partial \eta} = \frac{\partial}{\partial \xi}\left[J\Gamma(\nabla \xi \cdot \nabla \xi)\frac{\partial \phi}{\partial \xi}\right] + \frac{\partial}{\partial \eta}\left[J\Gamma(\nabla \eta \cdot \nabla \eta)\frac{\partial \phi}{\partial \eta}\right] + J(S' + S^\phi) \tag{2.6}$$

where U and V are the contravariant velocity components and S' is the source term associated with curvilinear nonorthogonal part of the viscous stress tensor.

$$U = J\left(\xi_x u + \xi_y v\right) \tag{2.7}$$

$$V = J\left(\eta_x u + \eta_y v\right) \tag{2.8}$$

$$S' = \frac{\partial}{\partial \xi}\left[J\Gamma(\nabla \xi \cdot \nabla \eta)\frac{\partial \phi}{\partial \eta}\right] + \frac{\partial}{\partial \eta}\left[J\Gamma(\nabla \eta \cdot \nabla \xi)\frac{\partial}{\partial \xi}\right] \tag{2.9}$$

with u and v as the Cartesian velocity components along x and y directions. S' is the additional source term which is generated during the transformation of the diffusion terms; it is zero for an orthogonal grid. J is the Jacobian of the transformation,

$$J = \frac{\partial(x,y)}{\partial(\xi,\eta)} = \begin{vmatrix} x_\xi & x_\eta \\ y_\xi & y_\eta \end{vmatrix} \tag{2.10}$$

The transformed continuity equation is

$$\frac{\partial(J\rho)}{\partial t} + \frac{\partial(\rho U)}{\partial \xi} + \frac{\partial(\rho V)}{\partial \eta} = 0 \qquad (2.11)$$

For the solution methods used in the present work the transport equations are integrated over a general computational cell in the grid to generate algebraic equations which link the variables in the cell with those in the surrounding cells.
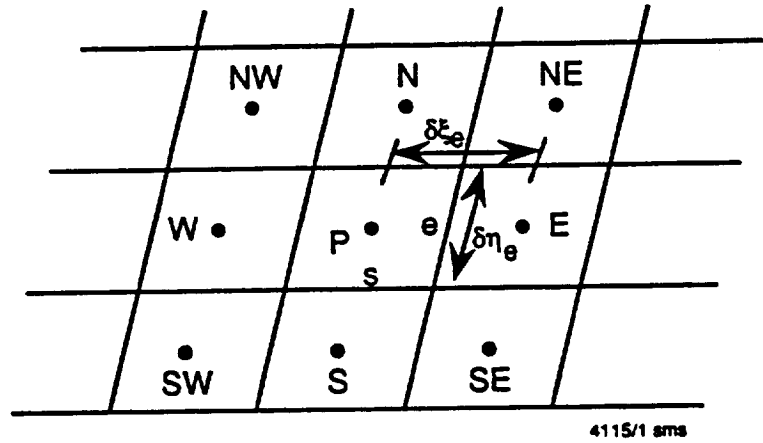
Figure 2.2 Computational Control Volume Grid and Nomenclature

The discretized transport equation for a variable ϕ then is given by

$$\left(a_{P\phi} + \rho \frac{\forall}{\Delta t}\right)\phi_P^* = \sum a_{nb\phi}\,\phi_{nb}^* + \rho\forall\,\frac{\phi^n}{\Delta t} + (S + S^\phi)\forall \qquad (2.12)$$

where $\forall$ is the volume of the cell ,the subscript nb denotes all neighboring cells and $a_{nb\phi}$ etc. are the link coefficients which consist of the convective and diffusive terms linking the cell centers with those around it, and the form of the coefficients depends on the method used for spatial differencing. Thus, e.g., for the upwind scheme,

$$a_{E\phi} = \frac{(J\Gamma\nabla\xi\cdot\nabla\xi)}{(\delta\xi)_e} \cdot (\delta\eta)_e + \max\left(0, -(\rho U)_e \, \delta\eta_e\right) \qquad (2.13)$$

$a_{P\phi}$ is obtained by summing all the link coefficients of neighboring cells.

The transport equation, Equation 2.12 is written for u and v velocities and solved sequentially to update the values of the components to u^* and v^*.

The updated velocity components at this point do not satisfy the continuity equation. To impose this the flow variables are assumed to have a form

$$u^{n+1} = u^* + u' \qquad (2.14)$$

$$v^{n+1} = v^* + v' \qquad (2.15)$$

$$p^{n+1} = p^* + p' \qquad (2.16)$$

$$\rho^{n+1} = \rho^* + \rho' \qquad (2.17)$$

The momentum equations are rewritten for the velocity corrections as

$$\left(a_{Pu} + \frac{\rho\forall}{\Delta t}\right)u_P' = \sum a_{nbu}\, u_{nb}' - \left(d_{u\xi}\, p_\xi'\, \xi_x + d_{u\eta}\, p_\eta'\, \eta_x\right) \qquad (2.18)$$

$$\left(a_{Pv} + \frac{\rho\forall}{\Delta t}\right)v_P' = \sum a_{nbv}\, v_{nb}' - \left(d_{v\xi}\, p_\xi'\, \xi_y + d_{v\eta}\, p_\eta'\, \eta_y\right) \qquad (2.19)$$

where the subscript for pressure denotes partial derivatives. The method of treatment of the term under the summation sign decides the algorithm which is being used. If $u_{nb}' = 0$ is assumed the summation term is simply dropped and a SIMPLEC type algorithm results. In the SIMPLEC algorithm the individual corrections at neighbors are taken to be the same as at point P, i.e. $u_{nb}' \approx u_P'$. With this approximation the summation term is merged with the term on the left hand side. In the PISO algorithm, discussed in section 2.2.3, the neighbor velocity corrections u_{nb}' are

evaluated with the last iteration (correction) level of the predictor-correctors procedure.

The continuity equation is then integrated over the typical computational cell to give

$$\frac{\rho'}{\Delta t} + (\rho U_e)' A_e \sin \alpha_e - (\rho U_w)' A_w \sin \alpha_w + (\rho V)'_n A_n \sin \alpha_n - (\rho V)'_s A_s \sin \alpha_s = m$$

where

$$m = (\rho U)_e A_e \sin \alpha_e - (\rho U)_w A_w \sin \alpha_w + (\rho V)_n A_n \sin \alpha_n - (\rho V)_s A_s \sin \alpha_s \qquad (2.20)$$
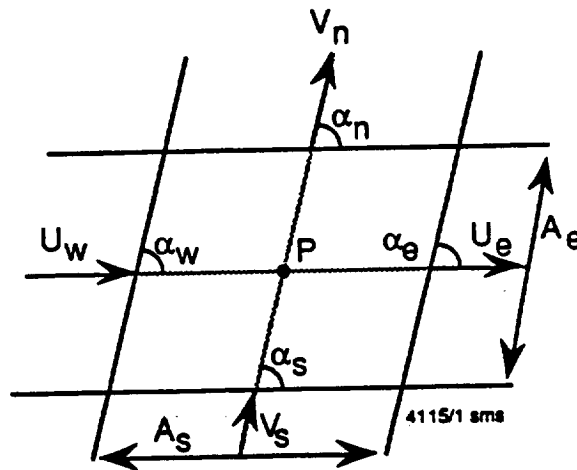
Figure 2.3 Control Volume Nomenclature for BFC Grids

Referring to Figure 2.3, α denotes the angle between the constant ξ and η lines, and the subscripts w,e,n,s refer to the sides of the cell, and A denotes the area of a cell side. The correction in the contravariant components are

$$U' = u'\xi_x + v'\xi_y \qquad (2.21)$$

$$V' = u'\eta_x + v'\eta_y \qquad (2.22)$$

2-9

Expressions for u' and v', Equations 2.21 and 2.22 are now substituted in Equation 2.20 to provide a pressure-correction equation of the form

$$\frac{\rho'}{\Delta t} + a_{Pp}\, p'_P = \sum a_{nbp}\, p'_{nb} - m \tag{2.23}$$

For incompressible flows the ρ' term is taken as zero. For compressible flows it is expressed as

$$\rho' = \frac{p'}{RT} = \frac{\rho}{p}\, p' \tag{2.24}$$

and is absorbed in the coefficient associated with p'_P. Solution of Equation 2.23 provides pressure corrections at the cell centers which then are used to calculate corrections in other variables:

$$u' = -\left(d'_{u\xi}\, p'_\xi\, \xi_x + d_{u\eta}\, p'_\eta\, \eta_x\right) \tag{2.25}$$

$$v' = -\left(d'_{v\xi}\, p'_\xi\, \xi_y + d_{v\eta}\, p'_\eta\, \eta_y\right) \tag{2.26}$$

$$\rho' = \frac{p'}{RT} \tag{2.27}$$

Finally these corrections are used to update the velocities, pressure and the density.

$$u^{n+1} = u^* + u' \tag{2.28}$$
$$v^{n+1} = v^* + v' \tag{2.29}$$
$$\rho^{n+1} = \rho^n + \rho' \tag{2.30}$$
$$p^{n+1} = p^n + p' \tag{2.31}$$

This completes a typical iteration in the SIMPLEC procedure for steady-state equations. For steady solutions the time-step Δt provides one form of underrelaxation. The PISO algorithm also follows similar steps, and at this point the predictor and the first corrector step in this algorithm would be complete.

Evaluation of the mass source term in Equation 2.20 is critical to the success of the colocated grid formulation. To calculate the mass source term the contravariant components at cell faces are needed which in turn are interpolated from the cell-centers. Improper interpolation procedures can lead to odd-even decoupling of pressure. The formulation used in the present work is described in the following subsection.

2.2.2 Mass-Carrying Velocity Interpolation

The basic concepts of this interpolation procedure will be developed for a 1-D problem for ease of understanding. The procedure outlined is similar to that in Reference 2. Extension to two dimensions is described next.
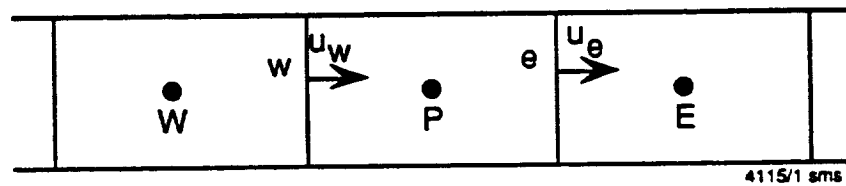
Figure 2.4 Schematic Grid for Mass-Carrying Velocity Interpolation

For this 1-D problem, the contravariant component, U, is the same as the Cartesian component u. The value of u at the cell face 'e' is to be calculated using the velocities at P and E. Use of a simple average to get:

$$u_e = \frac{1}{2}(u_P + u_E)$$

(2.32)

leads to odd-even decoupling of pressure. This is due to the fact that with this definition, the velocities at the cell faces do not directly depend on the pressure difference between the neighboring cell centers. This strong coupling is achieved in the staggered grid by physically shifting the location of cell face e. In the colocated grid formulation, the cell face velocities must be calculated with a direct coupling

with neighboring pressures. To achieve this, the momentum equations for the velocities at P, E and e are written:

$$u_P = \left(\sum a'_{nbu} u_{nb}\right)_P - d'_P \left(\frac{\partial p}{\partial x}\right)_P + S_P \qquad (2.33)$$

$$u_E = \left(\sum a'_{nbu} u_{nb}\right)_E - d'_E \left(\frac{\partial p}{\partial x}\right)_E + S_E \qquad (2.34)$$

$$u_e = \left(\sum a'_{nbu} u_{nb}\right)_e - d'_e \left(\frac{\partial p}{\partial x}\right)_e + S_e \qquad (2.35)$$

where $a'_{nb} = \frac{a_{nb}}{a_P}$, $d'_P = \frac{d_P}{a_P}$, etc.

[Here the prime denotes that the term is divided by the coefficient associated with the velocity at P or E or e.] At this point the effect of time step and/or underrelaxation is ignored; it will be added at a later stage.

The various terms in Equation 2.35 are then approximated using the corresponding terms in Equations 2.33 and 2.34. Thus

$$\left(\sum a'_{nbu} u_{nb} + S\right)_e = \frac{1}{2}\left[\left(\sum a'_{nbu} u_{nb} + S\right)_P + \left(\sum a'_{nbu} u_{nb} + S\right)_E\right] \qquad (2.36)$$

and

$$d'_e = \frac{1}{2}\left(d'_P + d'_E\right) \qquad (2.37)$$

Substitution in Equation 2.35 yields

$$u_e = \frac{1}{2}\left[\left(\sum a'_{nbu} u_{nb} + S\right)_P + \left(\sum a'_{nbu} u_{nb} + S\right)_E\right] - \left(\frac{d'_P + d'_E}{2}\right)\left(\frac{\partial p}{\partial x}\right)_e \qquad (2.38)$$

Expansion of the terms under the summation signs gives rise to a large connectivity with nodal velocities and is complicated to evaluate. Instead, these terms are expressed as

2-12

$$\left(\sum a'_{nbu} u_{nb} + S\right)_P = u_P - d'_P \left(\frac{\partial p}{\partial x}\right)_P \qquad (2.39)$$

$$\left(\sum a'_{nbu} u_{nb} + S\right)_E = u_E - d'_E \left(\frac{\partial p}{\partial x}\right)_E \qquad (2.40)$$

Using these expressions in Equation 2.38 one obtains

$$u_e = \frac{1}{2}[u_P + u_E] - d'_e \left(\frac{\partial p}{\partial x}\right)_e + \frac{1}{2}\left[d'_P \left(\frac{\partial p}{\partial x}\right)_P + d'_E \left(\frac{\partial p}{\partial x}\right)_E\right] \qquad (2.41)$$

which is much simpler to evaluate. If a further approximation is made:

$$\frac{1}{2}\left[d'_P \left(\frac{\partial p}{\partial x}\right)_P + d'_E \left(\frac{\partial p}{\partial x}\right)_E\right] \approx \frac{d'_e}{2}\left[\left(\frac{\partial p}{\partial x}\right)_P + \left(\frac{\partial p}{\partial x}\right)_E\right] \qquad (2.42)$$

the final form of u_e is obtained:

$$u_e = \frac{1}{2}(u_E + u_P) - d'_e \left\{\left(\frac{\partial p}{\partial x}\right)_e - \frac{1}{2}\left[\left(\frac{\partial p}{\partial x}\right)_P + \left(\frac{\partial p}{\partial x}\right)_E\right]\right\} \qquad (2.43)$$

The other cell face velocity, u_w now can be calculated in a similar fashion. When these velocities are used to calculate the mass source term, the pressure derivatives add together to generate a fourth-order derivative of pressure. This serves to suppress odd-even decoupling of pressure by providing a stronger coupling between cell pressures.

Next step is to include the effect of time derivatives and/or underrelaxation terms. Improperly done, this can give rise to steady-state solutions which depend on the size of the underrelaxation used. The following analysis is similar to that developed in Reference 4. Equations 2.39 to 2.41 are rewritten as

$$\left(a_{Pu} + \frac{\rho \forall}{\Delta t}\right) u_P = \left(\sum a_{nb} u_{nb}\right)_P - d_P \left(\frac{\partial p}{\partial x}\right)_P + S_P + \frac{\rho \forall}{\Delta t} u_P^\circ \qquad (2.44)$$

$$\left(a_{Pu} + \frac{\rho \forall}{\Delta t}\right) u_E = \left(\sum a_{nb} \, u_{nb}\right)_E - d_E \left(\frac{\partial p}{\partial x}\right)_E + S_E + \frac{\rho \forall}{\Delta t} u_E^o \qquad (2.45)$$

$$\left(a_{Pu} + \frac{\rho \forall}{\Delta t}\right) u_e = \left(\sum a_{nb} \, u_{nb}\right)_e - d_e \left(\frac{\partial p}{\partial x}\right)_e + S_e + \frac{\rho \forall}{\Delta t} u_e^o \qquad (2.46)$$

where it is assumed that the time term serves as the underrelaxation factor for steady solution. These equations now have a modified coefficient with the velocities, and also include a term with last iteration/time-step values of the velocities, denoted by the superscript o.

Following an analysis similar to that given earlier, the expression for u_e is now written as

$$u_e = \frac{1}{2}\left[u_P + u_E\right] - d_e' \left\{\left(\frac{\partial p}{\partial x}\right)_e - \frac{1}{2}\left[\left(\frac{\partial p}{\partial x}\right)_P + \left(\frac{\partial p}{\partial x}\right)_E\right]\right\} +$$

$$\frac{(\rho \forall)_e}{\Delta t} \cdot \frac{1}{\left(a_{Pu} + \frac{\rho \forall}{\Delta t}\right)_e} \cdot \left[u_e^o - \frac{1}{2}(u_P^o + u_E^o)\right] \qquad (2.47)$$

and the term associated with the time term is calculated as

$$\frac{1}{\left(a_{pu} + \frac{\rho \forall}{\Delta t}\right)_e} = \frac{1}{2}\left[\frac{1}{\left(a_{pu} + \frac{\rho \forall}{\Delta t}\right)_P} + \frac{1}{\left(a_{pu} + \frac{\rho \forall}{\Delta t}\right)_E}\right] \qquad (2.48)$$

Equation 2.48 is the final form of the interpolation procedure that can be used to calculate cell face velocities. Extension of these concepts to two-dimensional BFC grids is discussed below.

A typical computational cell in a 2-D BFC grid is shown in Figure 2.5. The contravariant components, U and V along the ξ and η axes are to be calculated using the velocities at the surrounding cell centers.
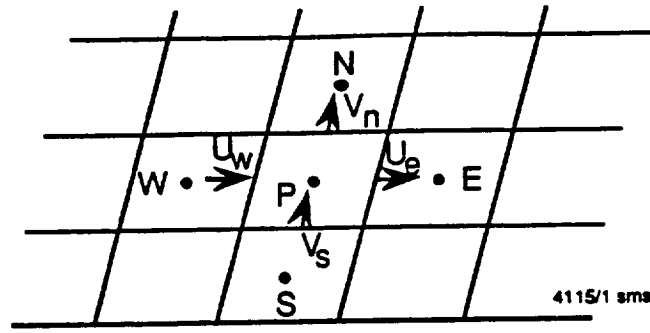
Figure 2.5 Convective Fluxes Passing Through BFC Control Volume Cell Faces

The components are given by

$$U_e = \left(uJ\xi_x + vJ\xi_y\right)_e \tag{2.49}$$

$$V_s = \left(uJ\eta_x + vJ\eta_y\right)_s \tag{2.50}$$

Thus, to arrive at the cell face contravariant components, both u and v have to be interpolated at each face. Consider the component at face 'e'. To calculate the Cartesian components the momentum equations at cell centers P and E are used. These are

$$u_E = \left(\sum a'_{nbu}\, u_{nb}\right)_E - d'_{u\xi E}\left(\frac{\partial p}{\partial \xi}\right)_E - d'_{u\eta E}\left(\frac{\partial p}{\partial \eta}\right)_E + S_{E,u} + \frac{\rho\forall}{\Delta t} u_E^o \tag{2.51}$$

$$v_E = \left(\sum a'_{nbv}\, v_{nb}\right)_E - d'_{v\xi E}\left(\frac{\partial p}{\partial \xi}\right)_E - d'_{v\eta E}\left(\frac{\partial p}{\partial \eta}\right)_E + S_{E,v} + \frac{\rho\forall}{\Delta t} v_E^o \tag{2.52}$$

where terms such as $d'_{u\xi E}$ now contain the metric coefficients which multiply the pressure derivatives. Similar expressions for these components at cell center P can be written. Since U_e is the component along the ξ direction, the pressure redistribution is applied only in the ξ direction. Thus,

$$u_e = \frac{1}{2}\left(u_P + u_E\right) - d'_{u\xi e}\left\{\left(\frac{\partial p}{\partial \xi}\right)_e - \frac{1}{2}\left[\left(\frac{\partial p}{\partial \xi}\right)_E + \left(\frac{\partial p}{\partial \xi}\right)_P\right]\right\} +$$

$$\frac{\left(\rho\forall\right)_e}{\Delta t} \cdot \frac{1}{\left(a_{pu} + \dfrac{\rho\forall}{\Delta t}\right)_e}\left(u_e^o - \frac{1}{2}\left(u_E^o + u_P^o\right)\right) \qquad (2.53)$$

$$v_e = \frac{1}{2}\left(v_P + v_E\right) - d'_{v\xi e}\left\{\left(\frac{\partial p}{\partial \xi}\right)_e - \frac{1}{2}\left[\left(\frac{\partial p}{\partial \xi}\right)_E + \left(\frac{\partial p}{\partial \xi}\right)_P\right]\right\} +$$

$$\frac{\left(\rho\forall\right)_e}{\Delta t} \cdot \frac{1}{\left(a_{pv} + \dfrac{\rho\forall}{\Delta t}\right)_e}\left(v_e^o - \frac{1}{2}\left(v_E^o + v_P^o\right)\right) \qquad (2.54)$$

Finally, the contravariant component U_e is calculated using Equation 2.49. The component along the η direction at, e.g., the south face is evaluated using the Cartesians at cell centers P and S, and the pressure redistribution terms along η direction only are taken into account.

This is the basic formulation which has been incorporated in the 2-D code to avoid the odd-even decoupling of pressure in the colocated grid formulation. Extension of this concept to a 3-D grid is straightforward, and not discussed here.

2.2.3 Solution Algorithms

A description of the solution algorithms currently implemented in the 2-D code is given in this subsection. The major solution steps are outlined for four schemes: 1) Modified SIMPLEC, 2) Crank-Nicholson, 3) Three-point backward time-differencing, and 4) PISO. The first three schemes use essentially the same basic solution algorithm, while the PISO scheme requires additional steps.

1. **Modified SIMPLEC:** This algorithm consists of three main steps.

  a. Evaluation of an intermediate velocity field, u^* and v^* by solving momentum equations such as 2.12 with lagged pressure terms;

b. The continuity equation, Equation 2.20 is solved next for pressure corrections. These are used to update pressures and velocities. Density is a updated for compressible flows;

In the standard SIMPLEC procedure this marks the end of an iteration and step (a) is taken next. In the modified SIMPLEC procedure, a step is added to ensure a tighter continuity condition.

c. With the updated flow variables in step (b) the mass source term in Equation 2.20 is reevaluated. Using the new mass source term the continuity equation is solved for pressure corrections. These are then used to update the flow variables again. The link coefficients in the pressure equation are kept frozen during this step. Step (c) is repeated till a suitable criterion is reached. At this point one iteration is considered complete and the next iteration started with step (a).

Steps (a) to (c) are repeated till a suitable convergence criterion is reached. This algorithm is the default option for steady-state flow solutions.

2. **Crank-Nicholson Scheme:** This algorithm is adopted for transient flow analysis and is formally second-order accurate in time. This is achieved by evaluating all convective and diffusive fluxes at time level *(n + 1/2)* where n is the old time level. The algorithm consists of the following steps:

a. Evaluate all flux terms using the last time-step variable values, *i.e.* at level n. These fluxes are not updated till the next time-step is taken;

b. Intermediate velocity field u^*, v^* is calculated using Equation 2.12 with lagged pressure. The convective and diffusive fluxes are calculated using the following expression.

$$(f_C + f_D) = \alpha (f_C + f_D)^k + (1 - \alpha)(f_C + f_D)^n \qquad (2.55)$$

where the superscript k denotes the iteration level. α is called the Crank-Nicholson parameter, and controls the implicitness of the scheme as well as the time-accuracy. The scheme is second order in time for $\alpha = 0.5;$.

c. Pressure corrections are evaluated using Equation 2.20. The mass source term in this equation is evaluated using

$$m = \alpha m^k + (1 - \alpha)m^n \qquad (2.56)$$

If needed, iterations on this step are done by updating the mass-source term. This is done in a fashion outlined in step (c) of the SIMPLEC procedure;

d. Steps (b) to (c) are repeated till a convergence criterion is reached. At this point the solutions at iteration level k are taken to be solutions at new time level $n+1$;

e. Time is advanced by a step, and calculations are started at step (a).

By changing the value of α, the order of accuracy and nature of the scheme can be changed. Thus $\alpha = 1$ corresponds to the Euler backward time discretization which is implicit in time and first-order accurate.

3. **Three-point backward time-discretization:** This is another second-order time-accurate method for transient flow analysis. The high-order accuracy is achieved by discretization of the time derivative using a three-point method.

$$\frac{\partial \phi}{\partial t} = \frac{3\phi^{n+1} - 4\phi^n + \phi^{n-1}}{2\Delta t} \qquad (2.57)$$

where superscripts $n-1$, n, and $n+1$ denote different time levels. This is also an iterative algorithm and the steps are:

a. Time terms are calculated based on the expression given above;

b. This step essentially involves iterations of the SIMPLEC procedure with the additional time term at n-1 carried as a source; and

c. At convergence of step (b), the variables are updated and a new time step is taken. Calculations for this step start from step (a).

4. PISO Algorithm: This is the non-iterative algorithm implemented in the 2-D code for transient flow analysis. The solution steps consist of a predictor step followed by a series of corrector steps; the basic procedure is outlined in a paper by Issa[5]. The algorithms for incompressible and compressible flows differ somewhat and each is outlined below.

Incompressible flows. For these flows there is no density variation, so that the energy equation need not be calculated during the predictor-corrector sequence for velocities and pressure. The algorithm steps are:

a. With a new time-step, an intermediate velocity field, u^* and v^* is calculated using momentum equations, Equation 2.12. This is the predictor step;

b. For the first corrector, the pressure correction equation, Equation 2.20 is solved to yield pressure corrections. These are then used to update flow variables to u^{**}, v^{**} and p^*;

c. A pressure correction equation followed by an explicit momentum corrector equation completes the second corrector step. The pressure correction equation is

$$\tilde{a}_{Pp}\, p'_P = \sum a_{nbp}\, p'_{nb} - m^{**} - \sum a_{nbu}\left(u^{**}_{nb} - u^*_{nb}\right) -$$
$$\sum a_{nbv}\left(v^{**}_{nb} - v^*_{nb}\right), \quad p' = p^{**} - p^* \tag{2.58}$$

The pressure corrections are used in the momentum correction equation for u'

$$\tilde{a}_{Pu}\, u_P' = \sum a_{nbu}\left(u_{nb}^{**} - u_{nb}^{*}\right) - d_P'\left(\frac{\partial p}{\partial x}\right), \qquad u_P' = u_P^{***} - u_P^{**} \tag{2.59}$$

where the tilde denotes that the time term has been absorbed in that term. A similar equation for v' is solved. With these corrections, the flow variables are updated to u^{***}, v^{***}, and p^{**}. This completes one time step in this algorithm. The corrected variable values are taken as the new time-level values; and

d. A new time step in taken and calculations started at step (a).

Compressible Flows. PISO algorithm for compressible flows is more involved, since the density variations have to be calculated. This is incorporated in the momentum and continuity equations. In addition, the energy equation has to be solved at each corrector stage to update the temperature. The solution steps in this method are:

a. With a new time-step the first predictor and corrector steps are taken using the procedures outlined in Equations 2.12 and 2.20. The values of the variables at this stage are u^{**}, v^{**}, p^*, and ρ^*;

b. Using the updated values, the energy equation is assembled and solved to generate the corrected values of the temperature T^*;

c. The second corrector step now involves solution of p' again using a correction equation. The form of this equation is:

$$\tilde{a}_{Pp}\, p_P' = \sum a_{nbp}\, p_{nb}' - \frac{\rho \forall}{\Delta t} - m^{**} - \sum \rho^* a_{nbu}\left(u_{nb}^{**} - u_{nb}^{*}\right) -$$
$$\sum \rho^* a_{nbv}\left(v_{nb}^{**} - v_{nb}^{*}\right) + b, \qquad p' = p^{**} - p^* \tag{2.60}$$

Solution of this equation, the p' field is then used to update the velocity fields to u^{***} and v^{***} using equations such as:

$$\tilde{a}_{Pu}\, u_P^{***} = \sum a_{nbu}\, u_{nb}^{**} - d\left(\frac{\partial p'}{\partial x}\right) + S_u \tag{2.61}$$

A similar equation for v^{***} is used. At the end of this step, the flow variables are updated to u^{***}, v^{***}, p^{**} and ρ^{**};

d. The energy equation is again assembled and solved to yield the corrected values of the temperature, T^{**}. This is the second energy corrector step;

e. This completes the so-called two stage scheme. If desired the steps (d) and (e) can be repeated to add more corrector stages. At the end of this series, the updated values of the flow variables are taken to be the new time level values; and

f. A new time step is taken and the calculations are started at step (a).

2.3   Status of the 2-D Code

In the present form, the 2-D code is based on the colocated grid formulation described above, and uses the Cartesian components as the primary velocity variables. The modified SIMPLEC algorithm is the default for steady-state flow solutions, while the schemes available for transient analyses are:

1. First-order accurate backward differencing;
2. Three-point, second-order accurate time differencing;
3. Crank-Nicholson scheme; and
4. PISO scheme.

A comprehensive set of boundary conditions is provided which includes:

1. Specified velocities;
2. Specified pressure;
3. Wall boundary;
4. Symmetry condition; and
5. Zero-gradient extrapolation condition.

Profiles for all the flow variables can also be specified at all boundaries if known, *e.g.* for pre-swirl inlet conditions in a seal flow.

In the colocated formulation, the pressure at cell faces is used to calculate the pressure derivatives needed in the momentum equations. Proper evaluation of pressures at the boundaries thus becomes important. Two types of second-order accurate pressure extrapolation procedures are used at the boundaries in the 2-D code.
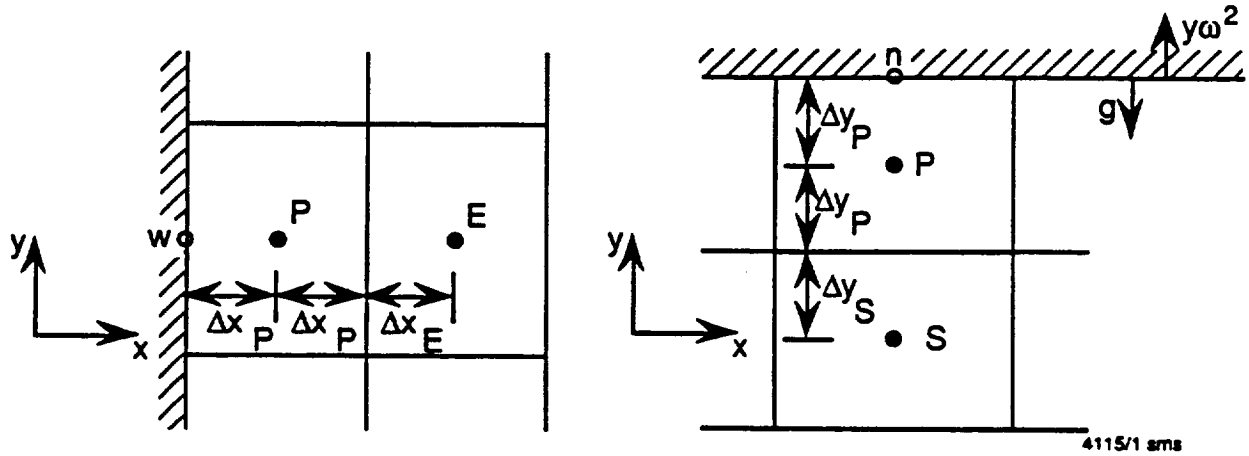
Figure 2.6 Nomenclature for Pressure Boundary Condition Interpolation

1. For an inflow condition the slope at the boundary is assumed to be the same as at the nearest cell center. Referring to Figure 2.6, the boundary pressure can be calculated as

$$p_w = \frac{\left(2\Delta x_P + 2\Delta x_E\right)}{\left(\Delta x_P + \Delta x_P\right)} p_P - \frac{\Delta x_P}{\left(\Delta x_P + \Delta x_E\right)} p_E$$

(2.62)

2. For extrapolation, symmetry, and wall conditions, the slope at the boundary is calculated using a second order extrapolation. The slope at the boundary is given by:

$$\frac{\partial p}{\partial y} = \frac{p_P \Delta x_P^2 - p_S \Delta x_P^2 - p_n\left[\left(2\Delta x_P + \Delta x_S\right)^2 - \Delta x_S^2\right]}{\left(2\Delta x_P + \Delta x_S\right)^2 \Delta x_P - \Delta x_P^2 \left(2\Delta x_P + \Delta x_S\right)}$$

(2.63)

If the slope is specified to be zero, the expression for the pressure at the boundary becomes

$$p_n = \frac{p_P \left(2\Delta x_P + \Delta x_S\right)^2 - p_S \, \Delta x_\beta^2}{\left(2\Delta x_P + \Delta x_S\right)^2 - \Delta x_\beta^2}$$

(2.64)

For swirling flows the centrifugal acceleration has to be taken into account. This is accomplished by specifying the pressure slope in terms of the angular speed ω at the boundary.

$$\left(\frac{\partial p}{\partial y}\right)_n = \left(\rho y \omega^2\right)_n$$

(2.65)

$$p_n = \frac{p_P \left(2\Delta x_P + \Delta x_S\right)^2 - p_S \, \Delta x_\beta^2}{\left(2\Delta x_P + \Delta x_S\right)^2 - \Delta x_\beta^2} + \frac{\left(\rho y \omega^2\right)_n \Delta x_P \left(2\Delta x_P + \Delta x_S\right)}{3\Delta x_P + \Delta x_S}$$

(2.66)

Finally, if a body-force is present, such as gravity, it is used to specify the pressure derivative. Thus, e.g. for gravity force, the pressure derivative and boundary pressure are given by

$$\left(\frac{\partial p}{\partial \xi}\right)_n = -\left(\rho g\right)_n$$

(2.67)

$$p_n = \frac{p_P \left(2\Delta x_P + \Delta x_S\right)^2 - p_S \, \Delta x_\beta^2}{\left(2\Delta x_P + \Delta x_S\right)^2 - \Delta x_\beta^2} - \frac{\left(\rho g\right)_n \Delta x_P \left(2\Delta x_P + \Delta x_S\right)}{3\Delta x_P + \Delta x_S}$$

(2.68)

The code is capable of handling incompressible and compressible flow. Several turbulence models are incorporated which are 1) mixing length model, 2) low Reynolds number k-ε model, 3) standard k-ε model with wall functions, and 4) multi-scale k-ε model.

One of the problems specific to seal geometries is a rotor undergoing whirling motion in a seal as shown in Figure 2.7. The 2-D code can be used to simulate such a rotor with the assumption that the axial pressure gradient is zero, or in other words, when there is no leakage. To facilitate this, a coordinate frame whirling with the

2-23

rotor is selected. When the whirl orbit is circular, this transformation reduces the time-dependent problem to a quasi-steady one. The momentum equations are then solved in terms of the relative velocities. Rotation of the axes gives rise to additional source terms, the Coriolis and centrifugal accelerations, which are added to the momentum equations.

$$\frac{\partial(\rho\vec{u}\xi)}{\partial t} + (\text{convective terms}) = (\text{Pressure} + \text{diffusive terms}) - \rho\vec{\Omega}\times(\vec{\Omega}\times\vec{r}) - 2\rho\vec{\Omega}\times\vec{u}$$

$$\qquad\qquad\qquad\qquad\qquad\qquad\qquad\qquad\qquad \underset{\text{Centrifugal}}{}\quad\underset{\text{Coriolis}}{} \qquad (2.69)$$

where Ω is the whirling angular speed. Finally, the velocity boundary conditions at the rotor and stator wall have to be modified, and are given by

$$\text{stator:} \quad \vec{u} = -\vec{\omega}\times\vec{r}$$
$$\text{rotor:} \quad (\vec{\Omega}-\vec{\omega})\times\vec{r} - (\vec{\Omega}-\vec{\omega})\times\vec{A}$$

where $\vec{A}$ is the position vector joining the centers of the rotor and the stator, and ω is the angular speed of the rotor. This formulation also has been incorporated in the 2-D code, and can be invoked by specifying a non-zero angular speed for precession.
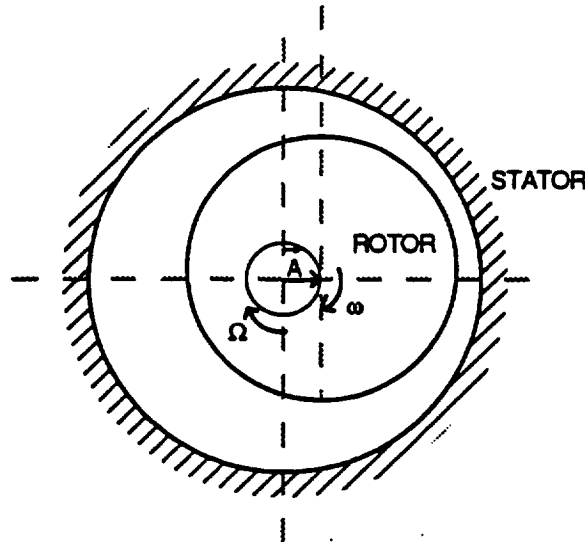
Figure 2.7 Schematics of Rotor/Stator Configuration With Circular Whirling Orbit

2.4   2-D Code Test Results

The 2-D code has already been used to calculate a range of standard flow solutions. These computational test cases were designed to assess overall accuracy of the code as well as the accuracy of the various physical models. Presented in this section are solutions for a number of selected test cases which have a direct relevance to the seals application. Accuracy of the numerical results is checked against analytical solutions in several cases. Two seal calculations are also presented at the end of the section which are checked against experimental data. These test cases serve to prove the capability of the computer code to calculate accurate and physically sound solutions.

2.4.1 Flow in an Annulus Between Two Cylinders
Problem Specification

- Developing flow in an annulus between two cylinders.
- Narrow annulus, ratio of inner to outer radii = 0.995.
- Laminar flow, Reynolds number based on outer radius = 100.
- Slug flow at inlet, fully-developed at the exit.

Benchmark Data

- Analytical solution for fully-developed flow.

Grid

- 20 cells in both axial and radial directions, evenly spaced.
- A maximum aspect ratio of 3×10^4.

Boundary Conditions

- Uniform flow at the inlet.
- Fixed pressure at the outlet.
- Wall conditions at both cylinder surfaces.

Results

- Flow description is given in Figure 2.8a.
- Figure 2.8b shows the calculated axial velocity as a function of radius at the last axial station. The analytical solution for the fully-developed flow is also plotted for comparison. Excellent agreement between numerical and analytical results is obtained.
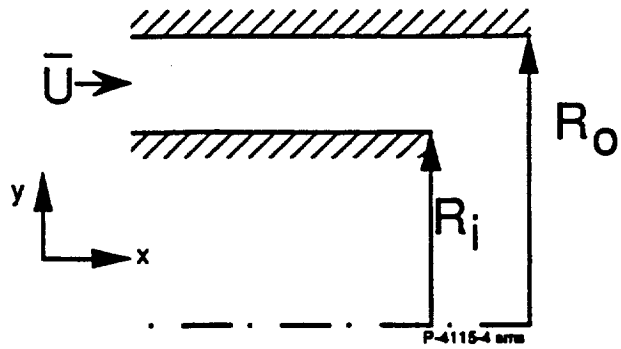
(a) Flow Geometry
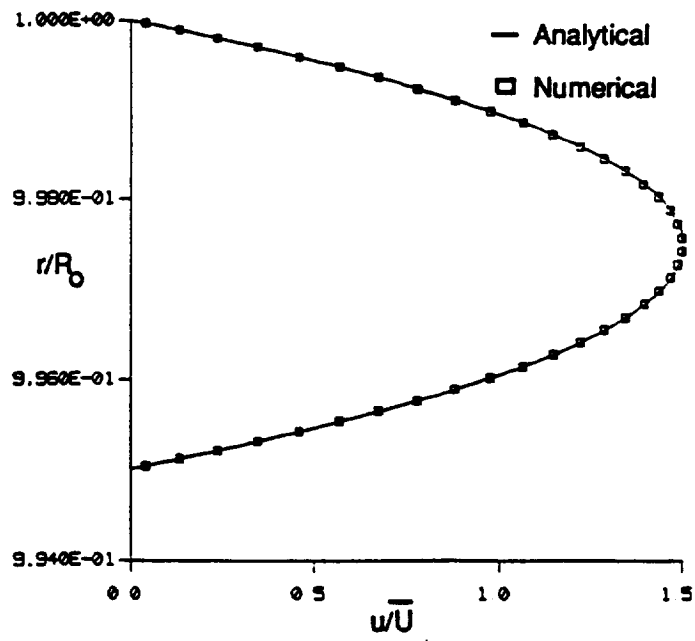
(b) u Velocity

Figure 2.8 Flow in an Annulus Between Two Cylinders. $R_i/R_o = 0.995$, 20 x 20 grid, grid aspect ratio = 3 x 10^4, $Re_{R_o} = 100$

2.4.2 Flow Between Rotating Cylinders
Problem specification

- Flow in the annulus between two cylinders.
- Inner cylinder rotating at 28650 rpm., stationary outer cylinder.
- Narrow annulus, ratio of inner to outer radii = 0.995.
- Laminar flow, no flow in axial and radial directions.

Benchmark data

- Analytical solution for the stable Taylor-Couette flow.

Grid

- 4 cells in the axial and 50 cells in the radial direction.
- Maximum aspect ratio = 3.6×10^4.

Boundary conditions

- Periodicity in axial direction, solutions at first and last axial stations are taken as identical.
- Wall conditions with specified angular speed =28650 rpm. at inner cylinder.
- Wall conditions with zero angular speed at outer cylinder.

Results

- Flow conditions and geometry shown in Figure 2.9a.
- Computed tangential velocity as a function of radius shown in Figure 2.9b. Corresponding analytical solution also plotted for comparison.
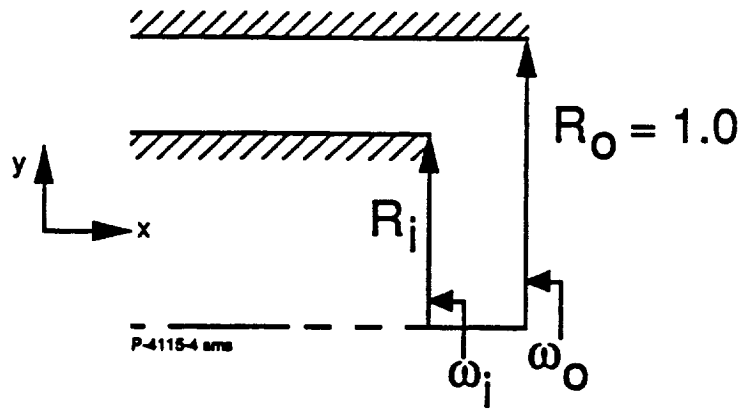
(a) Flow Geometry
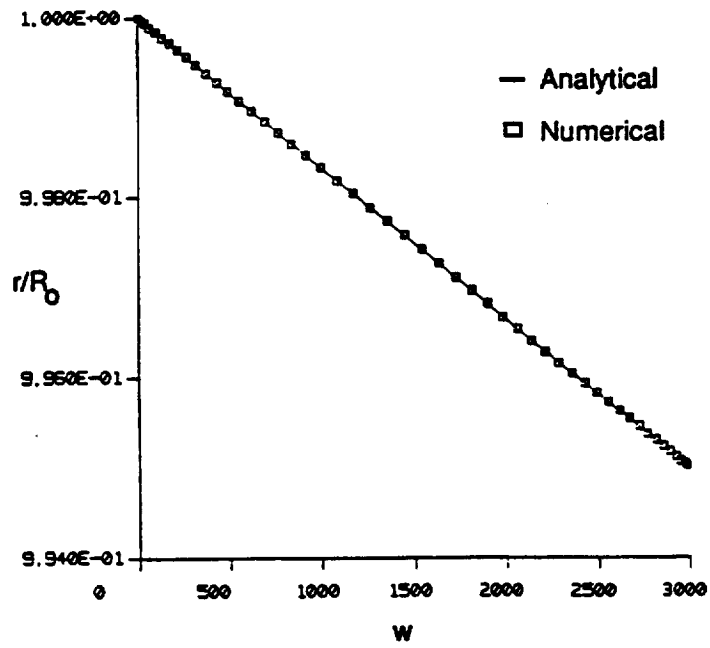
(b) Tangential Velocity w

Figure 2.9 Flow Between Rotating Cylinders, $R_i/R_o = 0.995$, $\omega_o = 0$, $\omega_i = 28650$ rpm.
4 x 50 grid, aspect ratio = 3.6 x 10⁴

2.4.3 Couette Flow
Problem specification

- Planar flow between two parallel, infinite plates.
- Top plate moving at a constant speed.
- Uniform pressure gradient is applied.

Benchmark data

- Analytical solution for Couette flow.

Grid

- 3 cells in the flow direction, 20 cells across the gap in the plates with even spacing in both directions.

Boundary conditions

- Periodicity conditions imposed at the cross-planes.
- Stationary wall at bottom plate.
- Wall condition with specified velocity at top plate.

Physical models

- The pressure gradient term is included as a special source term in the main-flow momentum equation.

Results

- Flow geometry and parameters are shown in Figure 2.10a.
- Flow solutions are obtained at several values of pressure gradient parameter ranging from -3 to +3. The corresponding numerical and analytical u velocity profiles are shown in Figure 2.10b.
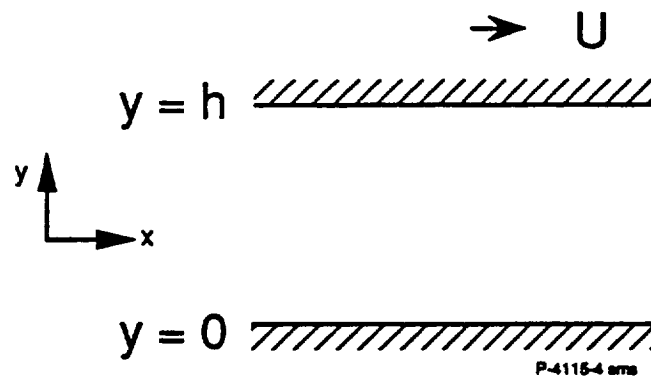
(a) Flow Geometry
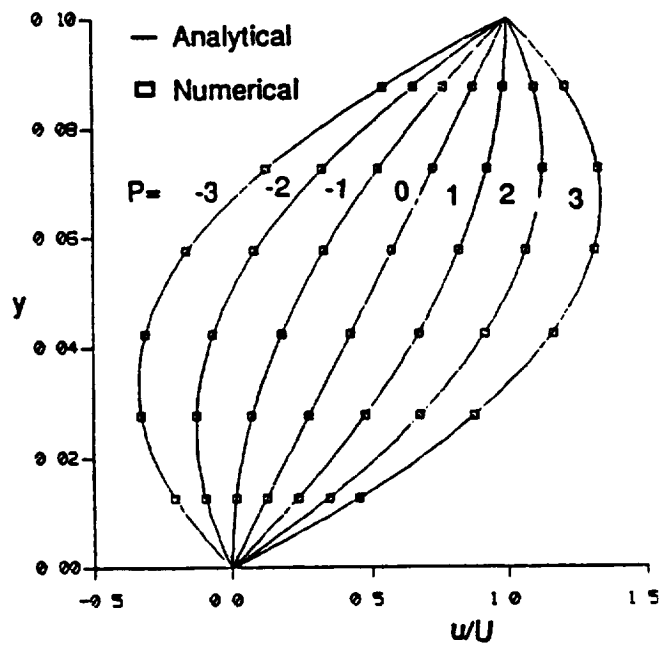
(b) u Velocity as a Function of P

Figure 2.10 Couette Flow. Pressure Gradient Coefficient $P = \dfrac{h^2}{2\mu U}\left(-\dfrac{\partial p}{\partial x}\right)$

2.4.4 Planar Wedge Flow
Problem specification

- Laminar flow in a narrow wedge-shaped passage. The top block is at rest; the bottom plate is moving.
- Flow passage is very narrow ($L/h = 3 \times 10^3$)

Benchmark data

- Analytical solution for the planar wedge flow.

Grid

- BFC grid with 192 cells along the length and 40 cells across the gap, evenly spaced.

Boundary conditions

- Wall condition on the slider block.
- Wall condition with specified velocity on the bottom plate.
- Specified pressures at the two passage openings.

Results

- Grid in shown in Figure 2.11a.
- Streamline pattern in the passage in shown in Figure 2.11b.
- Comparison of computed and analytical u velocity profiles at several locations along the length are shown in Figure 2.11c.
- Pressure across the passage is constant; computed and analytical pressure profiles along the length are shown in Figure 2.11d.
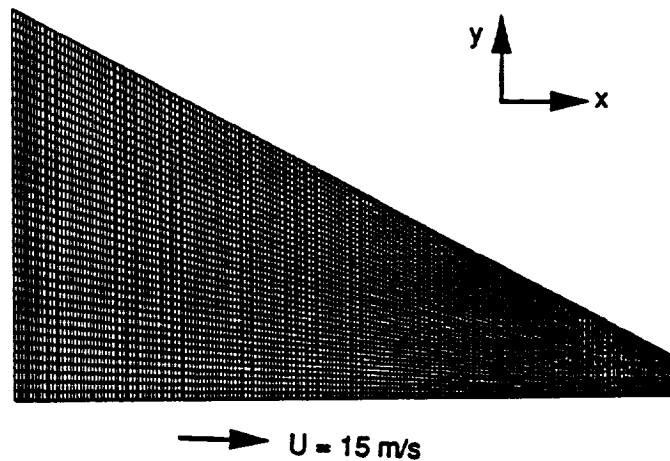
(a) 192 x 40 Computational Grid

U = 15 m/s
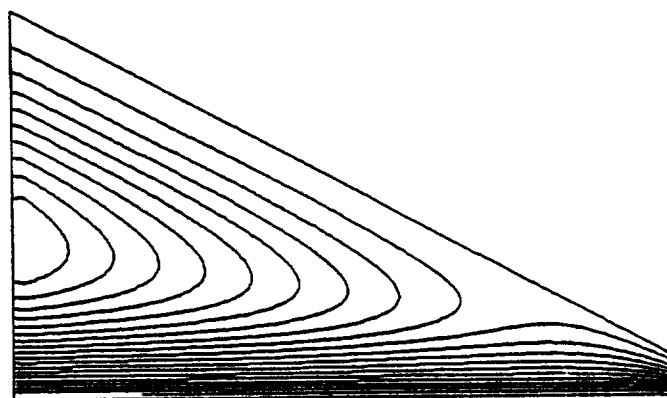
STRM	CONTOURS
FMIN	5 851E-03
FMAX	7 827E-01
CONTOUR	LEVELS
1	5 852E-03
2	4 469E-02
3	8 353E-02
4	1 224E-01
5	1 612E-01
6	2 001E-01
7	2 389E-01
8	2 777E-01
9	3 166E-01
10	3 554E-01
11	3 943E-01
12	4 331E-01
13	4 719E-01
14	5 108E-01
15	5 496E-01
21	7 826E-01

(b) Streamlines

Figure 2.11 Planar Wedge Flow. Length = 0.1m, Height: Minimum = 3 x 10^{-5}m, Maximum = 3 x 10^{-4}m, y Scale Enlarged 200 times in (a) and (b)
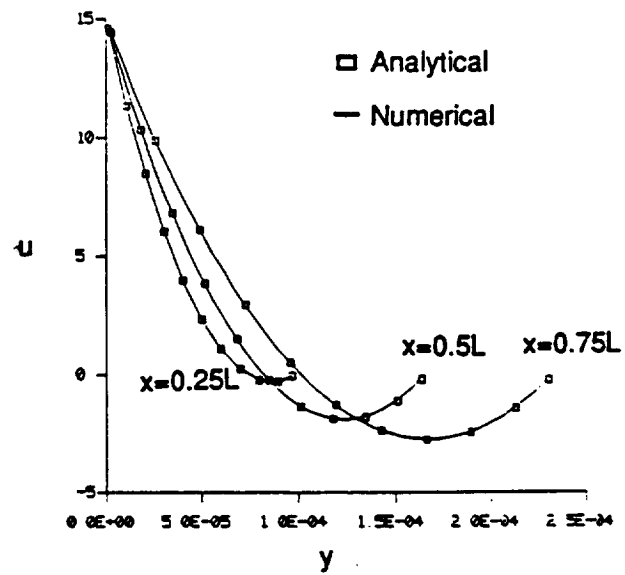
(c) u Velocity Profiles
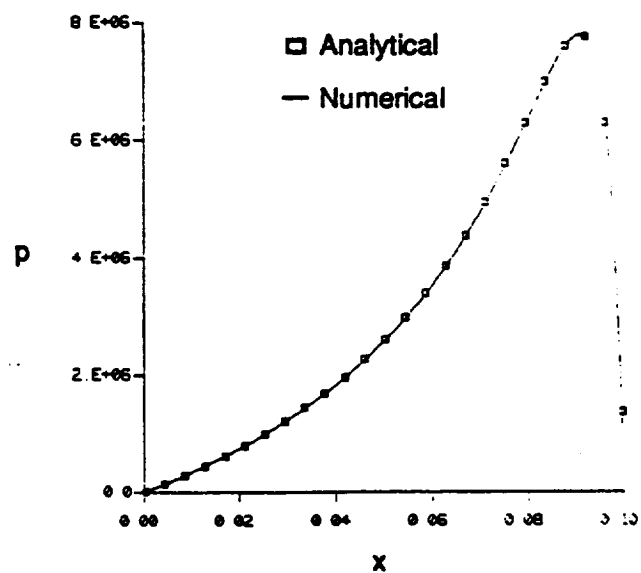
(d) Pressure

Figure 2.11 Planar Wedge Flow Continued

2.4.5 Laminar Flow Over Backstep
Problem specification

- Laminar flow over a planar backward facing step; expansion ratio = 1:1.94.
- Reynolds number = 100, 300, 389, 500 and 648.

Benchmark data

- Experimental data of Armaly, *et al.*[6].

Grid

- 110 cells in the flow-wise direction, 40 cells across. Cells clustered near the step in flow direction, and in the passage upstream of the step.

Boundary conditions

- Specified uniform axial velocity at inlet; value of the axial velocity varied depending of the Reynolds number.
- Specified pressure at outflow boundary.
- No-slip at all wall boundaries.

Results

- Reattachment length for the flow as a function of the Reynolds number is plotted in Figure 2.12a. Computed results are compared with experimental results[6].
- Figure 2.12b shows the streamline pattern for Reynolds number = 500.
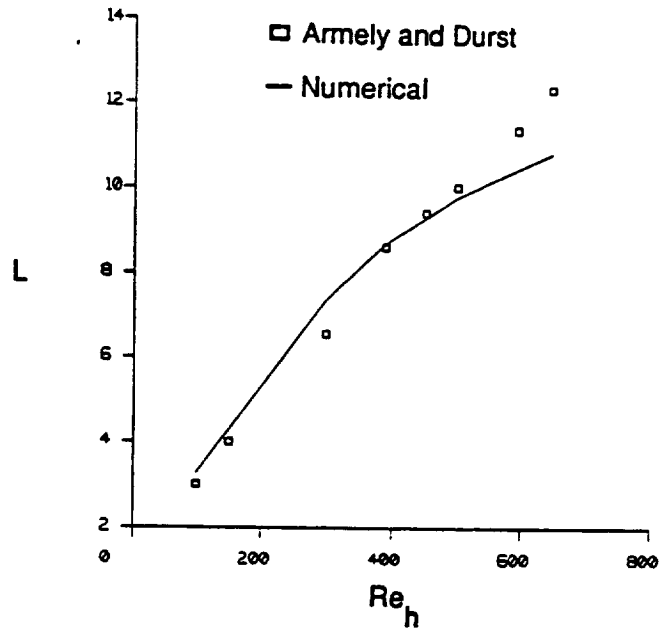
(a) Reattachment Length L = x/h
as a Function of Re_h

(b) Streamlines, Re_h = 500

```
STRM   CONTOURS
FMIN  -3 128E-04
FMAX   4 355E-03
CONTOUR LEVELS
  1    -3 000E-04
  2    -2 250E-04
  3    -1 500E-04
  4    -7 500E-05
  5     0 000E+00
  6     0 000E+00
  7     4 000E-04
  8     8 000E-04
  9     1 200E-03
 10     1 600E-03
 11     2 000E-03
 12     2 400E-03
 13     2 800E-03
 14     3 200E-03
 15     3 600E-03
 16     4 000E-03
```

Figure 2.12 Laminar Backstep Flow. 110 x 40 Grid

2.4.6 Turbulent Flow in a Plane Channel
Problem specification

- Turbulent flow in a planar channel; Reynolds number = 61,600.
- Treated as a developing flow problem, with fully developed flow at the channel end.

Benchmark data

- Hot-wire measurements by Laufer[7].

Grid

- 50 cells in the flow direction with even spacing. 40 cells in the cross direction with clustering near the wall for a specified cell width.

Boundary conditions

- Uniform flow specified at inlet.
- Constant pressure at the outflow.
- Wall conditions at upper and lower walls.

Physical models

- Standard k-ε model for turbulence with wall functions.

Results

- Flow details are shown in Figure 2.13a.
- Computed profiles of turbulence kinetic energy and streamwise velocity at the last station are plotted in Figures 2.13b and 2.13c. Also shown in these figures are the experimental data from Laufer[7].
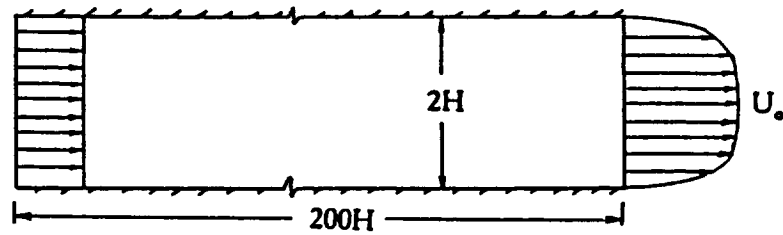
(a) Flow Geometry
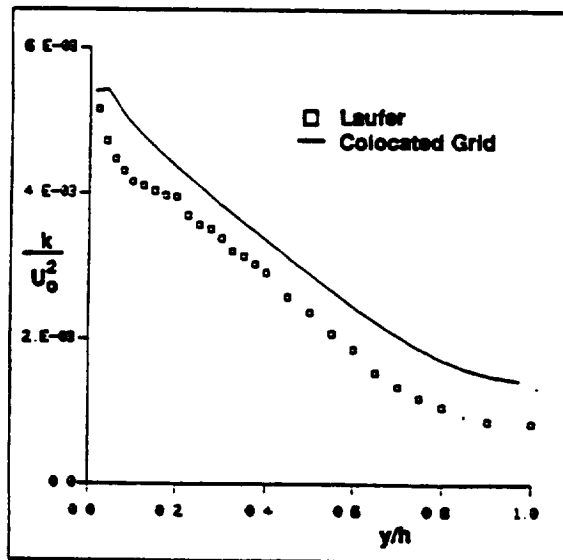
(b) Turbulent Kinetic Energy
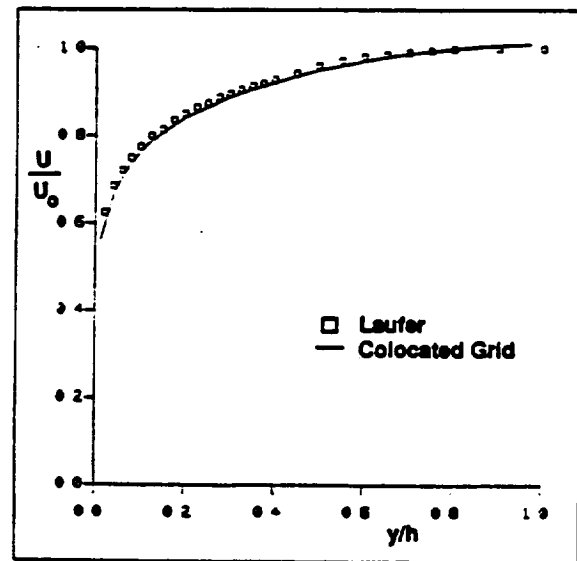
(c) Mean Velocity

Figure 2.13 Turbulent Flow in a Plane Channel.
Re = U_oH/y = 61,6000. Data from Laufer[7]

2.4.7 Turbulent Flow Induced by Rotating Disk in a Cavity
Problem specification

- Calculation of the flow induced by a rotating disk in an enclosed cavity.

Benchmark data

- Experimental measurements from Daily and Nece[8].

Grid

- 40 cells in the axial direction, 60 cells in the radial direction with clustering near the walls.

Boundary conditions

- Specified angular velocity for the rotor walls.
- Wall conditions for all other boundaries.

Numerics and physical models

- Central differencing with 0.05 damping.
- Standard k-ε model with wall functions.

Results

- Flow geometry as shown in Figure 2.14a.
- Normalized radial and tangential velocities at a given radius are shown in Figures 2.14b and 2.14c. Also shown in the figures are the experimental data from Daily and Nece[8].
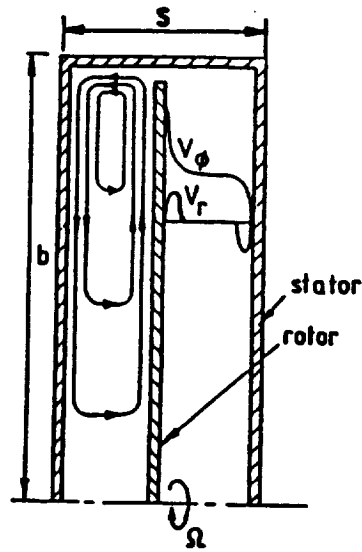
(a) Flow Geometry
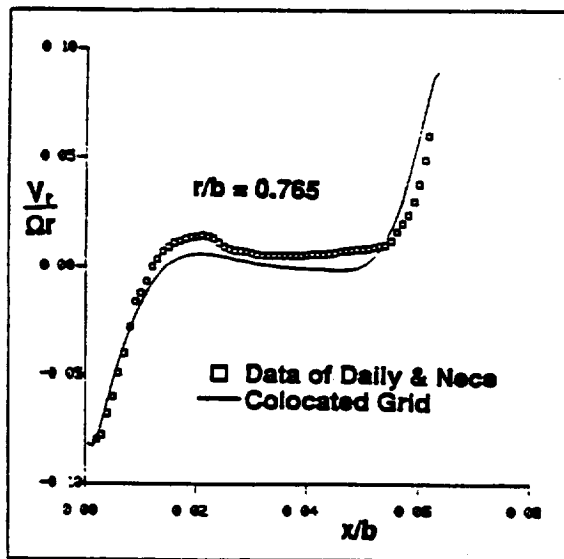
(b) Radial Velocity
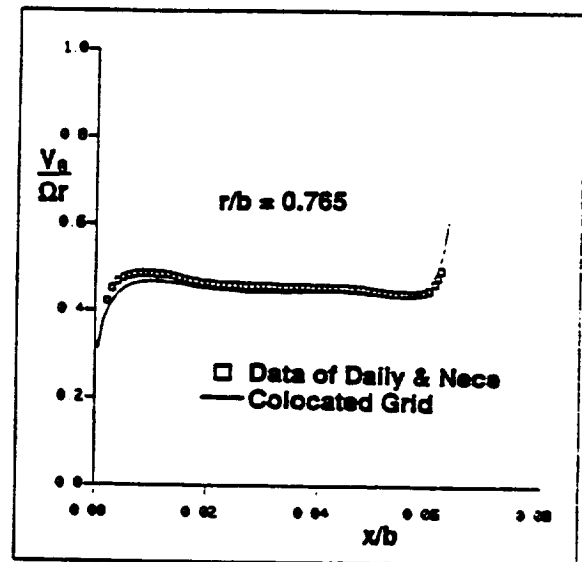
(c) Tangential Velocity

Figure 2.14 Turbulent Flow Due to a Rotor in an Enclosed Cavity.
Experimental Data from Daily and Nece[8]

2.4.8 Flow Between Stator and Whirling Rotor
Problem specification

- Flow in the clearance between a stator and a whirling rotor.
- Circular whirl orbit assumed. Calculations are performed in a coordinate frame whirling with the rotor.
- Solutions computed at whirl speeds of 0.01, 0.5 and 1 times the shaft angular speed.

Benchmark data

- None.

Grid

- 40 cells in the circumferential direction and 10 cells in the clearance, evenly spaced.

Boundary conditions

- Wall conditions with wall velocities corresponding to the transformed frame.
- Cyclic conditions assumed in the circumferential direction.

Numerics and physical models

- Central differencing with 0.05 damping.
- Standard k-ε model for turbulence.

Results

- Grid and flow geometry shown in Figure 2.15a.
- Pressure distribution in the clearance shown at the three whirl frequencies in Figures 2.15b through 2.15d.

(a) 40 x 10 Computational Grid

PRES	CONTOURS
FMIN	-3 003E+06
FMAX	6 197E+06

CONTOUR LEVELS

1	-3 003E+06
2	-2 519E+06
3	-2 035E+06
4	-1 551E+06
5	-1 066E+06
6	-5 822E+05
7	-9 792E+04
8	3 863E+05
9	8 706E+05
10	1 355E+06
11	1 839E+06
12	2 323E+06
13	2 808E+06
14	3 292E+06
15	3 776E+06
20	6 197E+06
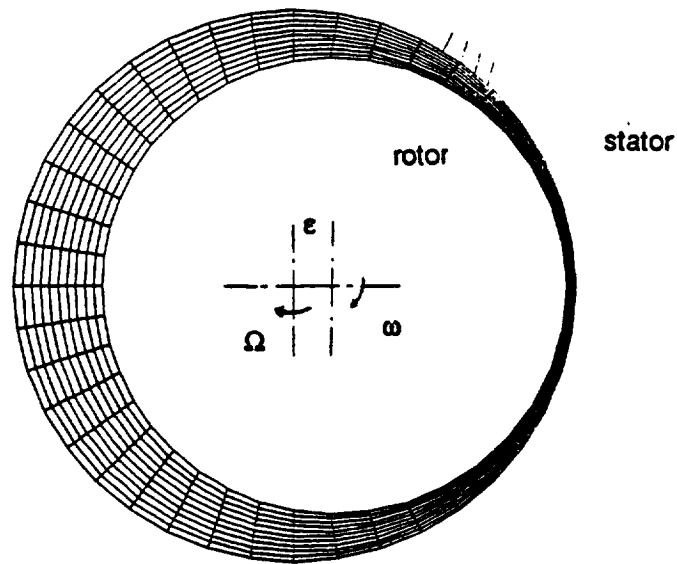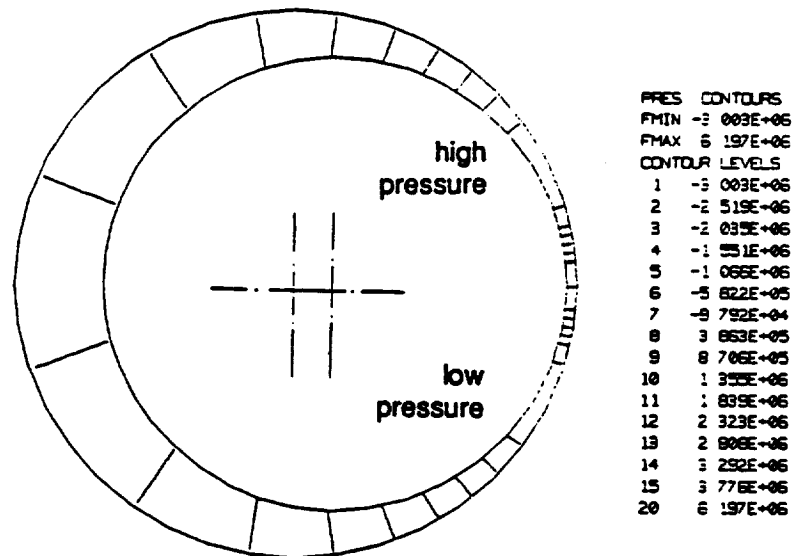
(b) Pressure Contours for Synchronous Whirl, $\Omega = \omega$

Figure 2.15 Flow in the Seal Clearance for a Whirling Rotor.
Stator Radius = 50.1478 x 10^{-3}m, Clearance = 495μm, ε = 0.8 x Clearance,
Shaft Rotation Speed ω = 5085rpm, Clearance Exaggerated for Clarity

PRES CONTOURS
FMIN -1 322E+05
FMAX 2 324E+04
CONTOUR LEVELS
1 -1 322E+05
2 -1 240E+05
3 -1 158E+05
4 -1 076E+05
5 -9 945E+04
6 -9 127E+04
7 -8 309E+04
8 -7 491E+04
9 -6 673E+04
10 -5 855E+04
11 -5 037E+04
12 -4 219E+04
13 -3 401E+04
14 -2 583E+04
15 -1 765E+04
20 2 324E+04

(c) Pressure Contours, Subsynchronous Whirl $\Omega = 0.5\omega$

PRES CONTOURS
FMIN -6 040E+06
FMAX 3 027E+06
CONTOUR LEVELS
1 -6 040E+06
2 -5 562E+06
3 -5 085E+06
4 -4 608E+06
5 -4 131E+06
6 -3 654E+06
7 -3 176E+06
8 -2 699E+06
9 -2 222E+06
10 -1 745E+06
11 -1 268E+06
12 -7 906E+05
13 -3 134E+05
14 1 638E+05
15 6 410E+05
20 3 027E+06

(d) Pressure Contours, Subsynchronous Whirl $\Omega = 0.01\omega$

Figure 2.15 Flow in the Seal Clearance for a Whirling Rotor Continued

2.4.9 Flow Over a Bank of Tubes (Brush Seals)
Problem specification

- Planar flow over a bank of tubes. This flow is similar to that in a brush seal.

Benchmark data

- None.

Grid

- Three rows of tubes with three tubes in each row considered.
- 60 cells in both directions; a BFC grid is employed.

Boundary conditions

- Specified uniform velocity at the inlet.
- Specified pressure at the outflow.
- Symmetry conditions specified at the two remaining outer boundaries.
- Wall conditions specified on all tube surfaces.
- Tubes simulated using blocked cells.

Results

- Grid and flow geometry is shown in Figure 2.16a.
- Computed pressure contours for this flow are shown in Figure 2.16b.

Symmetry

Pressure

Symmetry

Tube

(a) 60 x 60 Computational Grid

PRES CONTOURS
FMIN -4 346E+02
FMAX 6 687E+02
CONTOUR LEVELS
1   -4 346E+02
2   -3 794E+02
3   -3 243E+02
4   -2 691E+02
5   -2 140E+02
6   -1 588E+02
7   -1 036E+02
8   -4 847E+01
9   6 696E+00
10   6 186E+01
11   1 170E+02
12   1 722E+02
13   2 273E+02
14   2 825E+02
15   3 377E+02
21   6 687E+02
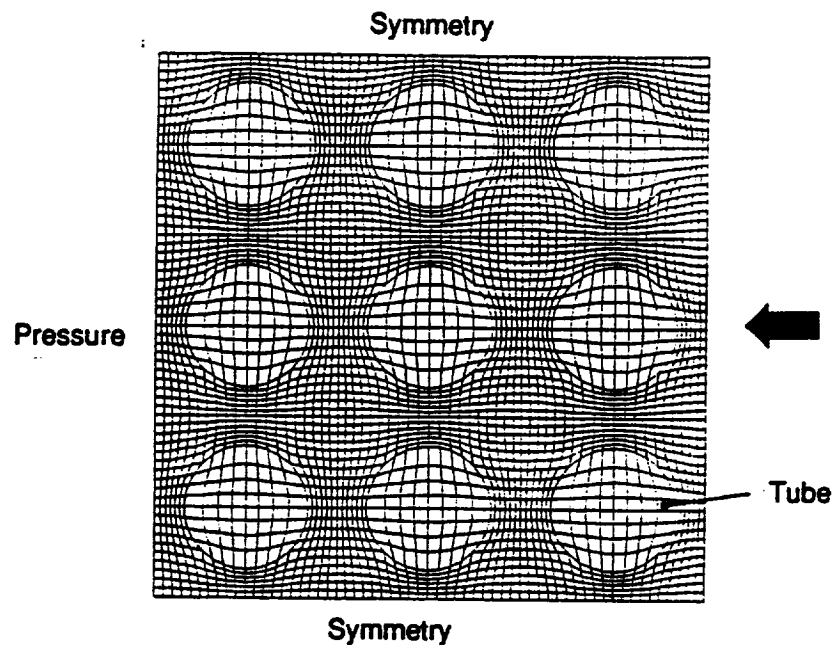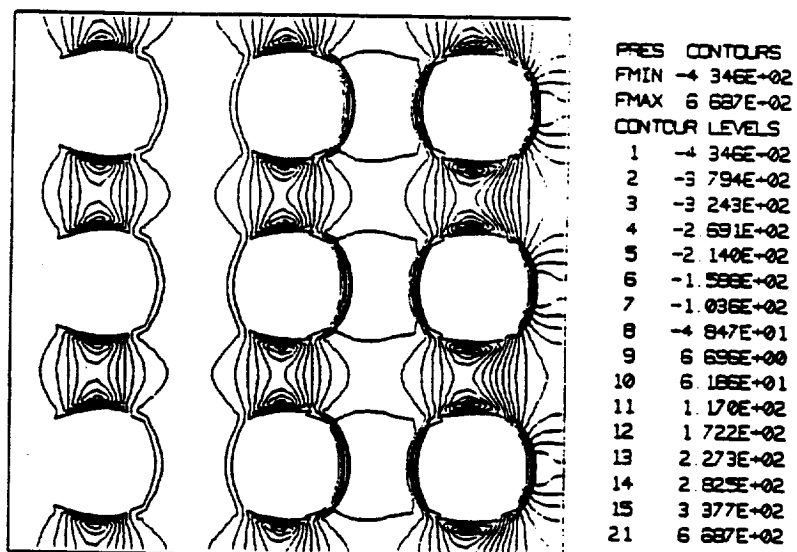
(b) Pressure Contours

Figure 2.16 Laminar Flow Over a Bank of Tubes

2.4.10   Annular Seal Flow
Problem specification

- Calculation of turbulent flow in an annular seal.

Experimental data

- Experimental data by Morrison, et al.[9].

Grid

- 25 cells in the radial direction, 58 cells in the axial direction; cells in radial direction clustered near the walls.

Boundary conditions

- Experimental profiles of the velocities and turbulence quantities at inlet boundary.
- Specified pressure at the outflow boundary.
- Wall condition with specified angular speed at rotor wall.
- Stationary wall conditions at stator wall.

Numerics and physical models

- Central differencing with 0.01 damping.
- Standard two equation k-e model for turbulence.

Results

- Geometry of the rotor is shown in Figure 2.17a, and the experimental setup is shown in Figure 2.17b.
- Computed and experimental contours of the axial, azimuthal and radial velocities are shown in Figures 2.18, 2.19 and 2.20, respectively.
- Figure 2.21 shows the computed turbulent kinetic energy profiles.
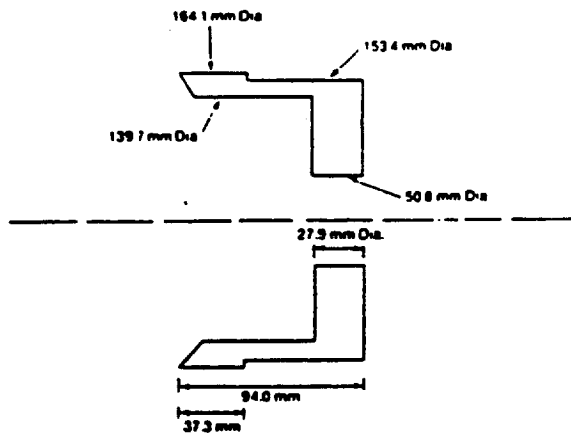
(a) Geometry of Annular Rotor
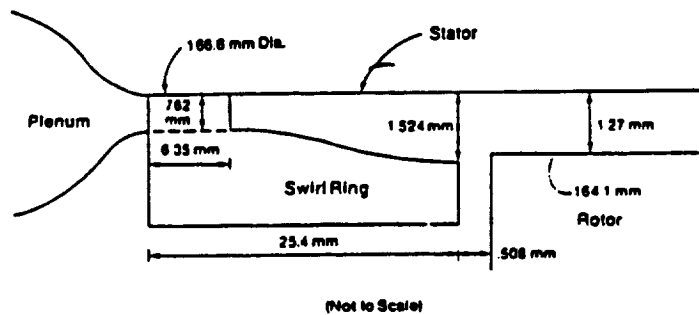
(b) Annular Seal Inlet Geometry

Figure 2.17 Flow Details for the Annular Seal. Reynolds Number Based on the gap = 27000, Taylor Number = 6600, Shaft Speed = 3600 rpm
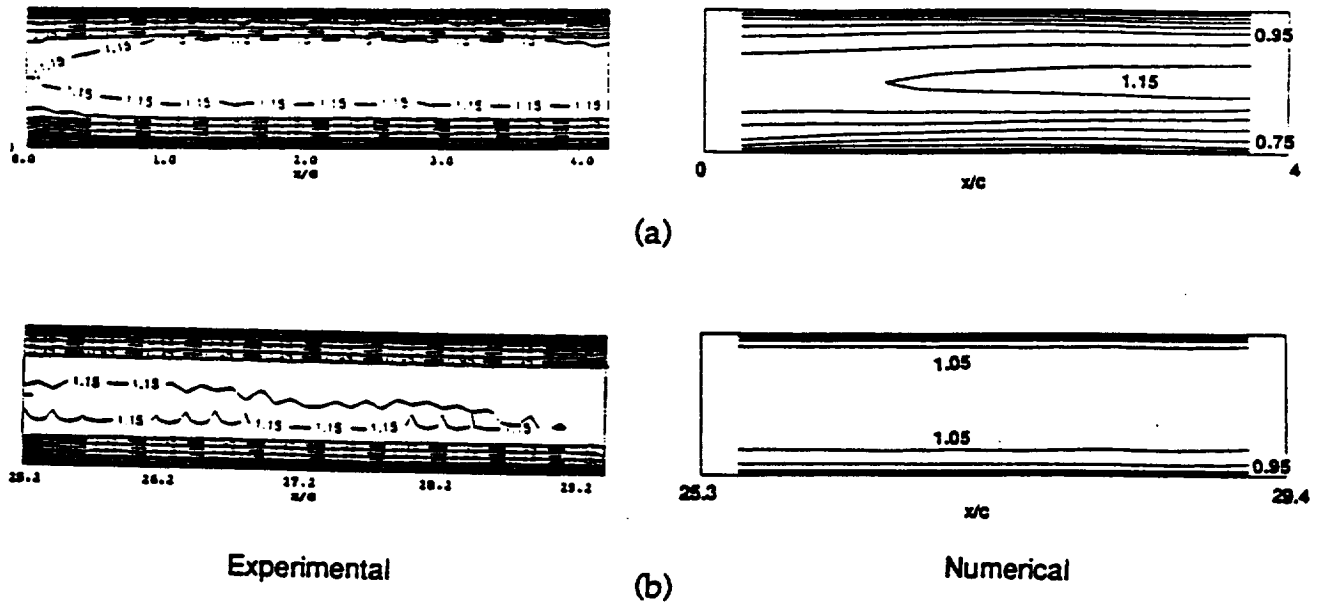
Figure 2.18 Annular Seal Flow. Contours of the Scaled Axial Velocity u_x/U. (a) Near Inlet ($0 < x/c < 4$), (b) Near Outlet ($25 < x/c < 29.4$)
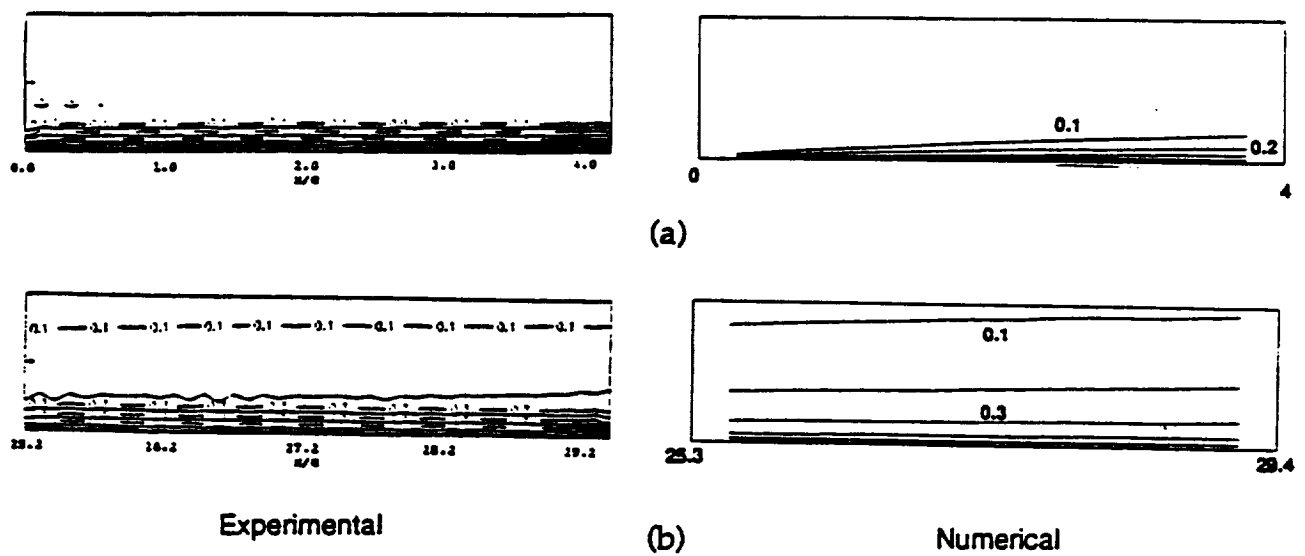
Figure 2.19 Annular Seal Flow. Contours of the Scaled Azimuthal Velocity, u_θ/w_{shaft} (a) Near Inlet ($0 < x/c < 4$), (b) Near Outlet ($25 < x/c < 29.4$)

Experimental   **Numerical**
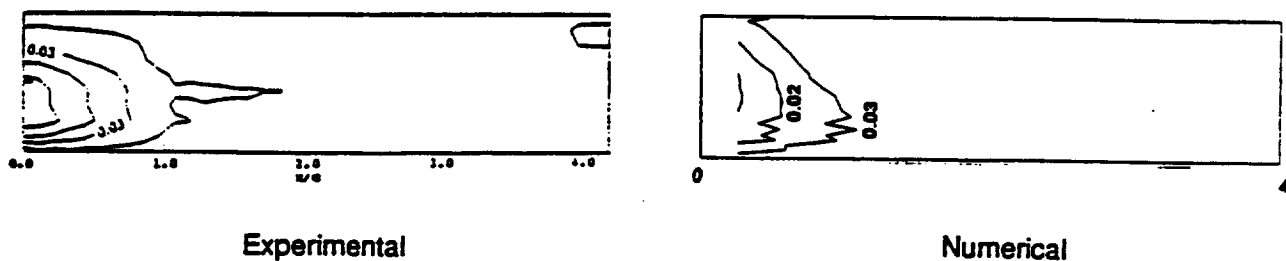
Figure 2.20 Annular Seal Flow. Contours of Scaled Radial Velocity u_r/U.
Near Inlet Details $(0 < x/c < 4)$

(a)   (b)
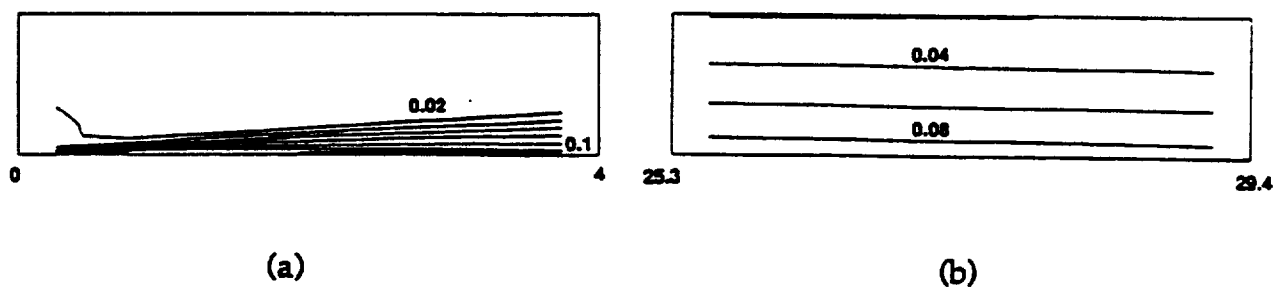
Figure 2.21 Annular Seal Flow. Contours of Scaled Turbulent Kinetic Energy,
$\frac{1}{2}\left(u_r'^2 + u_\theta'^2 + u_x'^2\right)/U^2$. Numerical Results, (a) Near Inlet $(0 < x/c < 4)$,
(b) Near Outlet $(25 < x/c < 29.4)$

2.4.11   Seven Cavity Labyrinth Seal
Problem specification

- Calculation of turbulent flow in a seven-cavity labyrinth seal.

Experimental data

- Experimental data by Morrison, *et al.*[10].

Grid

- 30 cells in the axial and radial directions per cavity.
- 10 cells in the radial clearance between the rotor tooth and the stator.
- Stretching used to cluster the grid near the rotor and stator walls.

Boundary conditions

- Experimental profiles for velocities and turbulence quantities at inlet boundary.
- Specified pressure at outflow boundary.
- Wall condition with specified angular velocity at rotor walls.
- Wall conditions at stator wall.

Numerics and physical models

- Central differencing with 0.01 damping.
- Standard two equation k-e model for turbulence.

Results

- Details of the rotor are shown in Figure 2.22a, and the experimental setup is shown in Figure 2.22b.
- Computed and numerical velocity vector plots are shown in Figure 2.23.
- Computed and experimental contours of the axial, radial and tangential velocities are shown in Figures 2.24, 2.25 and 2.26, respectively.
- Figure 2.27 shows computed contours of the turbulent kinetic energy.
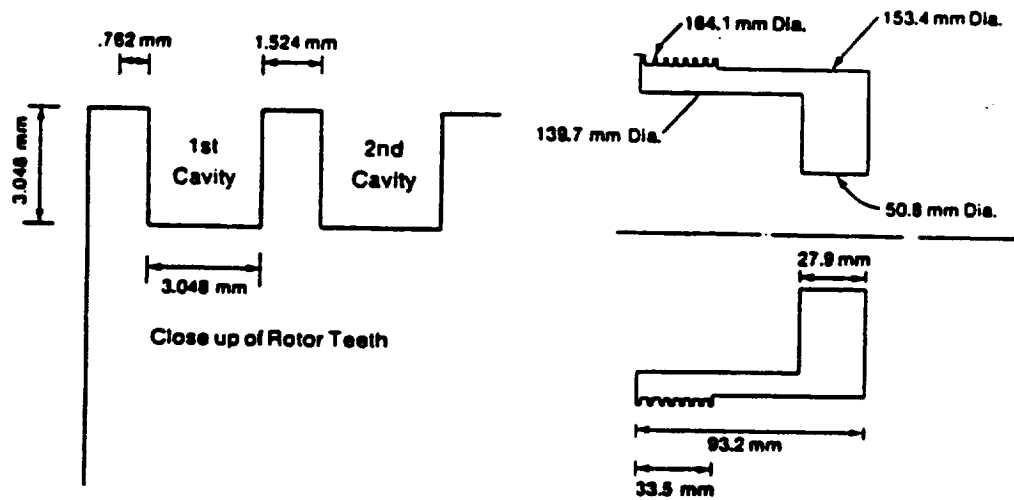
(a) Details of the Labyrinth Rotor
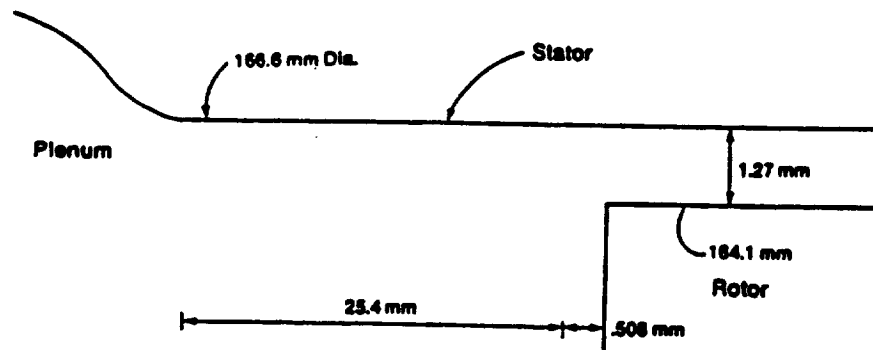
(b) Seal Inlet Geometry

Figure 2.22 Seven Cavity Labyrinth Seal Flow. Reynolds Number Based on the Clearance = 28000, Taylor Number = 7000, Shaft Speed = 3600 rpm
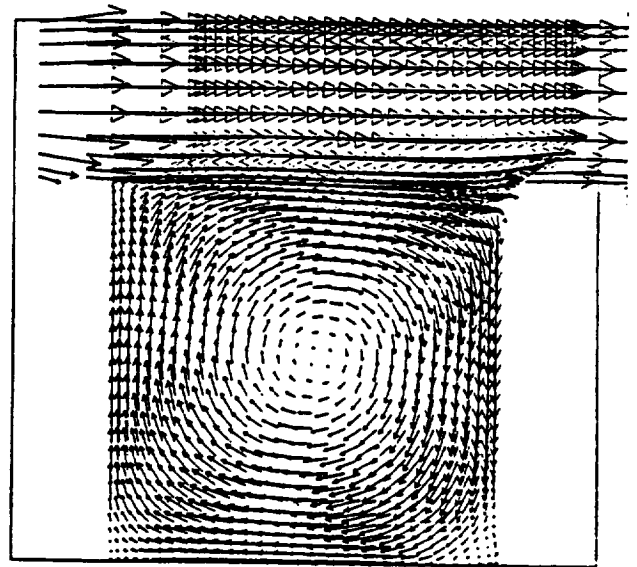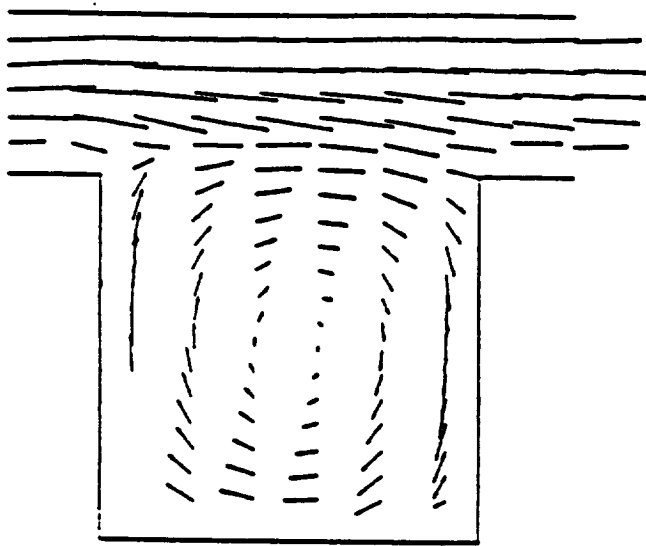
First Cavity
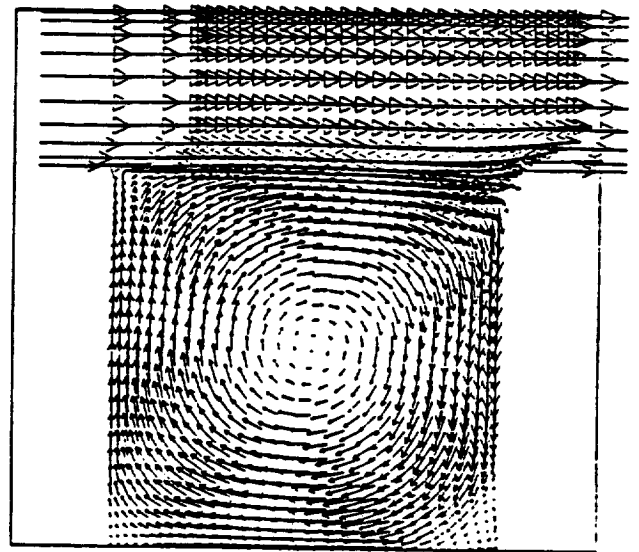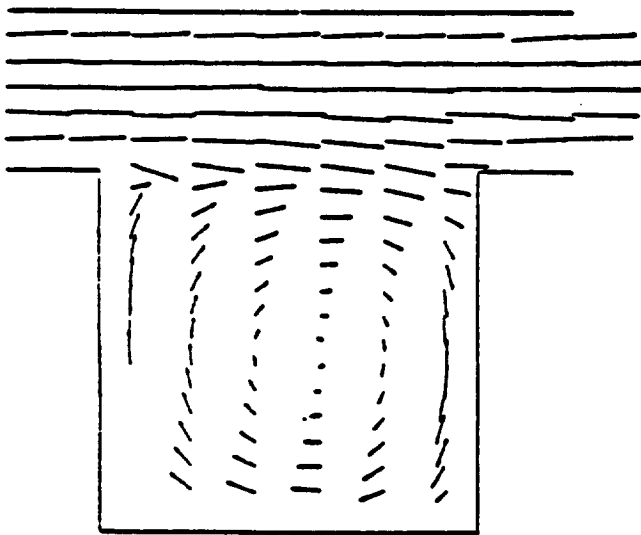
Experimental   Numerical

Third Cavity

Figure 2.23 Seven Cavity Labyrinth Seal. Velocity Vector Plot
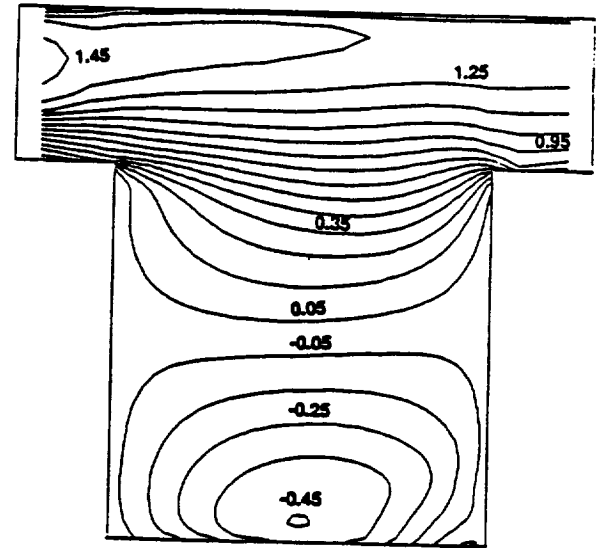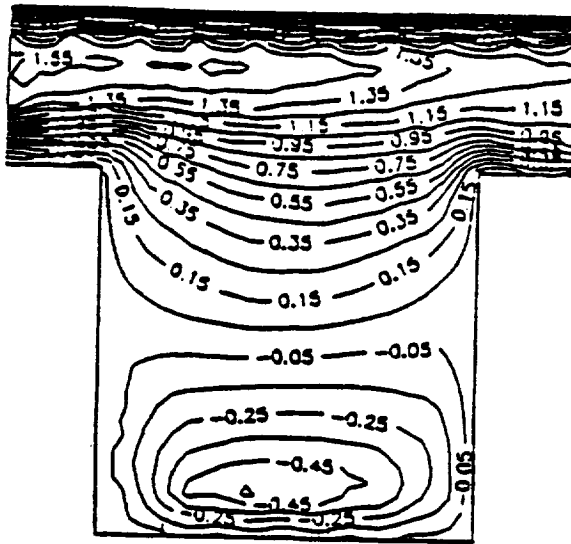
First Cavity
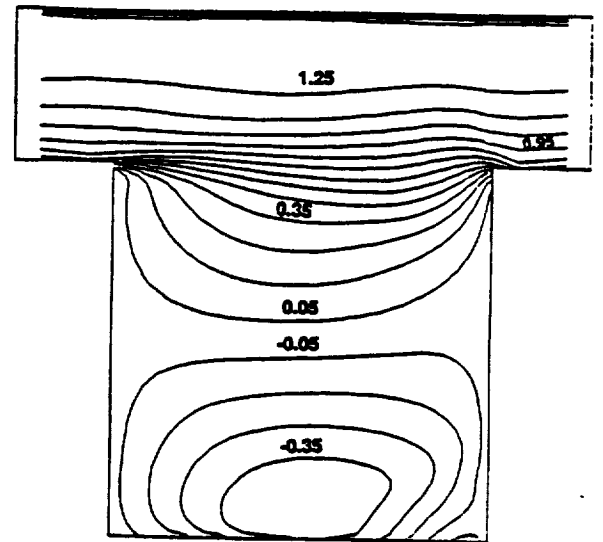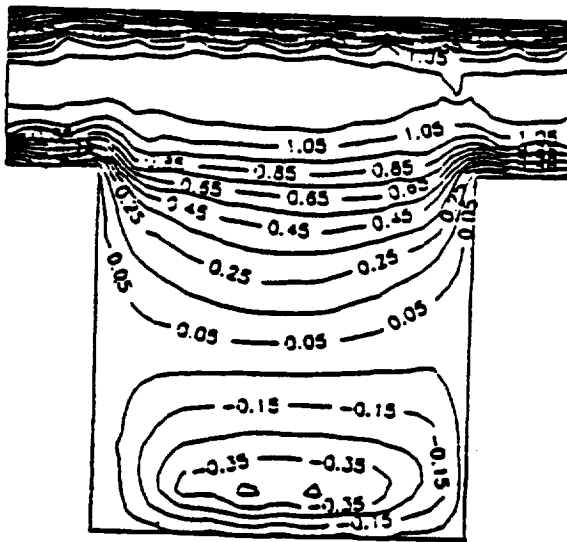
Experimental

Numerical

Third Cavity

Figure 2.24 Seven Cavity Labyrinth Seal. Contours of Scaled Axial Velocity, u_x/U
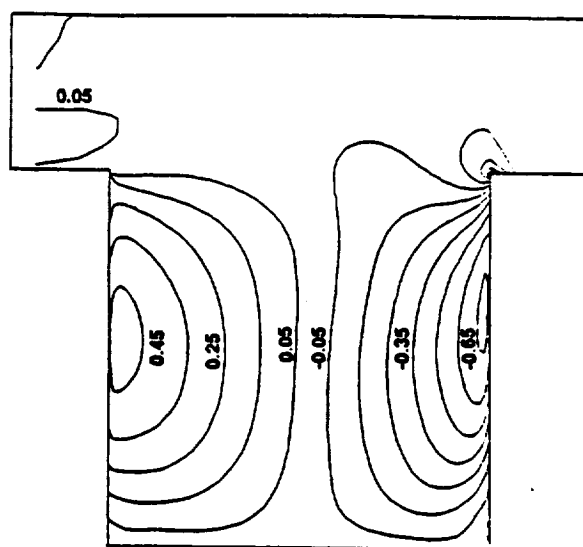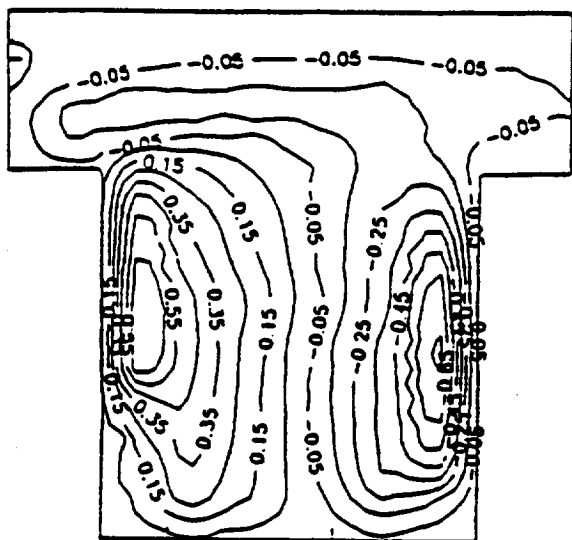
First Cavity
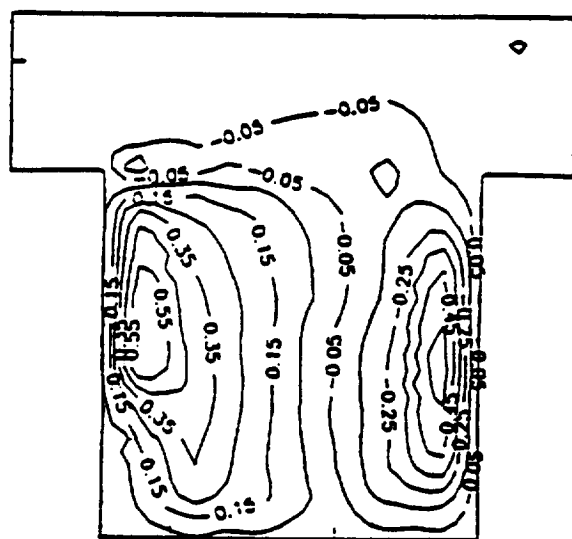
Experimental   Numerical
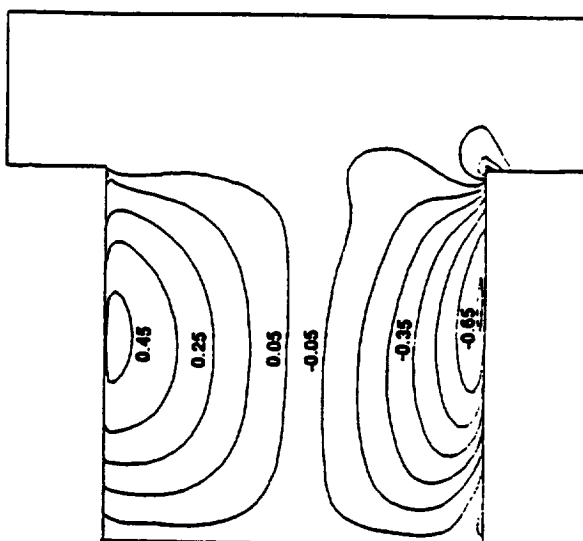
Third Cavity

Figure 2.25 Seven Cavity Labyrinth Seal. Contours of Scaled Radial Velocity, u_r/U
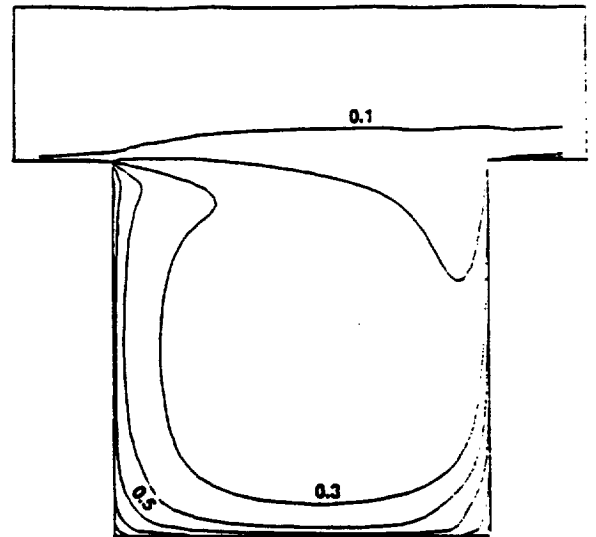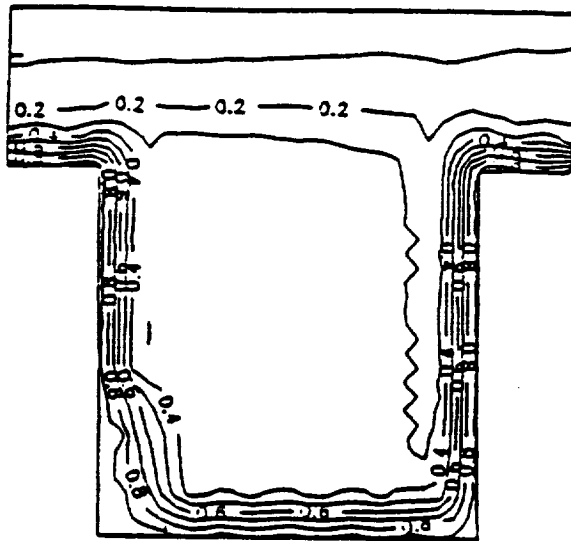
First Cavity
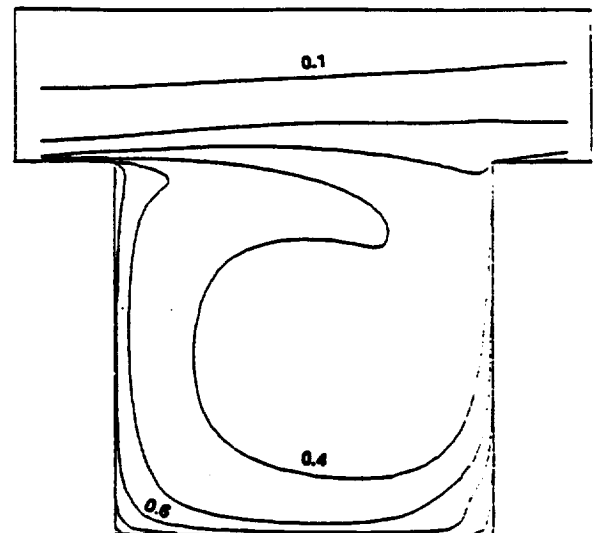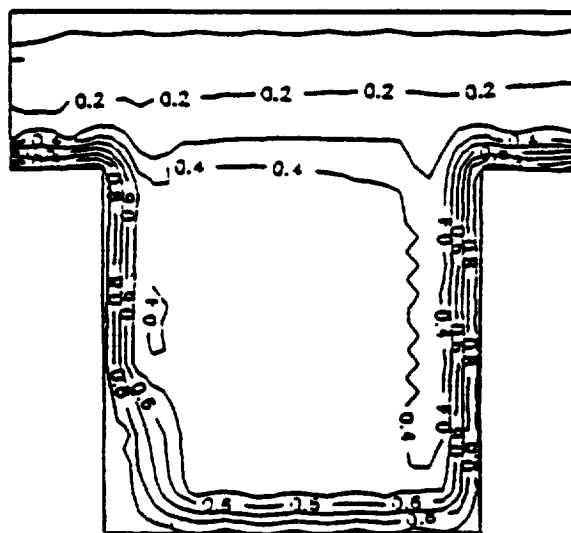
Experimental

Numerical

Third Cavity

Figure 2.26 Seven Cavity Labyrinth Seal.
Contours of Scaled Azimuthal Velocities, u_θ / w_{shaft}
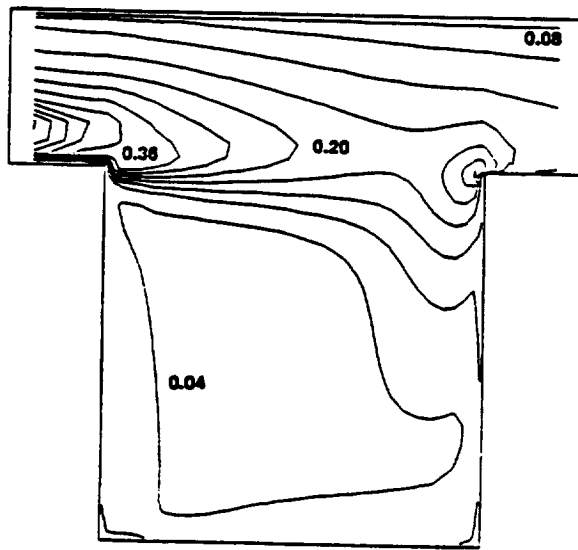
First Cavity
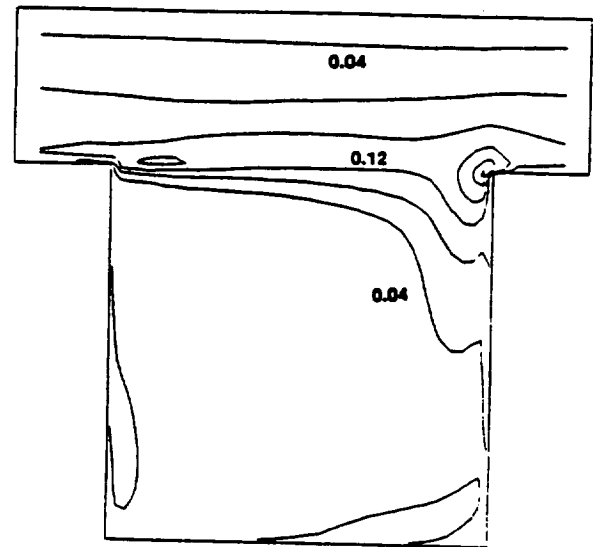
Third Cavity

Figure 2.27 Seven Cavity Labyrinth Seal Flow. Contours of Normalized Turbulent Kinetic Energy $\frac{1}{2}\left(u_r'^2 + u_\theta'^2 + u_x'^2\right)/U^2$. Numerical Results

REFERENCES

1. Peric, M., Kesseler, R., and Sheurer, G., "Comparison of Finite Volume Numerical Methods with Staggered and Colocated Grids," *Computers and Fluids*, Vol. 16, No. 4, 1988, pp. 389-403.

2. Rhie, C. M., and Chou, W. L., "Numerical Study of the Turbulent Flow Past an Airfoil with Trailing Edge Separation," *AIAA J.*, Vol. 21, 1983, p.1525.

3. Parameswaran, S., and Sun, R., "Numerical Simulation of Turbulent Flows Around a Car-Like Body Using the Non Staggered Grid System," AIAA Paper 89-1884, AIAA 20th Fluid Dynamics, Plasma Dynamics and Lasers Conference, Buffalo, NY, June 12-14, 1989.

4. Majumdar, S., "Role of Underrelaxation in Momentum Interpolation for Calculation of Flow with Nonstaggered Grids," *Numerical Heat Transfer*, Vol. 13, 1988, pp. 125-132.

5. Issa, R. I., "Solution of the Implicitly Discretised Fluid Flow Equations by Operator-Splitting," *J. of Comp. Phys.*, Vol. 64, 1985, pp. 40-65.

6. Armaly, B. F., Durst, F., Pareira, J. C. F., and Schonung, B., "Experimental and Theoretical Investigation of Backward-Facing Step Flow," *J. Fluid Mech.*, Vol. 127, 1983, pp.473-496.

7. Laufer, J., "Investigation of Turbulent Flow in a Two-Dimensional Channel," NACA Report 1053, 1951.

8. Daily, J. W., and Nece, R. E., "Chamber Dimension Effects on Induced Flow and Frictional Resistance of Enclosed Rotating Disks," *Trans. of ASME, J. of Basic Eng.*, Vol. 82, pp.217-232.

9. Morrison, G. L., Johnson, M. C., and Tatterson, G. B., " 3-D Laser Anemometer Measurements in an Annular Seal," ASME Paper 88-GT-64, ASME Gas Turbine and Aeroengine Congress, Amsterdam, The Netherlands, June 6-9, 1988.

10. Morrison, G. L., Johnson, M. C., and Tatterson, G. B., " 3-D Laser Anemometer Measurements in a Labyrinth Seal," ASME Paper 88-GT-63, ASME Gas Turbine and Aeroengine Congress, Amsterdam, The Netherlands, June 6-9, 1988.

3.0 Industrial Code SPIRALG - Gas-Lubricated, Spiral Groove, Cylindrical and Face Seals

Spiral groove bearings and seals are used to provide stability, load support and pumping for both cylindrical and face seal geometries. In the case of a cylindrical seal, grooves are usually designed to pump against each other in a symmetric arrangement to provide enhanced stability. A lightly loaded cylindrical seal operating at a low compressibility number will produce a force that is nearly 90 degrees out of phase with the displacement which will tend to destabilize the rotating shaft. The introduction of spiral grooves can significantly increase the component of force in phase with the displacement and decrease the out of phase component thereby improving stability.

In the case of a face seal or thrust bearing, spiral grooves are often introduced as the primary means of load support. Since a symmetric arrangement is not possible in a radial geometry, the grooves are usually designed to pump towards an ungrooved dam region. The resistance of the dam region increases as the film thickness decreases hence the pumping pressure rise increases thereby giving rise to a positive axial stiffness. The spiral grooves can also be used to pump against an applied pressure gradient thereby resulting in either reduced or reversed leakage.

The computer code SPIRALG predicts performance characteristics of gas lubricated, spiral-groove, cylindrical and face seals. Performance characteristics include load capacity, leakage flow, power requirements and dynamic characteristics in the form of stiffness and damping coefficients in 4 degrees of freedom for cylindrical seals and 3 degrees of freedom for face seals. These performance characteristics are computed as functions of seal and groove geometry, loads or film thicknesses, running speed, fluid viscosity, and boundary pressures.

The basic assumptions that have gone into the computer code are listed below:

1.   The flow is assumed to be laminar and isothermal.

2.   Inertial effects are neglected.

3.   The gas is assumed to be ideal.

4.   The film thickness is assumed to be small compared with seal lengths and diameters but large compared with surface roughness and the mean free path of the gas.

3-1

5. Narrow groove theory is used which characterizes the effects of grooves by a global pressure distribution without requiring computations on a groove by groove basis. This involves neglecting edge effects and local compressibility effects associated with groove to groove pressure variations. In general, narrow groove theory is valid when there are a sufficiently large number of grooves so that $2\pi \sin\beta / N_g << 1$, where β is the groove angle and N_g is the number of grooves.

6. Transient effects are treated with the use of small perturbations on a primary steady state flow. These transient effects are characterized by stiffness and damping coefficients that are dependent on the disturbance frequencies.

7. Although displacements and misalignments are treated, machined surfaces for face seals are assumed to be flat and machined clearances for cylindrical seals are assumed to be constant.

The above assumptions still leave the code applicable to a broad range of applications. Seals generally have small clearances and gasses have low densities resulting in sufficiently low Reynolds numbers for laminar flow. Practical designs should contain a fairly large number of grooves to ensure smooth, isotropic operation. At high sealed pressure differences, the flow could become sonic thereby invalidating the first two assumptions but this will usually not be the case and can readily be checked based on the predicted leakage flow. Elastic and thermal distortions as well as machining tolerances should also be estimated to validate the constant clearance assumption. The overall accuracy of the program will depend on the grid size used. Factors such as high compressibility or squeeze numbers, small values of the minimum film thickness to clearance ratio and large values of the length to diameter ratio could require either a large number of grid points or carefully selected variable grids.

3.1   Theoretical Development

The first formulation of the equations governing gas lubricated spiral groove bearings is generally credited to Vohr and Pan [1][*]. A more concise formulation is given in a second report [2] by these authors that has been used by Smalley [3] as a starting point in his generalized numerical treatment of the performance of spiral groove gas bearings. The work performed by Smalley may be applied to both bearings and seals. A principal limitation in all of the above references relates to the fact that solutions have only been provided for one dimensional forms of the equations which have been obtained by linearizing them based on near concentric and aligned conditions. The work described here deals with the numerical solution of the nonlinear equations for gas lubricated spiral groove seals at both eccentric and misaligned conditions.

Formulation of equations governing gas lubricated spiral groove seals

For completeness, a derivation of the narrow groove equations for spiral groove gas bearings and seals along the lines of that developed in Reference 2 will be provided here. Coordinate variables will be used to make the equations applicable to both cylindrical and face seals as can be seen with the aid of Figure 3-1. The circumferential coordinate, θ, is as shown in Figure 3-1. The transverse coordinate is described by the variable, s, which is taken to equal the radial coordinate, r, for a face seal and the axial coordinate, z, for a cylindrical seal. The quantity r, when it appears will denote radial position for a face seal and should be set equal to the shaft radius, R_0 for a cylindrical seal.

The isothermal, compressible form of the "Reynolds" equation may be written as a flow balance equating the divergence of the flow vector, $\bar{q}'$, to the flow per unit area squeezed out by the time rate of decrease of the film thickness, $q_A'^{[**]}$.

$$\nabla \cdot \bar{q}' = \frac{1}{r}\frac{\partial}{\partial s}(rq_s') + \frac{1}{r}\frac{\partial q_\theta'}{\partial \theta} = q_A' \quad , \tag{3-1}$$

The local flow vector $\bar{q}' = q_\theta'\bar{i} + q_s'\bar{j}$ represents the mass flow rate per unit transverse length divided by the density at a reference pressure, p_0, which may be written in vector form as

---

[*] Numbers in brackets refer to references given at the end of this section.

[**] Nomenclature is given at the end of this section.

Face Seal

Cylindrical Seal
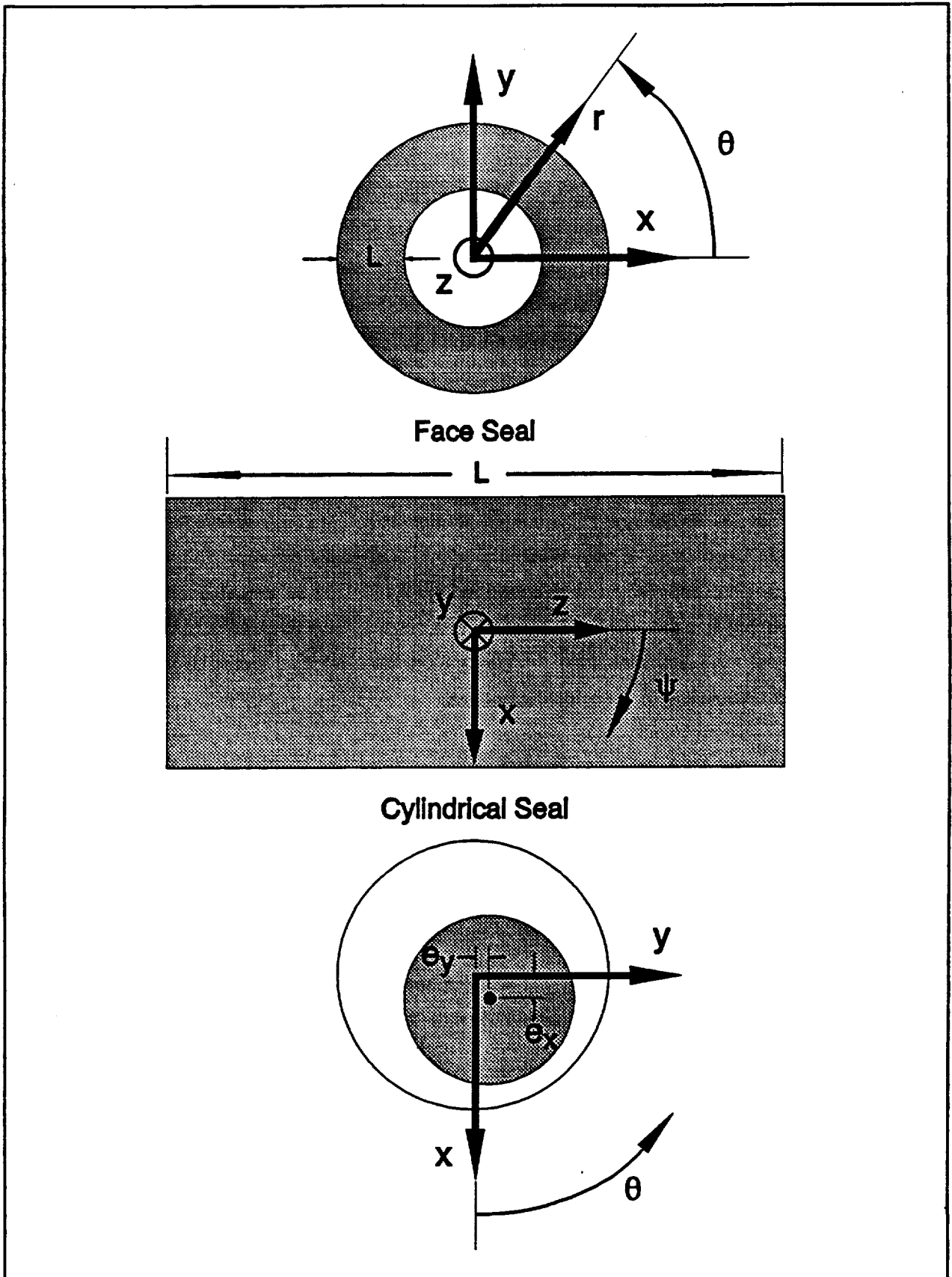
Figure 3-1 Coordinate system for spiral groove analysis.

$$\vec{q}' = -\frac{h^3}{12\mu}\frac{p'}{p_0}\vec{\nabla}p' + \frac{\vec{u}_1 + \vec{u}_2}{2}\frac{p'}{p_0}h \quad .$$

Since surface motion will be in the circumferential direction, the surface velocity vectors may be written as $\vec{u}_1 = r\omega_1\vec{i}$ and $\vec{u}_2 = r\omega_2\vec{i}$ and the components of $\vec{q}'$ become

$$q'_\theta = -\frac{h^3}{12\mu}\frac{p'}{p_0}\frac{1}{r}\frac{\partial p'}{\partial \theta} + r\frac{\omega_1 + \omega_2}{2}\frac{p'}{p_0}h \quad , \tag{3-2}$$

$$q'_s = -\frac{h^3}{12\mu}\frac{p'}{p_0}\frac{\partial p'}{\partial s} \quad . \tag{3-3}$$

The "squeeze film" term or displaced mass flow per unit area due to film motion, divided by the density at p_0 is

$$q'_A = -\frac{1}{p_0}\frac{\partial(p'h)}{\partial t} \tag{3-4}$$

One could substitute Equations (3-2) - (3-4) for the corresponding flow quantities in Equation (3-1) to obtain the usual form of the compressible Reynolds Equation which could in principle be solved, for any film thickness profile, $h(s,\theta)$ and appropriate boundary conditions, for the pressures or flow components to obtain the pressure distribution. These could in turn be integrated to obtain the various forces and moments associated with the given bearing geometry. The torque opposing the motion of say the smooth surface may be determined, once the pressure distribution is known, by integrating the shear stress relationship that arises in the development of Reynolds equation

$$\tau' = \frac{h}{2r}\frac{\partial p'}{\partial \theta} + \mu r\frac{\omega_2 - \omega_1}{h} \quad . \tag{3-5}$$

The difficulty encountered in obtaining full numerical solutions to the above equations relates to the complexity of the grid network necessary to adequately describe the geometry of a surface containing the large number of spiral grooves usually required to provide sufficiently smooth pressure distributions to make the load characteristics independent of whether shaft displacement is over a ridge or over a groove. Narrow groove theory is generally used to circumvent this difficulty (References 1 - 3). It will be implemented here, as well and is described below.

Narrow groove theory provides the limiting form of the solution to Equations (3-1) - (3-5) as the number of

3-5
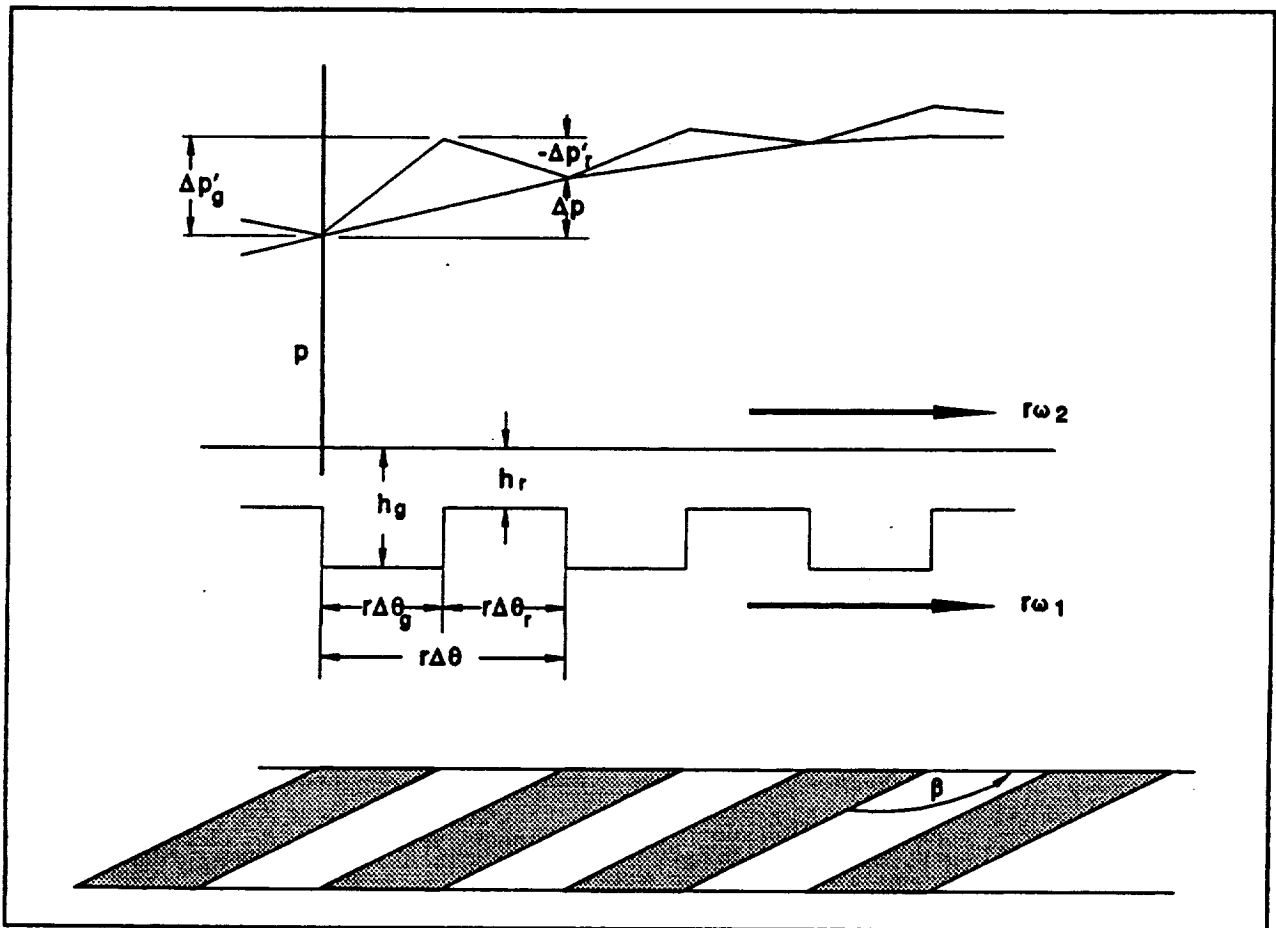
Figure 3-2 Schematic of spiral groove parameters, global and local pressures.

grooves, N_g, becomes large, with the groove angle, β and the groove to pitch ratio, α, held constant. The discontinuities in film thickness associated with the grooves will give rise to discontinuities in the pressure gradients at the ridge-groove interfaces as illustrated schematically in Figure 3-2. The local pressure profile p' is shown by the sawtooth lines whose lower vertices, for purposes of illustration, are connected by the "global" pressure profile, p. The global pressure profile does not necessarily lie at the lower vertices of the local pressure profile but could lie anywhere between the lower and upper vertices. In the limit as the number of grooves becomes large the curve connecting the upper vertices will approach the curve connecting the lower vertices. This limiting behavior is not true of $\partial p'/\partial\theta$, $\partial p'/\partial s$ or h, which will have different values over lands and grooves no matter how large the number of grooves. Narrow groove theory requires the development of expressions for the local (primed) quantities in terms of global quantities that approach single valued limits as the number of grooves becomes large. The local film thickness and pressure derivatives over the grooves will be denoted by h_g, $(\partial p'/\partial\theta)_g$ and $(\partial p'/\partial s)_g$ respectively and by h_r, $(\partial p'/\partial\theta)_r$ and $(\partial p'/\partial s)_r$ over the ridges. (The subscript r has been used here to denote ridges for consistency with References 1 - 3 and should not be confused when used in a different context later to denote the right hand boundary pressure or with the radial position variable, r, which is not used as a subscript.)

When the number of grooves becomes large, the sawtooth portion of the local pressure variation may be approximated with linear representations as shown in Figure 3-2. Thus, equating pressures over a groove-ridge pair in the circumferential direction

$$\frac{\Delta p}{\Delta\theta} = \frac{\Delta p_g'}{\Delta\theta} + \frac{\Delta p_r'}{\Delta\theta} = \left(\frac{\partial p'}{\partial\theta}\right)_g \frac{\Delta\theta_g}{\Delta\theta} + \left(\frac{\partial p'}{\partial\theta}\right)_r \frac{\Delta\theta_r}{\Delta\theta} \ .$$

Noting that $\Delta\theta_g/\Delta\theta = \alpha$ and $\Delta\theta_r/\Delta\theta = 1 - \alpha$ and replacing $\Delta p/\Delta\theta$ with $\partial p/\partial\theta$ as $\Delta\theta \to 0$, the above equation becomes

$$\frac{\partial p}{\partial\theta} = \alpha\left(\frac{\partial p'}{\partial\theta}\right)_g + (1-\alpha)\left(\frac{\partial p'}{\partial\theta}\right)_r \ . \tag{3-6}$$

The corresponding relationship in the transverse direction,

$$\frac{\partial p}{\partial s} = \alpha\left(\frac{\partial p'}{\partial s}\right)_g + (1-\alpha)\left(\frac{\partial p'}{\partial s}\right)_r \ . \tag{3-7}$$

is obtained in a similar manner.

The remaining two equations required to solve for the four local pressure derivatives are obtained from continuity considerations.

First, the pressure must be continuous at each groove-ridge interface, thus the derivative of the pressure in the direction of the interface, $\vec{\nabla}p' \cdot \vec{t}_\beta$, must also be continuous. The second requirement is for continuity of the flow normal to each groove-ridge interface as measured in a frame of reference moving with the grooves, $(\vec{q}' - r\omega_1 hp'/p_0 \vec{i}) \cdot \vec{n}_\beta$. The unit tangent and normal vectors for a logarithmic spiral are given by

$$\vec{t}_\beta = \cos\beta\,\vec{i} + \sin\beta\,\vec{j} \quad , \quad \vec{n}_\beta = \sin\beta\,\vec{i} - \cos\beta\,\vec{j} \quad .$$

The first of the above conditions requires continuity of

$$\frac{\cos\beta}{r}\frac{\partial p'}{\partial \theta} + \sin\beta\frac{\partial p'}{\partial s}$$

at each groove-ridge interface or

$$\frac{\cos\beta}{r}\left(\frac{\partial p'}{\partial \theta}\right)_g + \sin\beta\left(\frac{\partial p'}{\partial s}\right)_g = \frac{\cos\beta}{r}\left(\frac{\partial p'}{\partial \theta}\right)_r + \sin\beta\left(\frac{\partial p'}{\partial s}\right)_r \quad . \tag{3-8}$$

The second condition requires continuity of

$$(q_\theta' - r\omega h\frac{p'}{p_0})\sin\beta - q_r'\cos\beta \quad .$$

One may substitute Equations (3-2) and (3-3) for the circumferential and transverse components of the flow vector at each groove-ridge interface, respectively to obtain

$$-\frac{h_g^3}{12\mu}\left[\frac{\sin\beta}{r}\left(\frac{\partial p'}{\partial \theta}\right)_g - \cos\beta\left(\frac{\partial p'}{\partial s}\right)_g\right] + \frac{h_g}{2}r(\omega_2 - \omega_1)\sin\beta =$$

$$-\frac{h_r^3}{12\mu}\left[\frac{\sin\beta}{r}\left(\frac{\partial p'}{\partial \theta}\right)_r - \cos\beta\left(\frac{\partial p'}{\partial s}\right)_r\right] + \frac{h_r}{2}r(\omega_2 - \omega_1)\sin\beta \quad . \tag{3-9}$$

The density variation term, p'/p_0 is continuous at each interface and cancels out of Equation (3-9).

Equations (3-6) - (3-9) represent the four linear equations needed to solve for the local pressure derivatives. We may obtain the solution by first solving Equations (3-8) and (3-9) for the components of the local pressure gradient over the grooves in terms of those over the ridges. The resulting equations may be written as

$$\frac{1}{r}\left(\frac{\partial p'}{\partial \theta}\right)_g = \frac{h_g^3 \cos^2\beta + h_r^3 \sin^2\beta}{h_g^3} \frac{1}{r}\left(\frac{\partial p'}{\partial \theta}\right)_r + \frac{h_g^3 - h_r^3}{h_g^3} \sin\beta \cos\beta \left(\frac{\partial p'}{\partial s}\right)_r$$

$$+ 6\mu r(\omega_2 - \omega_1)\sin^2\beta \frac{h_g - h_r}{h_g^3} \quad , \tag{3-10}$$

$$\left(\frac{\partial p'}{\partial s}\right)_g = \frac{h_g^3 - h_r^3}{h_g^3}\sin\beta\cos\beta \frac{1}{r}\left(\frac{\partial p'}{\partial \theta}\right)_r + \frac{h_g^3 \sin^2\beta + h_r^3 \cos^2\beta}{h_g^3}\left(\frac{\partial p'}{\partial s}\right)_r$$

$$- 6\mu r(\omega_2 - \omega_1)\sin\beta\cos\beta \frac{h_g - h_r}{h_g^3} \quad . \tag{3-11}$$

One may now substitute Equation (3-10) for $(\partial p'/\partial \theta)_g$ in Equation (3-6) and Equation (3-11) for $(\partial p'/\partial s)_g$ in Equation (3-7) to obtain 2 linear equations for the components of the ridge pressure gradient which may in turn be solved to yield the following expressions:

$$\frac{1}{r}\left(\frac{\partial p'}{\partial \theta}\right)_r = \frac{[h_g^3 - \alpha(h_g^3 - h_r^3)\cos^2\beta)]\frac{1}{r}\frac{\partial p}{\partial \theta} - \alpha(h_g^3 - h_r^3)\sin\beta\cos\beta \frac{\partial p}{\partial s} - 6\mu r(\omega_2 - \omega_1)\alpha(h_g - h_r)\sin^2\beta}{(1-\alpha)h_g^3 + \alpha h_r^3} \quad , \tag{3-12}$$

$$\frac{1}{r}\left(\frac{\partial p'}{\partial s}\right)_r = \frac{-\alpha(h_g^3 - h_r^3)\sin\beta\cos\beta \frac{1}{r}\frac{\partial p}{\partial \theta} + [h_g^3 - \alpha(h_g^3 - h_r^3)\sin^2\beta)]\frac{\partial p}{\partial s} + 6\mu r(\omega_2 - \omega_1)\alpha(h_g - h_r)\sin\beta\cos\beta}{(1-\alpha)h_g^3 + \alpha h_r^3} \quad . \tag{3-13}$$

The components of the local groove pressure gradient may ge expressed in terms of the above ridge components by simple rearrangement of Equations (3-6) and (3-7):

$$\frac{1}{r}\left(\frac{\partial p'}{\partial \theta}\right)_g = -\frac{1-\alpha}{\alpha}\frac{1}{r}\left(\frac{\partial p'}{\partial \theta}\right)_r + \frac{1}{\alpha}\frac{1}{r}\frac{\partial p}{\partial \theta} \quad , \tag{3-14}$$

$$\left(\frac{\partial p'}{\partial s}\right)_g = -\frac{1-\alpha}{\alpha}\left(\frac{\partial p'}{\partial s}\right)_r + \frac{1}{\alpha}\frac{\partial p}{\partial s} \quad . \tag{3-15}$$

Now that expressions have been developed for the components of the local pressure gradients in terms of global ones, it is necessary to determine the global flow components q_s and q_θ and a global squeeze film term q_A that may be substituted for the local ones in the flow balance given by Equation (3-1). These global flow components are determined by matching mass flow rates over a groove-ridge pair with the mass flows obtained by integration of the local flow components over the same interval.

If θ_g is taken as the circumferential coordinate at the start of a groove, the transverse flow crossing an arc at fixed s, subtending a groove-ridge pair in the interval $\theta_g < \theta < \theta_g + \Delta\theta$ is given by the left hand term in the relationship

$$\int_{\theta_g}^{\theta_g+\Delta\theta} q'_s r d\theta \approx -\frac{h_g^3}{12\mu}\frac{p}{p_0}\left(\frac{\partial p'}{\partial s}\right)_g r\Delta\theta_g - \frac{h_r^3}{12\mu}\frac{p}{p_0}\left(\frac{\partial p'}{\partial s}\right)_r r\Delta\theta_r = q_s r\Delta\theta \quad .$$

The approximation to the integral in the above expression was obtained by dividing the integration interval, $\Delta\theta$ into sub-intervals for the groove, $\Delta\theta_g$ and ridge, $\Delta\theta_r$ and approximating q'_s, noting that as the number of grooves becomes large $\partial p'/\partial s$, will approach a constant value within each sub-interval. Since the pressure at the groove-ridge interface is continuous, the local density variation term, p'/p_0 was replaced by its global value p/p_0. The far right hand term in the above expression is based on the definition of the transverse component of the global flow rate described above. The right two equalities may be solved for q_s as

$$q_s = -\frac{h_g^3}{12\mu}\frac{p}{p_0}\alpha\left(\frac{\partial p'}{\partial s}\right)_g - \frac{h_r^3}{12\mu}\frac{p}{p_0}(1-\alpha)\left(\frac{\partial p'}{\partial s}\right)_r \quad . \tag{3-16}$$

One may obtain a relationship for the circumferential flow component q_θ in a similar manner by integrating q'_θ, given by Equation (3-3), at fixed θ, over a groove-ridge pair ($s_g < s < s_g + \Delta s$), approximating the integral over each sub-interval as above and equating the result to $q_\theta\Delta s$. The resulting expression may be written as

$$q_\theta = -\frac{h_g^3}{12\mu}\frac{p}{p_0}\alpha\frac{1}{r}\left(\frac{\partial p'}{\partial\theta}\right)_g - \frac{h_r^3}{12\mu}\frac{p}{p_0}(1-\alpha)\frac{1}{r}\left(\frac{\partial p'}{\partial\theta}\right)_r + r\frac{\omega_1+\omega_2}{2}\frac{p}{p_0}[\alpha h_g + (1-\alpha)h_r] \quad . \tag{3-17}$$

By integrating the squeeze film term q_A', given by Equation (3-4), over an area $r\Delta\theta\Delta s$, equating it to $q_A r\Delta\theta\Delta s$ and noting that the groove area fraction will be α and the ridge area fraction will be $1-\alpha$, the

following expression is obtained:

$$q_A = -\frac{1}{p_0}\frac{\partial}{\partial t}(p[\alpha h_g + (1-\alpha)h_r]) \quad . \tag{3-18}$$

The global shear stress τ, may be determined by integrating the local shear stress τ', given by Equation (3-5), with respect to θ over the interval $\theta_g < \theta < \theta_g + \Delta\theta$, invoking the narrow groove approximations and equating the result to $\tau\Delta\theta$. The resulting expression may be written in the form

$$\tau = \frac{\alpha h_g}{2}\frac{1}{r}\left(\frac{\partial p'}{\partial \theta}\right)_g + \frac{(1-\alpha)h_r}{2}\frac{1}{r}\left(\frac{\partial p'}{\partial \theta}\right)_r + \mu r(\omega_2 - \omega_1)\left(\frac{\alpha}{h_g} + \frac{1-\alpha}{h_r}\right) \quad . \tag{3-19}$$

Equation (3-1) may now be applied directly to the global flow vector $\bar{q} = q_\theta \bar{i} + q_s \bar{j}$, as $\bar{\nabla}\cdot\bar{q} = q_A$ and by substituting Equation (3-18) for q_A and putting the result in dimensionless form one obtains:

$$\bar{\nabla}\cdot\bar{Q} = \frac{1}{R}\frac{\partial}{\partial S}(RQ_s) + \frac{1}{R}\frac{\partial Q_\theta}{\partial \theta} = -\frac{\partial}{\partial t}[(\alpha\delta + H_r)(1+P)] \quad . \tag{3-20}$$

The components of the global flow vector, q_θ and q_s are given in terms of the local pressure derivatives by Equations (3-16) and (3-17) respectively. These local derivatives are, in turn, given in terms of the global ones by Equations (3-12) - (3-15). The global flow components may be expressed completely in terms of global pressure derivatives by first substituting Equations (3-14) and (3-15) for the local pressure derivatives over the grooves and then substituting Equations (3-12) and (3-13) for the local pressure derivatives over the ridges. One may then collect terms and put the resulting two equations in dimensionless form to obtain the following expressions for the components of the dimensionless flow vector $\bar{Q} = Q_\theta \bar{i} + Q_s \bar{j}$:

$$Q_\theta = -(1+P)\left[H_r^3\left(k_2\frac{\partial}{\partial S} + \frac{k_3}{R}\frac{\partial}{\partial \theta}\right)P + \Lambda_s k_4 R\sin\beta - \Lambda(\alpha\delta + H_r)R\right] \quad , \tag{3-21}$$

$$Q_s = -(1+P)\left[H_r^3\left(k_1\frac{\partial}{\partial S} + \frac{k_2}{R}\frac{\partial}{\partial \theta}\right)P - \Lambda_s k_4 R\cos\beta\right] \quad . \tag{3-22}$$

The dimensionless variables associated with the above equations are

The dimensionless gage pressure P in the above equations is taken relative to the absolute pressure p_0

$$P = \frac{p - p_0}{p_0} \,, \quad \bar{Q} = \frac{12\mu R_0}{C^3 p_0}\bar{q} \,, \quad H_r = \frac{h_r}{C} \,, \quad S = \frac{s}{R_0} \,, \quad R = \frac{r}{R_0} \,, \quad \bar{t} = \frac{\omega}{2\Lambda}t \,, \quad \Gamma = \frac{h_g}{h_r} \,. \tag{3-23}$$

which will henceforth be taken as the minimum of the two boundary pressures in absolute units. The dimensionless parameters associated with the above equations are

$$\Lambda = \frac{6\mu\omega R_0^2}{p_0 C^2} \,, \quad \Lambda_\delta = \Lambda\bar{\delta}\bar{\omega}\alpha(1-\alpha)\sin\beta \,, \quad \bar{\omega} = \frac{\omega_2 - \omega_1}{\omega} \,, \quad \bar{\delta} = \frac{(h_g - h_r)}{C} \,, \quad \alpha = \frac{l_g}{l_r + l_g} \tag{3-24}$$

and the column matrix containing spiral groove coefficients, $k_i(\alpha,\beta,\Gamma)$, in the above equations is

$$k = \left\{ \begin{array}{c} \dfrac{\alpha(1-\alpha)(\Gamma^3 - 1)^2\sin^2\beta + \Gamma^3}{(1-\alpha)\Gamma^3 + \alpha} \\[2mm] \dfrac{\alpha(1-\alpha)(\Gamma^3 - 1)^2\sin\beta\cos\beta}{(1-\alpha)\Gamma^3 + \alpha} \\[2mm] \dfrac{\alpha(1-\alpha)(\Gamma^3 - 1)^2\cos^2\beta + \Gamma^3}{(1-\alpha)\Gamma^3 + \alpha} \\[2mm] \dfrac{(\Gamma^3 - 1)}{(1-\alpha)\Gamma^3 + \alpha} \\[2mm] \dfrac{(1-\alpha)\Gamma + \alpha}{\Gamma} \\[2mm] \dfrac{(\Gamma - 1)\sin\beta}{(1-\alpha)\Gamma^3 + \alpha} \\[2mm] \dfrac{\alpha(1-\alpha)(\Gamma^3 - 1)(\Gamma - 1)\sin\beta\cos\beta}{(1-\alpha)\Gamma^3 + \alpha} \\[2mm] \dfrac{\alpha(1-\alpha)(\Gamma^3 - 1)(\Gamma - 1)\cos^2\beta + \alpha\Gamma + (1-\alpha)\Gamma^3}{(1-\alpha)\Gamma^3 + \alpha} \end{array} \right\} . \tag{3-25}$$

Only the first 4 components of k are used in Equations (3-21) - (3-22). The remaining components are used in evaluating the shear stress. The relationships for k_i, $i = 1,2,3,4$ derived here are consistent with Equation (3.27) of Reference 2.

The global shear stress is obtained by substituting Equation (3-14) for $(\partial p'/\partial\theta)_g/r$ in Equation (3-19) then substituting Equation (3-12) for $(\partial p'/\partial\theta)_r/r$ in the resulting expression. The latter result may be expressed in dimensionless form as

$$\bar{\tau} = \frac{1}{2}\left[k_6 \frac{\Lambda}{3}\frac{\bar{\omega}R}{H_r} + k_6 \Lambda_s \frac{R}{H_r^2} + k_7 H_r \frac{\partial P}{\partial S} + k_8 \frac{H_r}{R}\frac{\partial P}{\partial \theta}\right] , \tag{3-26}$$

which is consistent with Equation (3.88) of Reference 2.

The equations presented thus far are directly applicable to either a cylindrical seal or a face seal. As mentioned earlier, a face seal is represented in the above equations by setting the transverse coordinate s equal to the radial coordinate r. This is equivalent to setting S = R in dimensionless form. A cylindrical seal is represented in dimensionless form by setting S = Z and R = 1.

The quantities required to characterize the groove dimensions are shown in Figure 2. If by convention ω is taken to be positive (surface motion in the direction of increasing θ), then the groove angle, β, will be the angle measured from the groove to the direction of surface motion associated with ω. A positive acute value of β will tend to pump in the positive S direction if the grooves are on the stator and in the negative S direction for grooves on the rotor. By setting the groove depth parameter $\bar{\delta}$ = 0, Γ becomes 1 and Equations (3-20) - (3-26) reduce to those for ungrooved seals. By treating k and $\bar{\delta}$ as sectionally continuous functions of S, these equations may be applied to composite smooth and grooved geometries with Q_s and P held continuous at all transition boundaries.

The film thickness relationship for H_r which may be applied to either a cylindrical seal or a face seal is

$$H_r = 1 - \epsilon_z - (\epsilon_x + \psi S)\cos\theta - (\epsilon_y - \phi S)\sin\theta \tag{3-27}$$

with ϵ_z = 0 for a cylindrical seal and $\epsilon_x = \epsilon_y$ = 0 for a face seal.

The boundary pressures will be taken to be p_i and p_r at the inside and outside radii respectively for a face seal or at the two ends (z = -L/2 and Z = L/2) for a cylindrical seal. This is expressed in dimensionless form

$$P = P_i \text{ at } S = S_i , \quad P = P_r \text{ at } S = S_r . \tag{3-28}$$

The remaining boundary condition relates to periodicity with respect to θ which requires P and Q_θ to have the same values at θ = 0 as they do at θ = 2π:

$$P|_{\theta=0} = P|_{\theta=2\pi} \quad \text{and} \quad Q_\theta|_{\theta=0} = Q_\theta|_{\theta=2\pi} . \tag{3-29}$$

The above treatment is intended to represent a complete statement of the mathematical problem for

determining the pressures and surface shear stresses in plain or spiral groove face or cylindrical seals. The rest of this section will deal with the numerical determination of the pressure distribution and the computation of related quantities such as loads, leakage, power loss, stiffness and damping.

Discretization of pressure equations

Discretization will be carried out with the use of the cell method [4] which involves the performance of a flow balance about each interior grid point. One may integrate Equation (3-20) over an arbitrary control area ·within a seal

$$\int_A \vec{\nabla} \cdot \vec{Q} d\bar{A} + \int_A \frac{\partial}{\partial t}[(\alpha \delta + H_r)(1 + P)]d\bar{A} = 0$$

and apply the divergence theorem to the first integral on the left to obtain the relationship

$$\oint_S \vec{Q} \cdot \vec{n} d\bar{S} + \int_A \frac{\partial}{\partial t}[(\alpha \delta + H_r)(1 + P)]d\bar{A} = 0 \quad , \tag{3-30}$$

which will be used as a starting point in the discretization process.

A grid network may be set up along with flow control areas about each grid point as shown in Figure 3-3. The grid will contain M lines in the S direction including boundaries and N lines in the θ direction from $\theta = 0$ to $\theta = 2\pi$, inclusive. The grid points at the intersections of these lines are noted by the solid circles. Flow control areas to be used in evaluation of the integrals in Equation (3-30) are set up about each grid point as shown by the shaded area in Figure 3-3. The corners of the flow control area denoted by the shaded points marked 1,2,3, and 4 are located at the geometric centers of the rectangles formed by the grid lines and will be referred to as half grid points. The flow components labeled Q_{12}^+ etc., represent the components of the flow vector in the positive coordinate directions as indicated by the arrows. The subscripts (12 etc.) refer to the line connecting points 1 and 2, and the superscripts (+,-) refer to the positive or negative side of the point of intersection with the grid line.

We will adopt the convention that the subscripts i,j refer to grid points and subscripts such as i+½,j+½ refer to half grid points. The value of the radius R at half grid point 2 would thus be $R_{i-½}$. The differential control length, $d\bar{S}$, in Equation (3-30) will be approximated by the lengths of the various lines or arcs bounding the flow control area thus $\Delta \bar{S}_{12}^+$ refers to the length of the line associated with Q_{12}^+ described above which for this example would be $\Delta S_j/2$. Similarly the arc length associated with Q_{14}^- would be $\Delta \bar{S}_{14}^- = R_{i+½}\Delta \theta_{j-1}/2$.
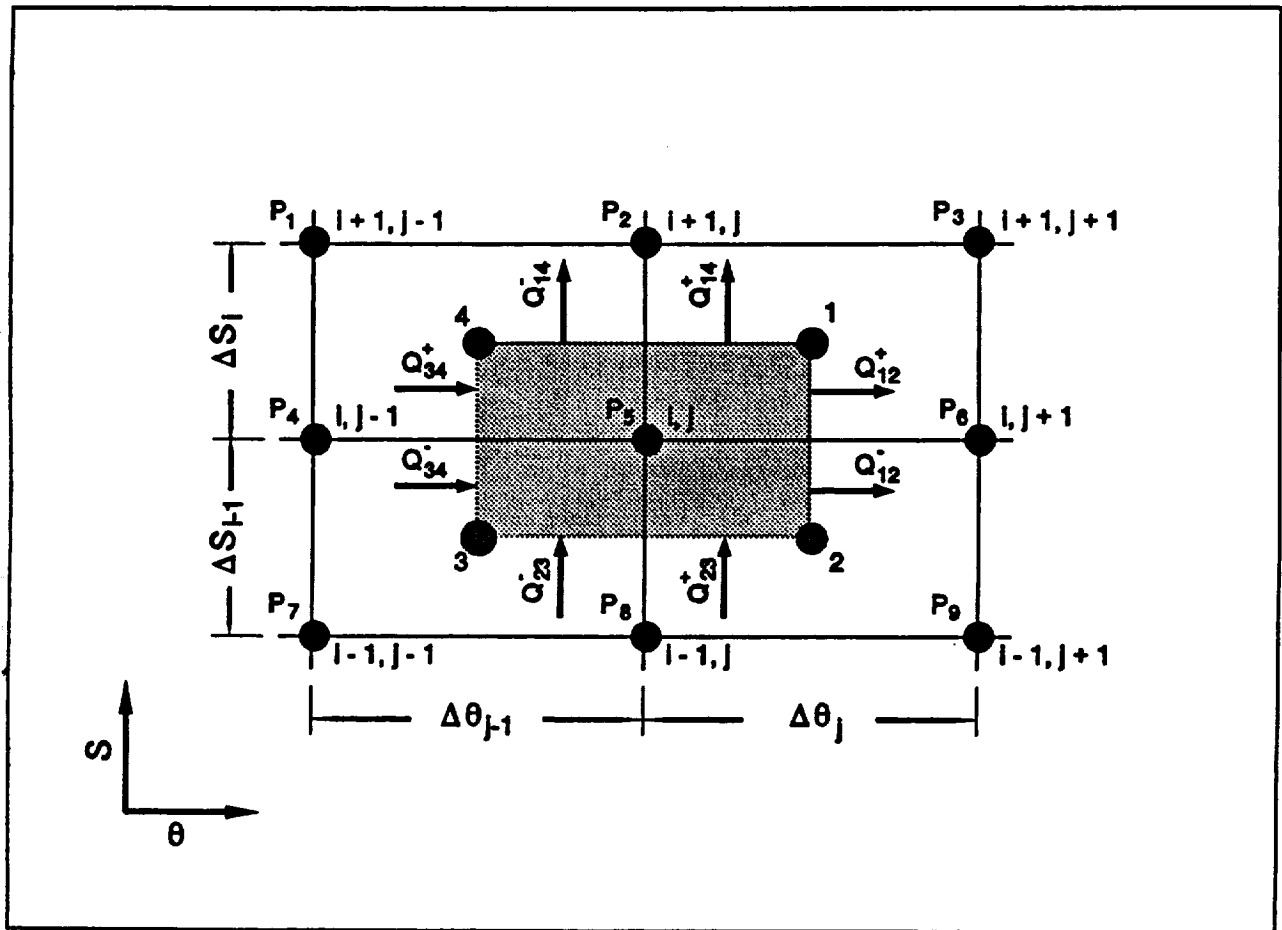
Figure 3-3 Schematic of grid network and flow control area for discretization process

The area element $d\bar{A}$ will be made up of the parts of the flow control area in each of the four quadrants about the center point (I,j) and numbered based on the shaded half grid point that each contains. Thus $\Delta\bar{A}_1 = (R_i + R_{i+\frac{1}{2}})\Delta\theta_j\Delta S_j/8$, etc. and the discretized form of Equation (3-30) may be written as:

$$Q_{12}^-\Delta\bar{S}_{12}^- + Q_{12}^+\Delta\bar{S}_{12}^+ + Q_{14}^-\Delta\bar{S}_{14}^- + Q_{14}^-\Delta\bar{S}_{14}^- - Q_{34}^+\Delta\bar{S}_{34}^+ - Q_{34}^-\Delta\bar{S}_{34}^- - Q_{23}^-\Delta\bar{S}_{23}^- - Q_{23}^+\Delta\bar{S}_{23}^+ = \quad (3\text{-}31)$$

$$-\frac{\partial}{\partial t}\left\{(1 + P_{ij})\left[(\alpha\bar{\delta} + H_r)_{i+\frac{1}{2},j+\frac{1}{2}}\Delta\bar{A}_1 + (\alpha\bar{\delta} + H_r)_{i+\frac{1}{2},j-\frac{1}{2}}\Delta\bar{A}_4 + (\alpha\bar{\delta} + H_r)_{i-\frac{1}{2},j-\frac{1}{2}}\Delta\bar{A}_3 + (\alpha\bar{\delta} + H_r)_{i-\frac{1}{2},j+\frac{1}{2}}\Delta\bar{A}_2\right]\right\}.$$

The flow components on the left hand side of Equation (3-31) are obtained from discretization of Equations (3-21) and (3-22). A numbering system for the 9 pressures at the grid point (I,j) and the 8 surrounding points is shown in Figure 3-1, where $P_1 = P_{i+1,j+1}$, $P_5 = P_{ij}$ etc. The determination of the flows out of the sub-area containing the half grid point labeled 1 is discussed here as an example. The flow component Q_{12}^+ is determined from Equation (3-21). The derivative of the pressure normal to the line connecting points 1 and 2 is evaluated at the intersection of the line with the grid line. The tangential derivative is evaluated at the half grid point, 1 as the average of the difference between P_3 and P_6 with that between P_2 and P_5, divided by ΔS_j. Thus,

$$\frac{1}{R}\frac{\partial P}{\partial\theta} \approx \frac{P_6 - P_5}{R_i\Delta\theta_j}, \quad \frac{\partial P}{\partial S} \approx \frac{(P_3 - P_6) + (P_2 - P_5)}{2\Delta S_j} \quad \text{(for } Q_{12}^+\text{)}.$$

The flow component Q_{14}^+ is determined in a similar manner from Equation (3-22). The normal derivative is approximated as the difference between P_2 and P_5 divided by ΔS_j and the tangential derivative is approximated as the average of the differences between P_3 and P_2 and P_6 and P_5, divided by $R_{i+\frac{1}{2}}\Delta\theta_j$.

$$\frac{\partial P}{\partial S} \approx \frac{P_2 - P_5}{\Delta S_j}, \quad \frac{1}{R}\frac{\partial P}{\partial\theta} \approx \frac{(P_3 - P_2) + (P_6 - P_5)}{2R_{i+\frac{1}{2}}\Delta\theta_j} \quad \text{(for } Q_{14}^+\text{)}.$$

For both of the above flow components the pressure in the (1+P) term appearing in Equations (3-21) and (3-22) is evaluated at the half grid point by averaging the four surrounding pressures $(P_2 + P_3 + P_5 + P_6)/4$. All of the remaining quantities $(R, H_r, k_1, k_2, k_3, k_4, \alpha, \beta$ and $\bar{\delta})$ are evaluated directly at the half grid point.

The flow balances over the other quadrants are performed in a similar manner. For steady state conditions, the right hand side of Equation (3-31) will be 0 and the flow balance about any interior grid point (I,j) may be written in the form

3-16

$$F_I(H_r, P_1, P_2, P_3, P_4, P_5, P_6, P_7, P_8, P_9) = 0 \ . \tag{3-32}$$

The definition of F_{ij} may be extended to make Equation (3-32) applicable to the ends of the seal as well as the interior points by applying Equation (3-28) at the endpoints as follows:

$$F_{1j} = P_5 - P_1 \quad (I = 1) \quad \text{and} \quad F_{Mj} = P_5 - P_r \quad (I = M) \ .$$

The solution to Equation (3-32) may be used to provide all of the steady state quantities such as pressures, forces, moments, flow rate and power loss. The inclusion of the right hand side of Equation (3-31) will be necessary for determination of frequency dependent stiffness and damping coefficients which will be discussed later.

Newton-Raphson linearization procedure

The Newton-Raphson [5] procedure is perhaps the most widely used method for obtaining solutions to non-linear systems of algebraic equations and is described in many textbooks on numerical methods such as Reference 5. A procedure similar to that used here is described in a paper by Artiles, Walowit and Shapiro [6].

The procedure is started with an initial pressure distribution that satisfies the end conditions given by Equation (3-28). A new set of approximations to the pressures in Equation (3-32), P_k^{new} may be obtained by linearizing F_{ij} about a previously established set of approximations P_k as follows:

$$F_I + \sum_{k=1}^{9} \frac{\partial F_I}{\partial P_k} \left(P_k^{new} - P_k \right) = 0 \tag{3-33}$$

where a forward difference

$$\frac{\partial F_I}{\partial P_k} = \frac{F_I(H_r, P_1, ..., P_k + \eta, ..., P_9) - F_I(H_r, P_1, ..., P_9)}{\eta}$$

may be used to numerically evaluate the partial derivatives.

Pressures without the superscript new relate to the previous or "old" approximation. It should be noted that the function F_{ij} will not be 0 unless the pressures comprising its arguments are exact. If we go back to using grid notation for P (P_{ij} in place of P_5 etc.) and introduce the column vector $\{P_j^{new}\}$ as the M new

3-17

pressures at the jth column of grid points, Equation (3-33) may be written in the following form:

$$[C^j]\{P_j^{new}\} + [E^j]\{P_{j-1}^{new}\} + [D^j]\{P_{j+1}^{new}\} = \{R^j\} , \qquad (3\text{-}34)$$

where $[C^j]$, $[E^j]$ and $[D^j]$ are tri-diagonal matrices whose interior elements, from Equation (3-33), are

$$C_{i,i+k}^j = \frac{\partial F_i}{\partial P_{i+k,j}} , \quad E_{i,i+k}^j = \frac{\partial F_i}{\partial P_{i+k,j-1}} , \quad D_{i,i+k}^j = \frac{\partial F_i}{\partial P_{i+k,j+1}} , \quad k = -1,0,1 ; \quad i = 2,\dots,M-1 .$$

The interior elements of the column vector $\{R^j\}$ are

$$R_i^j = \sum_{k=-1}^{1} \left(C_{i,i+k}^j P_{i+k,j} + E_{i,i+k}^j P_{i+k,j-1} + D_{i,i+k}^j P_{i+k,j+1} \right) - F_{ij} .$$

The above equations may also be applied to the corner elements to produce the result

$$C_{1,1}^j = C_{M,M}^j = 1 , \quad E_{1,1}^j = E_{M,M}^j = D_{1,1}^j = D_{M,M}^j = 0 , \quad R_1^j = P_i , \quad R_M^j = P_r .$$

Equation (3-34) represents a linear system of simultaneous equations that may be solved by various matrix inversion procedures. The method used here is the column or transfer matrix method, which is described in References 4 and 7. It has been used extensively in solving finite difference problems associated with various forms of the lubrication equations and produces accurate results in a fairly efficient manner. Convergence of the Newton-Raphson procedure is generally obtained within 3 - 6 iterations depending on degree of non-linearity and the accuracy required.

Determination of loads, moments, torque and leakage

The dimensionless loads and moments may be obtained by integrating the pressure distribution over the seal area as shown below:

$$\bar{W}_x = \int_0^{2\pi} \int_{S_i}^{S_r} P\cos\theta\, R\, dS\, d\theta , \quad \bar{W}_y = \int_0^{2\pi} \int_{S_i}^{S_r} P\sin\theta\, R\, dS\, d\theta , \quad \bar{W}_z = \int_0^{2\pi} \int_{S_i}^{S_r} P R\, dS\, d\theta ,$$

$$\bar{M}_x = -\int_0^{2\pi} \int_{S_i}^{S_r} P\sin\theta\, R S\, dS\, d\theta , \quad \bar{M}_y = \int_0^{2\pi} \int_{S_i}^{S_r} P\cos\theta\, R S\, dS\, d\theta . \qquad (3\text{-}35)$$

The dimensionless torque is obtained from integration of the shear stress given by Equation (3-26) over the seal area:

$$\bar{T} = \text{sign}(\bar{\omega}) \int_0^{2\pi} \int_{S_i}^{S_r} \bar{\tau} R \, dS \, d\theta \ . \tag{3-36}$$

The sign$(\bar{\omega})$ term has been added to make the torque positive when it opposes the net surface motion regardless of which surface (smooth or grooved) is moving.

Finally, the dimensionless leakage flow, Q_{in} going into the seal at $S = S_i$ may be obtained from integration of Q_θ, given by Equation (3-21), over the circumference of the seal:

$$Q_{in} = \int_0^{2\pi} Q_\theta R \, d\theta \ . \tag{3-37}$$

The integrand in the above expression is evaluated by summing the flow components to the right of the first θ grid line in the same manner as that used in developing Equation (3-31). It should be noted that any value of S can be used since Q_{in} is independent of S.

The physical quantities corresponding to the dimensionless ones given above are

$$W_{(x,y,z)} = R_0^2 p_0 \bar{W}_{(x,y,z)} \ , \quad M_{(x,y)} = R_0^3 p_0 \bar{M}_{(x,y)} \ , \quad q_{in} = \frac{C^3 p_0}{12\mu} Q_{in} \ , \quad T = R_0^2 p_0 C \bar{T} \ . \tag{3-38}$$

In the above equations the loads W_x and W_y apply only to a cylindrical seal and W_z applies only to a face seal. The leakage flow q_{in} is the volumetric flow rate going into the seal measured at pressure p_0.

3-19

Determination of stiffness and damping coefficients

Equation (3-20) with flow components Q_θ and Q_s given by Equations (3-21) and (3-22) represents a second order non-linear partial differential equation that may be used to define a second order non-linear operator G, such that

$$G(P,H_r) = -\frac{\partial}{\partial t}[(\alpha\bar{\delta} + H_r)(1 + P)] \ . \tag{3-39}$$

The determination of P under steady state conditions, where the right hand side of Equation (3-39) is 0, was described earlier in this section. These steady state pressures will now be referred to as $\hat{P}$. The various eccentricities and rotations used in determining H_r from Equation (3-27) may, for convenience, be put in the form of a row matrix as

$$[\epsilon] = \begin{cases} [\epsilon_z,\phi,\psi] \ , & \text{(face seal)} \\ [\epsilon_x,\epsilon_y,\phi,\psi] \ , & \text{(shaft seal)} \end{cases} \tag{3-40}$$

and Equation (3-27) may be written as

$$H_r = 1 + [\epsilon]\{a\} \ , \tag{3-41}$$

where the column vector $\{a\}$ is given by

$$\{a\} = \begin{cases} \{-1, S\sin\theta, -S\cos\theta\} \ , & \text{(face seal)} \\ \{-\cos\theta, -\sin\theta, S\sin\theta, -S\cos\theta\} \ , & \text{(shaft seal)} \end{cases} \tag{3-42}$$

One could develop a perturbation analysis for prediction of stiffness and damping coefficients with the following procedure: (a) perturb say the ith component of the eccentricity matrix in Equation (3-40) by $\eta\epsilon'$, where η is a small parameter and ϵ' is time dependent; (b) express H_r in the form $H_r = \hat{H} + \eta\epsilon'\{a\}$ and the corresponding pressures as $P = \hat{P} + \eta\{P'\}$; (c) substitute the above expressions for P and H_r in Equation (3-39); (d) expand the resulting expression neglecting terms of order η^2 and higher; (e) collect terms of order η. The resulting expression could be written in the form:

$$\mathfrak{L}\{P'\} + \{b\}\epsilon' = -(\alpha\bar{\delta} + \hat{H})\frac{\partial\{P'\}}{\partial t} - (1 + \hat{P})\{a\}\frac{\partial\epsilon'}{\partial t} \ , \tag{3-43}$$

where $\mathfrak{L}$ is a second order linear operator given by

$$\mathcal{L} = A_1 \frac{\partial^2}{\partial S^2} + A_2 \frac{\partial^2}{\partial S \partial \theta} + A_3 \frac{\partial^2}{\partial \theta^2} + A_4 \frac{\partial}{\partial S} + A_5 \frac{\partial}{\partial \theta} + A_6 \quad . \tag{3-44}$$

The coefficients in the above equations (A_1, A_2, {b} etc.) will depend on the coordinate variables as well as $\hat{P}$, $\hat{H}$ and their various derivatives. Only the form of the above equations is important to the numerical procedure under development and the significant amount of algebraic manipulation required to determine these coefficients will be shown to be unnecessary.

If the time dependence of the eccentricity is restricted to oscillatory disturbances one may set $\epsilon' = e^{\mathcal{S}\sigma \hat{t}}$ and look for solutions in the form $\{P'\} = \{P^*\}e^{\mathcal{S}\sigma \hat{t}}$, where $\{P^*\}$ is complex but independent of time. When this transformation is introduced into Equation (3-43), the result is

$$\mathcal{L}\{P^*\} + \{b\} = -\mathcal{S}\sigma\left[(\alpha\bar{\delta} + \hat{H})\{P^*\} + (1 + \hat{P})\{a\}\right] \quad . \tag{3-45}$$

The representation of $\{P^*\}$ and the eccentricity coefficients {a} as column vectors relates to the fact that each of the eccentricities must be perturbed to obtain the compete stiffness matrix but Equation (3-45) is solved independently for each perturbation. The periodic boundary conditions given by Equation (3-29) also apply to Equation (3-39) (continuity of $\{P^*\}$ and $\partial\{P^*\}/\partial\theta$ is sufficient when H_f and the spiral groove coefficients $k_1,...,k_4$ are continuous functions of θ as they are here). The end boundary conditions given by Equation (3-28) become $\{P^*\} = 0$ at $S = S_l$ and $S = S_r$.

If Equation (3-45) were solved for $\{P^*\}$ subject to the above boundary conditions, all of the dimensionless stiffness and damping coefficients could be obtained by substituting $\{P^*\}$ for P in Equation (3-35). The real parts of the computed forces and moments would be in phase with the eccentricity perturbations and constitute the dimensionless stiffness coefficients. Thus $\bar{K}_{yx}$ would correspond to the real part of $\bar{W}_y$ computed from the component of $\{P^*\}$ associated with the perturbation in ϵ_x and $\bar{K}_{\phi y}$ would correspond to the real part of $\bar{M}_x$ computed from the component of $\{P^*\}$ associated with the perturbation in ϵ_y etc. In a similar manner, the dimensionless damping coefficients which are 90° out of phase with the eccentricity perturbations would be obtained by dividing the imaginary parts of the forces and moments computed in the manner described above by σ.

The parameter σ, is a dimensionless disturbance frequency referred to as the "squeeze number" and is given by $\sigma = 2\Lambda\Omega/\omega$ where Ω is the angular velocity of the disturbance. The limiting form of the stiffness and damping coefficients as $\sigma \rightarrow 0$, is of interest as it applies to incompressible flow, and the limiting stiffnesses are used in the homing procedure that has been implemented for determining eccentricities from given loads which will be described later. This limiting form may be obtained by expressing Equation (3-45) in terms

3-21

of its real and imaginary parts as

$$\mathcal{L}\{P_R\} + \{b\} = \sigma^2(\alpha\bar{\delta} + \hat{H})\{P_S\} \quad . \tag{3-46}$$

$$\mathcal{L}\{P_S\} = -(\alpha\bar{\delta} + \hat{H})\{P_R\} - (1 + \hat{P})\{a\} \quad , \tag{3-47}$$

where

$$\{P^*\} = \{P_R\} + \Im\sigma\{P_S\} \quad . \tag{3-48}$$

The column vectors $\{P_R\}$ and $\{P_S\}$ are the "stiffness" and "damping" pressures respectively. If one formally sets $\sigma = 0$ in Equation (3-46) it decouples from Equation (3-47) and may be solved directly. Since the right hand side of Equation (3-46) becomes 0, the stiffness pressures are the same as those that would be obtained by computing the steady state pressures at a perturbed eccentricity, subtracting the unperturbed pressures and dividing by the eccentricity perturbation. This latter method is frequently used for computing steady state stiffnesses in incompressible flow and has been implemented here for the computation of "stiffnesses at 0 frequency" used in the above mentioned homing procedure. The 0 frequency damping pressures may be obtained by solving Equation (3-47) with $\{P_R\}$ as determined from the solution to Equation (3-46).

The above discussion assumed that the perturbation coefficients in Equations (3-40) - (3-42) were determined prior to setting up the finite discretized equations for their solution. Identical results can be achieved by direct numerical perturbation of the difference equations. This approach, which has been implemented here and is described below, avoids algebraic error in determining the perturbation coefficients and may be used in complex situations where analytical determination of the perturbation coefficients is not feasible.

After desired convergence of the Newton-Raphson process has been achieved under steady (unperturbed) conditions one may denote the resulting steady state pressure vectors as $\{\hat{P}_j\}$ and the coefficient matrices as $[\hat{C}^j]$, etc. and Equation (3-34) may be written as

$$[\hat{C}^j]\{\hat{P}_j\} + [\hat{E}^j]\{\hat{P}_{j-1}\} + [\hat{D}^j]\{\hat{P}_{j+1}\} = \{\hat{A}^j\} \quad . \tag{3-49}$$

One may now perturb the kth component of the eccentricity vector by an amount η, recalculate $[\hat{C}^j]$ at the new film thickness (but old pressure distribution, $\hat{P}$) then subtract $[\hat{C}^j]$ at the old film thickness and divide the difference by η to numerically obtain the derivative of $[\hat{C}^j]$ with respect to ϵ_k which will be denoted by

$[\hat{C}^{j,k}]$. Thus

$$[\hat{C}^{j,k}] = \frac{[\hat{C}^j]|_{\epsilon_k+\eta} - [\hat{C}^j]|_{\epsilon_k}}{\eta} \; .$$

The matrices $[\hat{E}^{j,k}]$, $[\hat{D}^{j,k}]$ and $\{\hat{R}^{j,k}\}$ are obtained in a similar manner from the other coefficient matrices. If we introduce a disturbance to ϵ_k of magnitude $\epsilon'\eta$, as was done in deriving Equation (3-43), then the change in the coefficient matrix $[\hat{C}^j]$ would be $\epsilon'\eta\,[\hat{C}^{j,k}]$ with corresponding changes in the other coefficient matrices. If we disturb Equation (3-49) by replacing $\{\hat{P}_j\}$ with $\{\hat{P}_j\} + \eta\,\{P_j^{'k}\}$, $[\hat{C}_j]$ with $[\hat{C}^j] + \epsilon'\eta\,[\hat{C}^{j,k}]$, etc. and collect terms of order η, the following expression is obtained:

$$[\hat{C}^j]\{P_j^{'k}\} + [\hat{E}^j]\{P_{j-1}^{'k}\} + [\hat{D}^j]\{P_{j+1}^{'k}\} = \left(\{\hat{R}^{j,k}\} - [\hat{C}^{j,k}]\{\hat{P}_j\} - [\hat{E}^{j,k}]\{\hat{P}_{j-1}\} - [\hat{D}^{j,k}]\{\hat{P}_{j+1}\}\right)\epsilon' \; . \quad (3\text{-}50)$$

If we set ϵ' to unity in Equation (3-50) then $\{P_j^{'k}\}$ will become the 0 frequency stiffness pressure (the change in steady state pressure per unit change in eccentricity). It should be noted that the coefficients of the 0 frequency stiffness pressures in Equation (3-50) are the same as those for the steady state pressures in Equation (3-49); only the right hand side has changed. Equation (3-50) thus represents the construction of the discretized form of Equation (3-43) when $\sigma = 0$. In order to complete the process for $\sigma \neq 0$, one may introduce the same disturbances to the right hand side of Equation (3-31), with $H_r = \hat{H} + \epsilon'\eta\,\{a\}$ and add the terms of order η to the right hand side of Equation (3-50). The terms to be added are $-\partial([\bar{C}^j]\{P_j^{'k}\} + \{\bar{R}^{j,k}\}\epsilon')/\partial\hat{t}$, where $[\bar{C}^j]$ are diagonal matrices whose components are

$$\bar{C}_i^j = (\alpha\bar{\delta} + \bar{H})_{i+\frac{1}{2},j+\frac{1}{2}}\Delta\bar{A}_1 + (\alpha\bar{\delta} + \bar{H})_{i+\frac{1}{2},j-\frac{1}{2}}\Delta\bar{A}_4 + (\alpha\bar{\delta} + \bar{H})_{i-\frac{1}{2},j-\frac{1}{2}}\Delta\bar{A}_3 + (\alpha\bar{\delta} + \bar{H})_{i-\frac{1}{2},j+\frac{1}{2}}\Delta\bar{A}_2 \quad (3\text{-}51)$$

and $\{\bar{R}^{j,k}\}$ are column vectors whose components are

$$\bar{R}_i^{j,k} = (1 + \hat{P}_{ij})(a_{i+\frac{1}{2},j+\frac{1}{2}}^k\Delta\bar{A}_1 + a_{i+\frac{1}{2},j-\frac{1}{2}}^k\Delta\bar{A}_4 + a_{i-\frac{1}{2},j-\frac{1}{2}}^k\Delta\bar{A}_3 + a_{i-\frac{1}{2},j+\frac{1}{2}}^k\Delta\bar{A}_2) = (1 + \hat{P}_{ij})a_{ij}^k\Delta\bar{A} \; . \quad (3\text{-}52)$$

The far right side of Equation (3-52) is a quadradically equivalent representation that was used in the computer program described in Section 3. One may now set $\epsilon' = e^{\bar{s}\sigma\hat{t}}$ in Equation (3-50) and look for solutions in the form $\{P_j^{'k}\} = \{P_j^{*k}\}e^{\bar{s}\sigma\hat{t}}$, by introducing these substitutions into Equation (3-50) and combining terms to obtain the final set of linear difference equations for the complex stiffness pressures $\{P_j^{*k}\}$:

$$[C^{*j}]\{P_j^{*k}\} + [\hat{E}^j]\{P_{j-1}^{*k}\} + [\hat{D}^j]\{P_{j+1}^{*k}\} = \{R^{j,k}\} - [\hat{C}^{j,k}]\{\hat{P}_j\} - [\hat{E}^{j,k}]\{\hat{P}_{j-1}\} - [\hat{D}^{j,k}]\{\hat{P}_{j+1}\} \; , \quad (3\text{-}53)$$

3-23

where $[C^*_j] = [\hat{C}_j] + \mathcal{G}\sigma[\bar{C}_j]$ and $\{R^{j,k}\} = \{\hat{R}^{j,k}\} - \mathcal{G}\sigma\{\bar{R}^{j,k}\}$.

The system of equations given by Equation (3-53) has been solved by the column method in a directly analogous manner to that used in solving Equation (3-34). The principal difference lies in the fact that all of the matrix operations were performed using complex arithmetic. The dimensionless, frequency dependent stiffness and damping coefficients were computed from the complex stiffness pressures in the previously described manner. Relationships of the following type may be used to calculate the physical stiffness and damping coefficients from the dimensionless ones:

$$K_{xx} = K_0 \mathcal{K}_{xx} \ , \quad K_{\phi\phi} = K_0 R_0^2 \mathcal{K}_{\phi\phi} \ , \quad K_{x\phi} = K_0 R_0 \mathcal{K}_{x\phi} \tag{3-54}$$

and

$$B_{xx} = B_0 \mathcal{B}_{xx} \ , \quad B_{\phi\phi} = B_0 R_0^2 \mathcal{B}_{\phi\phi} \ , \quad B_{x\phi} = B_0 R_0 \mathcal{B}_{x\phi} \ , \tag{3-55}$$

where $K_0 = p_0 R_0^2 / C$ and $B_0 = 12 \mu R_0^4 / C^3$.

Optimization of groove parameters for maximum stagnation pressure in a concentric cylindrical seal

Since spiral grooves are solely responsible for the axial stiffness of an aligned, gas lubricated face seal with parallel surfaces under steady state conditions, it is often desirable to optimize groove parameters for maximum axial stiffness. An optimization procedure for doing this has been implemented in the computer code SPIRALP described in Reference 8. The analogous situation is not as evident in a concentric gas lubricated cylindrical seal which will have considerable, if not maximum stiffness without spiral grooves. A large portion of the stiffness in the absence of spiral grooves will be cross coupled, particularly at low values of Λ, thus giving rise to stability problems which may be alleviated with the use of spiral grooves. The criteria for optimizing groove geometry from a dynamic standpoint would thus depend on both the desired load capacity and the various other elements in the system affecting rotordynamic performance.

An alternate approach for developing a stand alone criterion for optimizing groove geometry in a cylindrical seal is to maximize the pressure gradient that the grooves can generate at stagnation. If the grooves are being used to pump against a pressure gradient, the maximum stagnation pressure gradient would represent the maximum pressure gradient that the grooves could pump against without allowing any net flow to go through. It would also represent the maximum axial pressure gradient that the grooves could generate in an aligned, symmetric herringbone bearing in the absence of an imposed pressure gradient. In any event, the stagnation pressure gradient is a strong measure of spiral groove performance and even though optimizing it is not a precise criterion for optimizing dynamic performance, computations obtained with

3-24

geometries optimized in this manner should provide a strong indication of the maximum benefits obtainable with the use of spiral grooves.

The stagnation pressure gradient for a cylindrical seal under concentric conditions may be obtained from Equation (3-22) by setting $Q_s = 0$ (stagnation), $\partial P/\partial\theta = 0$, $H_r = 1$ (concentric), $S = Z$ and $R = 1$ (cylindrical seal). The resulting equation may be solved for $\Delta P/\Delta Z$ making use of the definition of Λ_δ given by Equation (3-24) and the definitions of k_1 and k_4 given by Equation (3-25) to obtain the following relationship

$$\frac{\partial P}{\partial Z} = \Lambda\bar{\omega}\frac{\delta\alpha(1-\alpha)\sin\beta\cos\beta(\Gamma^\delta-1)}{\alpha(1-\alpha)(\Gamma^\delta-1)^2\sin^2\beta+\Gamma^\delta} \ .$$

The right hand side of the above equation may be treated as a function of α, β and $\bar{\delta}$ ($\Gamma = 1 + \bar{\delta}$) and has a maximum value of $\partial P/\partial Z = 0.09118\,\Lambda\bar{\omega}$ at $\alpha_{opt} = 0.5$, $\beta_{opt} = 0.2736$ (15.68°) and $\bar{\delta} = 2.653$.

The variation of the pressure gradient near the optimum point is shown in Figure 3-4. The curve marked α was obtained by holding β and $\bar{\delta}$ at their optimum values and varying α. The other curves were obtained in an analogous manner. The curves show the sensitivity of the optimum pressure gradient to the various parameters and verify the existence of a relative maximum at the optimum point.

Other approaches to the optimization problem are given in Reference 2 for spiral groove bearings and Reference 9 for spiral groove viscous pumps.

3-25
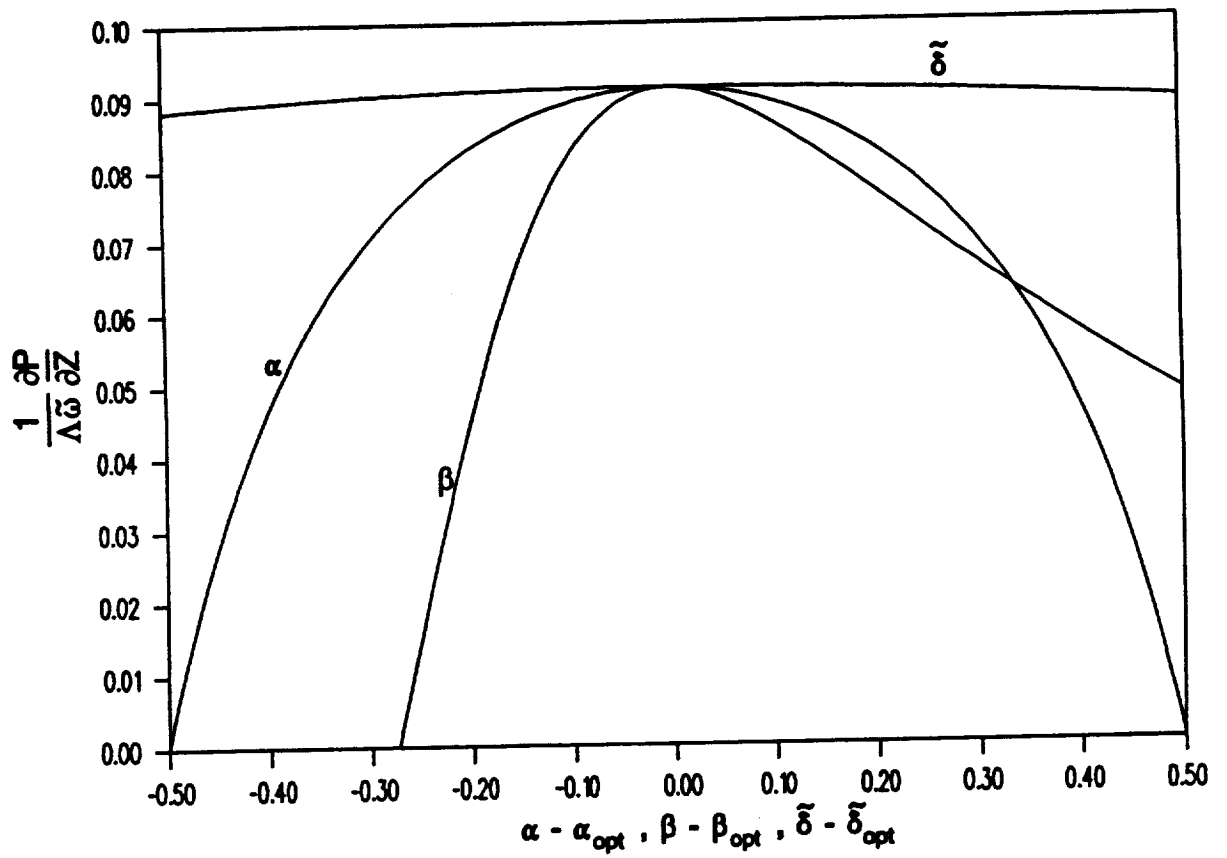
Figure 3-4 The variation of the stagnation pressure gradient about the optimum point

3.2 Description of Computer Code SPIRALG and Subroutine SPIRAL

A FORTRAN subroutine, SPIRAL, has been written to implement the analysis developed under Section 3.1.2 in dimensionless form. The analysis has been programmed in this form to permit easy incorporation into the knowledge base system currently under development. SPIRAL and its associated sub-programs constitute a self contained system that has no input-output other than the arguments passed to it through SPIRAL and is thus independent of the operating system. SPIRAL has been compiled, in its present form with Version 5.0 of the Microsoft Fortran Compiler and should work with many other compilers with relatively little modification. Significant user information is included in the Users Manual, Reference (10).

The analytical procedure contained in Section 3-2 has been oriented toward determining pressure distribution, load, flow, torque, stiffness and damping for a given film thickness distribution. In practice it is often desirable to determine the equilibrium film thickness or eccentricities from prescribed loads and possibly moments. SPIRAL provides a homing option for determining the eccentricities based on the steady state bearing stiffnesses. This homing option is based on the procedure described below.

If one were to write the dimensionless load and eccentricity as column vectors $\{\tilde{W}\}$ and $\{\epsilon\}$ (transpose row matrix $\lfloor \epsilon \rfloor$) and take the previous estimate (or initial guess) of $\{\epsilon\}$ as $\{\epsilon\}_{old}$ and the load vector computed from $\{\epsilon\}_{old}$ as $\{\tilde{W}\}_{old}$, the steady state stiffness matrix $[\tilde{K}]$ could be used to arrive at a new approximation for $\{\epsilon\}$. The method for doing this is shown by first writing the equation for the change in load as $\{\tilde{W}\} - \{\tilde{W}\}_{old} = [\tilde{K}](\{\epsilon\} - \{\epsilon\}_{old})$. The new approximation to $\{\epsilon\}$ is obtained by inverting the stiffness matrix and solving for $\{\epsilon\}$ as $\{\epsilon\} = \{\epsilon\}_{old} + [\tilde{K}]^{-1}(\{\tilde{W}\} - \{\tilde{W}\}_{old})$. This approach is in effect the application of the Newton-Raphson method for determining the eccentricities.

While the above approach can be very effective it can also diverge if the initial guesses are bad. This divergence is usually accompanied by the generation of negative film thicknesses in the course of the iteration process. In order to attempt to correct this problem, an optional numerical damping algorithm has been implemented which replaces $\{\epsilon\}$ with $\{\epsilon\} = \{\epsilon\}_{old} + \bar{\beta} [\tilde{K}]^{-1}(\{\tilde{W}\} - \{\tilde{W}\}_{old})$ when the originally calculated value of $\{\epsilon\}$ would result in a negative film thickness.

The cell method of discretization is designed to obtain quadratic accuracy. Numerical testing indicates that this has apparently been achieved. One may make use of this property to obtain greater accuracy, (or the same degree of accuracy with coarser grids and ensuing reductions in computer time) with the use of Romberg extrapolation. Suppose for example we computed the dimensionless torque $\bar{T}$ with a coarse grid and denoted it by $\bar{T}_c$ then halved the grid spacing in both directions and recomputed $\bar{T}$ denoting it as $\bar{T}_f$ (subscript denotes fine grid). If the truncation error were to approach 0 as the square of the grid spacing and $\bar{T}_r$ were the true solution then $(\bar{T}_f - \bar{T}_r) = (\bar{T}_c - \bar{T}_r)/4$, or $\bar{T}_r = (4\bar{T}_f - \bar{T}_c)/3$. The above extrapolation

can, in principal, increase the rate of convergence from quadratic to cubic. The subroutine SPIRAL, provides the option of implementing Romberg extrapolation.

The logic used in SPIRAL for performing the pressure iterations, computing stiffness and damping coefficients, homing in on eccentricities and implementing Romberg extrapolation is shown in Figure 3-5. It can be seen there that when the homing process is implemented, it is completed for both coarse grid and fine grid solutions prior to performing the Romberg extrapolation. The extrapolation is thus performed with solutions obtained at two different displacements. When the displacements are specified, extrapolations are performed with solutions obtained at the same displacement, which is believed to be a more accurate approach. If one were to compute displacements for a given loading and then recompute the loading from the displacements using Romberg extrapolation for both computations the computed loading would thus differ slightly from the input loading even though all tolerances were met. The degree of this difference will depend on the grid size and caution should be exercised in using Romberg extrapolation when homing in on the displacements with very coarse grids.
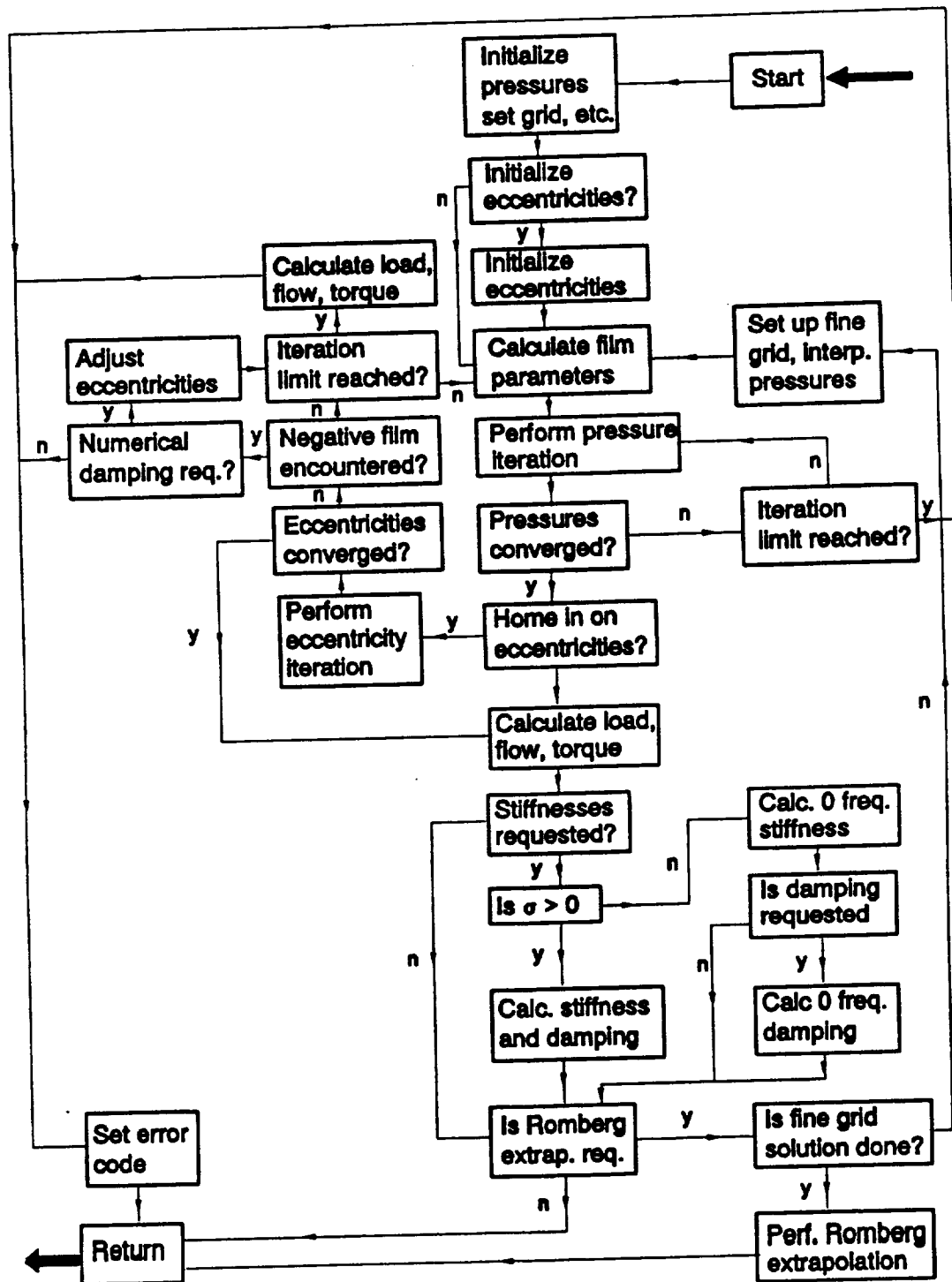
Figure 3-5   Flow diagram for logic used in SUBROUTINE SPIRAL

3.3 Sample Problems

A number of sample problems have been prepared to demonstrate the behavior and various features of the computer program. They are intended primarily for illustration and do not necessarily represent recommended seal designs.

Cases 1 - 3 serve to show the improvement in accuracy that can be obtained with the use of Romberg extrapolation for a concentric, asymmetric cylindrical seal. The seal is divided into two regions of equal length as shown in Figure 3-7. The stationary surface in the first region has a groove geometry optimized for maximum stagnation pressure as described at the end of Section 3-2. The grooves are oriented to produce a pumping component in the positive axial direction to partially offset the larger negative one caused by the imposed pressure gradient. The second region is smooth. The case 1 results were obtained without the use of Romberg extrapolation. Romberg extrapolation was used in Case 2 with coarse grid solution obtained for the same grid geometry as used in Case 1. Since the grid spacing is halved in each direction when obtaining the fine grid solution, Case 2 should represent a much more accurate solution than Case 1. It also took approximately 11 times as long to run. Romberg extrapolation was used in Case 3 with twice the grid spacing as that used in Case 2 and took only 25% longer to run than Case 1. The direct stiffness coefficients, K_{xx}, calculated for Cases 1 - 3 are 54684, 57622 and 57342 lb/in, respectively. Using Case 2 as a standard, the error in the Case 1 stiffness is 5.1% while the error in the Case 3 stiffness is only .5%.

A symmetric "herringbone groove" pattern is used in Case 4 with the same overall geometry as that used in Cases 1 - 3. The groove pattern on the stator in region 2 is the same as that for region 1 with the exception of the sign of the groove angle. The grid geometry is the same as that used in Case 1 but the operating conditions differ in that there is no imposed pressure gradient and the shaft is displaced in the x direction and tilted about the y axis. It can be seen that the imposed displacement and tilt produces non-zero values for the calculated forces and moments. The results of Case 5 were obtained by prescribing the forces and moments computed for Case 4. The initial guess for the shaft displacement for Case 5 was taken to be somewhat larger than prescribed for Case 4 and initial guess for the tilt was taken as 0. The displacements calculated for Case 5 are essentially the same as those imposed in Case 4. Case 6 illustrates the use of the program with SI units.

The remaining 2 cases correspond to a mechanical face seal under a very high imposed pressure gradient with spiral grooves on the outside surface of the stator oriented to pump inward with the pressure gradient. The stator geometry is shown schematically in Figure 3-8, with the land width somewhat enlarged for clarity. The inward pumping is induced by the counterclockwise motion of the rotor. Solutions to this problem will

be approximate in nature in that choking is likely to occur (not treated here as a result of assumed isothermal flow with negligible inertia) which will raise the effective film pressure at the inside radius to a value somewhat higher than that prescribed. These cases are provided to illustrate the use of the program with a face seal and the evaluation of the internal accuracy of the program. Case 8 was obtained by halving the grid spacing used in Case 7, in both directions. This procedure provides a test for truncation error, which is small in this case, that is recommended for frequent use in determining appropriate grid spacing.
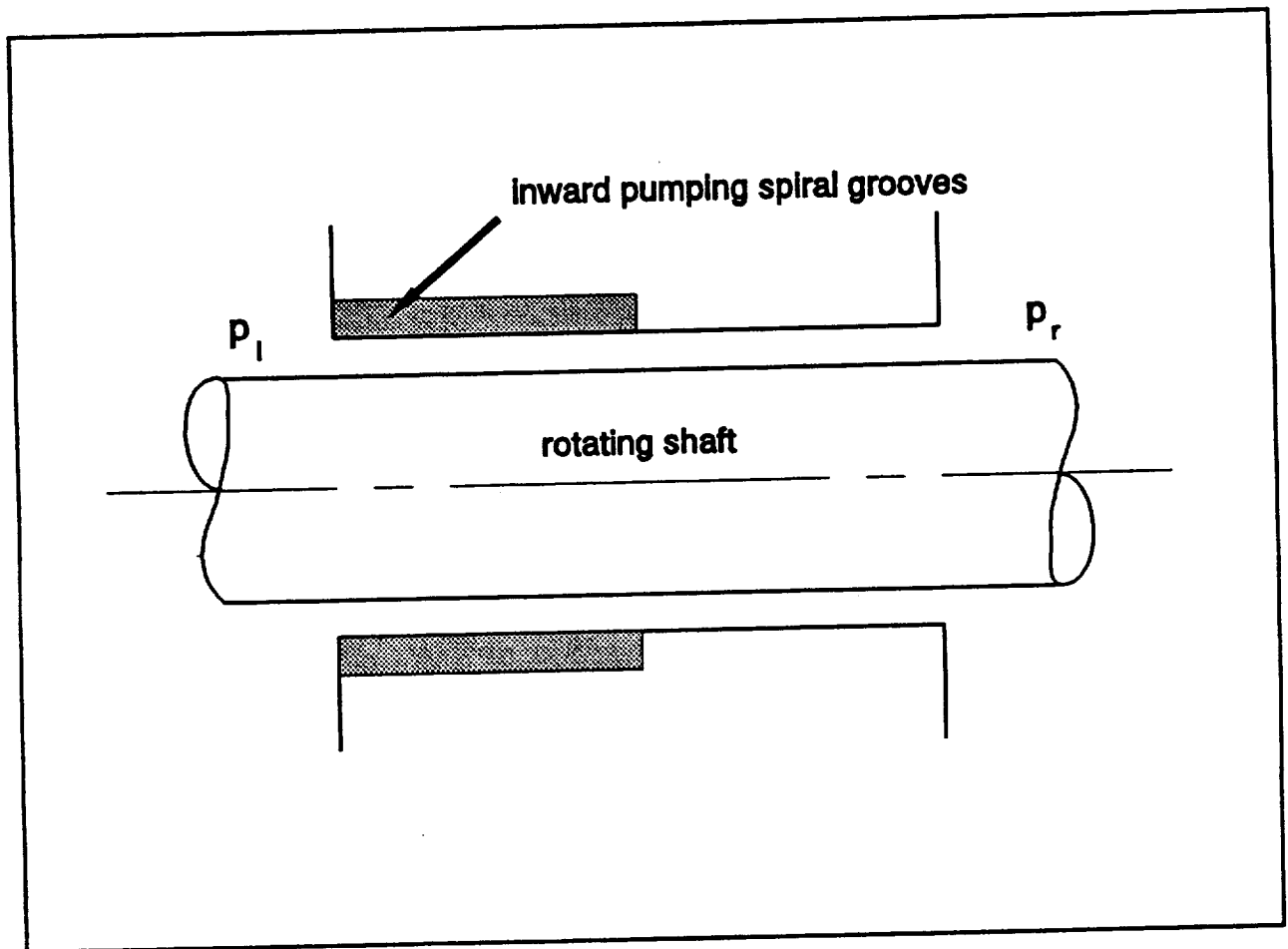
Figure 3-6   Schematic of shaft seal for Cases 1 - 3

(CASE 1) Asymmetric cyl. seal with grooves pumping against pres. grad.

SPIRAL GROOVE SHAFT SEAL, ROTATING SURFACE IS SMOOTH
LENGTH, DIAMETER, CLEARANCE - 2.0000E+00, 2.0000E+00, 5.0000E-04 (IN)
ROTATION SPEED, DISTURBANCE SPEED - 1.0000E+04, 1.0000E+04 (RPM)
PRESSURE AT START, END AXIAL BOUNDARIES - 1.4700E+01, 6.4700E+01 (PSI)
VISCOSITY - 2.9000E-09 (PSI-SEC),   AMBIENT PRESSURE - 1.4700E+01 (PSI)
ITERATIONS AND ERROR CODE IN LAST PRESSURE CALCULATION - 3 0
CALCULATED FORCES IN X,Y DIRECTIONS - -2.1540E-14, 1.2544E-13 (LB)
CALCULATED MOMENTS ABOUT X,Y AXES - -8.6002E-15, -2.2927E-14 (IN-LB)
MINIMUM FILM THICKNESS - 5.0000E-04 (IN)
FLOW - -2.1757E+00 (IN**3/SEC) MEASURED AT 1.4700E+01 (PSI)
TORQUE - 7.4543E-02 (IN-LB),   FILM POWER LOSS - 1.1827E-02 (HP)
COMPRESSIBILITY NUMBER - 4.9582E+00,   SQUEEZE NUMBER - 9.9163E+00
          DYNAMIC COEFFICIENTS (FORCE UNIT / DISP. UNIT)

DISP.	x (IN)	y (IN)	phi (RAD)	psi (RAD)	FORCE UNIT
Kx	5.4684E+04	3.0916E+04	-2.7046E+04	-6.0468E+04	LB
Ky	-3.0916E+04	5.4684E+04	6.0468E+04	-2.7046E+04	LB
Kphi	7.8082E+03	-8.1693E+03	-3.4030E+03	1.0593E+04	IN-LB
Kpsi	8.1693E+03	7.8082E+03	-1.0593E+04	-3.4030E+03	IN-LB
Bx	1.1158E+02	-2.9219E+01	1.8107E+01	6.2395E+01	LB-SEC
By	2.9219E+01	1.1158E+02	-6.2395E+01	1.8107E+01	LB-SEC
Bphi	-1.0745E+01	-1.7276E+01	1.7903E+01	-7.7389E+00	IN-LB-SEC
Bpsi	1.7276E+01	-1.0745E+01	7.7389E+00	1.7903E+01	IN-LB-SEC

(CASE 2) Romberg extrapolation with coarse grid the same as Case 1

SPIRAL GROOVE SHAFT SEAL,   ROTATING SURFACE IS SMOOTH

LENGTH, DIAMETER, CLEARANCE = 2.0000E+00, 2.0000E+00, 5.0000E-04 (IN)

ROTATION SPEED, DISTURBANCE SPEED = 1.0000E+04, 1.0000E+04 (RPM)

PRESSURE AT START, END AXIAL BOUNDARIES = 1.4700E+01, 6.4700E+01 (PSI)

VISCOSITY = 2.9000E-09 (PSI-SEC),   AMBIENT PRESSURE = 1.4700E+01 (PSI)

ITERATIONS AND ERROR CODE IN LAST PRESSURE CALCULATION = 3 0

CALCULATED FORCES IN X,Y DIRECTIONS = 3.0897E-13, 1.7781E-13 (LB)
CALCULATED MOMENTS ABOUT X,Y AXES = -9.7768E-14, 1.3279E-13 (IN-LB)

MINIMUM FILM THICKNESS = 5.0000E-04 (IN)

FLOW = -2.1749E+00 (IN**3/SEC) MEASURED AT 1.4700E+01 (PSI)

TORQUE = 7.4550E-02 (IN-LB),   FILM POWER LOSS = 1.1829E-02 (HP)

COMPRESSIBILITY NUMBER = 4.9582E+00,   SQUEEZE NUMBER = 9.9163E+00

DYNAMIC COEFFICIENTS (FORCE UNIT / DISP. UNIT)

DISP.	x (IN)	y (IN)	phi (RAD)	psi (RAD)	FORCE UNIT
Kx	5.7622E+04	3.2577E+04	-2.9332E+04	-6.4855E+04	LB
Ky	-3.2577E+04	5.7622E+04	6.4855E+04	-2.9332E+04	LB
Kphi	8.1664E+03	-8.4866E+03	-3.6583E+03	1.2003E+04	IN-LB
Kpsi	8.4866E+03	8.1664E+03	-1.2003E+04	-3.6583E+03	IN-LB
Bx	1.1837E+02	-3.1897E+01	2.0183E+01	6.7544E+01	LB-SEC
By	3.1897E+01	1.1837E+02	-6.7544E+01	2.0183E+01	LB-SEC
Bphi	-1.2229E+01	-1.8217E+01	1.9551E+01	-9.0828E+00	IN-LB-SEC
Bpsi	1.8217E+01	-1.2229E+01	9.0828E+00	1.9551E+01	IN-LB-SEC

(CASE 3) Romberg extrapolation with fine grid the same as Case 1

SPIRAL GROOVE SHAFT SEAL, ROTATING SURFACE IS SMOOTH

LENGTH, DIAMETER, CLEARANCE - 2.0000E+00, 2.0000E+00, 5.0000E-04 (IN)

ROTATION SPEED, DISTURBANCE SPEED - 1.0000E+04, 1.0000E+04 (RPM)

PRESSURE AT START, END AXIAL BOUNDARIES - 1.4700E+01, 6.4700E+01 (PSI)

VISCOSITY - 2.9000E-09 (PSI-SEC), AMBIENT PRESSURE - 1.4700E+01 (PSI)

ITERATIONS AND ERROR CODE IN LAST PRESSURE CALCULATION - 3 0

CALCULATED FORCES IN X,Y DIRECTIONS - -2.5045E-14, 8.0461E-14 (LB)
CALCULATED MOMENTS ABOUT X,Y AXES - -3.2816E-14, -1.0084E-14 (IN-LB)

MINIMUM FILM THICKNESS - 5.0000E-04 (IN)

FLOW - -2.1750E+00 (IN**3/SEC) MEASURED AT 1.4700E+01 (PSI)

TORQUE - 7.4549E-02 (IN-LB), FILM POWER LOSS - 1.1828E-02 (HP)

COMPRESSIBILITY NUMBER - 4.9582E+00, SQUEEZE NUMBER - 9.9163E+00

DYNAMIC COEFFICIENTS (FORCE UNIT / DISP. UNIT)

DISP.	x (IN)	y (IN)	phi (RAD)	psi (RAD)	FORCE UNIT
Kx	5.7342E+04	3.2559E+04	-2.9001E+04	-6.4238E+04	LB
Ky	-3.2559E+04	5.7342E+04	6.4238E+04	-2.9001E+04	LB
Kphi	8.2990E+03	-8.5936E+03	-3.7301E+03	1.1766E+04	IN-LB
Kpsi	8.5936E+03	8.2990E+03	-1.1766E+04	-3.7301E+03	IN-LB
Bx	1.1766E+02	-3.1507E+01	1.9728E+01	6.6992E+01	LB-SEC
By	3.1507E+01	1.1766E+02	-6.6992E+01	1.9728E+01	LB-SEC
Bphi	-1.1932E+01	-1.8433E+01	1.9494E+01	-8.7410E+00	IN-LB-SEC
Bpsi	1.8433E+01	-1.1932E+01	8.7410E+00	1.9494E+01	IN-LB-SEC

(CASE 4) Displaced and tilted symmetric cyl. seal, no pres. grad.

SPIRAL GROOVE SHAFT SEAL, ROTATING SURFACE IS SMOOTH

LENGTH, DIAMETER, CLEARANCE = 2.0000E+00, 2.0000E+00, 5.0000E-04 (IN)

ROTATION SPEED, DISTURBANCE SPEED = 1.0000E+04, 1.0000E+04 (RPM)

PRESSURE AT START, END AXIAL BOUNDARIES = 1.4700E+01, 1.4700E+01 (PSI)

VISCOSITY = 2.9000E-09 (PSI-SEC), AMBIENT PRESSURE = 1.4700E+01 (PSI)

ITERATIONS AND ERROR CODE IN LAST PRESSURE CALCULATION = 4 0

CALCULATED FORCES IN X,Y DIRECTIONS = 3.3938E+00, -3.0660E+00 (LB)
CALCULATED MOMENTS ABOUT X,Y AXES = 2.6476E-01, 3.6468E-01 (IN-LB)

MINIMUM FILM THICKNESS = 2.5000E-04 (IN)

FLOW = 2.0302E-02 (IN**3/SEC) MEASURED AT 1.4700E+01 (PSI)

TORQUE = 5.8726E-02 (IN-LB), FILM POWER LOSS = 9.3178E-03 (HP)

COMPRESSIBILITY NUMBER = 4.9582E+00, SQUEEZE NUMBER = 9.9163E+00

DYNAMIC COEFFICIENTS (FORCE UNIT / DISP. UNIT)

DISP.	x (IN)	y (IN)	phi (RAD)	psi (RAD)	FORCE UNIT
Kx	4.0657E+04	9.7405E+03	-8.3206E+01	-2.8523E+02	LB
Ky	-9.4351E+03	4.0515E+04	2.5345E+02	1.2957E+02	LB
Kphi	-2.9470E+01	2.1556E+02	4.8420E+03	1.5075E+03	IN-LB
Kpsi	-1.2690E+02	7.3977E+01	-1.4889E+03	4.8095E+03	IN-LB
Bx	2.3280E+01	-1.3471E+01	1.0865E-01	6.3426E-01	LB-SEC
By	1.3609E+01	2.2299E+01	-1.3412E-01	2.1028E-01	LB-SEC
Bphi	-7.2952E-02	-1.0697E-01	4.5324E+00	-1.0203E+00	IN-LB-SEC
Bpsi	4.7944E-01	-7.1164E-02	9.5944E-01	4.8461E+00	IN-LB-SEC

(CASE 5) Same seal as Case 4 with applied forces instead of displ.

SPIRAL GROOVE SHAFT SEAL, ROTATING SURFACE IS SMOOTH

LENGTH, DIAMETER, CLEARANCE - 2.0000E+00, 2.0000E+00, 5.0000E-04 (IN)

ROTATION SPEED, DISTURBANCE SPEED - 1.0000E+04, 1.0000E+04 (RPM)

PRESSURE AT START, END AXIAL BOUNDARIES - 1.4700E+01, 1.4700E+01 (PSI)

VISCOSITY - 2.9000E-09 (PSI-SEC), AMBIENT PRESSURE - 1.4700E+01 (PSI)

ERROR CODE - 0, ITERATIONS IN HOMING PROCESS - 3

CALCULATED DISPLACEMENTS IN X,Y DIRECTIONS - 1.2500E-04, -1.1010E-09 (IN)
CALCULATED TILTS ABOUT X,Y AXES - 9.8499E-10, 1.2500E-04 (RAD)

ITERATIONS IN LAST PRESSURE CALCULATION - 1

CALCULATED FORCES IN X,Y DIRECTIONS - 3.3938E+00, -3.0660E+00 (LB)
CALCULATED MOMENTS ABOUT X,Y AXES - 2.6476E-01, 3.6468E-01 (IN-LB)

MINIMUM FILM THICKNESS - 2.5000E-04 (IN)

FLOW - 2.0301E-02 (IN**3/SEC) MEASURED AT 1.4700E+01 (PSI)

TORQUE - 5.8726E-02 (IN-LB), FILM POWER LOSS - 9.3178E-03 (HP)

COMPRESSIBILITY NUMBER - 4.9582E+00, SQUEEZE NUMBER - 9.9163E+00

DYNAMIC COEFFICIENTS (FORCE UNIT / DISP. UNIT)

DISP.	x (IN)	y (IN)	phi (RAD)	psi (RAD)	FORCE UNIT
Kx	4.0657E+04	9.7405E+03	-8.3205E+01	-2.8523E+02	LB
Ky	-9.4351E+03	4.0515E+04	2.5345E+02	1.2957E+02	LB
Kphi	-2.9469E+01	2.1556E+02	4.8420E+03	1.5075E+03	IN-LB
Kpsi	-1.2690E+02	7.3975E+01	-1.4889E+03	4.8095E+03	IN-LB
Bx	2.3280E+01	-1.3471E+01	1.0865E-01	6.3425E-01	LB-SEC
By	1.3609E+01	2.2299E+01	-1.3412E-01	2.1028E-01	LB-SEC
Bphi	-7.2948E-02	-1.0696E-01	4.5324E+00	-1.0203E+00	IN-LB-SEC
Bpsi	4.7943E-01	-7.1166E-02	9.5944E-01	4.8461E+00	IN-LB-SEC

3-37

(CASE 6)   Same as Case 4 with SI units

SPIRAL GROOVE SHAFT SEAL, ROTATING SURFACE IS SMOOTH

LENGTH, DIAMETER, CLEARANCE - 5.0800E-02, 5.0800E-02, 1.2700E-05 (m)

ROTATION SPEED, DISTURBANCE SPEED - 1.0000E+04, 1.0000E+04 (RPM)

PRESSURE AT START, END AXIAL BOUNDARIES - 1.0135E+05, 1.0135E+05 (Pa)

VISCOSITY - 1.9995E-05 (Pa-SEC),   AMBIENT PRESSURE - 1.0135E+05 (Pa)

ITERATIONS AND ERROR CODE IN LAST PRESSURE CALCULATION - 4 0

CALCULATED FORCES IN X,Y DIRECTIONS - 1.5097E+01, -1.3638E+01 (N)
CALCULATED MOMENTS ABOUT X,Y AXES - 2.9914E-02, 4.1204E-02 (N-m)

MINIMUM FILM THICKNESS - 6.3500E-06 (m)

FLOW - 3.3268E-07 (m**3/SEC) MEASURED AT 1.0135E+05 (Pa)

TORQUE - 6.6352E-03 (N-m),   FILM POWER LOSS - 6.9483E+00 (WATT)

COMPRESSIBILITY NUMBER - 4.9584E+00,   SQUEEZE NUMBER - 9.9167E+00

        DYNAMIC COEFFICIENTS (FORCE UNIT / DISP. UNIT)

DISP.	x (m)	y (m)	phi (RAD)	psi (RAD)	FORCE UNIT
Kx	7.1202E+06	1.7058E+06	-3.7010E+02	-1.2688E+03	N
Ky	-1.6523E+06	7.0953E+06	1.1274E+03	5.7639E+02	N
Kphi	-1.3110E+02	9.5888E+02	5.4708E+02	1.7032E+02	N-m
Kpsi	-5.6446E+02	3.2904E+02	-1.6822E+02	5.4341E+02	N-m
Bx	4.0768E+03	-2.3592E+03	4.8331E-01	2.8213E+00	N-SEC
By	2.3833E+03	3.9051E+03	-5.9660E-01	9.3536E-01	N-SEC
Bphi	-3.2450E-01	-4.7582E-01	5.1209E-01	-1.1528E-01	N-m-SEC
Bpsi	2.1326E+00	-3.1658E-01	1.0841E-01	5.4754E-01	N-m-SEC
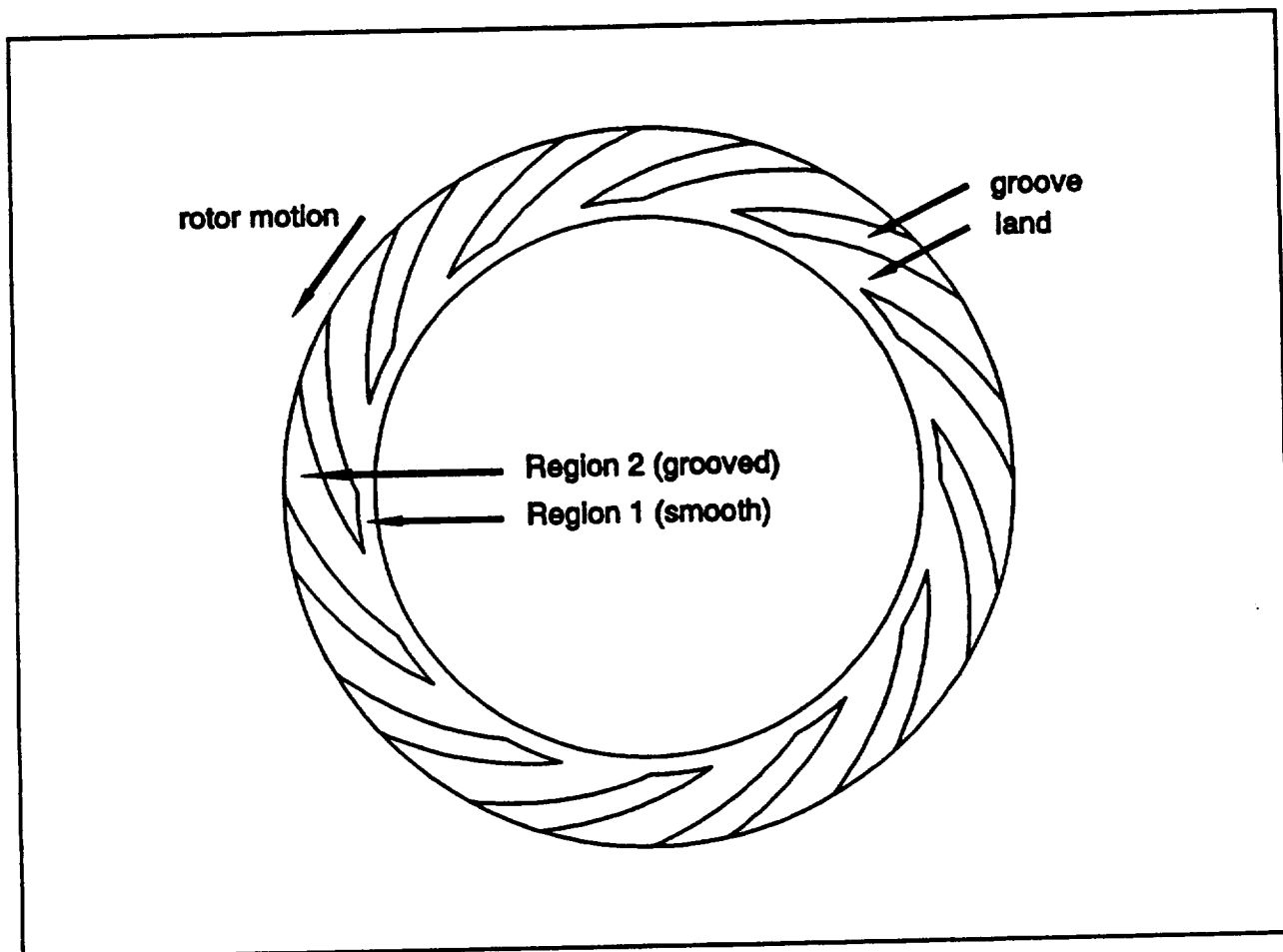
Figure 3-7 Stator with inward pumping grooves for Cases 7 and 8

(CASE 7) Face seal for pipe line compressor

SPIRAL GROOVE FACE SEAL, ROTATING SURFACE IS SMOOTH
ID, OD, REFERENCE FILM THICKNESS - 3.7930E+00, 4.5050E+00, 1.0000E-04 (IN)
ROTATION SPEED, DISTURBANCE SPEED - 1.4500E+04, 1.4500E+04 (RPM)
INSIDE, OUTSIDE PRESSURE - 1.4700E+01, 9.1470E+02 (PSI)
VISCOSITY - 1.7500E-09 (PSI-SEC),   AMBIENT PRESSURE - 1.4700E+01 (PSI)
ITERATIONS AND ERROR CODE IN LAST PRESSURE CALCULATION - 4 0
CALCULATED FORCE IN Z DIRECTION - 3.4246E+03 (LB)
CALCULATED MOMENTS ABOUT X,Y AXES - -1.0069E-12, -5.7018E-12 (IN-LB)
MINIMUM FILM THICKNESS - 1.0000E-04 (IN)
FLOW - -1.3026E+02 (IN**3/SEC) MEASURED AT 1.4700E+01 (PSI)
TORQUE - 3.2695E-01 (IN-LB),   FILM POWER LOSS - 7.5219E-02 (HP)
COMPRESSIBILITY NUMBER - 5.5030E+02,   SQUEEZE NUMBER - 1.1006E+03

DYNAMIC COEFFICIENTS (FORCE UNIT / DISP. UNIT)

DISP.	z (IN)	phi (RAD)	psi (RAD)	FORCE UNIT
Kz	7.0137E+06	-5.7802E+00	-5.7791E+00	LB
Kphi	-6.0544E-03	1.2466E+07	1.6134E+06	IN-LB
Kpsi	2.0659E-02	-1.6134E+06	1.2466E+07	IN-LB
Bz	2.8634E+02	1.7180E-04	1.7161E-04	LB-SEC
Bphi	-2.2269E-07	6.6669E+02	-7.0380E+01	IN-LB-SEC
Bpsi	-1.0207E-06	7.0380E+01	6.6669E+02	IN-LB-SEC

(CASE 8) Same as case 7 with half the grid spacing in each direction

SPIRAL GROOVE FACE SEAL, ROTATING SURFACE IS SMOOTH

ID, OD, REFERENCE FILM THICKNESS - 3.7930E+00, 4.5050E+00, 1.0000E-04 (IN)

ROTATION SPEED, DISTURBANCE SPEED - 1.4500E+04, 1.4500E+04 (RPM)

INSIDE, OUTSIDE PRESSURE - 1.4700E+01, 9.1470E+02 (PSI)

VISCOSITY - 1.7500E-09 (PSI-SEC), AMBIENT PRESSURE - 1.4700E+01 (PSI)

ITERATIONS AND ERROR CODE IN LAST PRESSURE CALCULATION - 4 0

CALCULATED FORCE IN Z DIRECTION - 3.4282E+03 (LB)
CALCULATED MOMENTS ABOUT X,Y AXES - 5.0522E-12, 2.5739E-12 (IN-LB)

MINIMUM FILM THICKNESS - 1.0000E-04 (IN)

FLOW - -1.3026E+02 (IN**3/SEC) MEASURED AT 1.4700E+01 (PSI)

TORQUE - 3.2695E-01 (IN-LB), FILM POWER LOSS - 7.5219E-02 (HP)

COMPRESSIBILITY NUMBER - 5.5030E+02, SQUEEZE NUMBER - 1.1006E+03

DYNAMIC COEFFICIENTS (FORCE UNIT / DISP. UNIT)

DISP.	z (IN)	phi (RAD)	psi (RAD)	FORCE UNIT
Kz	7.0318E+06	-5.8003E+00	-5.8209E+00	LB
Kphi	-4.1461E-02	1.2507E+07	1.6209E+06	IN-LB
Kpsi	-1.4393E-02	-1.6209E+06	1.2507E+07	IN-LB
Bz	2.8690E+02	1.7193E-04	1.7350E-04	LB-SEC
Bphi	6.6840E-07	6.6815E+02	-7.0687E+01	IN-LB-SEC
Bpsi	7.0000E-07	7.0687E+01	6.6815E+02	IN-LB-SEC

3.4 Verification

SPIRALG has been compared with the results of two computer codes. The first of these is MTI Computer Code PN471 which is fully described in Reference 3. The program is based on perturbation analyses and is only applicable to bearings and seals operating in the concentric, aligned position $(\epsilon_x = \epsilon_y = \phi = \psi = 0)$. The program does not predict loads and moments that would occur at finite displacements but it does predict stiffness and damping values as well as flow, torque, and power loss for spiral groove bearings as well as cylindrical and face seals. Since the program solves ordinary rather than partial differential equations it can be made to rapidly produce highly accurate results for evaluating the accuracy of SPIRALG. The second MTI computer code, named GASBEAR, is used to verify SPIRALG under displaced and misaligned conditions. GASBEAR was written for use in conjunction with plane journal bearings and cylindrical seals. It does not treat spiral grooves or face seals. Since SPIRALG does not contain any special instructions for treating concentric behavior and has relatively few instructions for distinguishing between face and cylindrical seals, the above two programs should provide reasonable verification. Since the treatment of the effects of spiral grooves under eccentric and misaligned conditions is believed to be new, terms that become significant only under those conditions remain unverified.

The results of 7 verification tests are reported on the following pages. A SPIRALG output listing followed by the relevant output from the verification code, converted to equivalent units and format, is given for each case. The somewhat strange looking input values (unit ambient pressure, high RPM but low viscosity etc.) were selected to simplify the conversion process between dimensional quantities and the dimensionless ones that were used throughout the development of the code. The compressibility number of $\Lambda = 10$ used for all cases and the seal pressure ratio of 2 used for imposed pressure gradients should be typical of many practical applications under fairly compressible conditions.

Cases 1 - 6 show comparisons between SPIRALG and PN471. Romberg extrapolation was used for each of these cases, with 21 grid points in the circumferential direction and 5 sub-intervals in each of the two regions in the transverse direction for the coarse grid solution. The fine grid solutions thus use 41 circumferential points and 10 sub-intervals per region in the transverse direction.

The first case verifies stiffness and damping values for a synchronous disturbance acting on a cylindrical seal with a herringbone groove pattern and an imposed pressure gradient. Cases 2 and 3 verify the differences in stiffness and damping values predicted to occur for a cylindrical seal when grooves are placed on the rotor (with groove angles reversed) rather than on the stator. The static quantities (flow, torque and power loss) remain unchanged. Cases 4 - 6 show comparisons between SPIRALG and PN471 for a spiral groove face seal with an imposed pressure gradient at three different disturbance frequencies; zero (case 4), synchronous (case 5) and ten times synchronous (case 6).

Case 7 shows a comparison between SPIRALG and GASBEAR for and eccentric, tilted cylindrical seal with an imposed pressure gradient. The grid size was chosen to match the maximum size allowable for the available version of GASBEAR. A separate program was written to perform Romberg extrapolations with the results of GASBEAR. The agreement between the two programs is good. The apparent discrepancy between the moments about the y axis is a result of the fact that the component is very small. The relative error obtained by dividing the discrepancy by the absolute magnitude of the moment vector is 0.33%.

(CASE 1) Concentric cyl. seal with pres. grad. lamda=10, sigma=20

SPIRAL GROOVE SHAFT SEAL, ROTATING SURFACE IS SMOOTH

LENGTH, DIAMETER, CLEARANCE = 2.0000E+00, 2.0000E+00, 1.0000E-03 (IN)

ROTATION SPEED, DISTURBANCE SPEED = 1.9099E+05, 1.9099E+05 (RPM)

PRESSURE AT START, END AXIAL BOUNDARIES = 2.0000E+00, 1.0000E+00 (PSI)

VISCOSITY = 8.3333E-11 (PSI-SEC), AMBIENT PRESSURE = 1.0000E+00 (PSI)

ITERATIONS AND ERROR CODE IN LAST PRESSURE CALCULATION = 2 0

CALCULATED FORCES IN X,Y DIRECTIONS = -1.0902E-15, -8.1153E-16 (LB)
CALCULATED MOMENTS ABOUT X,Y AXES = -9.3565E-16, -2.4405E-16 (IN-LB)

MINIMUM FILM THICKNESS = 1.0000E-03 (IN)

FLOW = 1.2816E+01 (IN**3/SEC) MEASURED AT 1.0000E+00 (PSI)

TORQUE = 1.7015E-02 (IN-LB), FILM POWER LOSS = 5.1562E-02 (HP)

COMPRESSIBILITY NUMBER = 1.0000E+01, SQUEEZE NUMBER = 2.0000E+01

DYNAMIC COEFFICIENTS (FORCE UNIT / DISP. UNIT)

DISP.	x (IN)	y (IN)	phi (RAD)	psi (RAD)	FORCE UNIT
Kx	5.4607E+03	9.0379E+01	-6.8886E+01	2.6847E+02	LB
Ky	-9.0379E+01	5.4607E+03	-2.6847E+02	-6.8886E+01	LB
Kphi	-1.0824E+02	-1.7773E+01	7.0561E+02	1.9521E+02	IN-LB
Kpsi	1.7773E+01	-1.0824E+02	-1.9521E+02	7.0561E+02	IN-LB
Bx	7.3200E-02	-5.5832E-02	-1.5172E-02	-2.9538E-02	LB-SEC
By	5.5832E-02	7.3200E-02	2.9538E-02	-1.5172E-02	LB-SEC
Bphi	1.9442E-03	6.9321E-03	2.7091E-02	-1.1690E-02	IN-LB-SEC
Bpsi	-6.9321E-03	1.9442E-03	1.1690E-02	2.7091E-02	IN-LB-SEC

COMPARISON OF CASE 1 WITH PN471

FLOW = 1.282E+01 (IN**3/SEC) MEASURED AT 1.0000E+00 (PSI)

TORQUE = 1.701E-02 (IN-LB), FILM POWER LOSS = 5.156E-02 (HP)

DYNAMIC COEFFICIENTS (FORCE UNIT / DISP. UNIT)

DISP.	x (IN)	y (IN)	phi (RAD)	psi (RAD)	FORCE UNIT
Kx	5.4608E+03	9.0292E+01	-6.8846E+01	2.6823E+02	LB
Ky	-9.0292E+01	5.4608E+03	-2.6823E+02	-6.8846E+01	LB
Kphi	-1.0809E+02	-1.7525E+01	7.0356E+02	1.9537E+02	IN-LB
Kpsi	1.7525E+01	-1.0809E+02	-1.9537E+02	7.0356E+02	IN-LB
Bx	7.3215E-02	-5.5805E-02	-1.5192E-02	-2.9534E-02	LB-SEC
By	5.5805E-02	7.3215E-02	2.9534E-02	-1.5192E-02	LB-SEC
Bphi	1.9403E-03	6.9195E-03	2.7097E-02	-1.1667E-02	IN-LB-SEC
Bpsi	-6.9195E-03	1.9403E-03	1.1667E-02	2.7097E-02	IN-LB-SEC

(CASE 2) Concentric asymmetric cyl. seal, lamda=10, sigma=0

SPIRAL GROOVE SHAFT SEAL, ROTATING SURFACE IS SMOOTH

LENGTH, DIAMETER, CLEARANCE = 2.0000E+00, 2.0000E+00, 1.0000E-03 (IN)

ROTATION SPEED, DISTURBANCE SPEED = 1.9099E+05, 0.0000E+00 (RPM)

PRESSURE AT START, END AXIAL BOUNDARIES = 1.0000E+00, 1.0000E+00 (PSI)

VISCOSITY = 8.3333E-11 (PSI-SEC), AMBIENT PRESSURE = 1.0000E+00 (PSI)

ITERATIONS AND ERROR CODE IN LAST PRESSURE CALCULATION = 2 0

CALCULATED FORCES IN X,Y DIRECTIONS = -2.8151E-15, -1.6233E-15 (LB)
CALCULATED MOMENTS ABOUT X,Y AXES = 2.7524E-16, -5.2158E-17 (IN-LB)

MINIMUM FILM THICKNESS = 1.0000E-03 (IN)

FLOW = 3.5000E+00 (IN**3/SEC) MEASURED AT 1.0000E+00 (PSI)

TORQUE = 1.8850E-02 (IN-LB), FILM POWER LOSS = 5.7122E-02 (HP)

COMPRESSIBILITY NUMBER = 1.0000E+01, SQUEEZE NUMBER = 0.0000E+00

DYNAMIC COEFFICIENTS (FORCE UNIT / DISP. UNIT)

DISP.	x (IN)	y (IN)	phi (RAD)	psi (RAD)	FORCE UNIT
Kx	4.9657E+03	1.5689E+03	-4.9960E+02	2.6673E+02	LB
Ky	-1.5689E+03	4.9657E+03	-2.6673E+02	-4.9960E+02	LB
Kphi	5.3012E+01	-3.6877E+02	6.0778E+02	5.3984E+02	IN-LB
Kpsi	3.6877E+02	5.3012E+01	-5.3984E+02	6.0778E+02	IN-LB
Bx	-6.9953E-02	-1.1123E-01	4.3933E-02	-1.2462E-02	LB-SEC
By	1.1123E-01	-6.9953E-02	1.2462E-02	4.3933E-02	LB-SEC
Bphi	-8.3037E-03	-4.4522E-03	2.2471E-02	-4.3624E-02	IN-LB-SEC
Bpsi	4.4522E-03	-8.3037E-03	4.3624E-02	2.2471E-02	IN-LB-SEC

COMPARISON OF CASE 2 WITH PN471

FLOW = 3.500E+00 (IN**3/SEC) MEASURED AT 1.0000E+00 (PSI)

TORQUE = 1.885E-02 (IN-LB), FILM POWER LOSS = 5.712E-02 (HP)

DYNAMIC COEFFICIENTS (FORCE UNIT / DISP. UNIT)

DISP.	x (IN)	y (IN)	phi (RAD)	psi (RAD)	FORCE UNIT
Kx	4.9648E+03	1.5692E+03	-4.9982E+02	2.6552E+02	LB
Ky	-1.5692E+03	4.9648E+03	-2.6552E+02	-4.9982E+02	LB
Kphi	5.3156E+01	-3.6793E+02	6.0602E+02	5.3900E+02	IN-LB
Kpsi	3.6793E+02	5.3156E+01	-5.3900E+02	6.0602E+02	IN-LB
Bx	-6.9955E-02	-1.1143E-01	4.3975E-02	-1.2344E-02	LB-SEC
By	1.1143E-01	-6.9955E-02	1.2344E-02	4.3975E-02	LB-SEC
Bphi	-8.3373E-03	-4.4940E-03	2.2617E-02	-4.3536E-02	IN-LB-SEC
Bpsi	4.4940E-03	-8.3373E-03	4.3536E-02	2.2617E-02	IN-LB-SEC

(CASE 3) Same case with grooves on moving surf., groove angle rev.

SPIRAL GROOVE SHAFT SEAL, ROTATING SURFACE IS GROOVED

LENGTH, DIAMETER, CLEARANCE - 2.0000E+00, 2.0000E+00, 1.0000E-03 (IN)

ROTATION SPEED, DISTURBANCE SPEED - 1.9099E+05, 0.0000E+00 (RPM)

PRESSURE AT START, END AXIAL BOUNDARIES - 1.0000E+00, 1.0000E+00 (PSI)

VISCOSITY - 8.3333E-11 (PSI-SEC),   AMBIENT PRESSURE - 1.0000E+00 (PSI)

ITERATIONS AND ERROR CODE IN LAST PRESSURE CALCULATION - 2 0

CALCULATED FORCES IN X,Y DIRECTIONS - -3.4729E-16, -1.2658E-15 (LB)
CALCULATED MOMENTS ABOUT X,Y AXES - 1.6213E-16, 6.2386E-17 (IN-LB)

MINIMUM FILM THICKNESS - 1.0000E-03 (IN)

FLOW - 3.5000E+00 (IN**3/SEC) MEASURED AT 1.0000E+00 (PSI)

TORQUE - 1.8850E-02 (IN-LB),   FILM POWER LOSS - 5.7122E-02 (HP)

COMPRESSIBILITY NUMBER - 1.0000E+01,   SQUEEZE NUMBER - 0.0000E+00

DYNAMIC COEFFICIENTS (FORCE UNIT / DISP. UNIT)

DISP.	x (IN)	y (IN)	phi (RAD)	psi (RAD)	FORCE UNIT
Kx	4.5241E+03	1.2933E+03	-3.6977E+02	2.1989E+02	LB
Ky	-1.2933E+03	4.5241E+03	-2.1989E+02	-3.6977E+02	LB
Kphi	3.4694E+02	-4.7068E+02	5.9016E+02	5.1362E+02	IN-LB
Kpsi	4.7068E+02	3.4694E+02	-5.1362E+02	5.9016E+02	IN-LB
Bx	-2.3432E-02	-1.2667E-01	3.4823E-02	-5.9373E-03	LB-SEC
By	1.2667E-01	-2.3432E-02	5.9373E-03	3.4823E-02	LB-SEC
Bphi	-2.7769E-02	6.0874E-03	2.3559E-02	-4.4038E-02	IN-LB-SEC
Bpsi	-6.0874E-03	-2.7769E-02	4.4038E-02	2.3559E-02	IN-LB-SEC

COMPARISON OF CASE 3 WITH PN471

FLOW = 3.500E+00 (IN**3/SEC) MEASURED AT 1.0000E+00 (PSI)

TORQUE = 1.885E-02 (IN-LB), FILM POWER LOSS = 5.712E-02 (HP)

DYNAMIC COEFFICIENTS (FORCE UNIT / DISP. UNIT)

DISP.	x (IN)	y (IN)	phi (RAD)	psi (RAD)	FORCE UNIT
Kx	4.5236E+03	1.2934E+03	-3.6992E+02	2.1883E+02	LB
Ky	-1.2934E+03	4.5236E+03	-2.1883E+02	-3.6992E+02	LB
Kphi	3.4697E+02	-4.6939E+02	5.8843E+02	5.1292E+02	IN-LB
Kpsi	4.6939E+02	3.4697E+02	-5.1292E+02	5.8843E+02	IN-LB
Bx	-2.3471E-02	-1.2673E-01	3.4849E-02	-5.8520E-03	LB-SEC
By	1.2673E-01	-2.3471E-02	5.8520E-03	3.4849E-02	LB-SEC
Bphi	-2.7798E-02	5.9155E-03	2.3693E-02	-4.3962E-02	IN-LB-SEC
Bpsi	-5.9155E-03	-2.7798E-02	4.3962E-02	2.3693E-02	IN-LB-SEC

(CASE 4) Face seal, no tilt, with pres. grad., lamda=10, sigma=0

SPIRAL GROOVE FACE SEAL, ROTATING SURFACE IS SMOOTH

ID, OD, REFERENCE FILM THICKNESS = 1.0000E+00, 2.0000E+00, 1.0000E-03 (IN)

ROTATION SPEED, DISTURBANCE SPEED = 1.9099E+05, 0.0000E+00 (RPM)

INSIDE, OUTSIDE PRESSURE = 2.0000E+00, 1.0000E+00 (PSI)

VISCOSITY = 8.3333E-11 (PSI-SEC),   AMBIENT PRESSURE = 1.0000E+00 (PSI)

ITERATIONS AND ERROR CODE IN LAST PRESSURE CALCULATION = 2 0

CALCULATED FORCE IN Z DIRECTION = 1.3612E+00 (LB)
CALCULATED MOMENTS ABOUT X,Y AXES = -3.0782E-16, 1.1794E-15 (IN-LB)

MINIMUM FILM THICKNESS = 1.0000E-03 (IN)

FLOW = 2.2763E+01 (IN**3/SEC) MEASURED AT 1.0000E+00 (PSI)

TORQUE = 2.2645E-03 (IN-LB),   FILM POWER LOSS = 6.8621E-03 (HP)

COMPRESSIBILITY NUMBER = 1.0000E+01,   SQUEEZE NUMBER = 0.0000E+00

DYNAMIC COEFFICIENTS (FORCE UNIT / DISP. UNIT)

DISP.	z (IN)	phi (RAD)	psi (RAD)	FORCE UNIT
Kz	3.9524E+02	-4.8585E-04	-4.8576E-04	LB
Kphi	-6.1349E-07	2.0998E+02	8.2256E+01	IN-LB
Kpsi	-3.0546E-07	-8.2256E+01	2.0998E+02	IN-LB
Bz	2.9491E-02	-7.3530E-07	-7.3551E-07	LB-SEC
Bphi	-1.1280E-09	7.0914E-03	-1.8082E-03	IN-LB-SEC
Bpsi	-2.3148E-09	1.8082E-03	7.0914E-03	IN-LB-SEC

COMPARISON OF CASE 4 WITH PN471

CALCULATED FORCE IN Z DIRECTION = 1.3612E+00 (LB)

FLOW = 2.2763E+01 (IN**3/SEC) MEASURED AT 1.0000E+00 (PSI)

TORQUE = 2.2644E-03 (IN-LB), FILM POWER LOSS = 6.8620E-03 (HP)

DYNAMIC COEFFICIENTS (FORCE UNIT / DISP. UNIT)

DISP.	z (IN)	phi (RAD)	psi (RAD)	FORCE UNIT
Kz	3.9524E+02			LB
Kphi		2.0998E+02	8.2240E+01	IN-LB
Kpsi		-8.2240E+01	2.0998E+02	IN-LB
Bz	2.9485E-02			LB-SEC
Bphi		7.0901E-03	-1.8058E-03	IN-LB-SEC
Bpsi		1.8058E-03	7.0901E-03	IN-LB-SEC

(CASE 5) Face seal, no tilt, with pres. grad., lamda-10, sigma-20

SPIRAL GROOVE FACE SEAL, ROTATING SURFACE IS SMOOTH

ID, OD, REFERENCE FILM THICKNESS - 1.0000E+00, 2.0000E+00, 1.0000E-03 (IN)

ROTATION SPEED, DISTURBANCE SPEED - 1.9099E+05, 1.9099E+05 (RPM)

INSIDE, OUTSIDE PRESSURE - 2.0000E+00, 1.0000E+00 (PSI)

VISCOSITY - 8.3333E-11 (PSI-SEC), AMBIENT PRESSURE - 1.0000E+00 (PSI)

ITERATIONS AND ERROR CODE IN LAST PRESSURE CALCULATION - 2 0

CALCULATED FORCE IN Z DIRECTION - 1.3612E+00 (LB)
CALCULATED MOMENTS ABOUT X,Y AXES - -3.0782E-16, 1.1794E-15 (IN-LB)

MINIMUM FILM THICKNESS - 1.0000E-03 (IN)

FLOW - 2.2763E+01 (IN**3/SEC) MEASURED AT 1.0000E+00 (PSI)

TORQUE - 2.2645E-03 (IN-LB), FILM POWER LOSS - 6.8621E-03 (HP)

COMPRESSIBILITY NUMBER - 1.0000E+01, SQUEEZE NUMBER - 2.0000E+01

DYNAMIC COEFFICIENTS (FORCE UNIT / DISP. UNIT)

DISP.	z (IN)	phi (RAD)	psi (RAD)	FORCE UNIT
Kz	5.3566E+02	-2.9756E-04	-2.9746E-04	LB
Kphi	-2.1294E-07	2.4013E+02	7.0968E+01	IN-LB
Kpsi	2.5103E-07	-7.0968E+01	2.4013E+02	IN-LB
Bz	2.7697E-02	3.8068E-09	3.8070E-09	LB-SEC
Bphi	2.2173E-12	6.7533E-03	-1.6346E-03	IN-LB-SEC
Bpsi	-2.0783E-12	1.6346E-03	6.7533E-03	IN-LB-SEC

COMPARISON OF CASE 5 WITH PN471

CALCULATED FORCE IN Z DIRECTION — 1.3612E+00 (LB)

FLOW — 2.2763E+01 (IN**3/SEC) MEASURED AT 1.0000E+00 (PSI)

TORQUE — 2.2644E-03 (IN-LB),   FILM POWER LOSS — 6.8620E-03 (HP)

DYNAMIC COEFFICIENTS (FORCE UNIT / DISP. UNIT)

DISP.	z (IN)	phi (RAD)	psi (RAD)	FORCE UNIT
Kz	5.3557E+02			LB
Kphi		2.4011E+02	7.0959E+01	IN-LB
Kpsi		-7.0959E+01	2.4011E+02	IN-LB
Bz	2.7692E-02			LB-SEC
Bphi		6.7528E-03	-1.6341E-03	IN-LB-SEC
Bpsi		1.6341E-03	6.7528E-03	IN-LB-SEC

(CASE 6) Face seal, no tilt, with pres. grad., lamda-10, sigma-200

SPIRAL GROOVE FACE SEAL, ROTATING SURFACE IS SMOOTH

ID, OD, REFERENCE FILM THICKNESS - 1.0000E+00, 2.0000E+00, 1.0000E-03 (IN)

ROTATION SPEED, DISTURBANCE SPEED - 1.9099E+05, 1.9099E+06 (RPM)

INSIDE, OUTSIDE PRESSURE - 2.0000E+00, 1.0000E+00 (PSI)

VISCOSITY - 8.3333E-11 (PSI-SEC),   AMBIENT PRESSURE - 1.0000E+00   (PSI)

ITERATIONS AND ERROR CODE IN LAST PRESSURE CALCULATION - 2 0

CALCULATED FORCE IN Z DIRECTION - 1.3612E+00 (LB)
CALCULATED MOMENTS ABOUT X,Y AXES - -3.0782E-16, 1.1794E-15 (IN-LB)

MINIMUM FILM THICKNESS - 1.0000E-03 (IN)

FLOW - 2.2763E+01 (IN**3/SEC) MEASURED AT 1.0000E+00 (PSI)

TORQUE - 2.2645E-03 (IN-LB),   FILM POWER LOSS - 6.8621E-03 (HP)

COMPRESSIBILITY NUMBER - 1.0000E+01,   SQUEEZE NUMBER - 2.0000E+02

DYNAMIC COEFFICIENTS (FORCE UNIT / DISP. UNIT)

DISP.	z (IN)	phi (RAD)	psi (RAD)	FORCE UNIT
Kz	2.3872E+03	-4.1732E-05	-4.1685E-05	LB
Kphi	-2.5267E-08	7.2912E+02	-7.4833E+00	IN-LB
Kpsi	5.8389E-08	7.4833E+00	7.2912E+02	IN-LB
Bz	4.1358E-03	5.3850E-10	5.3818E-10	LB-SEC
Bphi	4.2377E-13	1.2426E-03	-5.8922E-05	IN-LB-SEC
Bpsi	-5.5928E-13	5.8922E-05	1.2426E-03	IN-LB-SEC

COMPARISON OF CASE 6 WITH PN471

CALCULATED FORCE IN Z DIRECTION = 1.3612E+00 (LB)

FLOW = 2.2763E+01 (IN**3/SEC) MEASURED AT 1.0000E+00 (PSI)

TORQUE = 2.2644E-03 (IN-LB),   FILM POWER LOSS = 6.8620E-03 (HP)

         DYNAMIC COEFFICIENTS (FORCE UNIT / DISP. UNIT)

DISP.	z (IN)	phi (RAD)	psi (RAD)	FORCE UNIT
Kz	2.3870E+03			LB
Kphi		7.2907E+02	-7.4987E+00	IN-LB
Kpsi		7.4987E+00	7.2907E+02	IN-LB
Bz	4.1383E-03			LB-SEC
Bphi		1.2438E-03	-5.8939E-05	IN-LB-SEC
Bpsi		5.8939E-05	1.2438E-03	IN-LB-SEC

(CASE 7) Misaligned shaft seal with pres. grad. to comp. w/ GASBEAR

SPIRAL GROOVE SHAFT SEAL, ROTATING SURFACE IS SMOOTH

LENGTH, DIAMETER, CLEARANCE - 2.0000E+00, 2.0000E+00, 1.0000E-03 (IN)

ROTATION SPEED, DISTURBANCE SPEED - 1.9099E+05, 0.0000E+00 (RPM)

PRESSURE AT START, END AXIAL BOUNDARIES - 2.0000E+00, 1.0000E+00 (PSI)

VISCOSITY - 8.3333E-11 (PSI-SEC), AMBIENT PRESSURE - 1.0000E+00 (PSI)

ITERATIONS AND ERROR CODE IN LAST PRESSURE CALCULATION - 3 0

CALCULATED FORCES IN X,Y DIRECTIONS - 3.1535E+00, 1.2350E+00 (LB)
CALCULATED MOMENTS ABOUT X,Y AXES - 3.7793E-01, -1.9883E-03 (IN-LB)

MINIMUM FILM THICKNESS - 5.0000E-04 (IN)

FLOW - 4.7315E+00 (IN**3/SEC) MEASURED AT 1.0000E+00 (PSI)

TORQUE - 2.3248E-02 (IN-LB), FILM POWER LOSS - 7.0448E-02 (HP)

COMPRESSIBILITY NUMBER - 1.0000E+01, SQUEEZE NUMBER - 0.0000E+00

DYNAMIC COEFFICIENTS (FORCE UNIT / DISP. UNIT)

DISP.	x (IN)	y (IN)	phi (RAD)	psi (RAD)	FORCE UNIT
Kx	9.2287E+03	4.8183E+03	1.1084E+03	5.7870E+02	LB
Ky	-2.6167E+03	9.5964E+03	4.7033E+02	8.7124E+02	LB
Kphi	-9.8594E+01	6.5068E+02	1.5189E+03	7.7760E+02	IN-LB
Kpsi	7.1674E+02	-9.7210E+01	-1.0491E+03	1.2765E+03	IN-LB
Bx	-2.0553E-01	-4.5816E-01	-1.0900E-01	6.2037E-02	LB-SEC
By	2.5253E-01	-2.9852E-01	-6.7612E-02	-7.7454E-02	LB-SEC
Bphi	2.3869E-02	1.4706E-02	3.7737E-02	-8.3553E-02	IN-LB-SEC
Bpsi	-7.4893E-02	-5.8155E-02	5.7003E-02	6.7719E-02	IN-LB-SEC

COMPARISON OF CASE 7 WITH GASBEAR USING SAME GRID AND ROMBERG EXTRAPOLATION

CALCULATED FORCES IN X,Y DIRECTIONS = 3.1529E+00, 1.2362E+00 (LB)
CALCULATED MOMENTS ABOUT X,Y AXES = 3.7751E-01, -7.3904E-04 (IN-LB)

DYNAMIC COEFFICIENTS (FORCE UNIT / DISP. UNIT)

DISP.	x (IN)	y (IN)	phi (RAD)	psi (RAD)	FORCE UNIT
Kx	9.2287E+03	4.8097E+03	1.1044E+03	5.7867E+02	LB
Ky	-2.6113E+03	9.5993E+03	4.7249E+02	8.7343E+02	LB
Kphi	-1.0249E+02	6.5339E+02	1.5237E+03	7.7076E+02	IN-LB
Kpsi	7.1455E+02	-9.4976E+01	-1.0403E+03	1.2793E+03	IN-LB
Bx	-2.0561E-01	-4.5802E-01	-1.0909E-01	6.1715E-02	LB-SEC
By	2.5292E-01	-2.9885E-01	-6.7494E-02	-7.7535E-02	LB-SEC
Bphi	2.3875E-02	1.4639E-02	3.7502E-02	-8.3706E-02	IN-LB-SEC
Bpsi	-7.4561E-02	-5.7965E-02	5.6982E-02	6.7347E-02	IN-LB-SEC

3.5 References

1.   Vohr, J.H. and Pan, C.H.T., *"On the Spiral Grooved Self Acting Gas Bearing"*, MTI-63TR52, Mechanical Technology Incorporated, Latham, NY, (1962)

2.   Vohr, J.H. and Pan, C.H.T., *"Design Data: Gas Lubricated Spin-Axis Bearings for Gyroscopes"*, MTI-68TR29, Mechanical Technology Incorporated, Latham, NY, (1968)

3.   Smalley, A.J., *"The Narrow Groove Theory of Spiral Grooved Gas Bearings: Development and Application of a Generalized Formulation for Numerical Solution"*, ASME J. Lub. Tech., V 94, 1, (1972), pp. 86-92

4.   Castelli, V. and Pirvics, J., *"Review of Methods In Gas Bearing Film Analysis"*, Trans. ASME, (1968), pp. 777-792

5.   Press, W.H., Flannery, B.P., Teukolsky, S.A. and Vetterling, W.T., *"Numerical Recipes"*, Cambridge University Press, (1986)

6.   Artiles, A.,A., Walowit, J.A. and Shapiro, W., *"Analysis of Hybrid Fluid Film Journal Bearings with Turbulence and Inertia Effects"*, Proc. ASME Symposium In Advances In Computer-Aided Design, (1982), pp. 25-52

7.   Castelli, V., *"Design of Gas Bearings - Volume 1, Part 4: Numerical Methods"*, Gas Bearing Course Notes, Mechanical Technology Incorporated, Latham, NY, (1971)

8.   Shapiro, W., *"Computer Code SPIRALP for Gas-Lubricated Spiral-Groove Bearings and Seals"*, MTI 88TM2, Prepared for NASA under Contract No. NAS3-24645, (1988)

9.   Sato, Y., Ono, K. and Iwama, A., *"The Optimum Groove Geometry for Spiral Groove Viscous Pumps"*, ASME J. Tribology, V 112, 2, (1990), pp. 409-112

10.   Walowit, J.,*"Users Manual For Computer Code SPIRALG Gas Lubricated Spiral Grooved Cylindrical And Face Seals"*, Mechanical Technology Inc. report 91TM11, September 1991

3.6 Nomenclature

$\bar{A}$ dimensionless flow control area, (area/R_0^2)

A_i coefficients of second order linear operator defined by Eq. (44), $1 = 1,...,6$

$\{a\}$ column vector of eccentricity coefficients defined by Eq. (41)

$a_{i,j}^k$ kth component of $\{a\}$ evaluated at grid point (i,j)

B_{xy} damping coefficient relating force in x direction to velocity in y direction, B_{xx}, B_{yx}, B_{yy} and B_{zz} are similarly defined

$B_{\phi\psi}$ damping coefficient relating moment about x axis to angular velocity about y axis, $B_{\phi\phi}$, $B_{\psi\phi}$ and $B_{\psi\psi}$ are similarly defined

$B_{x\phi}$ damping coefficient relating force in x direction to angular velocity about x axis, $B_{x\psi}$, $B_{y\phi}$, $B_{y\psi}$, $B_{z\phi}$ and $B_{z\psi}$ are similarly defined

$B_{\phi x}$ damping coefficient relating moment about x axis to velocity in x direction, $B_{\psi x}$, $B_{\phi y}$, $B_{\psi y}$, $B_{\phi z}$ and $B_{\psi z}$ are similarly defined

$\bar{B}_{xy}$ dimensionless damping coefficient B_{xy}/B_0, same definitions apply to B_{xx}, B_{yx}, B_{yy}, B_{zz}

$\bar{B}_{\phi\psi}$ dimensionless damping coefficient $B_{\phi\psi}/(B_0R_0^2)$, same definitions apply to $B_{\phi\phi}$, $B_{\psi\phi}$, $B_{\psi\psi}$

$\bar{B}_{x\phi}$ dimensionless damping coefficient $B_{x\phi}/(B_0R_0)$, same definitions apply to $B_{x\psi}$, $B_{y\phi}$, $B_{y\psi}$, $B_{z\phi}$, $B_{z\psi}$

$\bar{B}_{\phi x}$ dimensionless damping coefficient $B_{\phi x}/(B_0R_0)$, same definitions apply to $B_{\psi x}$, $B_{\phi y}$, $B_{\psi y}$, $B_{\phi z}$, $B_{\psi z}$

B_0 characteristic damping constant, $12\mu R_0^4/C^3$

$[B]$ dimensionless damping coefficients in matrix form

$\{b\}$ column vector of coefficients of ϵ', arising from linearization of Eq. (39)

C clearance (cylindrical seal) or reference film thickness (face seal)

$[C^j]$ coefficient matrix used in Newton-Raphson linearization procedure, see Eq. (34)

$[\bar{C}^j]$ coefficient matrix obtained from steady state solution

$[\bar{C}^{j,k}]$ derivative of $[\bar{C}^j]$ with respect to ϵ_k

$[\tilde{C}^j]$ diagonal coefficient matrix whose components are given by Eq. (51)

$[C^{*j}]$ complex coefficient matrix used in complex stiffness solution, $[\bar{C}^j] + \tilde{S}\sigma[\tilde{C}^j]$

$[D^j]$ coefficient matrix used in Newton-Raphson linearization procedure, see Eq. (34)

$[\bar{D}^j]$ coefficient matrix obtained from steady state solution

$[\bar{D}^{j,k}]$ derivative of $[\bar{D}^j]$ with respect to ϵ_k

$[E^j]$ coefficient matrix used in Newton-Raphson linearization procedure, see Eq. (34)

$[\bar{E}^j]$ coefficient matrix obtained from steady state solution

$[\bar{E}^{j,k}]$ derivative of $[\bar{E}^j]$ with respect to ϵ_k

e_x, e_y eccentricity in x,y direction (cylindrical seal)

e_z axial displacement, (face seal)

$F_{i,j}$ residual outflow function from flow balance at grid point (i,j)

G second order non-linear operator defined by Eq. (39)

H steady state, unperturbed, value of H_r

H_r	dimensionless film thickness, h_r/C
h_g	film thickness over grooves, see Fig. 2
h_r	film thickness over ridges, see Fig. 2
i,j,k	subscripts used generically as indices
$\bar{i},\bar{j}$	unit vectors in θ,s directions
$\mathfrak{J}$	unit imaginary number, $\sqrt{-1}$
K_{xy}	stiffness coefficient relating force in x direction to displacement in y direction, K_{xx}, K_{yx}, K_{yy} and K_{zz} are similarly defined
$K_{\phi\psi}$	stiffness coefficient relating moment about x axis to rotation about y axis, $K_{\phi\phi}$, $K_{\psi\phi}$ and $K_{\psi\psi}$ are similarly defined
$K_{x\phi}$	stiffness coefficient relating force in x direction to rotation about x axis, $K_{x\psi}$, $K_{y\phi}$, $K_{y\psi}$, $K_{z\phi}$ and $K_{z\psi}$ are similarly defined
$K_{\phi x}$	stiffness coefficient relating moment about x axis to displacement in x direction, $K_{\phi x}$, $K_{\phi y}$, $K_{\psi y}$, $K_{\phi z}$ and $K_{\psi z}$ are similarly defined
$\bar{K}_{xy}$	dimensionless stiffness coefficient K_{xy}/K_0, same definitions apply to K_{xx}, K_{yx}, K_{yy}, K_{zz}
$\bar{K}_{\phi\psi}$	dimensionless stiffness coefficient $K_{\phi\psi}/(K_0R_0^2)$, same definitions apply to $K_{\phi\phi}$, $K_{\psi\phi}$, $K_{\psi\psi}$
$\bar{K}_{x\phi}$	dimensionless stiffness coefficient $K_{x\phi}/(K_0R_0)$, same definitions apply to $K_{x\psi}$, $K_{y\phi}$, $K_{y\psi}$, $K_{z\phi}$, $K_{z\psi}$
$\bar{K}_{\phi x}$	dimensionless stiffness coefficient $K_{\phi x}/(K_0R_0)$, same definitions apply to $K_{\psi x}$, $K_{\phi y}$, $K_{\psi y}$, $K_{\phi z}$, $K_{\psi z}$
K_0	characteristic stiffness constant, $p_0R_0^2/C$
$[K]$	dimensionless stiffnesses in matrix form
k_i	spiral groove coefficient defined by Eq. (25), $i=1,2,...,8$
L	seal length, see Fig. 1
$\bar{L}$	dimensionless length, $L/(2R_0)$
l_g	groove width, $r\Delta\theta_g$
l_r	ridge width, $r\Delta\theta_r$
$\mathcal{L}$	second order linear operator defined by Eq. (44)
M	number of grid points in s direction
M_x,M_y	applied moment about x,y axis
$\bar{M}_x,\bar{M}_y$	dimensionless moment, $(M_x,M_y)/(R_0^3p_0)$
N	number of grid points in θ direction
N_g	number of spiral grooves
$\bar{n}$	unit vector normal to $\bar{S}$
$\bar{n}_g$	unit vector normal to groove
P	dimensionless pressure, $(p-p_0)/p_0$
$\bar{P}$	steady state unperturbed value of P
$P_{i,j}$	dimensionless pressure, P, at grid point (i,j)
P_i	dimensionless pressure, P, at point i shown in Fig. 3, $i=1,...,9$
P_l,P_r	dimensionless boundary pressures $(p_l-p_0)/p_0$, $(p_r-p_0)/p_0$

$\{P'\}$	column vector of dimensionless pressure disturbances due to perturbation in $\{\epsilon\}$
$\{P'_j{}^k\}$	column vector of disturbance pressures associated with ϵ_k
$\{P^*\}$	complex amplitude of $\{P'\}$, $\{P'\} = \{P^*\}e^{\Im\sigma \bar{t}}$
$\{P_j^{*k}\}$	column vector of complex stiffness pressures associated with ϵ_k
$\{P_{\mathfrak{R}}\}$	real part of $\{P^*\}$
$\{P_{\mathfrak{J}}\}$	imaginary part of $\{P^*\}$
p	global pressure in absolute units
p'	local pressure in absolute units
p_0	reference pressure in absolute units, normally taken to be the minimum of the boundary pressures
p_l, p_r	boundary pressures in absolute units at s_l, s_r
$\bar{Q}$	dimensionless flow vector, $12 R_0 \bar{q}/(p_0 C^3)$
Q_s, Q_θ	components of dimensionless flow vector in s, θ directions
Q_{ij}^+, Q_{ij}^-	dimensionless flow components shown in Fig. 3
Q_{in}	dimensionless flow rate, $12 q_{in}/(p_0 C^3)$
$\bar{q}$	global flow vector, mass flow rate per unit transverse length divided by density at pressure p_0
q_s, q_θ	components of $\bar{q}$ in s, θ directions
q_A	global mass flow rate per unit area displaced by rate of decrease of film, divided by density at p_0
q_{in}	volumetric flow rate measured at pressure p_0
$\bar{q}'$	local flow vector, mass flow rate per unit transverse length divided by density at pressure p_0
q'_s, q'_θ	components of $\bar{q}'$ in s, θ directions
q'_A	local mass flow rate per unit area displaced by rate of decrease of film, divided by density at p_0
R	dimensionless coordinate, r/R_0, taken as 1 for cylindrical seal
R_0	reference radius, taken as outside radius for face seal and shaft radius for cylindrical seal
R_i	inside radius of face seal
$\{R^j\}$	column vector used in Newton-Raphson linearization procedure, see Eq. (34)
$\{R^j\}$	column vector obtained from steady state solution
$\{R^{j,k}\}$	derivative of $\{R^j\}$ with respect to ϵ_k
$\{R_i^{j,k}\}$	column vectors whose components are given by Eq. (52)
$\{R^{j,k}\}$	complex column vectors used complex stiffness solution $\{R^{j,k}\} - \Im\sigma\{R^{j,k}\}$
r	radial coordinate, taken as R_0 for cylindrical seal
S	dimensionless coordinate, s/R_0
S_l, S_r	dimensionless boundary coordinates s_l/R_0, s_r/R_0
$\bar{S}$	dimensionless length of line surrounding flow control area (length/R_0)
s	transverse coordinate, $s = r$ for a face seal and $s = z$ for a cylindrical seal
s_g	transverse coordinate at start of groove
s_l	left boundary coordinate, $s_l = R_i$ for face seal and $s_l = -L/2$ for cylindrical seal
s_r	right boundary coordinate, $s_r = R_0$ for face seal and $s_r = L/2$ for cylindrical seal
T	torque

T	dimensionless torque, $T/(p_0 R_0^2 C)$
T_c	T obtained with course grid in Romberg extrapolation example
T_f	T obtained with fine grid in Romberg extrapolation example
T_r	T obtained by Romberg extrapolation
t	time
$\bar{t}$	dimensionless time, $\omega t/(2\Lambda)$
$\bar{t}_\beta$	unit vector tangential to groove
$\bar{u}_1$	velocity of grooved surface
$\bar{u}_2$	velocity of smooth surface
W_x, W_y	applied loads in x,y direction (cylindrical seal)
$\bar{W}_x, \bar{W}_y$	dimensionless loads $(W_x, W_y)/(p_0 R_0^2)$
W_z	applied load in z direction (face seal)
$\bar{W}_z$	dimensionless load, $W_z/(p_0 R_0^2)$
$\{\bar{W}\}$	column vector containing dimensionless loads and moments $\{\bar{W}_x, \bar{W}_y, \bar{M}_x, \bar{M}_y\}$ for cylindrical seal, $\{\bar{W}_z, \bar{M}_x, \bar{M}_y\}$ for face seal
$\{\bar{W}\}_{old}$	$\{\bar{W}\}$ at previous iteration in eccentricity homing process
x, y	coordinate variables, see Fig. 1
Z	dimensionless axial coordinate for cylindrical seal, z/R_0
z	axial coordinate, measured from axial center for cyl. seal or from reference film, C, for face seal
α	groove to pitch ratio, $l_g/(l_g + l_r)$
α_{opt}	value of α for maximum stagnation pressure gradient in concentric cylindrical seal
β	spiral groove angle, angle between grooves and surface velocity
β_{opt}	value of β for maximum stagnation pressure gradient in concentric cylindrical seal
β	numerical damping factor used in eccentricity homing process
Γ	film thickness ratio, h_g/h_r
$\Delta \bar{A}$	dimensionless flow control area about single grid point, shaded area in Fig. 3
$\Delta \bar{A}_i$	portion of $\Delta \bar{A}$ in quadrant containing point i, see Fig. 3
Δp	global pressure difference, see Fig. 2
Δp_g	pressure difference across groove, see Fig. 2
Δp_r	pressure difference across ridge, see Fig. 2
ΔS_{ij}^+	line or arc length associated with Q_{ij}^+
ΔS_{ij}^-	line or arc length associated with Q_{ij}^-
Δs	transverse length of groove-ridge pair
$\Delta \theta$	circumferential extent of groove-ridge pair, see Fig. 2; (also used generally for change in θ)
$\Delta \theta_g$	circumferential extent of groove, see Fig. 2
$\Delta \theta_r$	circumferential extent of ridge, see Fig. 2
δ	dimensionless groove depth, $(h_g - h_r)/C$
δ_{opt}	value of δ for maximum stagnation pressure gradient in concentric cylindrical seal

ϵ_x, ϵ_y	eccentricity ratio, $(e_x, e_y)/C$ (cylindrical seal)
ϵ_z	axial displacement ratio e_z/C, (face seal)
ϵ_k	kth component of eccentricity matrix
$[\epsilon]$	row matrix of eccentricity components, $[\epsilon_z, \phi, \psi]$ (face seal) and $[\epsilon_x, \epsilon_y, \phi, \psi]$ (cylindrical seal)
$\{\epsilon\}$	column vector, transpose of $[\epsilon]$
$\{\epsilon\}_{old}$	$\{\epsilon\}$ at previous iteration in homing process
ϵ'	eccentricity disturbance function (scaler)
η	small increment used in perturbations and in evaluating derivatives
$\dot\theta$	angular coordinate, see Fig. 1
θ	angular coordinate at start of groove
Λ	compressibility number, $6\mu\omega R_0^2/(p_0 C^2)$
Λ_δ	groove compressibility number, $\Lambda \bar\delta \bar\omega \alpha (1-\alpha)\sin\beta$
μ	viscosity
σ	squeeze number, $2\Lambda\bar\Omega$
τ	global shear stress
$\bar\tau$	dimensionless shear stress, $\tau R_0/(p_0 C)$
τ'	local shear stress
Φ	rotation about x axis
ϕ	reduced rotation, $\Phi R_0/C$
Ψ	rotation about y axis
ψ	reduced rotation $\Psi R_0/C$
Ω	angular velocity of disturbance
$\bar\Omega$	dimensionless disturbance frequency, Ω/ω
ω	total angular velocity, $\omega_1 + \omega_2$
$\bar\omega$	dimensionless angular velocity ratio, $(\omega_2 - \omega_1)/\omega$
ω_1	angular velocity of grooved surface
ω_2	angular velocity of smooth surface
$\bar\nabla$	gradient operator, $(1/r)(\partial/\partial\theta)\bar i + (\partial/\partial s)\bar j$, on dimensional quantities and $(1/R)(\partial/\partial\theta)\bar i + (\partial/\partial S)\bar j$, on dimensionless quantities

4.0 Industrial Code ICYL-Incompressible, Cylindrical Seals

Incompressible cylindrical seals are used to reduce leakage from higher pressures. The pressures generated in plain cylindrical seals with incompressible fluids typically result in forces which are normal to the displacement and therefore tend to destabilize the rotating shaft. Surface roughness, geometry alterations, and external pressurization are ways in which the direct stiffness and damping coefficients can be improved and the cross-coupled stiffness decreased in order to improve stability.

The computer code ICYL was developed to evaluate the performance of cylindrical seals operating with incompressible fluids. The pressure and velocity distributions within the seal clearance are first evaluated from the governing equations. From these, design quantities such as seal leakage flows, power loss and resulting forces and moments are calculated. Minimum film thicknesses and maximum pressures as well as critical rotor-dynamics coefficients such as stiffness, damping and critical mass are evaluated.

Program capabilities:

1. 2-D incompressible isoviscous flow in cylindrical geometry.
2. Rotation of both rotor and housing.
3. Roughness of both rotor and housing.
4. Arbitrary film thickness distribution, including features such as steps, pockets, tapers and preloaded arcs
5. Rotor position described by four degrees of freedom (translational and rotational)
6. Up to 32 dynamic coefficients as well as the critical mass may be calculated for use in rotor-dynamic design, including system response and stability calculations.
7. External forces and moments may be prescribed independently to find rotor

position.

8.   Pocket pressures or orifice size are prescribed.

9.   Laminar or turbulent flow.

10.   Cavitation.

11.   Inertia pressure drop at inlets to fluid film (from ends of seal and from pressurized pockets).

Assumptions

1.   The film thickness is assumed to be small compared with seal lengths and diameters but large compared with surface roughness.

2.   Pockets supplied from an external pressure source through an orifice restriction are assumed to be sufficiently deep that the pressure is constant within them.

3.   Wall roughness is assumed to be isotropic and represented by an "equivalent sand roughness" height.

4.   Fluid inertia effects in the film are negligible.

4.1 THEORETICAL DESCRIPTION AND NUMERICAL METHODS

Figures 4-1 through 4-3 illustrate the geometry of a cylindrical seal as well as the coordinate system used here to describe it. Figure 4-1 shows the seal housing of length L separated from the rotor by the film thickness H. The coordinate system is placed at the mid-length of the seal with the circumferential coordinate θ measured from the x-axis. Figure 4-2 illustrates the displaced, misaligned rotor, while figure 4-3 shows an axial cross-section of the film thickness.

The film thickness and time rate-of-change thereof are written:

$$H = H_o - (e_x + ZB)\cos\theta - (e_y - ZA)\sin\theta$$

$$\frac{\partial H}{\partial t} = -\left(\frac{\partial e_x}{\partial t} + Z\frac{\partial B}{\partial t}\right)\cos\theta - \left(\frac{\partial e_y}{\partial t} - Z\frac{\partial A}{\partial t}\right)\sin\theta \qquad (4\text{-}1)$$

where H_o, an arbitrary function of film coordinates (θ,Z), represents the film thickness distribution for a rotor that is aligned and centered with the housing. e_x and e_y represent the components of rotor eccentricity at the seal mid-length, while A and B represent the angles of rotor rotation about the x and y axes, respectively. The former are referred to as the radial or lateral displacements and the latter as the angular displacements.

Governing equations

The equations governing the flow of incompressible fluids in thin films are obtained [10,11,15] by integrating the Navier-Stokes momentum and continuity equations

CYLINDRICAL SEAL GEOMETRY SCHEMATIC
(CONCENTRIC ALIGNED POSITION)
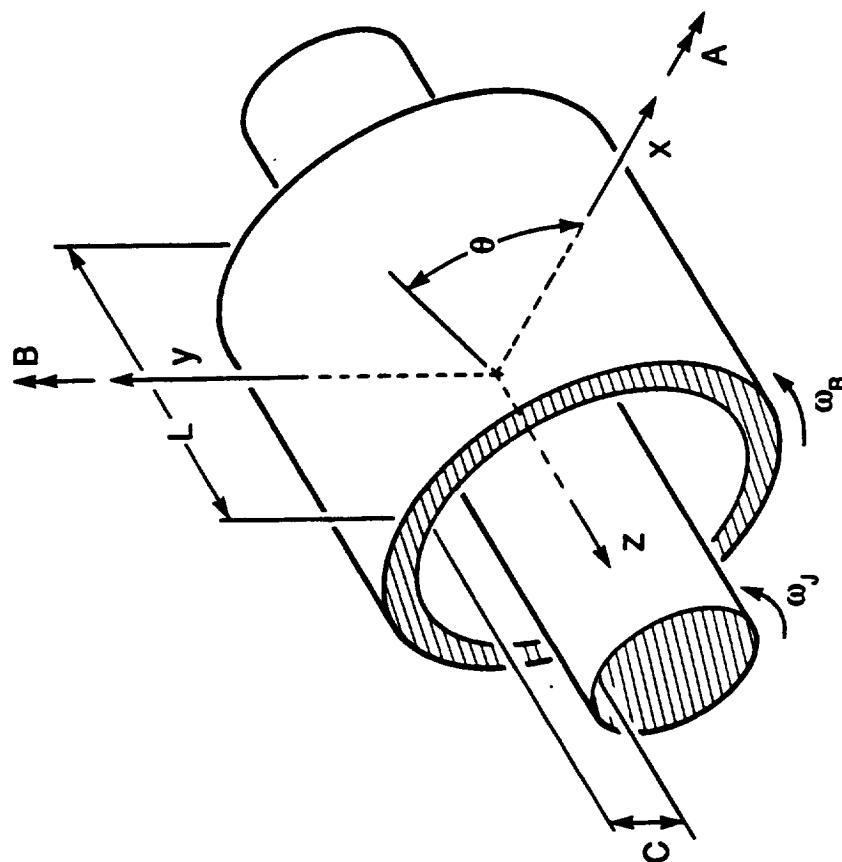
Figure 4-1   Cylindrical Seal Geometry
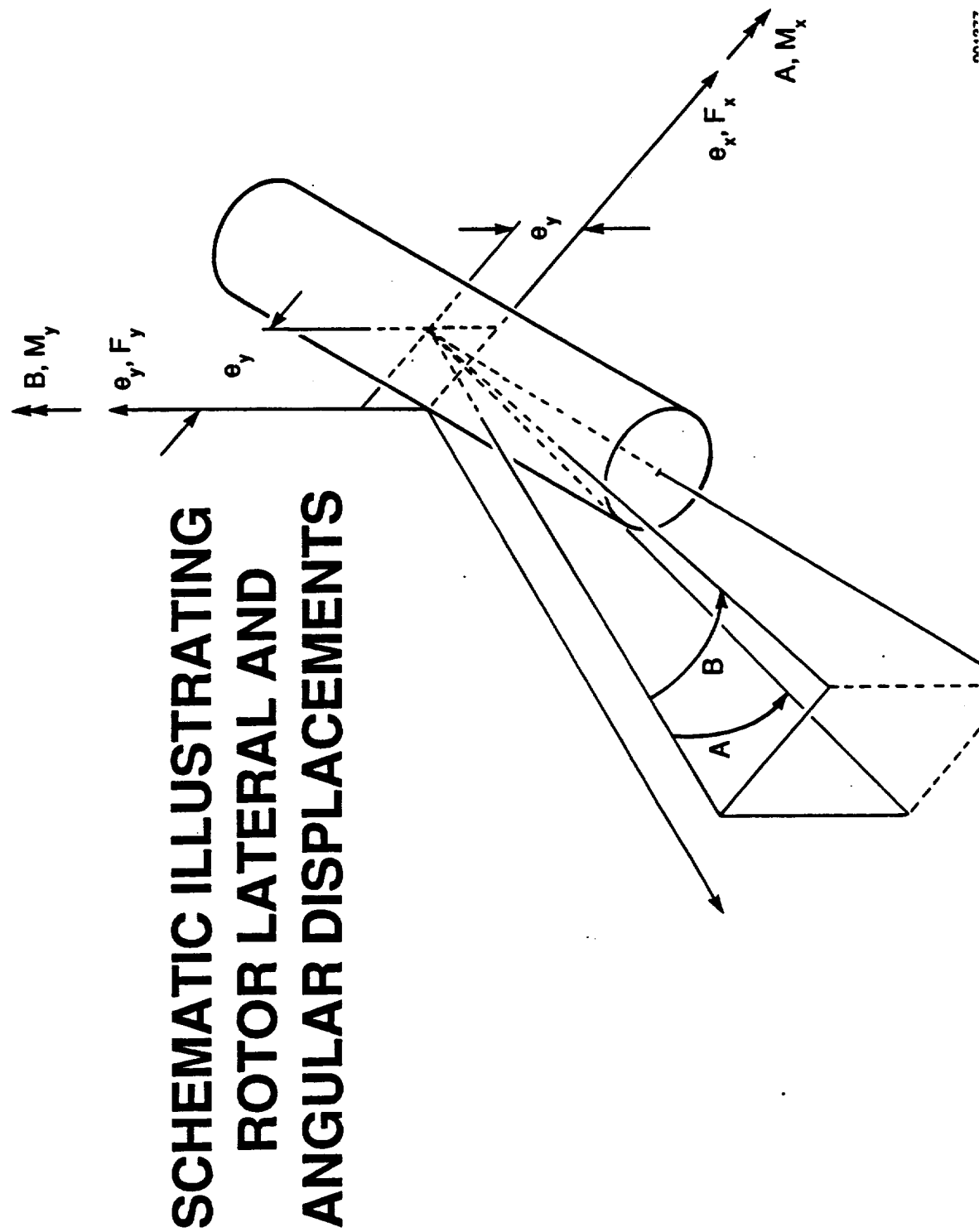
Figure 4-2   Rotor with Lateral and Angular Displacements

4-5

AXIAL CROSS SECTION OF SEAL
WITH ECCENTRIC ROTOR
(FILM THICKNESS EXAGGERATED)
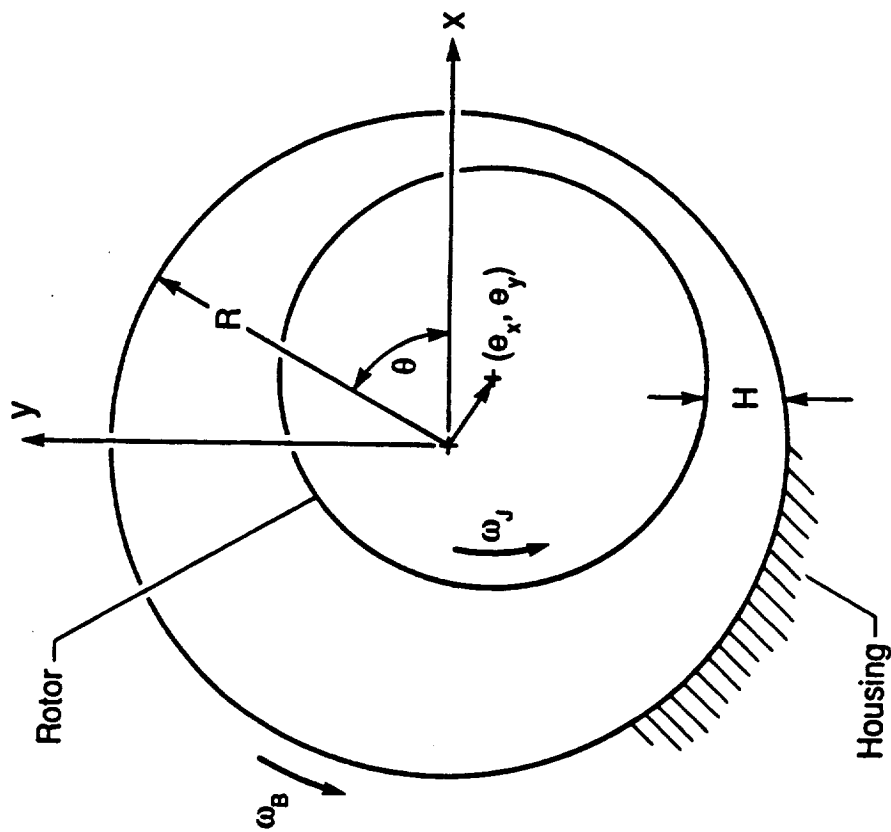
Figure 4-3   Axial Cross-Section of Seal with Eccentric Rotor

across the film[1]:

$$\frac{(f_j Re_j + f_b Re_b)}{2} U = -\frac{H^2}{\mu R}\frac{\partial P}{\partial \theta} + \frac{(Re_j f_j U_j + Re_b f_b U_b)}{2} \qquad (4\text{-}2)$$

$$\frac{(f_j Re_j + f_b Re_b)}{2} V = -\frac{H^2}{\mu}\frac{\partial P}{\partial Z}$$

$$\frac{1}{R}\frac{\partial}{\partial \theta}(UH) + \frac{\partial}{\partial Z}(VH) + \frac{\partial H}{\partial t} = 0 \qquad (4\text{-}3)$$

where f_j and f_b are the friction factors relative to the housing and journal surfaces, respectively, and are functions of the Reynolds numbers relative to these surfaces as well as of their roughness. They are given by:

$$Re_i = \frac{\rho H}{\mu}\sqrt{(U-U_i)^2 + V^2} \qquad (4\text{-}4)$$

where i=j,b, and:

$$f_i = \begin{cases} \dfrac{12}{Re_i}, & Re_i \leq 1000 \quad (\textit{laminar}) \\[2mm] \dfrac{12}{Re_i}(1-3\xi^2+2\xi^3) + f_i^*(3\xi^2-2\xi^3), & 1000 < Re_i < 3000 \\[2mm] f_i^*, & Re_i \geq 3000 \quad (\textit{turbulent}) \end{cases} \qquad (4\text{-}5)$$

$$\xi = \frac{Re_i - 1000}{2000} \qquad (4\text{-}6)$$

$$f_i^* = 0.001375\left[1 + \left(\frac{10^4 e_i}{H} + \frac{10^6}{4Re_i}\right)^{\frac{1}{3}}\right]$$

The friction factor for turbulent flow through pipes, f^*, in equation (4-6) uses the curve-fit obtained by Nelson [12] to Moody's data. The transition from laminar to

---

[1] the word *film* or the term *film thickness* will be used to mean the gap of lubricant separating the rotor and housing.

turbulent flow is obtained using a cubic polynomial which matches values and slopes at both ends, as reflected by equation (4-5). Figure 4-4 is a plot of the friction factor versus Reynolds number and surface roughness, while Figure 4-5 is an enlargement showing the detail of the transition region.

Under laminar flow with the friction factors equal to 12/Re, the velocities can be solved explicitly in terms of the pressure gradients:

$$u = -12h^2\frac{\partial p}{\partial \theta} + \Lambda_j + \Lambda_b$$

$$v = -12h^2\frac{\partial p}{\partial z}$$

(4-7)

Lubrication Background:

In the classical theory of lubrication, when the housing is stationary and the rotor wall velocity is $U_j = \omega R$, the fluid velocity components are expressed explicitly in terms of the pressure gradients:

$$U = -\frac{H^2 G_x}{12\mu R}\frac{\partial p}{\partial \theta} + \frac{\omega R}{2}, \quad V = -\frac{H^2 G_z}{12\mu}\frac{\partial p}{\partial z}$$

(4-8)

where G_x and G_z are turbulence coefficients[1] which become unity in the laminar regime. Substituting these velocity components into the continuity equation, results in the classical Reynold's equation:

$$\frac{1}{R^2}\frac{\partial}{\partial \theta}\left(H^3 G_x\frac{\partial P}{\partial \theta}\right) + \frac{\partial}{\partial Z}\left(H^3 G_z\frac{\partial P}{\partial Z}\right) = 6\mu\omega\frac{\partial H}{\partial \theta} + 12\mu\frac{\partial H}{\partial t}$$

(4-9)

Boundary conditions

Boundary conditions on the film pressure distribution consist on prescribing either the pressure at the boundaries of the film, the flow normal to these boundaries, or a relation between these two quantities.
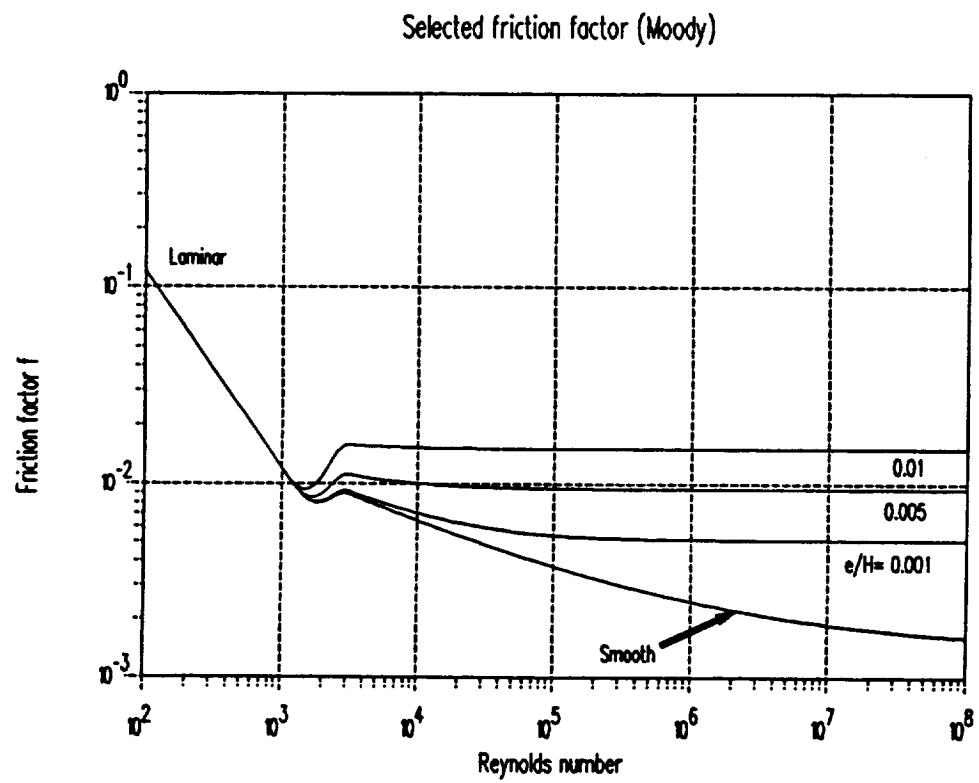
Figure 4-4 Friction factor versus Reynolds number

Fig.1 Transition friction factor
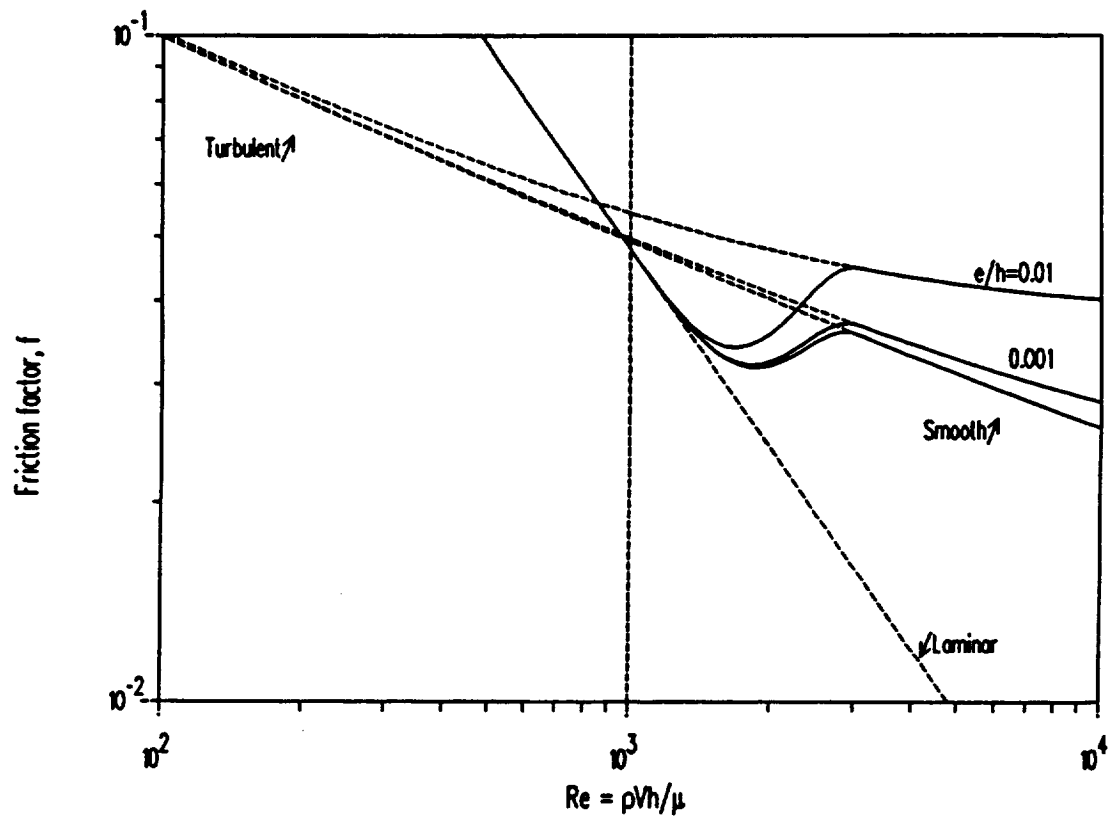
Figure 4-5 Detail of friction factor in transition region

At the circumferential ends of the seal surface model, either the pressures are prescribed: $P(Z, \theta_s) = 0$ and $P(Z, \theta_e) = 0$,

or periodic boundary conditions exists:

$$P(Z, \theta_s) = P(Z, \theta_e) \text{ and } U(Z, \theta_s) = U(Z, \theta_e).$$

Periodic boundary conditions are used, for example, for a 360° seal, where $\theta_e = \theta_s + 2\pi$.

At the left end of the seal surface model, the pressure/flow relationship is prescribed:

$$P(-L/2, \theta) = P_l - K_e \tfrac{1}{2}\rho V_n^2.$$

At the right end either the same relationship is used:

$$P(L/2, \theta) = P_r - K_e \tfrac{1}{2}\rho V_n^2,$$

or the axial velocity is set to zero:

$$V(0, \theta) = 0$$

when a symmetry boundary is present at the seal mid-length.

Finally, at pocket boundaries:

$$P(Z, \theta) = P_p - K_e \tfrac{1}{2}\rho V_n^2.$$

In all of the above relationships,

$$V_n = \begin{cases} \vec{V} \cdot \hat{n}, & \vec{V} \cdot \hat{n} > 0 \\ 0, & \vec{V} \cdot \hat{n} \leq 0 \end{cases} \qquad (4\text{-}10)$$

$$\vec{V} = U \hat{\theta}_z + V \hat{\theta}_\theta$$

is the flow velocity at the entrance to the film, normal to the pressurized boundary. No pressure drop exists in the case of reverse flow (i.e., flow into the pressurized boundary).

External pressurization

The pressure drop across the orifice supplying the pocket is given by:

$$P_s - P_p = sgn(Q_r)\,\frac{\rho}{2}\left(\frac{Q_r}{A_oC_d}\right)^2 \tag{4-11}$$

where A_o is the orifice area, C_d is the discharge coefficient and the flow Q_r is obtained by satisfying continuity over the pocket volume:

$$Q_r = \oint_{S_p} H\,\mathbf{V}\cdot\hat{n}\,dS + \int_{A_p}\frac{\partial H}{\partial t}\,dA \tag{4-12}$$

where A_p is the pocket area, S_p is its perimeter. Note that the contribution of $\mathbf{V}\bullet\hat{n}$ to this last equation may be positive or negative.

Dimensionless variables

Using the following transformation to dimensionless variables,

$b = B\,(C^3/12\mu R^4)$

$f = F/(P_oR^2)$

$h = H/C$

$k = K\,(C/P_oR^2)$

$m = M/(P_oR^3)$

$p = P/P_o$

$q_r = Q_r\,(12\mu/P_oC^3)$

$u = U\,(12\mu R/C^2P_o)$

$v = V\,(12\mu R/C^2P_o)$

$z = Z/R$

$\tau = t\,(C^2P_o/12\mu R^2)$

$\Lambda_b = 6\mu U_b R/(C^2P_o)$

$\Lambda_j = 6\mu U_j R/(C^2P_o)$

$\epsilon = e/C$

$\alpha = A\,(R/C)$

$\beta = B\,(R/C)$

$Re^* = \rho h^3 \nabla p/\mu^2$

$Re_o^* = \rho C^3 P_o/(R\mu^2)$

$\Lambda_r = \rho C^6 P_o/(288\,A_o^2 C_d^2\,\mu^2)$

$\quad = (Re_o^*/288)\,(C^3R/A_o^2 C_d^2)$

$\Lambda_\bullet = K_\bullet\,(Re_o^* C/288\,R)$,

4-12

equations (4-1), (4-2), (4-3) and (4-4) become:

$$h = h_o - (\epsilon_x + z\beta)\cos\theta - (\epsilon_y - z\alpha)\sin\theta$$

$$\frac{\partial h}{\partial \tau} = -\left(\frac{\partial \epsilon_x}{\partial \tau} + z\frac{\partial \beta}{\partial \tau}\right)\cos\theta - \left(\frac{\partial \epsilon_y}{\partial \tau} - z\frac{\partial \alpha}{\partial \tau}\right)\sin\theta \tag{4-13}$$

$$\frac{(f_j Re_j + f_b Re_b)}{2}u = -12h^2\frac{\partial p}{\partial \theta} + (Re_j f_j \Lambda_j + Re_b f_b \Lambda_b)$$

$$\frac{(f_j Re_j + f_b Re_b)}{2}v = -12h^2\frac{\partial p}{\partial z} \tag{4-14}$$

$$\frac{\partial}{\partial \theta}(uh) + \frac{\partial}{\partial z}(vh) + \frac{\partial h}{\partial \tau} = 0 \tag{4-15}$$

$$Re_j = \frac{Re_o^* h}{12}\sqrt{(u - 2\Lambda_j)^2 + v^2}, \quad i = j, b \tag{4-16}$$

Equations (4-5) and (4-6) remained unaltered, as they were already dimensionless.

The dimensionless form of the boundary conditions now become:

At the circumferential ends, either:

$$p(z, \theta_s) = 0 \text{ and } p(z, \theta_e) = 0$$

or:

$$p(z, \theta_s) = p(z, \theta_e) \text{ and } u(z, \theta_s) = u(z, \theta_e).$$

when periodic boundary conditions are present.

At the left end:

$$p(-L/D,\theta) = p_l - \Lambda_s v_n^2,$$

and at the right end either:

$$p(L/D,\theta) = p_r - \Lambda_s v_n^2$$

or:

$$v(0,\theta) = 0.$$

At pocket boundaries: $p(z,\theta) = p_p - \Lambda_s v_n^2$

where:

$$v_n = \begin{cases} \mathbf{v}\cdot\hat{n}, & \mathbf{v}\cdot\hat{n} > 0 \\ 0, & \mathbf{v}\cdot\hat{n} \leq 0 \end{cases} \tag{4-17}$$

$$\mathbf{v} = u\hat{\delta}_z + v\hat{\delta}_\theta$$

Equations (4-11) and (4-12) governing the external pressurization become:

$$p_s - p_p = sgn(q_r)\,\Lambda_r q_r^2 \tag{4-18}$$

$$q_r = \oint_{S_p} h\, \mathbf{v}\cdot\hat{n}\, ds + \int_{A_p} \frac{\partial h}{\partial \tau}\, d\theta\, dz \tag{4-19}$$

Solution of film pressures

Discretization of the seal surface is done by using a rectangular grid, with **M** lines in the axial direction and **N** lines in the circumferential direction. The grid lines are separated by variable increments. The pressure distribution is represented by discrete values at the grid points located at the intersections of the grid lines. There must be grid lines coincident with the boundaries of the seal surface ($Z = \pm L/2, \theta = \theta_s, \theta = \theta_e$) and with the pocket boundaries. Using the cell method [3], a control area or cell is centered at each grid point and extending half way to the neighboring grid lines, as shown by the shaded area in Figure 4-6. The grid points are noted by the solid circles and have grid coordinates i,j. The film thickness is evaluated at the corners of the cell (denoted by the shaded circles marked h_1, h_2, h_3, and h_4) located at the geometric centers of the rectangles formed by the grid lines. This staggered configuration allows a discontinuous film thickness to be treated, as occurs, for example in a seal with a Rayleigh-step. Circumferential and axial components of velocity are also associated with each of the four cell corners.

Using the divergence theorem, the continuity equation may be integrated over the
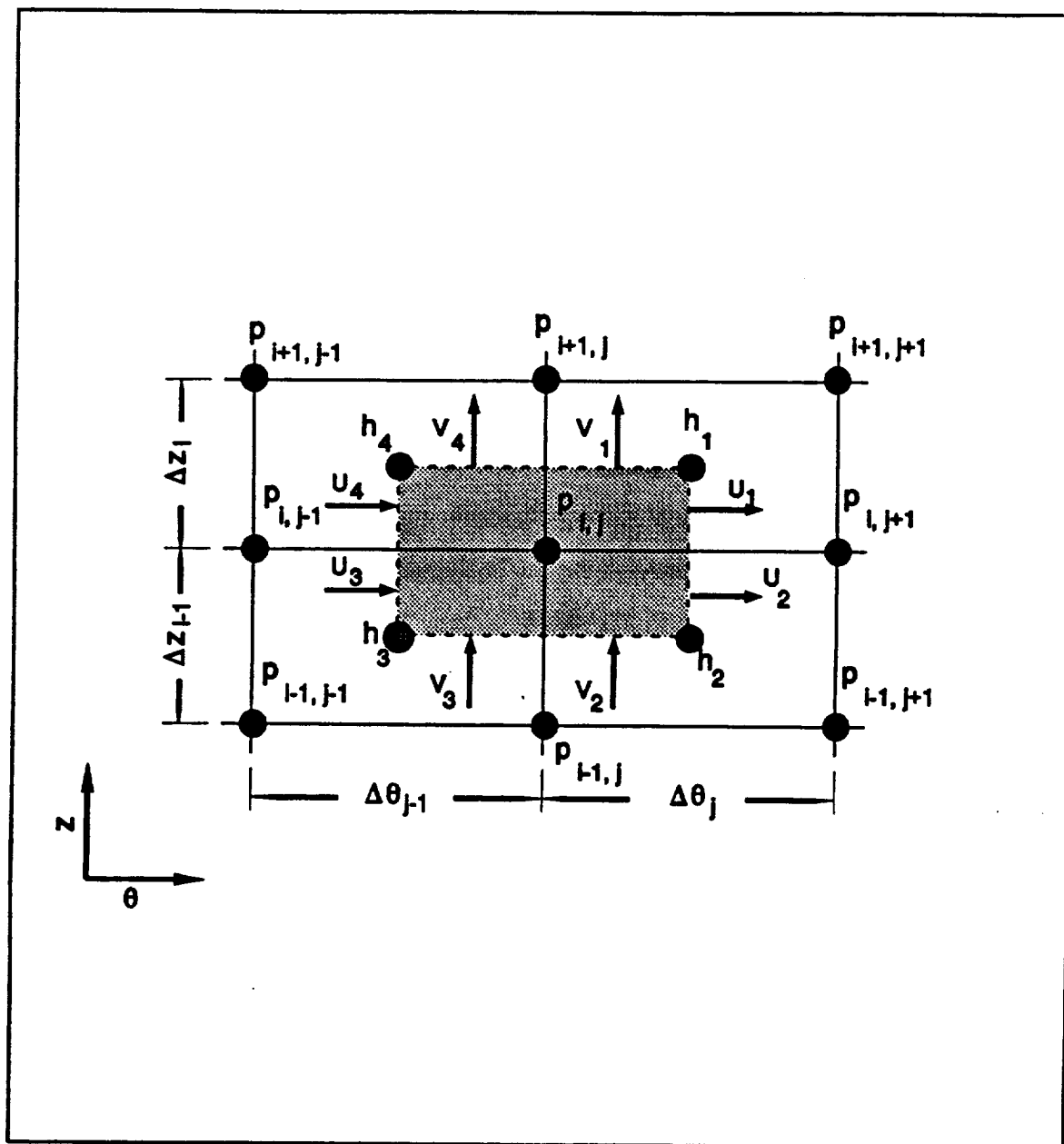
Figure 4-6 Flow control area about grid point i,j.

cell to give:

$$-\oint_{S_e} \mathbf{v} \cdot \hat{n} \, dS = \int_{A_e} \frac{\partial h}{\partial \tau} \, dA \qquad (4\text{-}20)$$

where A_c and S_c are the cell area and perimeters, respectively. The left hand side of the above equation is the sum of the flows out of the cell while the right hand side is the rate of change of the cell volume. The finite-difference form of this equation is:

$$
\begin{aligned}
F_{ij} = & \frac{\Delta z_j}{2}(u_1 h_1 - u_4 h_4) + \frac{\Delta z_{j-1}}{2}(u_2 h_2 - u_3 h_3) + \\
& + \frac{\Delta \theta_j}{2}(v_1 h_1 - v_2 h_2) + \frac{\Delta \theta_{j-1}}{2}(v_4 h_4 - v_3 h_3) - \qquad (4\text{-}21) \\
& - \frac{1}{4}\frac{\partial h_{ij}}{\partial \tau}(\Delta z_j + \Delta z_{j-1})(\Delta \theta_j + \Delta \theta_{j-1}) = 0
\end{aligned}
$$

where F_{ij} is the error in satisfying continuity of flow in the cell centered at i,j. Although the time rate of change of film thickness has been evaluated at the center of the cell, it could have alternatively been evaluated at each of the four cell corners.

When the grid point falls on a pressurized boundary, such as a pocket or seal end, the film pressure error is:

$$F_{ij} = p_b - p_{ij} - \Lambda_e \max(0, v_n)^2 = 0$$

$$v_n = \frac{\Sigma_{ij}}{s_b h_{ij}} \qquad (4\text{-}22)$$

where p_b is the dimensionless boundary pressure[2], v_n is the mean velocity of the flow that crosses the portion of the boundary perimeter that intersects the cell, and Σ_{ij} represents the sum of the appropriate terms in equation (4-21) contributing to the cell flow. Figure 4-7 shows an example of the cell i,j located at the right bottom

---

[2] P_i/P_o, P_r/P_o or P_p/P_o.

corner of a pocket. In this case, the mean velocity would be evaluated as:

$$v_n = \left[\frac{\Delta z_i}{2}(u_1 h_1) + \frac{\Delta z_{i-1}}{2}(u_2 h_2 - u_3 h_3) + \frac{\Delta \theta_j}{2}(v_1 h_1 - v_2 h_2) - \frac{\Delta \theta_{j-1}}{2}(v_3 h_3) - \right.$$

$$\left. - \frac{\partial h_{ij}}{\partial \tau} \frac{(\Delta z_i + \Delta z_{i-1})\Delta \theta_j + \Delta z_{i-1}\Delta \theta_{j-1}}{4} \right] + \left[\frac{(\Delta \theta_{j-1} + \Delta z_i)h_{ij}}{2} \right]$$

(4-23)

Equations (4-21) and (4-22) represent the finite-difference form of the continuity equation that must be solved for the pressures. The eight components of velocity used in these equations are functions of the nine pressures at or neighboring grid point i,j, and are evaluated as described in section 2.3. Following the procedure described in reference 1, these highly nonlinear equations can be solved using the Newton-Raphson iteration method [14]. The procedure is started with an initially guessed or previously calculated pressure distribution, $p_{i,j}$. The error function F_{ij} is then linearized about this guess in order to obtain a better approximation to the pressures $p_{i,j}^{new}$:

$$F_i + \sum_{\substack{k=i-1,i+1 \\ l=j-1,j+1}} \frac{\partial F_i}{\partial P_{kl}}\left(P_{kl}^{new} - P_{kl}\right) = 0$$

(4-24)

where a forward difference or a central difference may optionally be used to numerically evaluate the partial derivatives. Pressures without the superscript new relate to the previous or "old" approximation. If we introduce the column vector $\{p_j^{new}\}$ as the M new pressures at the jth column of grid points, Equation (4-24) may be written:

$$[C^j]\{p_j^{new}\} + [E^j]\{p_{j-1}^{new}\} + [D^j]\{p_{j+1}^{new}\} = \{R^j\} ,$$

(4-25)

where $[C^j]$, $[E^j]$ and $[D^j]$ are tri-diagonal matrices whose interior elements are:

$$C_{i,i+k}^j = \frac{\partial F_i}{\partial P_{i+k,j}} , \quad E_{i,i+k}^j = \frac{\partial F_i}{\partial P_{i+k,j-1}} , \quad D_{i,i+k}^j = \frac{\partial F_i}{\partial P_{i+k,j+1}} , \quad k = -1,0,1 ; \quad I = 2,...,M-1 .$$

The interior elements of the column vector $\{R^j\}$ are:
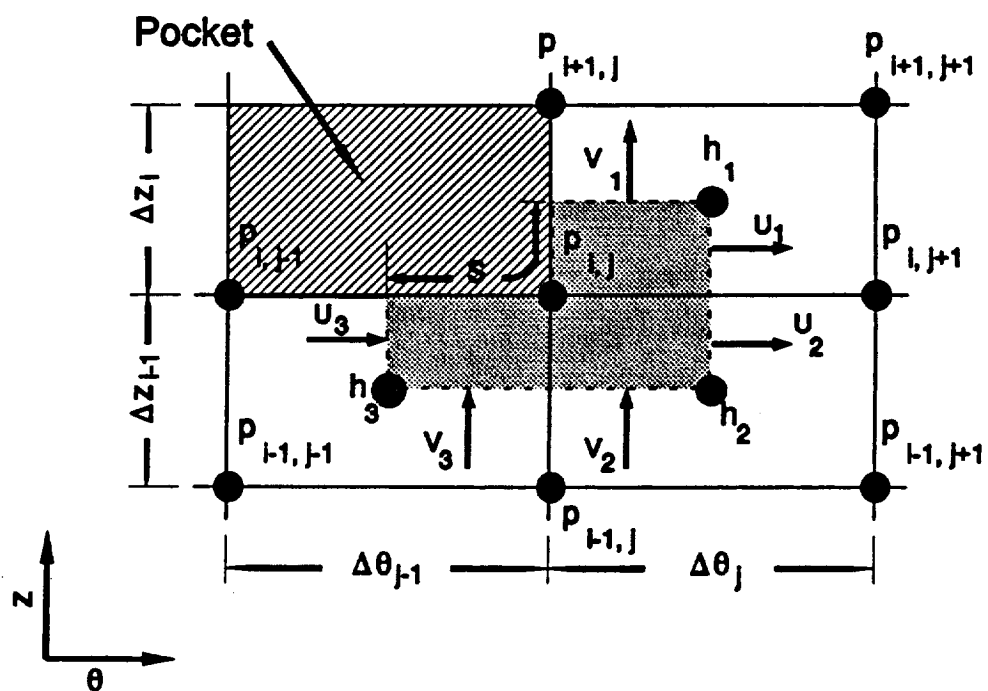
Figure 4-7 Example of cell at corner of pocket.

$$R_i^j = \sum_{k=-1}^{1} \left(C_{i,i+k}^j P_{i+k,j} + E_{i,i+k}^j P_{i+k,j-1} + D_{i,i+k}^j P_{i+k,j+1} \right) - F_{ij} \quad .$$

The set of linear equations (4-26) that result for the next guess of pressure distribution is in a form suitable for solution by the column method which is described in detail in References 3 and 4. This method makes use of the banded nature of the equations in order to minimize computer time.

Solution of flow velocity

The momentum equations (4-14) are used in order to evaluate the velocity components from the pressure gradients. These equations may be rewritten in the generic form:

$$G_u\left[\frac{\partial p}{\partial \theta}, u, v\right] = \frac{f_j Re_j + f_b Re_b}{2} u + 12h^2 \frac{\partial p}{\partial \theta} - \left(Re_j f_j \Lambda_j + Re_b f_b \Lambda_b\right) = 0,$$

$$G_v\left[\frac{\partial p}{\partial z}, u, v\right] = \frac{f_j Re_j + f_b Re_b}{2} v + 12h^2 \frac{\partial p}{\partial z} = 0,$$

(4-26)

where the Reynolds numbers used to evaluate the friction factors are based on the *magnitude* of the local fluid velocity relative to each surface:

$$Re_j = \frac{Re_o^* h}{12} \sqrt{(u - 2\Lambda_j)^2 + v^2},$$

$$Re_b = \frac{Re_o^* h}{12} \sqrt{(u - 2\Lambda_b)^2 + v^2},$$

(4-27)

The dependence of the friction factors on velocity components orthogonal to each momentum direction couples the two momentum equations. Figure 4-8 is a schematic of the rectangular region between axial grid lines i and i+1 and circumferential grid lines j and j+1. In order to preserve continuity, it is essential that the same equation be used to evaluate the velocity components for adjacent
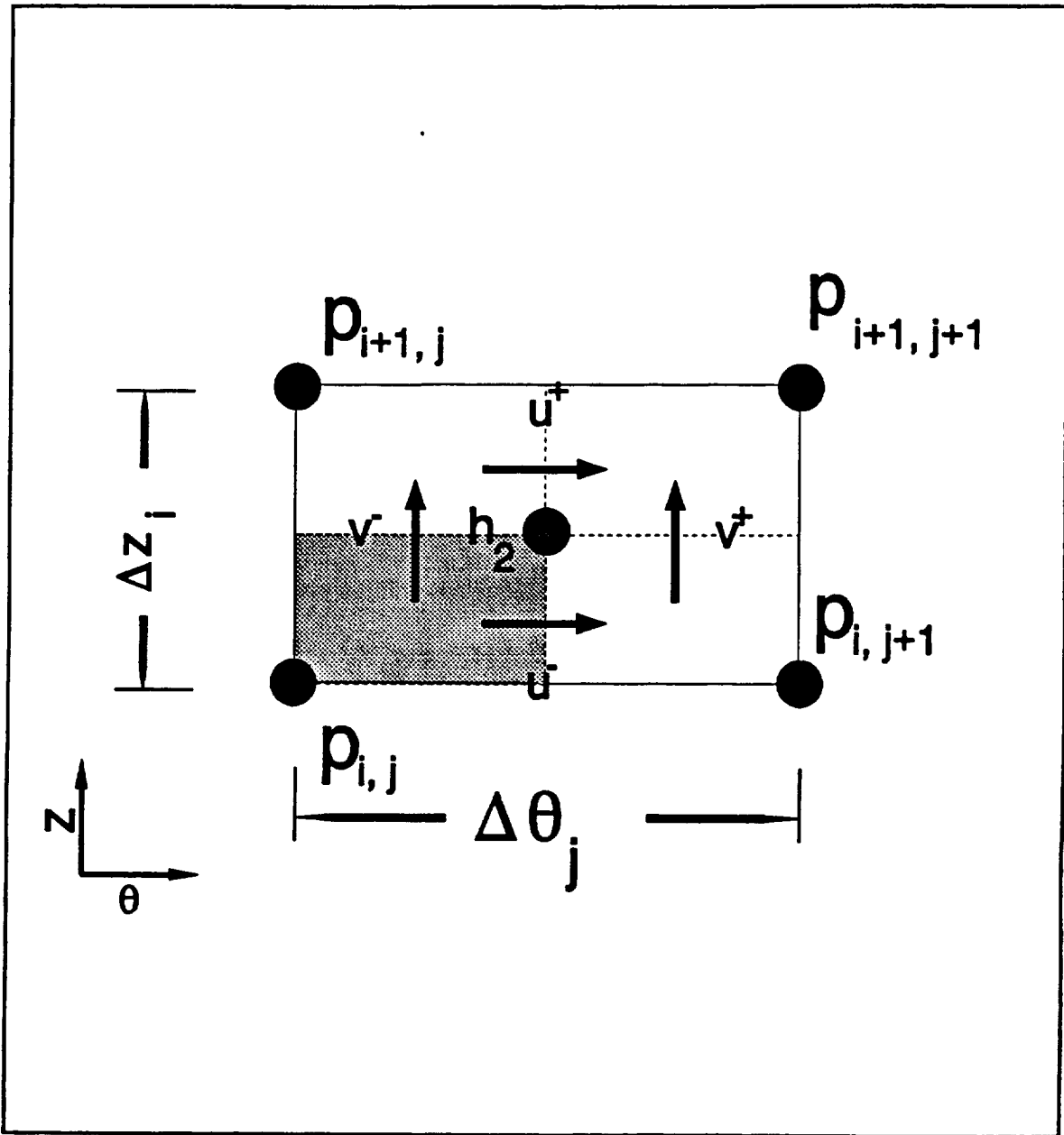
Figure 4-8   Schematic of rectangular region between grid lines.

cells. That is, the velocity u_1 out of the shaded cell centered at i,j must have the same value as the velocity u_4 into the cell centered at i,j+1. This value is designated as u^- in the figure. Similarly, the velocity v_1 out of the cell i,j must be the same as v_2 into the cell at i+1,j, and is designated as v^-. This is achieved by using the average of the two corresponding orthogonal components. Thus, the component u^- is determined by the u-momentum equation:

$$G_u\left[\frac{p_{i,j+1}-p_{i,j}}{\Delta\theta_j}, u^-, \frac{v^-+v^+}{2}\right] = 0 \qquad\qquad \text{(4-28)}$$

while the component v^- is determined by the v-momentum equation:

$$G_v\left[\frac{p_{i+1,j}-p_{i,j}}{\Delta z_i}, \frac{u^-+u^+}{2}, v^-\right] = 0 \qquad\qquad \text{(4-29)}$$

Similarly, u^+ and v^+ are determined by:

$$G_u\left[\frac{p_{i+1,j+1}-p_{i+1,j}}{\Delta\theta_j}, u^+, \frac{v^-+v^+}{2}\right] = 0$$

$$\qquad\qquad \text{(4-30)}$$

$$G_v\left[\frac{p_{i+1,j+1}-p_{i,j+1}}{\Delta z_i}, \frac{u^-+u^+}{2}, v^+\right] = 0$$

Equations (4-28), (4-29) and (4-30) are four coupled equations that determine the velocity components from the four pressures at the corners of the rectangle between grid lines and must be solved simultaneously. This is done using an inner Newton-Raphson iteration loop. By performing the differentiation of the error functions (Gu, Gv, ...) with respect to the four unknown velocities, analytically instead of numerically, significant computer time is saved. If the velocities have not been previously calculated initial guesses may be obtained from equations (4-7) assuming laminar flow. Once the iterations for the velocities have converged, their values are saved to provide a good starting guess for the next time they must be calculated.

One simplification is possible by assuming that the friction factors are constant

within the rectangular region and the Reynolds numbers are based on the averaged flow velocity components, $\frac{1}{2}(u^- + u^+)$ and $\frac{1}{2}(v^- + v^+)$. Although this does not uncouple the four equations, it requires less number of evaluations of the square root in equation (4-16). Since this assumption saves some computer time without introducing significant errors, it was chosen as the default program option (**IFRIC=3**). However, occasionally when the grid is not very fine and the pressure gradients vary rapidly, the iterations will diverge and the more rigorous formulation, which uses distinct friction factors for each of the four momentum equations, should be used with the **IFRIC=4** option.

If the surfaces are smooth and the housing is stationary so that the continuity equation takes the form of equation (4-9), the simpler formulation described in detail in Reference 1 may be used by selecting the option **IFRIC=0**, resulting in significant reduction in computer time.

Fluid film load, moment and torque

The forces and moments on the rotor generated by the fluid film pressure distribution are obtained by integration of the pressure distribution over the cylindrical seal surface:

$$\begin{Bmatrix} F_x \\ F_y \\ M_x \\ M_y \end{Bmatrix} = \int_{-L}^{L} \int_{\theta_o}^{\theta_o} P \begin{Bmatrix} \cos\theta \\ \sin\theta \\ -Z\sin\theta \\ Z\cos\theta \end{Bmatrix} R d\theta \, dZ \qquad (4\text{-}31)$$

The dimensionless form this equation is written:

$$\begin{Bmatrix} f_x \\ f_y \\ m_x \\ m_y \end{Bmatrix} = \int_{-\frac{L}{D}}^{\frac{L}{D}} \int_{\theta_o}^{\theta_o} p \begin{Bmatrix} \cos\theta \\ \sin\theta \\ -z\sin\theta \\ z\cos\theta \end{Bmatrix} d\theta \, dz \qquad (4\text{-}32)$$

The differential of torque transmitted from the housing to the rotor is given by the cross product of the position vector $\vec{r}$ and the shear traction vector acting on the

housing $\vec{t}$:

For laminar regime, $f_j Re_j = f_b Re_b = 12$, and the equation simplifies to:

$$\vec{T} = T\hat{e}_z = \iint_{A_f} \vec{r} \times \vec{f} \, dA$$

$$= R \iint_{A_f} \hat{e}_r \times (\bar{\tau} \cdot \hat{e}_r) \, dA \qquad (4\text{-}33)$$

$$T = \frac{P_o R^2}{2C_o} \iint_{A_f} \{h\frac{\partial p}{\partial \theta} - \frac{f_j R_j (u - 2\Lambda_j) - f_b R_b (u - 2\Lambda_b)}{72h}\} \, d\theta \, dZ$$

$$T = \frac{P_o R^2}{2C_o} \iint_{A_f} \{h\frac{\partial p}{\partial \theta} - \frac{\Lambda_j - \Lambda_b}{3h}\} \, d\theta \, dZ \qquad (4\text{-}34)$$

The power loss due to the difference in velocities across the two surfaces is obtained by doting this torque with the relative velocity:

$$P = T(\omega_b - \omega_j)$$

$$= \frac{P_o R^2}{2C_o} \iint_{A_f} \{h\frac{\partial p}{\partial \theta} - \frac{f_j R_j (u - 2\Lambda_j) - f_b R_b (u - 2\Lambda_b)}{72h}\} (\Lambda_j - \Lambda_b) \, d\theta \, dZ \qquad (4\text{-}35)$$

Stiffness and damping coefficients

Defining **W** to be a generalized vector of forces and moments generated by the fluid film pressure and $\vec{r}$ to be a generalized vector of lateral and angular

displacements:

$$
W = \begin{Bmatrix} f_x \\ f_y \\ m_x \\ m_y \end{Bmatrix} \qquad
r = \begin{Bmatrix} \epsilon_x \\ \epsilon_y \\ \alpha \\ \beta \end{Bmatrix} \qquad
\dot{r} = \frac{\partial}{\partial \tau} \begin{Bmatrix} \epsilon_x \\ \epsilon_y \\ \alpha \\ \beta \end{Bmatrix} \qquad (4\text{-}36)
$$

the matrices of stiffness and damping coefficients can be written:

$$
k_i = -\frac{\partial W_i}{\partial r_j} \qquad b_i = -\frac{\partial W_i}{\partial \dot{r}_j} \qquad (4\text{-}37)
$$

where the subscripts i and j range over x, y, α and β. These coefficients are evaluated by numerical differentiation of **W**, using a forward difference. For example:

$$
K_{y\alpha} = \frac{F_y(\epsilon_x, \epsilon_y, \alpha + \delta, \beta) - F_y(\epsilon_x, \epsilon_y, \alpha, \beta)}{\delta} \qquad (4\text{-}38)
$$

Solution of rotor position and pocket pressures

If the rotor position is specified, equation (4-36) is used to solve for the fluid film forces and moments in terms of the calculated pressure field. Similarly, if the pocket pressures are specified, equation (4-11) is used to solve for the orifice size in terms of the supply pressure and calculated pocket flow.

On the other hand, if externally applied loads and moments on the rotor (f_{x0}, f_{y0}, m_{x0} and m_{y0}) are specified they must be balanced by the fluid film forces to maintain static equilibrium. Similarly, once the orifice size is specified, equation (4-11) must be satisfied by the pressure in each pocket. The global set of equations that must be satisfied by the rotor displacements and pocket pressures

are:

$$f_x(r) = -f_{xg}$$

$$f_y(r) = -f_{yg}$$

$$m_x(r) = -m_{xg}$$

$$m_y(r) = -m_{yg}$$

(4-39)

$$p_s - p_{p1} = sng(q_{r1}) \Lambda_{r1}(q_{r1})^2, \quad \text{for pocket 1,}$$

$$p_s - p_{p2} = sng(q_{r2}) \Lambda_{r2}(q_{r2})^2, \quad \text{for pocket 2, etc.}$$

The vector **r** can now be redefined to include the pocket pressures and a generalized vector of errors in forces, moments and pocket pressures W_e can be defined:

$$r = \begin{Bmatrix} \varepsilon_x \\ \varepsilon_y \\ \alpha \\ \beta \\ p_{p1} \\ p_{p2} \\ \vdots \end{Bmatrix} \qquad W_e = \begin{Bmatrix} f_x + f_{xg} \\ f_y + f_{yg} \\ m_x + m_{xg} \\ m_y + m_{yg} \\ p_s - p_{p1} - sgn(q_{r1}) \Lambda_{r2}(q_{r1})^2 \\ p_s - p_{p2} - sgn(q_{r2}) \Lambda_{r2}(q_{r2})^2 \\ \vdots \end{Bmatrix}$$

(4-40)

Solution of the global equations is performed by Newton-Raphson iterations, as follows:

$$W_e + \left[\frac{\partial W_e}{\partial r} \right] (r^{new} - r) = 0$$

(4-41)

where, as before, the superscript **new** indicates the newer values of the vector **r**.

4-25

4.2 SAMPLE PROBLEMS

A number of sample problems have been prepared to demonstrate the behavior and various features of the computer program. They are intended primarily for illustration and do not necessarily represent recommended seal designs. Table 4-1 summarizes the mesh size, approximate execution times (on a 20Mz 386 PC) as well as a list of what variables where specified and iterated for in the outer loop for the sample problems.

Samples EX1, EX2 and EX3 were selected with a coarse (5x11) mesh covering a 90° sector in order to demonstrate the use of pressurized pockets and iterations for rotor position within a reasonable execution time. A pocket with a supply pressure of 100 psi was centered on the seal sector modeled.

Sample **EX1** contained two cases. In the first case, the pocket pressure was specified as 50 psi, resulting in an orifice diameter of 0.0137 inches calculated by the program. Both components of the resulting fluid film force are equal and the moments are zero, as would be expected at the concentric position. In the second case, the rotor was moved with to eccentricity ratio of ϵ_x = 0.1 and given a misalignment ratio of β =0.1 about the y-axis. With the value of orifice diameter already assigned from the first case, the pocket pressure and forces rise slightly, generating non-zero moments.

In sample **EX2**, external forces and moments equal to the negative of those resulting in EX1 were specified, in order to have the program iterate for the rotor radial and angular positions. Five unknowns, the four displacement components (ϵ_x ,ϵ_y, α, and β) as well as the pocket pressure, are iterated for simultaneously. Although it wasn't needed, IREADP = 1 and READP = 'ICYLEX1.888' where specified in order to illustrate the use of reading the

Table 4-1   Summary of sample cases

Case	Mesh Size	ISYM	Variable Found[*]	Variable Specified	App.exec time[**]	Features
EX1	5x11	0	dorif,P_{pock}	P_{pock},E_x,dorif	4.6 min	1-pocket
EX2	5x11	0	ϵ_x,ϵ_y,α,β,P_{pock}	F_x,F_y,M_x,M_y,dorif	11.6 min	1-pocket
EX3	5x11	0	α,β,P_{pock}	M_x,M_y,dorif	6.2 min	Tapered pocket
F3	9x61	1	-	all	29 min	Raleigh-step
F4	7x61	0	-	all	7.8 min	Axial taper
F9	5x73	1	K,B	all (3 preloads)	1.6 hrs	3-lobe
I1	5x61	1	dorif	P_{pock}	7 min	4-pocket
I2	5x61	1	P_{pock},K	ϵ_x,dorif	1.8 hrs	4-pocket
I3	5x61	1	ϵ_x,ϵ_y,P_{pock}	F_x,F_y,dorif	1.9 hrs	4-pocket
I4	9x61	0	K,B,P_{pock}	ϵ_x,α,dorif	7.7 hrs	4-pocket
I5	11x61	0	dorif	P_{pock}	5.2 min	8-pocket
I6	11x61	0	P_{pock}	dorif,ϵ_x,α	3.1 hrs	8-pocket
O15	5x31	0	K,B	all	1 hr 45 sec	Roughness

[*] K,B indicate whether stiffness, damping coefficients were requested.
[**] on an IBM PS/2 model 70 (386 20-Mhz) computer.

pressure distribution from a previous run. Since the iteration was begun at the concentric position where the orifice was sized, the pocket flow error was zero and *increased* when the rotor was moved in the first iteration, causing the run to abort. When the limit on diverging iterations (MAXDIT) was increased to 2, the iterations converged in only 3 iterations to within a small error of the values expected (ϵ_x = 0.1, β =0.1).

In sample **EX3**, an axial taper of ±30% of the clearance from end to end was superimposed. This calculation might be desirable to see the effect of machining tolerances or imperfection on seal components. This was accomplished by decreasing the clearance by 0.0003 inches (DELTA(1,1)=-0.003) as well as using DELTA(2,1)=0.006. In this sample,

the program was asked to find the angular rotor position such that no external moments where required, while the rotor eccentricity was varied, using ϵ_x = 0.1, 0.3 and 0.5 for the 1st, 2nd and 3rd cases, respectively. The results show that as the eccentricity is increased in the x-direction, the rotor twists about the y-axis in order for the moments generated by the film to be zero, resulting in β =0.050 and 0.17 at ϵ_x = 0.1 and 0.3, respectively. The case of ϵ_x=0.5 resulted in a negative film thickness with the appropriate error message and recommended user action:

      o REDUCE THE SPECIFIED APPLIED FORCES/MOMENTS

      o REDUCE THE SPECIFIED ECCENTRICITY/MISALIGNMENT

The resulting film thickness is shown in Figure 4-9 and the pressure distributions are shown in Figure 4-10.

Sample **F3** shows a 120° sector with a Raleigh step of linearly varying depth. The resulting film thickness and pressure distributions are shown in Figures 4-11 and 4-12, respectively.

Sample **F4** shows a 120° sector with an axial taper in the right half (4<i<7) of 0.001 inches. Since two less intervals were used in the axial direction than in the previous cases, and since half as many iterations were required for the pressure distributions, the execution time was reduced from about 29 to 8 minutes. The film thickness and pressure distributions are shown in Figures 4-13 and 4-14, respectively.

Sample **F9** is that of a full 360° seal with three 60° lobes. The dynamic coefficients was requested as the preload was increased from 0.1 to 0.3 in the middle case, to 0.8 at the last case. The film thickness and pressure distributions are shown in Figures 4-15 and 4-16, respectively.

ICYL: ICYLEX3   FILM THICKNESS DISTRIBUTION
90 DEG SECTOR: CALCULATE ANGLULAR POSITION FOR ZERO MO
    RADIUS=   1.0000   SPEED=   1000.0
    LENGTH=   4.0000
    CLEARANCE=   .10000E-02
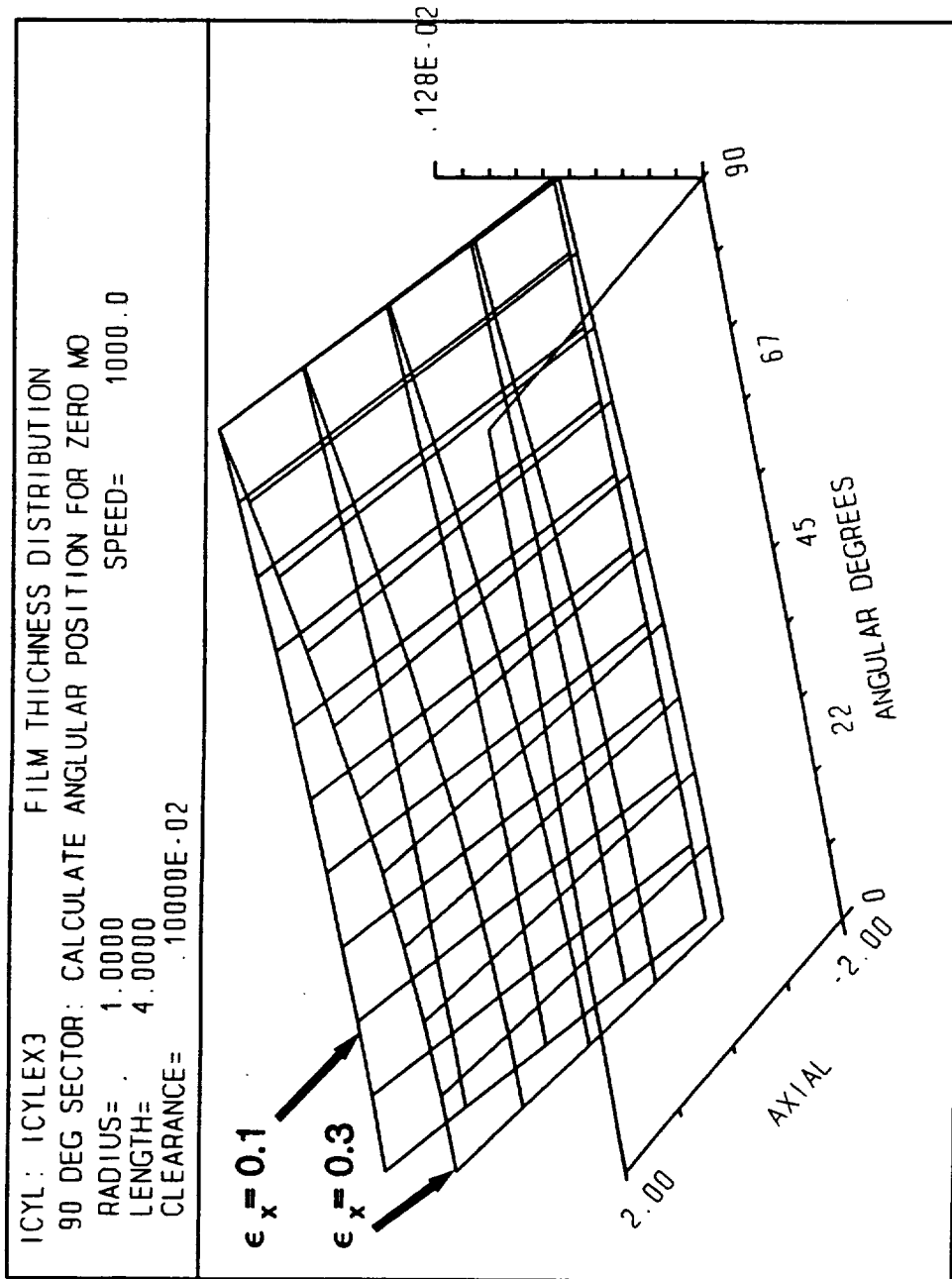
Figure 4-9   Film thickness distribution for sample EX3

ICYL: ICYLEX3   PRESSURE DISTRIBUTION
90 DEG SECTOR: CALCULATE ANGLULAR POSITION FOR ZERO MO
    RADIUS=   1.0000   SPEED=   1000.0
    LENGTH=   4.0000
    CLEARANCE=   .10000E-02

.487E+02

90

67

45   ANGULAR DEGREES

22

0

-2.00

2.00

AXIAL

Figure 4-10   Pressure distribution for sample EX3

ICYL: ICYLF3   FILM THICHNESS DISTRIBUTION

RALEIGH STEP WITH VARIABLE DEPTH

RADIUS=   4.0000   SPEED=   1000.0
LENGTH=   2.0000
CLEARANCE=   .10000E-02

.300E-02

120

90

60

30

ANGULAR DEGREES

.25 0

.00

AXIAL
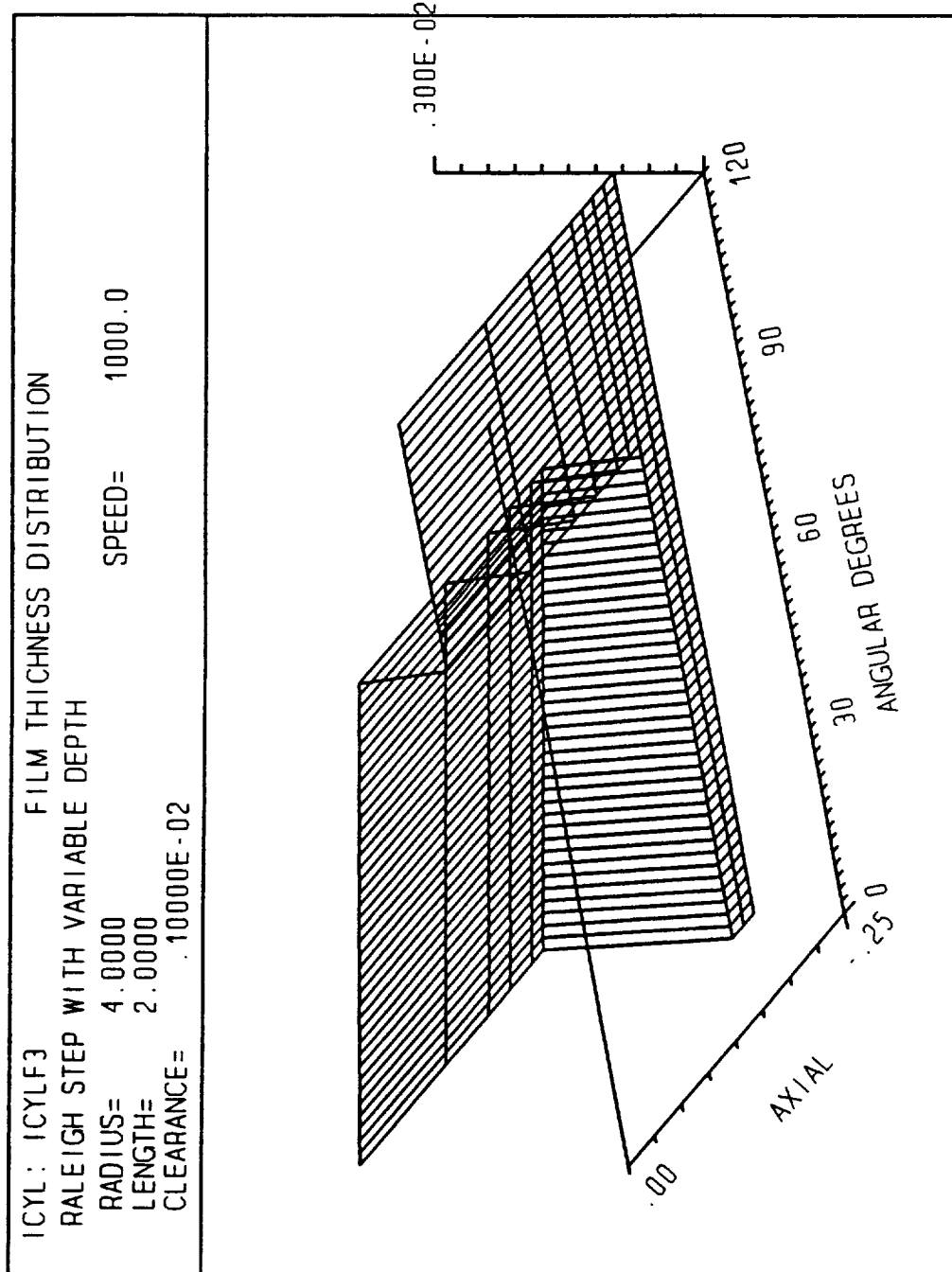
Figure 4-11   Film thickness distribution for sample F3

4-31

ICYL: ICYLF3   PRESSURE DISTRIBUTION

RALEIGH STEP WITH VARIABLE DEPTH   SPEED=   1000.0

RADIUS=   4.0000
LENGTH=   2.0000
CLEARANCE=   .10000E-02

.134E+02

120   90   60   30   .25 0   .00

ANGULAR DEGREES

AXIAL
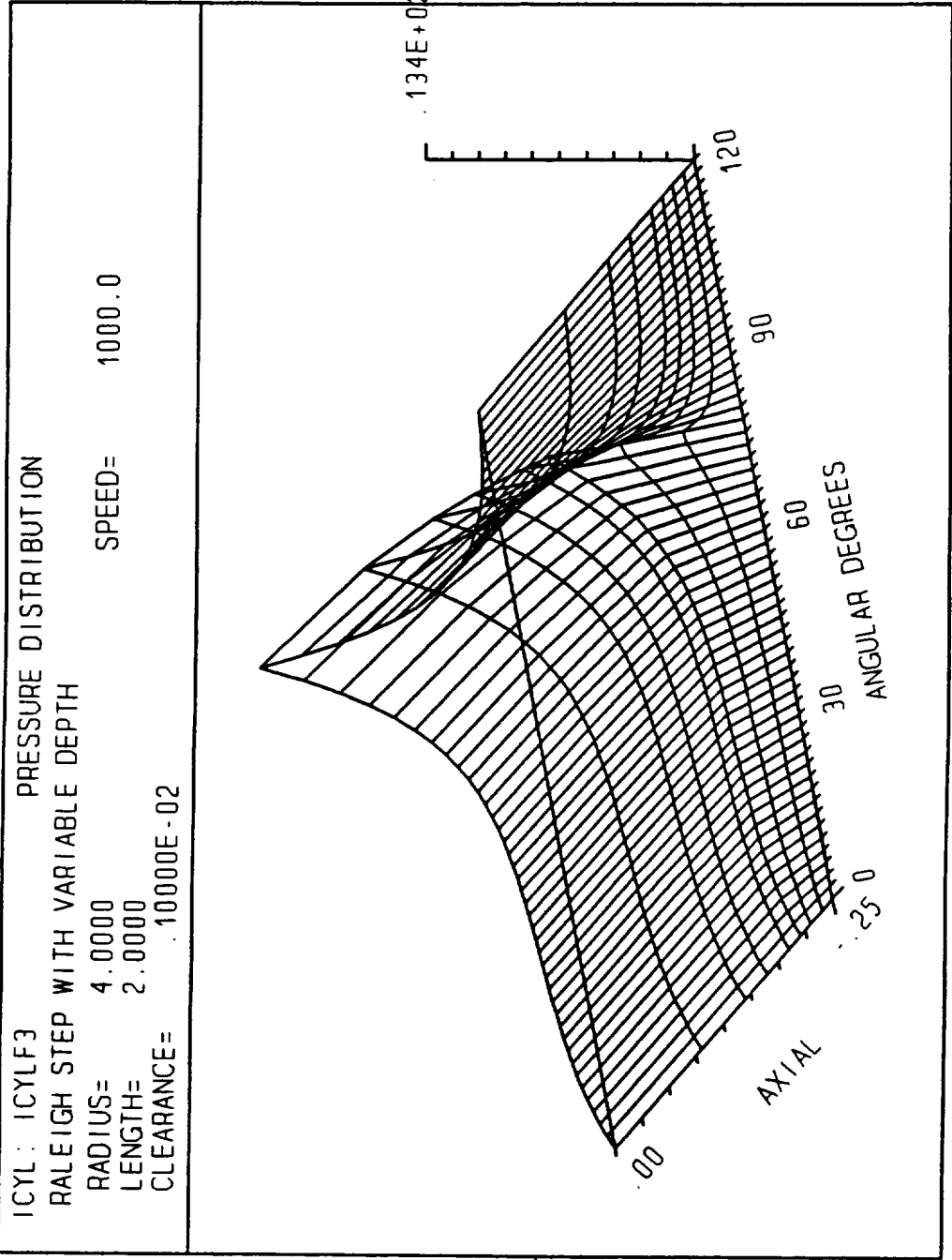
Figure 4-12   Pressure distribution for sample F3
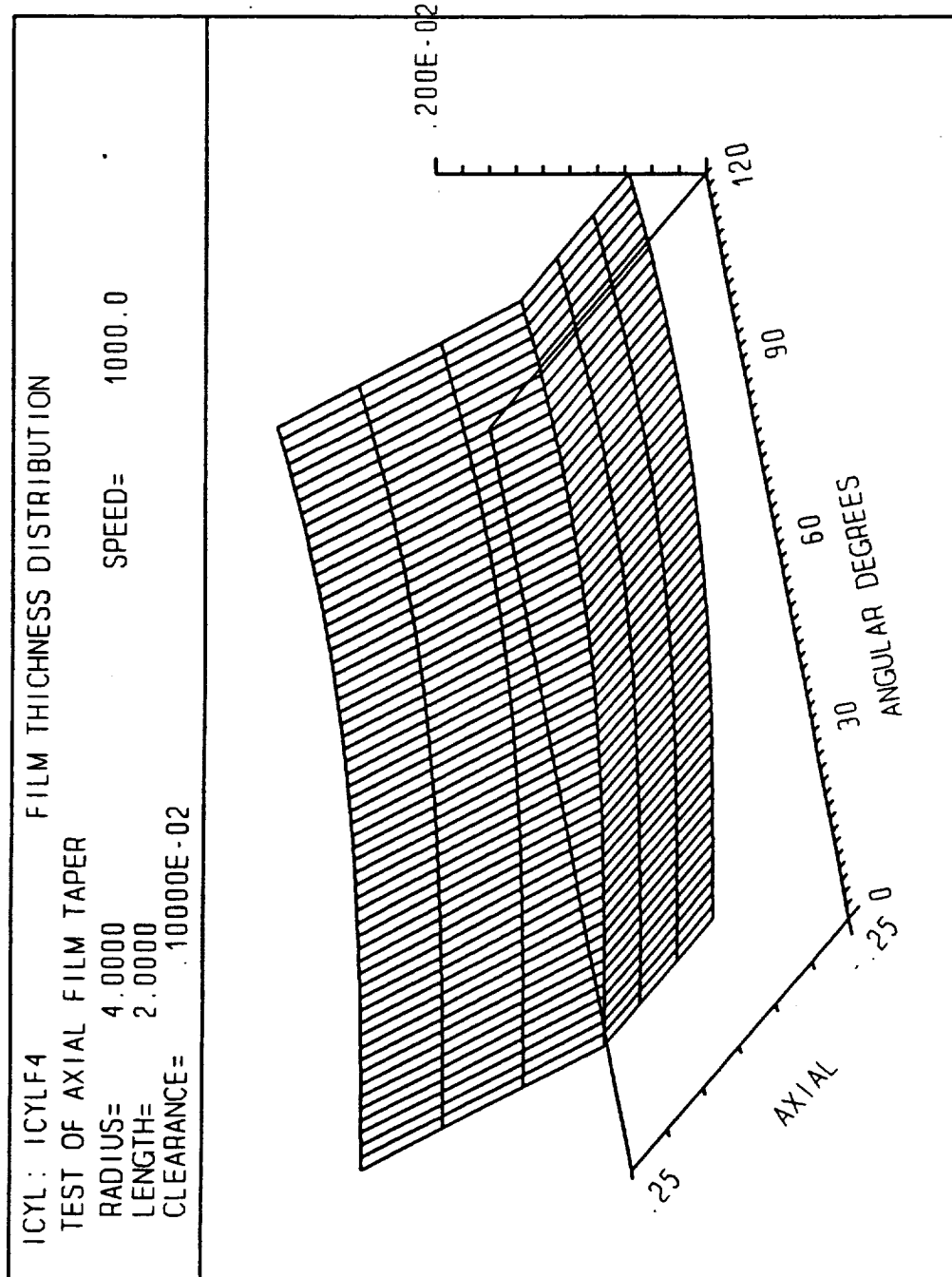
Figure 4-13 Film thickness distribution for sample F4
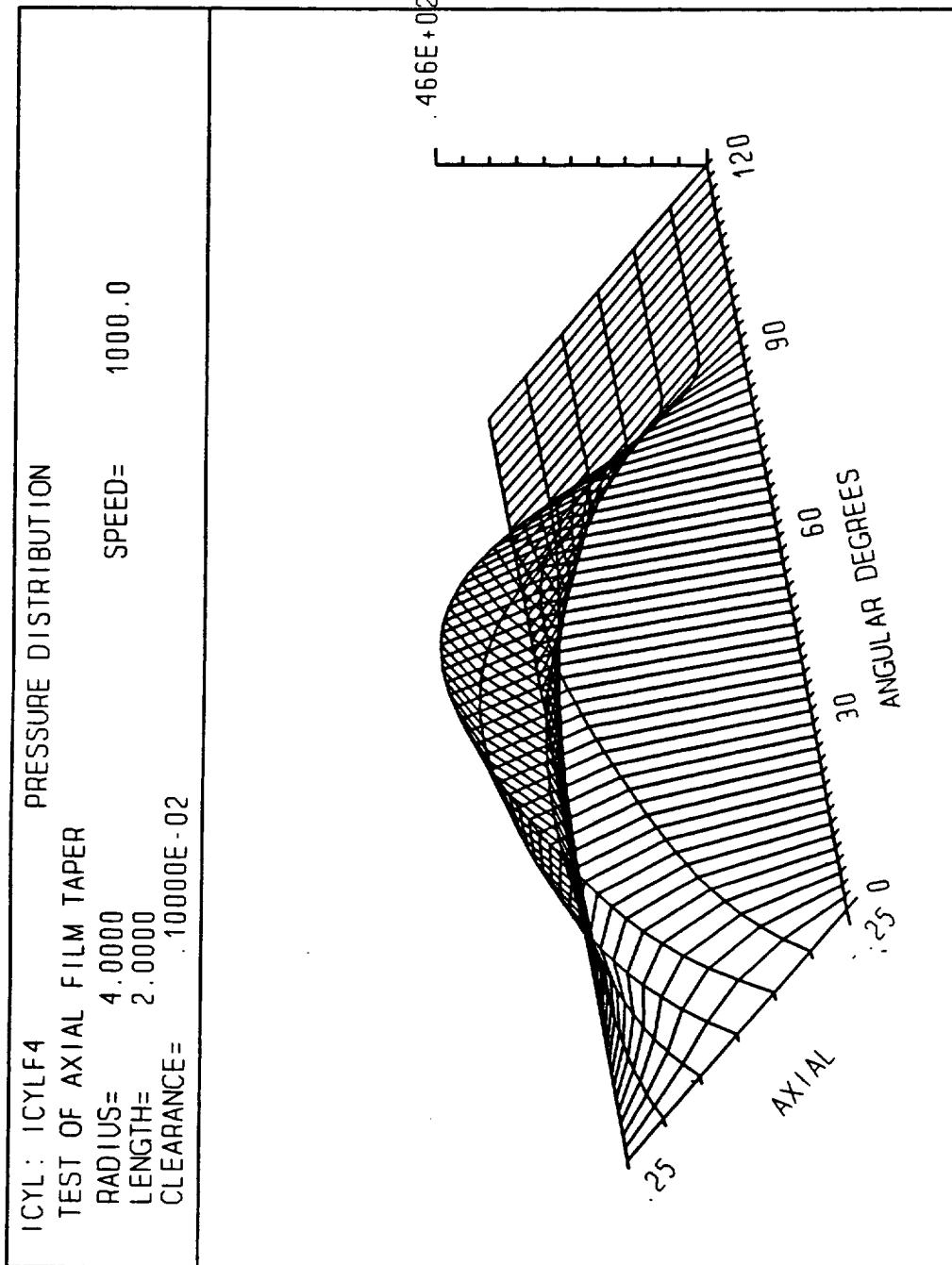
Figure 4-14   Pressure distribution for sample F4
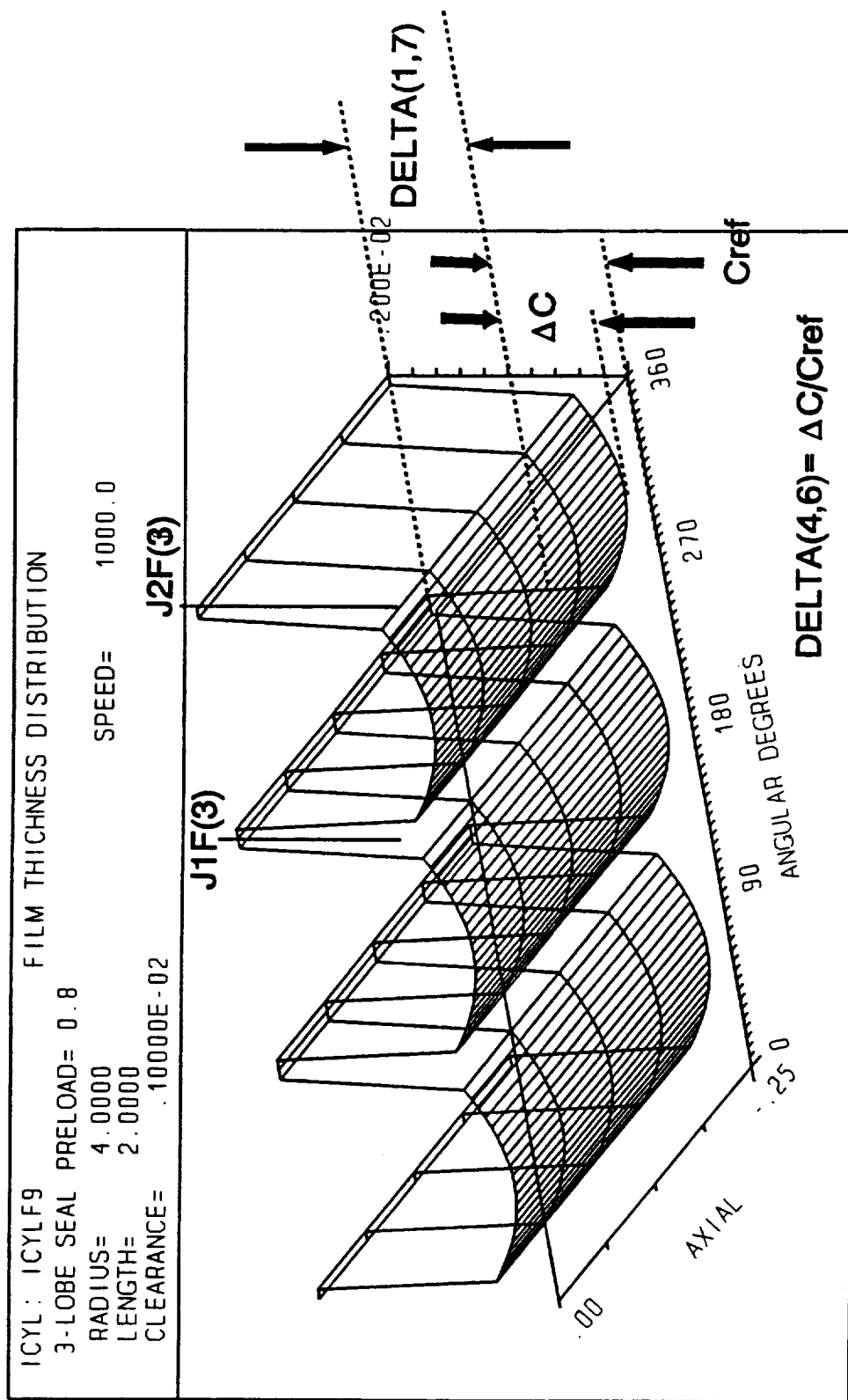
Figure 4-15 Film thickness distribution for sample **F9**

ICYL: ICYLF9   PRESSURE DISTRIBUTION
3-LOBE SEAL PRELOAD= 0.8
                                SPEED=   1000.0
RADIUS=   4.0000
LENGTH=   2.0000
CLEARANCE=   .10000E-02

.106E+03

360

270

180   ANGULAR DEGREES

90

.25 0

AXIAL

.00

Figure 4-16   Pressure distribution for sample F9

Figure 4-17   Pressure distribution for sample I1

4-37

Samples I1 through I4 are more realistic models since they represent the full circumference. In sample I1, the program takes about 7 minutes to calculate the orifice diameter for given pocket pressures. The resulting pressure distribution is shown in Figures 4-17. Sample I2 is the same as I1 except that the eccentricity and orifice diameter were prescribed, requiring the program to solve for the four pocket pressures. The resulting film thickness and pressure distributions are shown in Figures 4-18 and 4-19, respectively. In sample I3, the orifice diameter as well as the radial force were prescribed, requiring the program to solve for the radial position as well as the pocket pressures.

Sample I4 shows the dramatic increase in execution time with the number of axial grid lines, M. Sample I1 is a model of only half of the seal (ISYM = 1) at the concentric position with the pocket pressures specified. This run executes in less than 7 minutes in spite of the 5x61 mesh. Samples I4 is a model of the full axial length (ISYM = 0), with an 11x61 mesh, in which non-zero ϵ_x, α and orifice size are specified and all 32 dynamic coefficients are requested. This run took 7.7 hours to execute. Calculations for each of these coefficients require convergence of the outer iteration loop with four unknown pocket pressures.

Sample I5 and I6 are models representing the full circumference and length with two rows of 4 pockets. The orifice size is calculated in the concentric aligned position in I5 while I6 calculates what happens when the rotor is displaced to the $\epsilon_x = 0.4$ position and rotated about the x-axis by $\alpha = 0.4$. For I5, the resulting pressure distribution is shown in Figure 4-20. For I6, the film thickness and pressure distributions are shown in Figures 4-21 and 4-22, respectively.
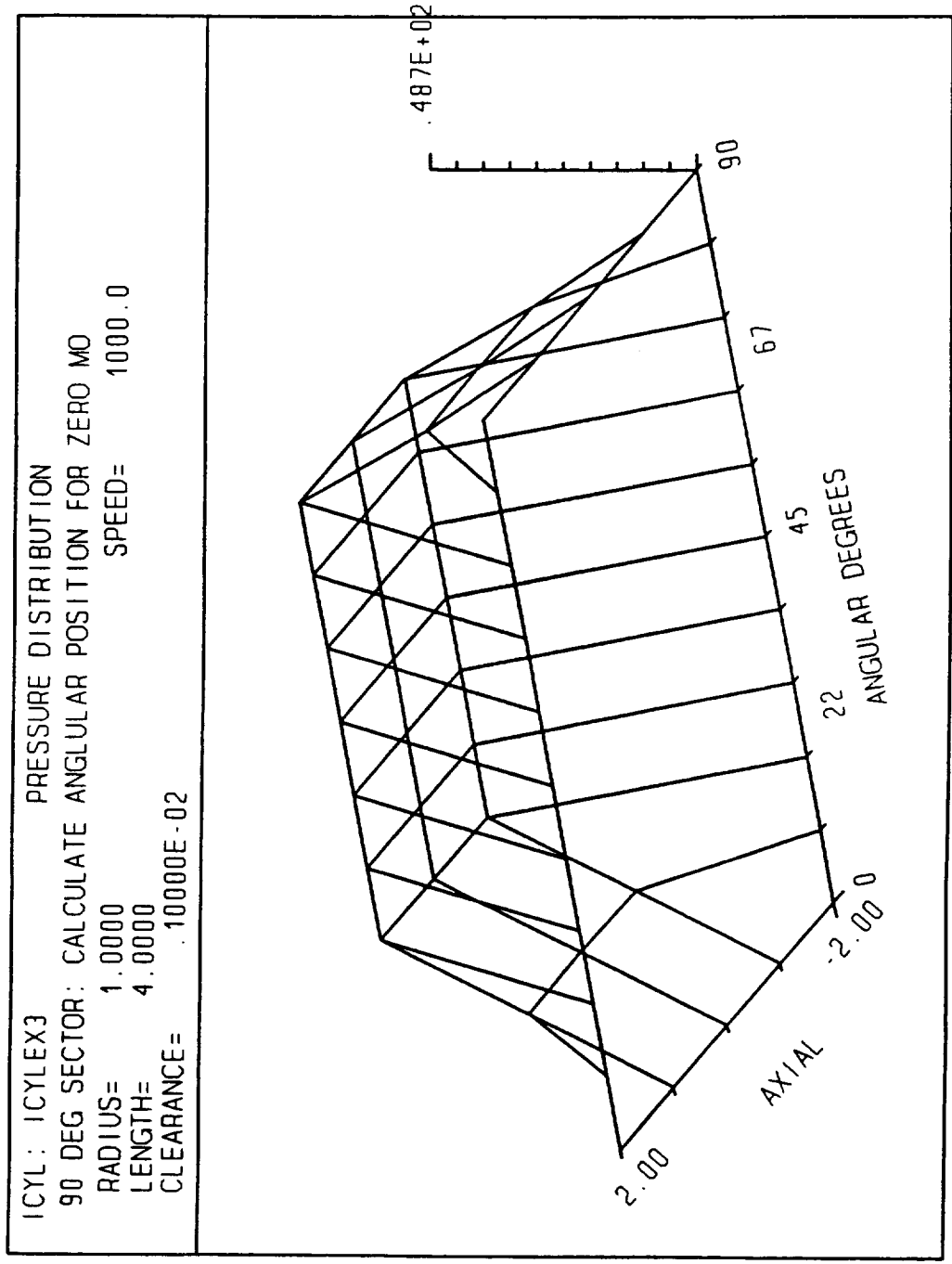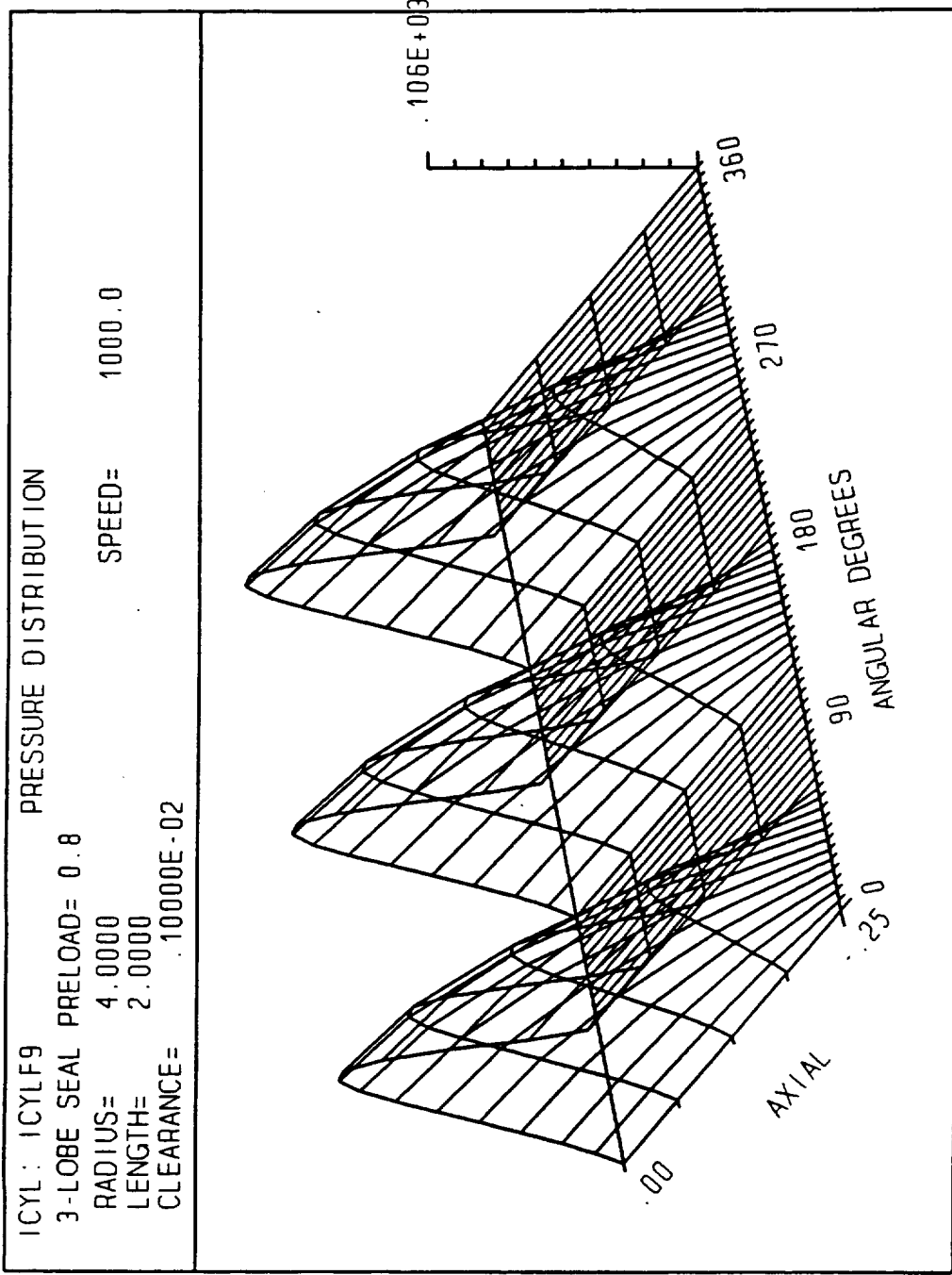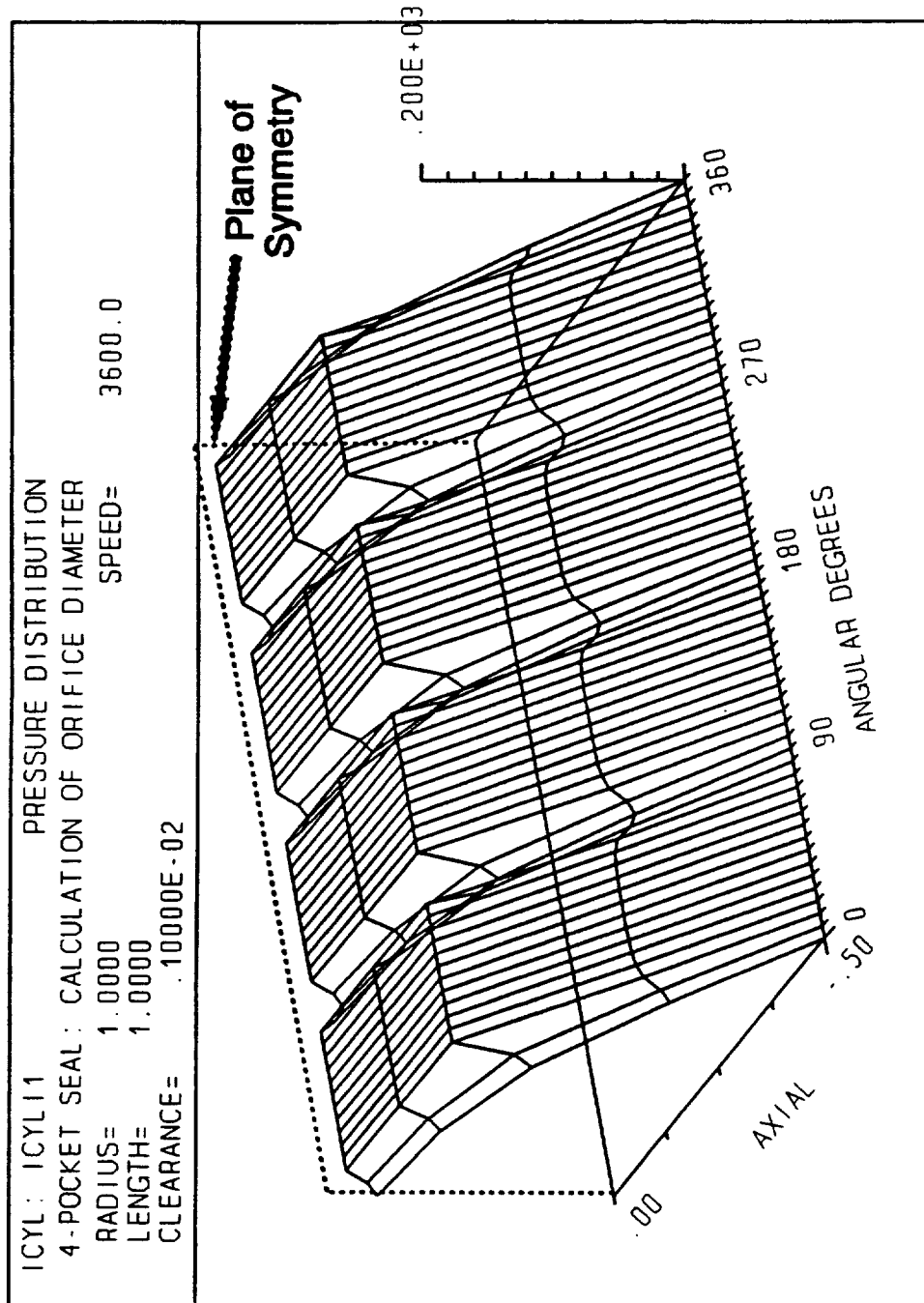
ICYL : ICYL I2   FILM THICHNESS DISTRIBUTION

4-POCKET SEAL : CALCULATION OF ECCENTRIC PERFORMANCE

RADIUS=   1.0000   SPEED=   3600.0
LENGTH=   1.0000
CLEARANCE=   .10000E-02

.110E-02

360   270   180   90   0

ANGULAR DEGREES

AXIAL

.00   -.50
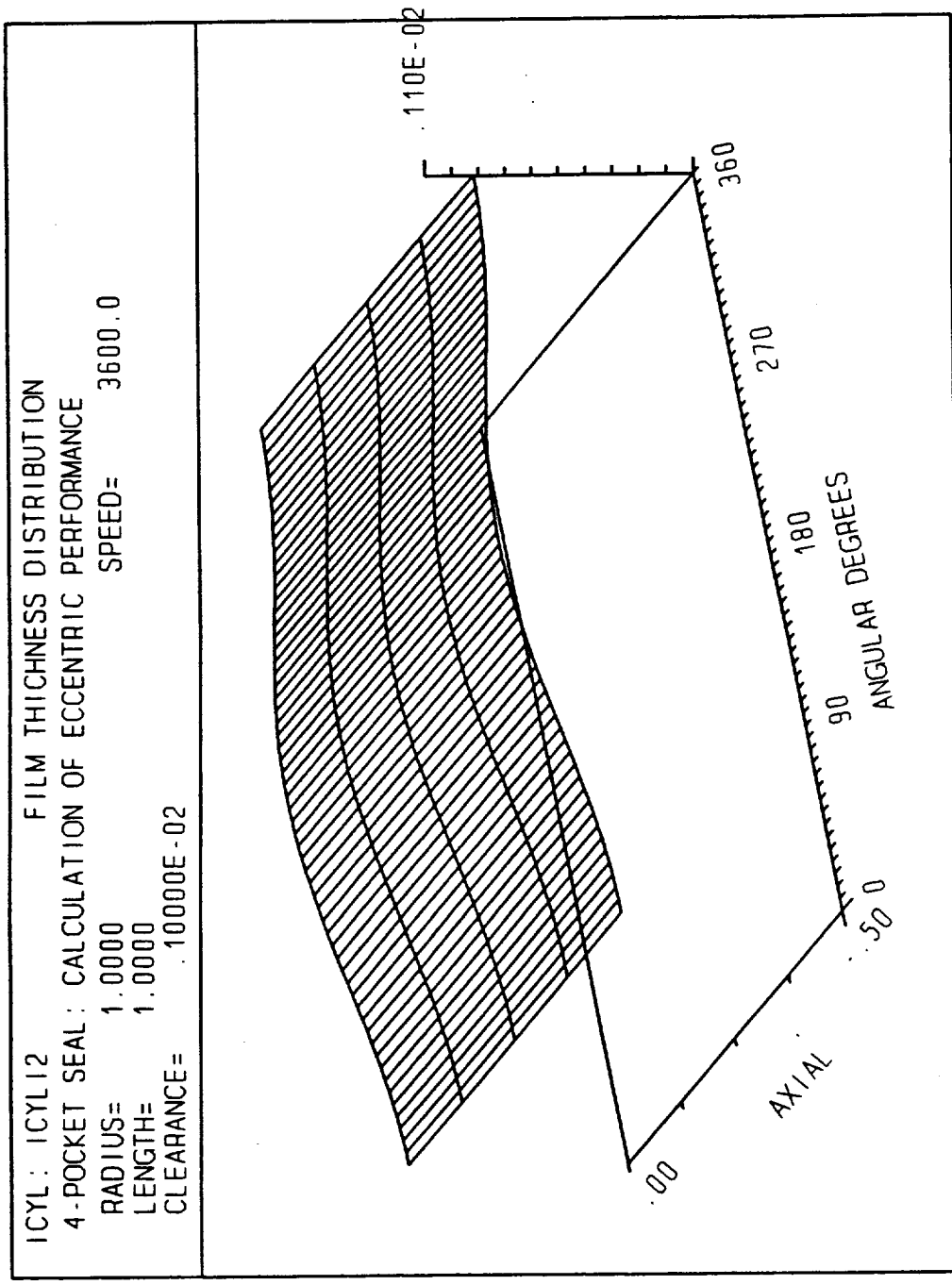
Figure 4-18   Film thickness distribution for sample I2

ICYL: ICYL12   PRESSURE DISTRIBUTION
4-POCKET SEAL: CALCULATION OF ECCENTRIC PERFORMANCE
   RADIUS=   1.0000   SPEED=   3600.0
   LENGTH=   1.0000
   CLEARANCE=   .10000E-02

.232E+03

360

270

180   ANGULAR DEGREES

90

.50 0

AXIAL

.00
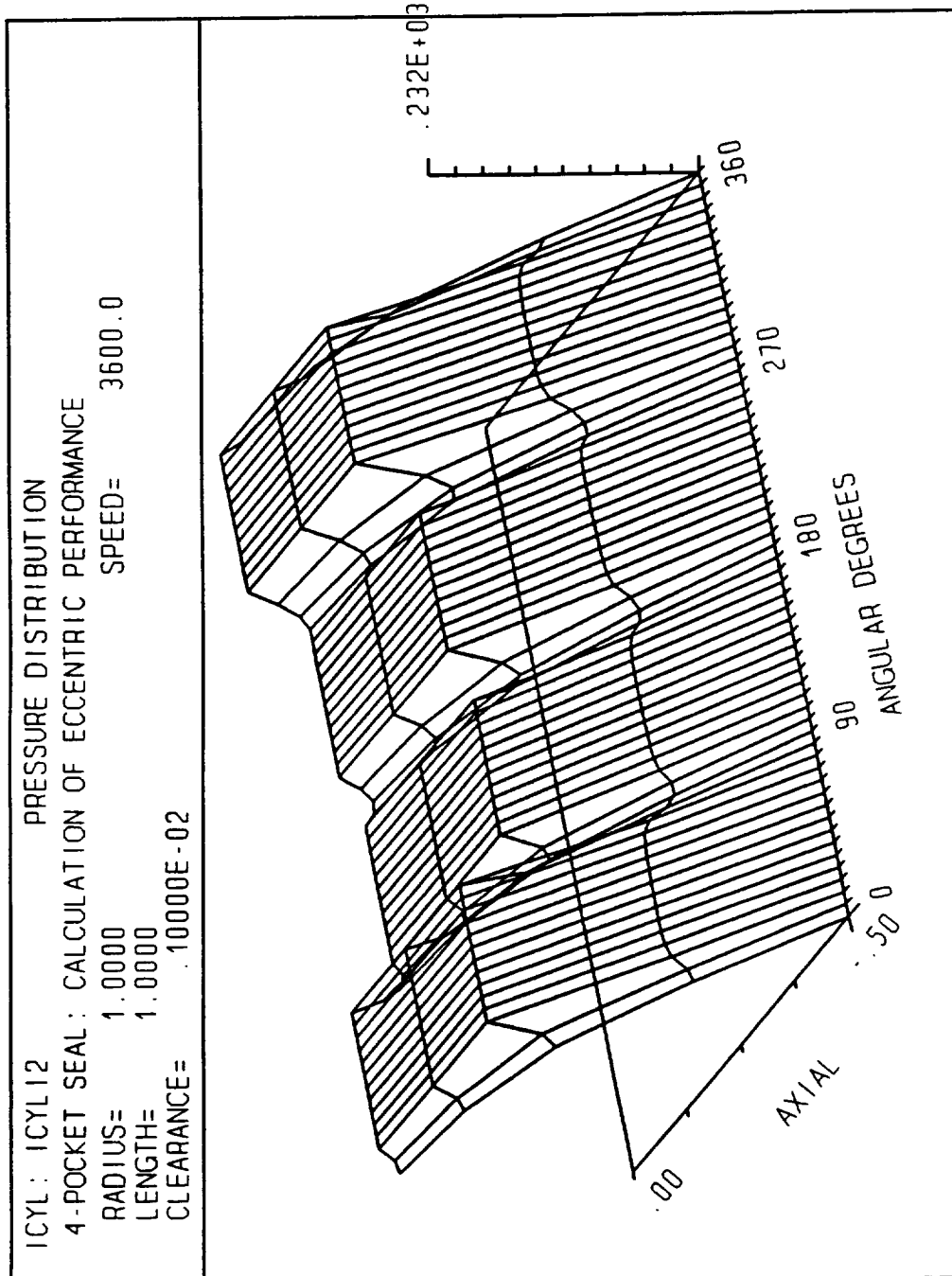
Figure 4-19   Pressure distribution for sample I2

4-40
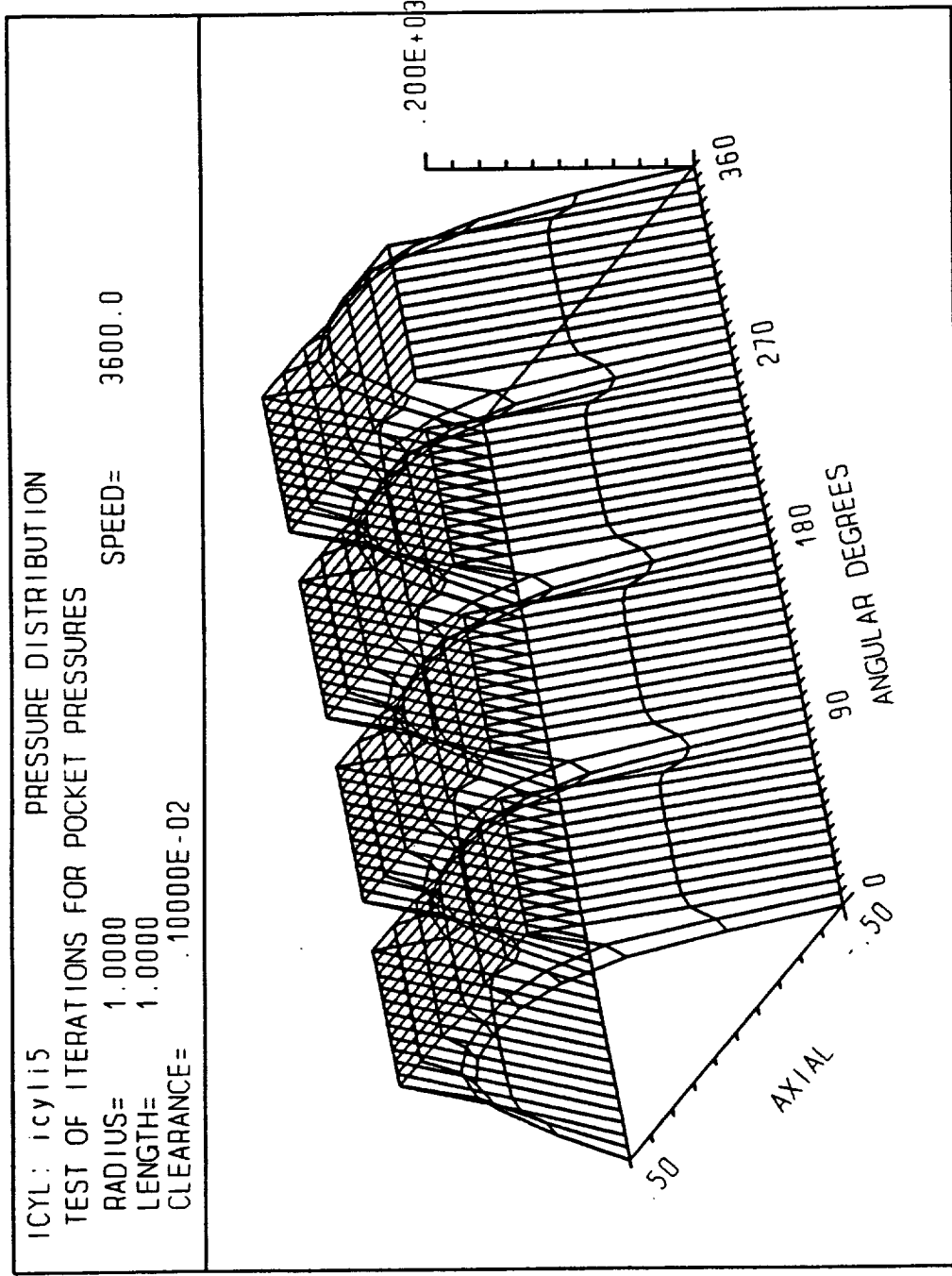
Figure 4-20   Pressure distribution for sample I5
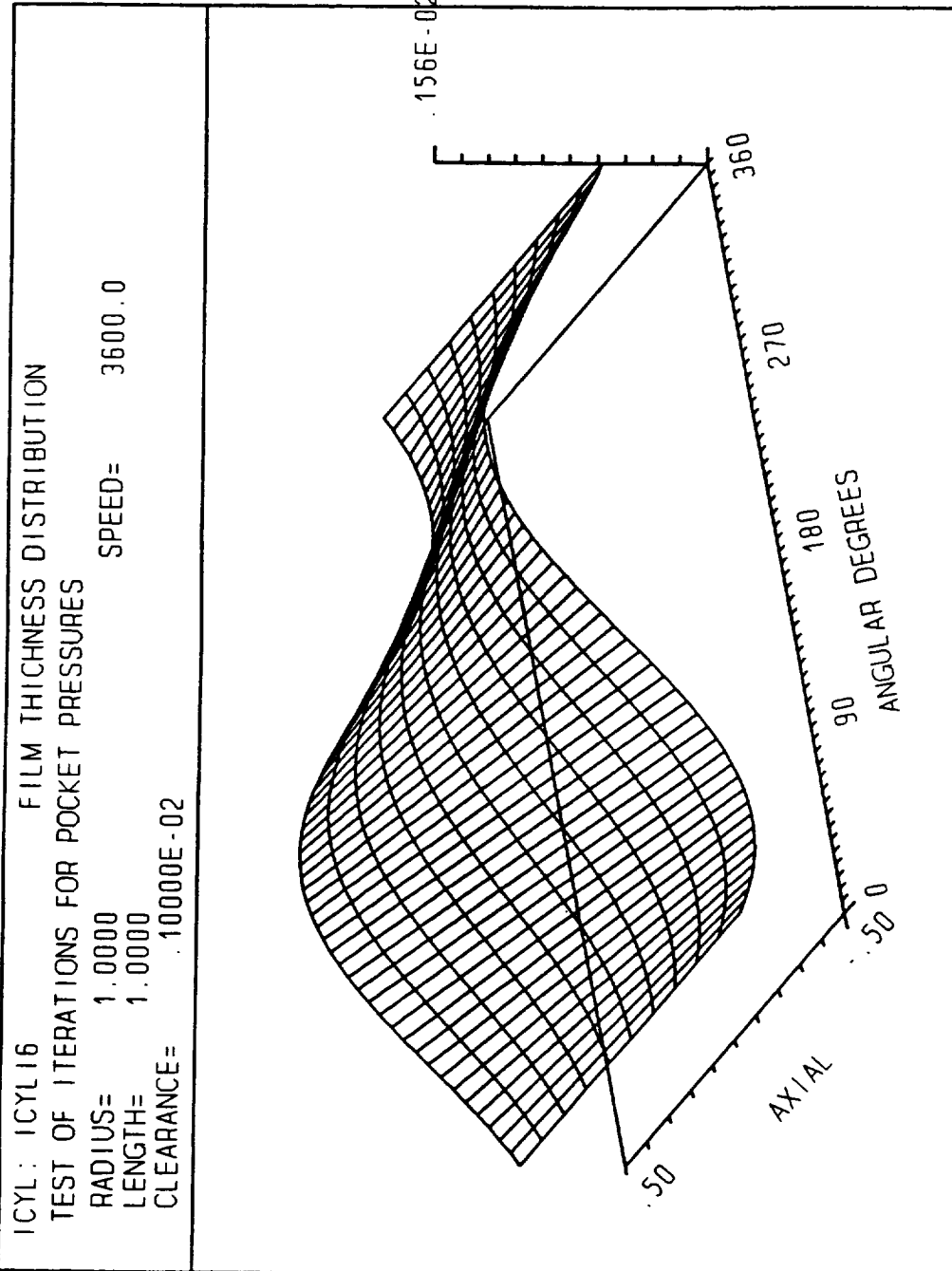
Figure 4-21   Film thickness distribution for sample I6

ICYL: ICYLI6   PRESSURE DISTRIBUTION
TEST OF ITERATIONS FOR POCKET PRESSURES

RADIUS=   1.0000   SPEED=   3600.0
LENGTH=   1.0000
CLEARANCE=   .10000E-02

.364E+03

360

270

180
ANGULAR DEGREES

90

.50 0

AXIAL

50
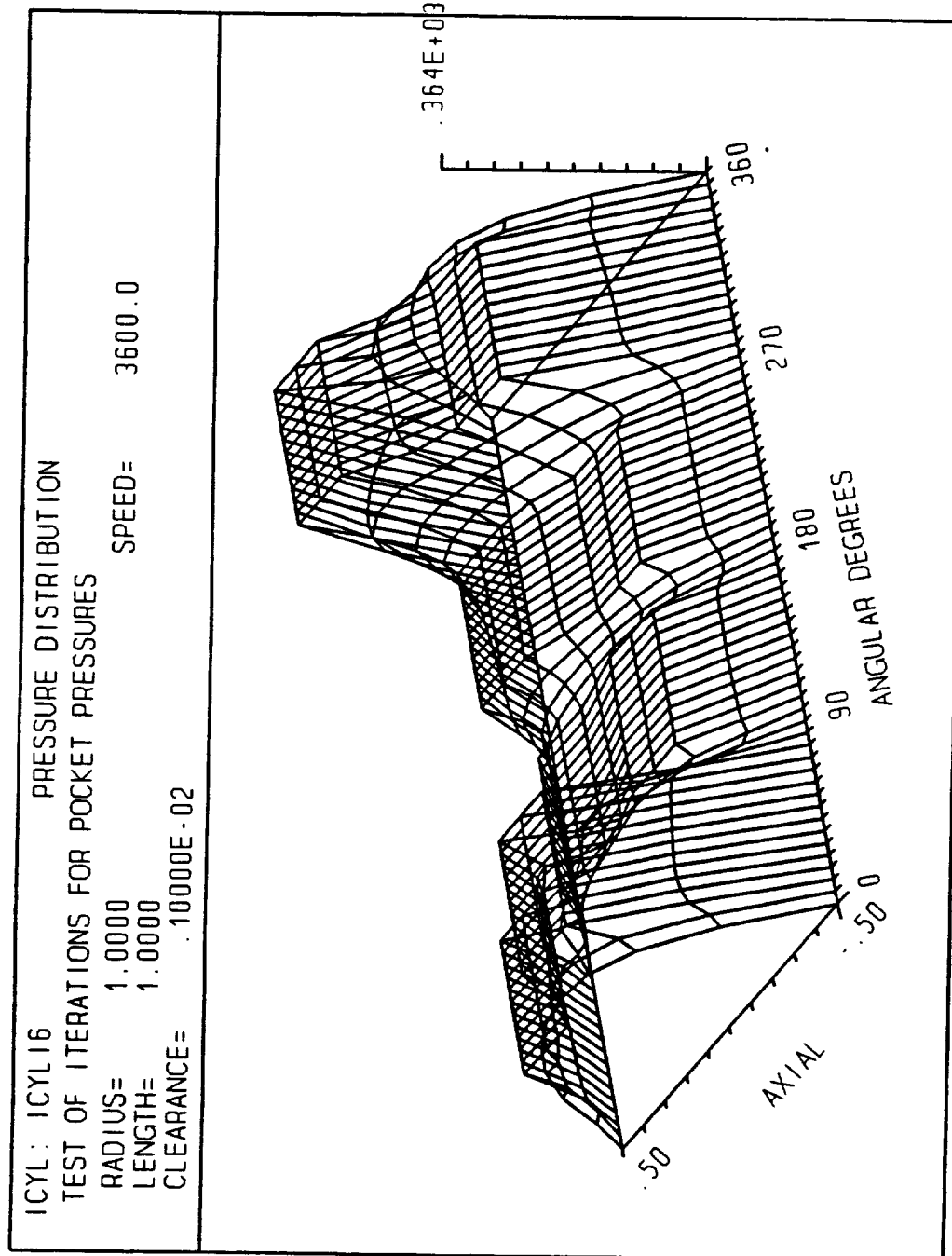
Figure 4-22   Pressure distribution for sample I6

Sample **O15** is a case of a plain cylindrical seal with increasing housing wall roughness. The wall roughness (ROUGHB) was varied from 1×10^{-6} to 1×10^{-3} inches in a logarithmic scale using IPAR = 14 and NPAR = -4. This input was used to generate the top curve of critical mass versus roughness shown in Figure 4-23. The stabilizing effect of housing roughness is more pronounced at the higher pressures due to the increased effect of inlet inertia. The last lines in the input file show how one would run additional values of pressure within the same run. These were not run because they were placed after the line with ISTOP = 1 in order to reduce the size of the output file.
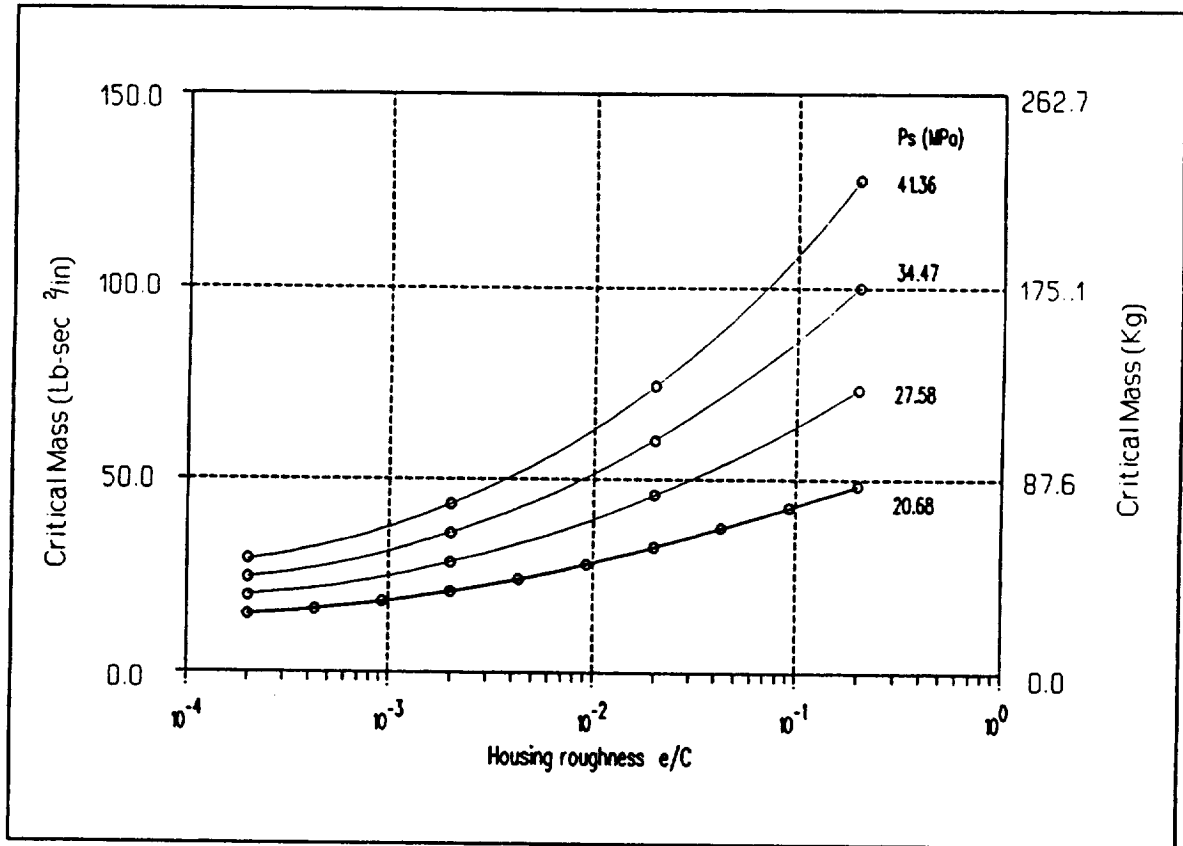
Figure 4-23 Critical mass versus housing roughness

4.3 VERIFICATION

ICYL has been compared with the results of two other MTI computer codes as well as currently published data. The first comparison was against a generic bearing program with many similar capabilities (GBEAR) based on the turbulent lubrication theory of Ng and Pan. A second comparison against a laminar bearing program (GASBEAR) was used to verify the calculations of moments and angular coefficients. Finally, comparison were made against calculations published by San Andrés in Reference [16].

Comparison against MTI other codes

The first of the MTI computer codes is GBEAR which is fully described in Reference 1. This program is based on the turbulent lubrication theory of Ng and Pan[13], and does not include surface roughness, housing rotation or calculation of misalignment coefficients. It includes inertia pressure drop at exit from pockets but not from the seal ends.

Calculations were made with a 90° seal sector at an eccentricity ratio of 0.5 and with a pocket at its center with a prescribed pressure ratio of 0.5. Table 4-2 shows a comparison of pocket flow, orifices size, force, and stiffness and damping coefficients. As expected, comparisons of GBEAR against ICYL with the same friction model (IFRIC=0) yielded nearly identical results. With the new friction model that includes surface roughness effects, ICYL calculates lower torque(-32%), lower pocket flow (-13%) and orifice size (-7%), and force components(-6%). Very good agreement in the stiffness coefficients (-4%), and slightly higher damping coefficients(+13%) are obtained.

Other comparisons against GBEAR in the laminar regime and without pockets yielded identical results.

Table 4-2   Comparison against GBEAR.

	GBEAR	ICYL IFRIC=0	ICYL IFRIC=3	ICYL IFRIC=4
Recess flow (in^3/s)	25.75	25.21	20.931	22.316
Orifice diam. (in)	0.0833	0.0820	0.0752	0.0776
Torque (lb-in)	14.38	14.32	8.791	9.771
Power (Lb-in/s)	45,171	44,971	27,617	30,696
Fx (Lb)	3,694	3,358	3,352	3,477
Fy (Lb)	-3,488	-3,122	-3,083	-3,346
Kxx (10^6 Lb/in)	2.352	2.267	2.329	2.344
Kxy (10^6 Lb/in)	-1.461	-1.378	-1.280	-1.397
Kyx (10^6 Lb/in)	-1.998	-1.874	-1.871	-1.961
Kyy (10^6 Lb/in)	1.573	1.481	1.406	1.564
Bxx (Lb/in)	232.08	234.79	269.01	274.46
Bxy (Lb/in)	-175.53	-175.87	-194.38	-199.65
Byx (Lb/in)	-174.78	-174.10	-192.40	-200.56
Byy (Lb/in)	173.87	173.79	187.57	196.53

A second MTI computer code with the fluid compressibility turned off (GASBEAR) was used to verify the calculation of the 24 stiffness and damping coefficients which involve rotor misalignment. GASBEAR was written for use in conjunction with plane journal bearings and cylindrical seals and does not treat turbulence or pressurized pockets. The comparison, in the laminar regime and with the same finite difference mesh, yielded identical coefficients.

Comparison against published data

A detailed comparison was made of the 5-pad hydrostatic bearing discussed by San Andrés in Reference [16]. This high speed hybrid journal bearing operates at relatively high levels of pressurization and relatively low viscosity lubricants, in which the effects of pressure-induced turbulence become important. Fluid inertia may also be important. Figure 4-24 is a plot of the pressure distribution at the

concentric position, while Figure 4-25 and Figure 4-26 plot it for 40% eccentricity ratio of the journal between pockets and over a pocket center, respectively. Reproductions of the corresponding pressure distributions published by San Andres are included in the figures for comparison. It is noticed that the size of the pressure drops at the pocket exits (i.e., entrance to the film) as well as the general pressure distribution are comparable for both analyses.

At the concentric position, bearing flow requirements calculated by ICYL is 42 versus about 44 l/min reported by San Andres. Figure 4-27 and Figure 4-28 are plots comparing the direct and cross coupled stiffness coefficients while, Figure 4-29 and Figure 4-30 compare the direct and cross coupled damping coefficients, respectively, versus eccentricity ratio. In general, ICYL predicts about 35% higher direct stiffness, 10% lower cross coupled stiffness coefficients, and 15% lower direct damping at the concentric position. With increasing eccentricity ratio, the coefficients are observed to behave similarly and some of the discrepancies decrease. The cross-coupled damping coefficients with ICYL are equal in magnitude, opposite in sign and zero at the concentric position, as is expected with an incompressible fluid. San Andres' non-zero concentric value (60 kN-s/m) is due to the fluid compressibility in the pocket. Figure 4-31 shows the critical mass versus eccentricity. The concentric value of 119 Kg shows better stability than predicted by San Andrés, which predicts an unstable bearing with a 30 Kg mass.

The analysis of San Andrés includes the effect of fluid inertia in the film as well as some special effects inside the pocket, such as fluid compressibility and a one-dimensional circumferential pressure rise downstream of the orifice. There is also a slight difference in friction law used: MTI's analysis follows the formula derived by Nelson[12] for Moody diagram, in which the term containing the Reynolds number is raised to the 1/3 power while San Andres uses the same formula with the power changed to 1/2.65 for a more restricted range of Reynolds numbers.

Eccentricity = 0

ICYL

.475E+03

0
90
180
270
360
ANGULAR DEGREES

©   ex=0.0
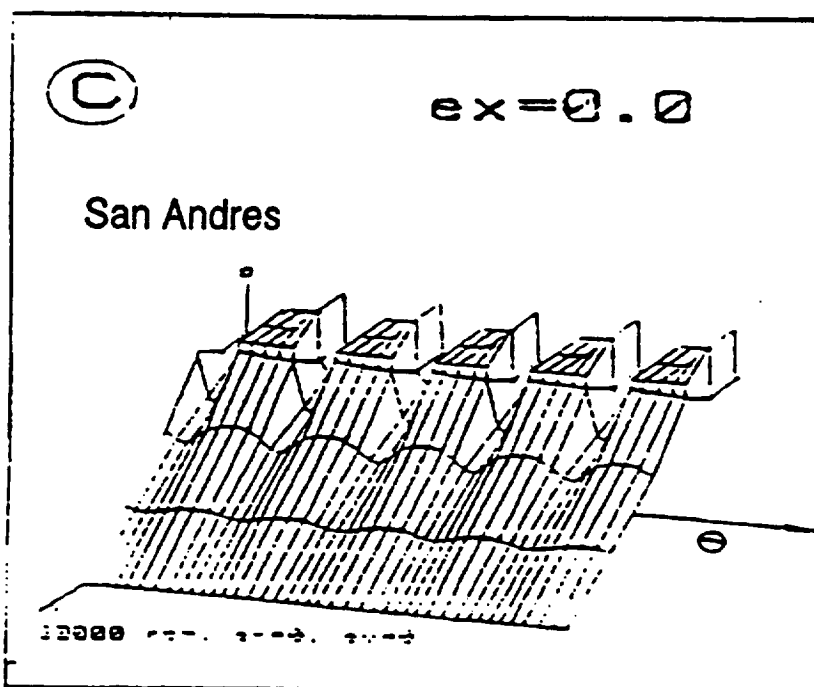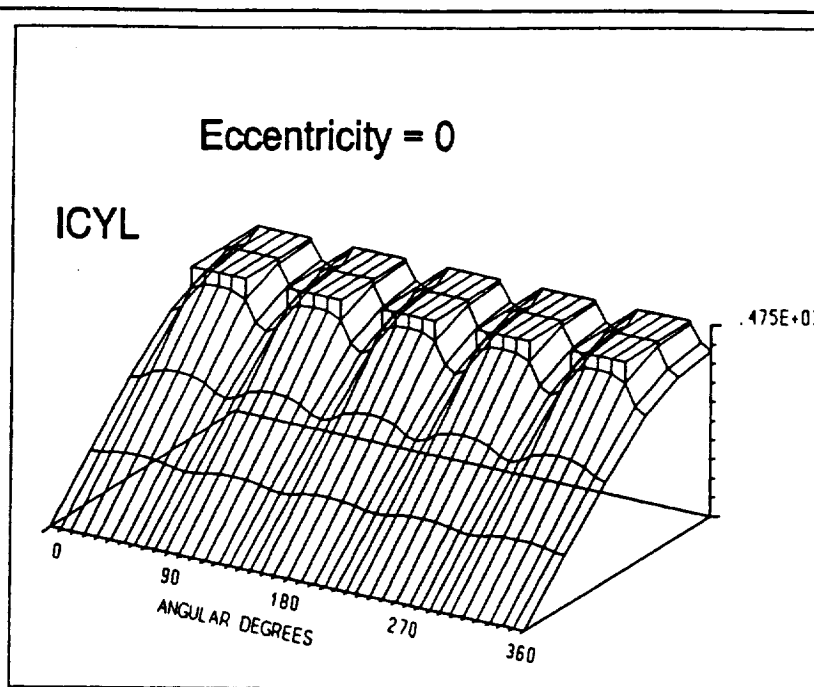
San Andres

Figure 4-24 Comparison to SanAndres' 5-pad bearing at concentric position

eccentricity

ICYL

.752E+03

0   90   180   270   360
ANGULAR DEGREES

ex=0.40
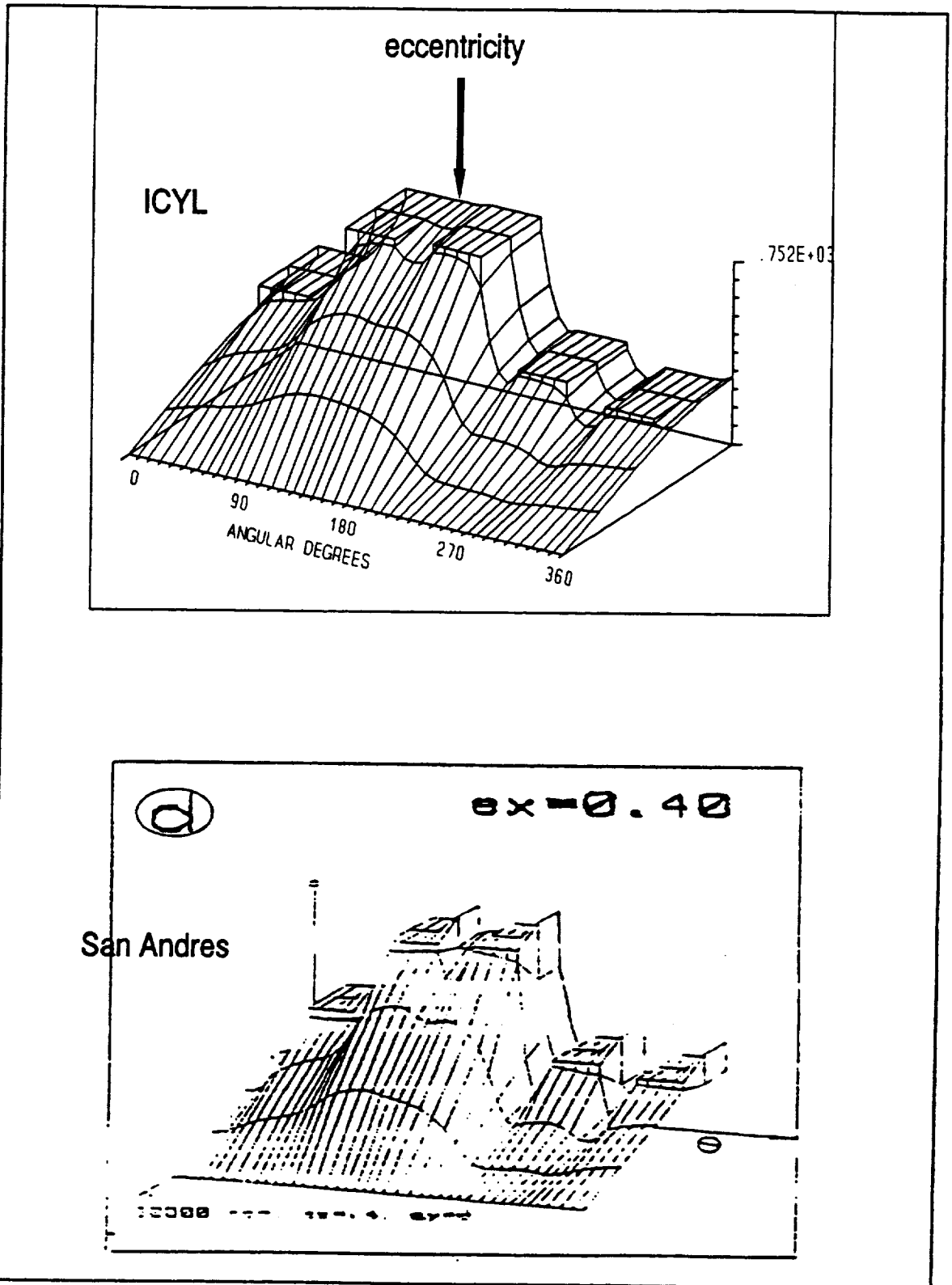
San Andres

Figure 4-25 Comparison to SanAndres' 5-pad bearing with 40% eccentricity between pockets

ICYL: ICYLSA9B   PRESSURE DISTRIBUTION
COMPARISON TO SAN ANDRES 5-POCKET BEARING EPS= .4
   RADIUS=   1.5000   SPEED=   30000.
   LENGTH=   3.0000
   CLEARANCE=   .30000E-02

ICYL   Eccentricity

                                        .824E+03

     0
        90
           180
ANGULAR DEGREES   270
                      360

ex=-0.40

San Andres

Figure 4-26 Comparison to SanAndres' 5-pad bearing with 40% eccentricity over pocket
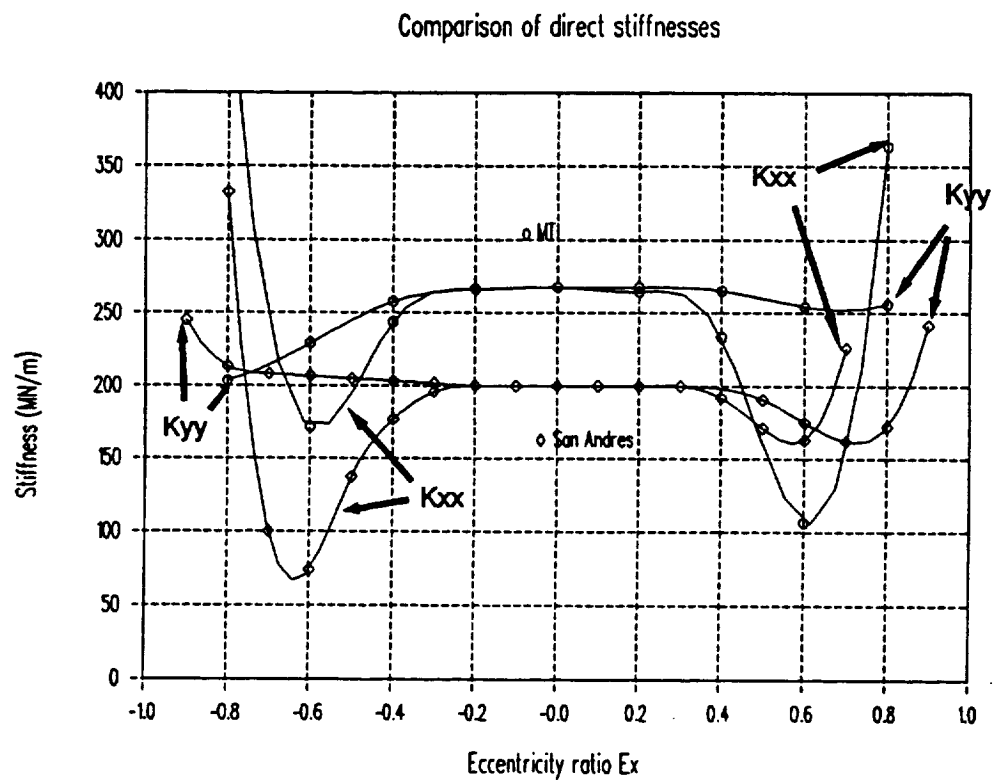
Figure 4-27 Comparison of direct stiffness coefficient
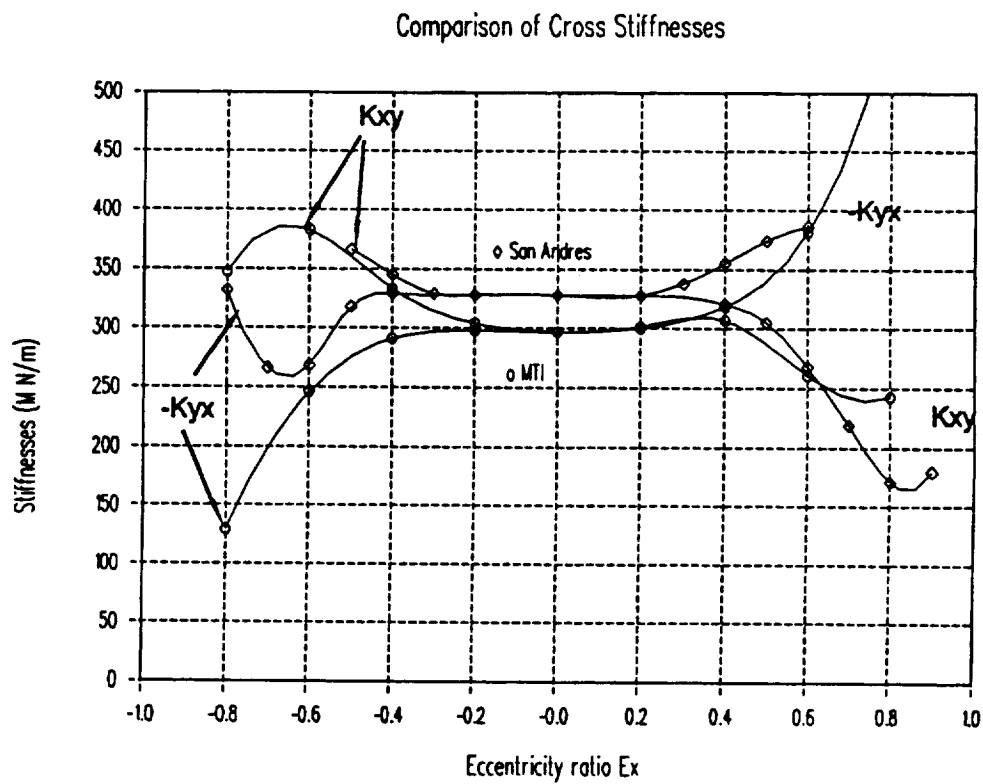
Figure 4-28 Comparison of cross stiffness coefficients

Figure 4-29 Comparison of direct damping coefficients

Figure 4-30 Comparison of cross damping coefficients

4-54
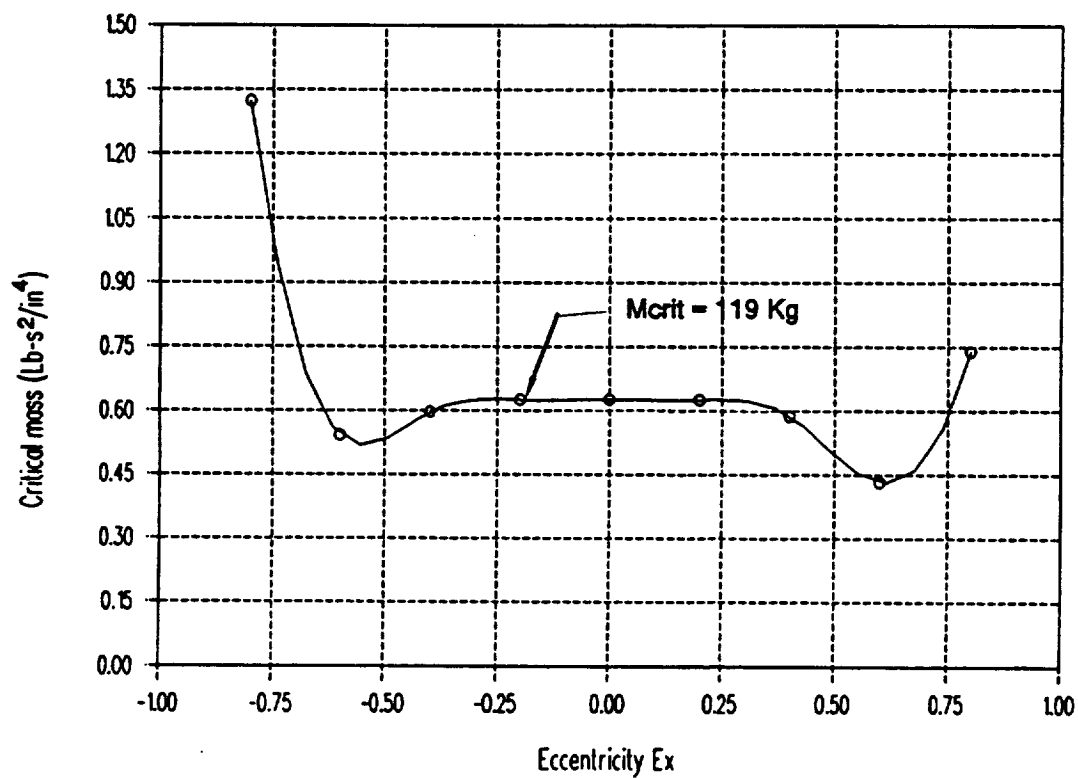
Figure 4-31 Critical mass versus eccentricity ratio

The above comparisons should provide reasonable verification, as the only discrepancies between the results can be explained by the different friction models and features between the codes.

4.4 REFERENCES

1.   Artiles, A., Walowit, J., and Shapiro, W., 1982, *Analysis of Hybrid Fluid Film Journal Bearings with Turbulence and Inertia Effects*, **Advances in Computer Aided Bearing Design**, ASME Publication G00220, pp.25-52.
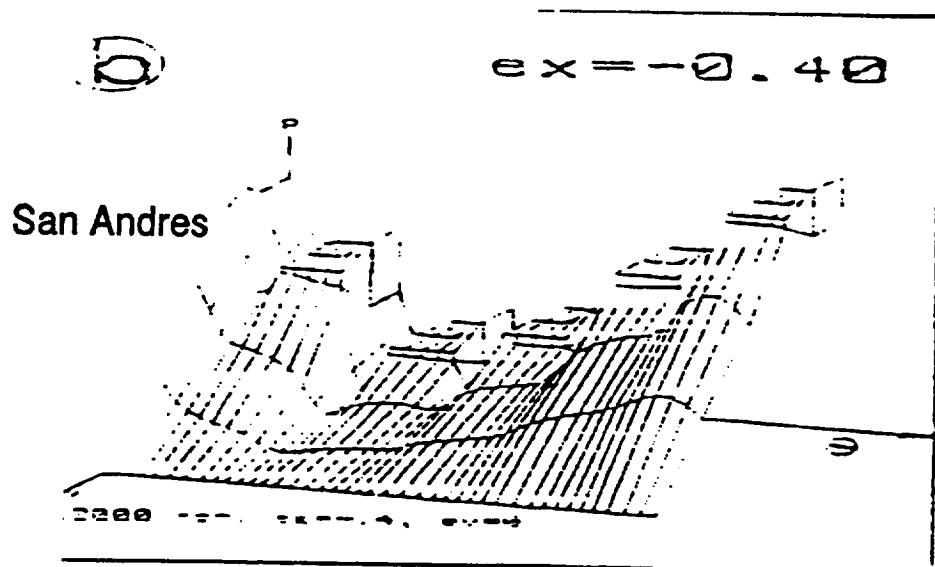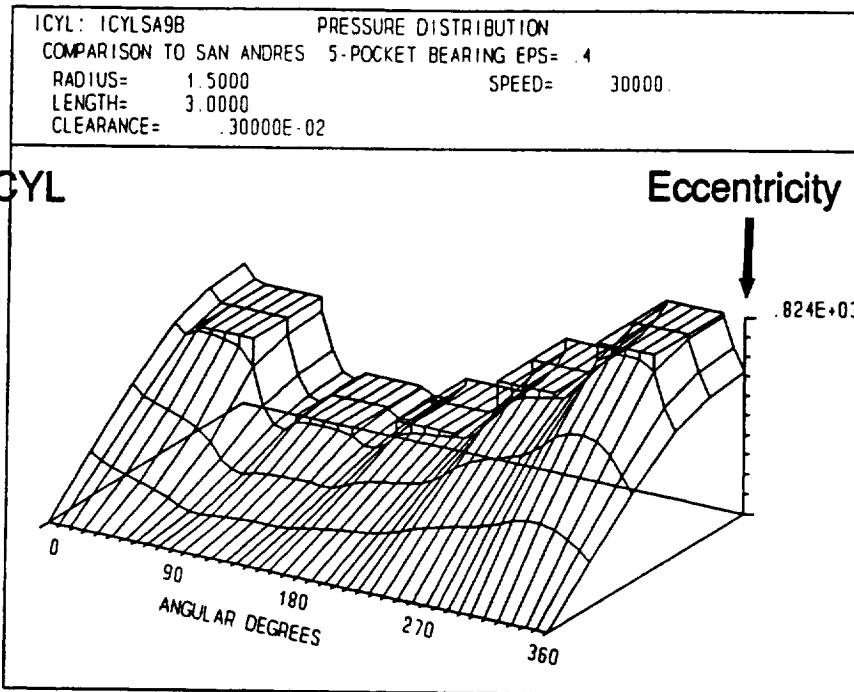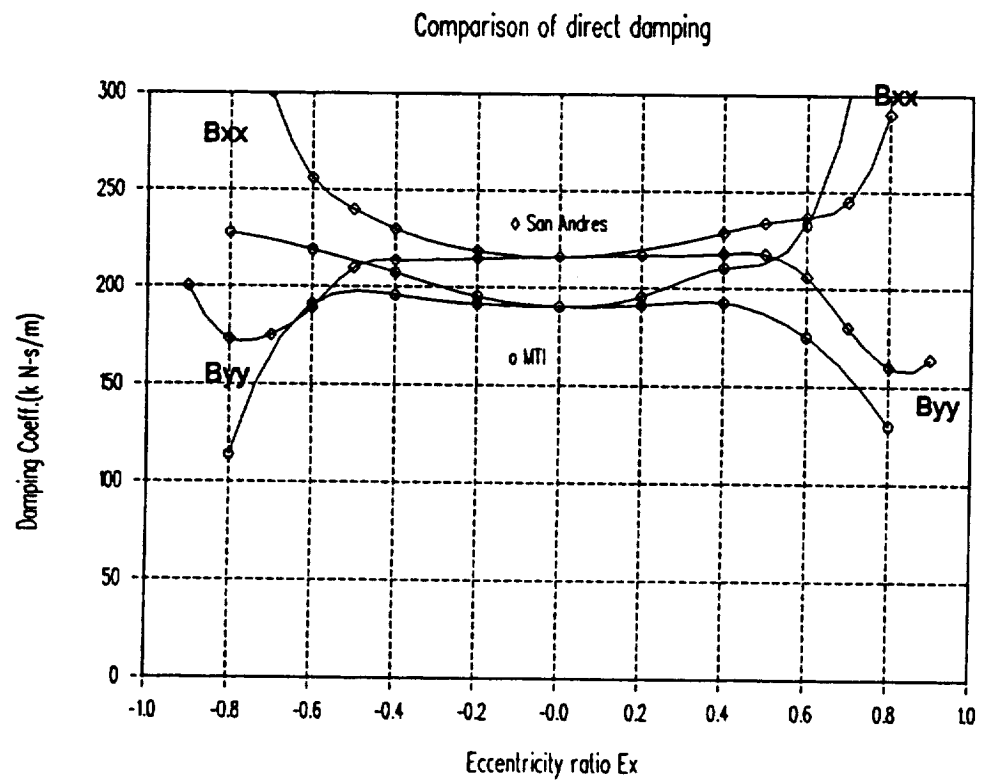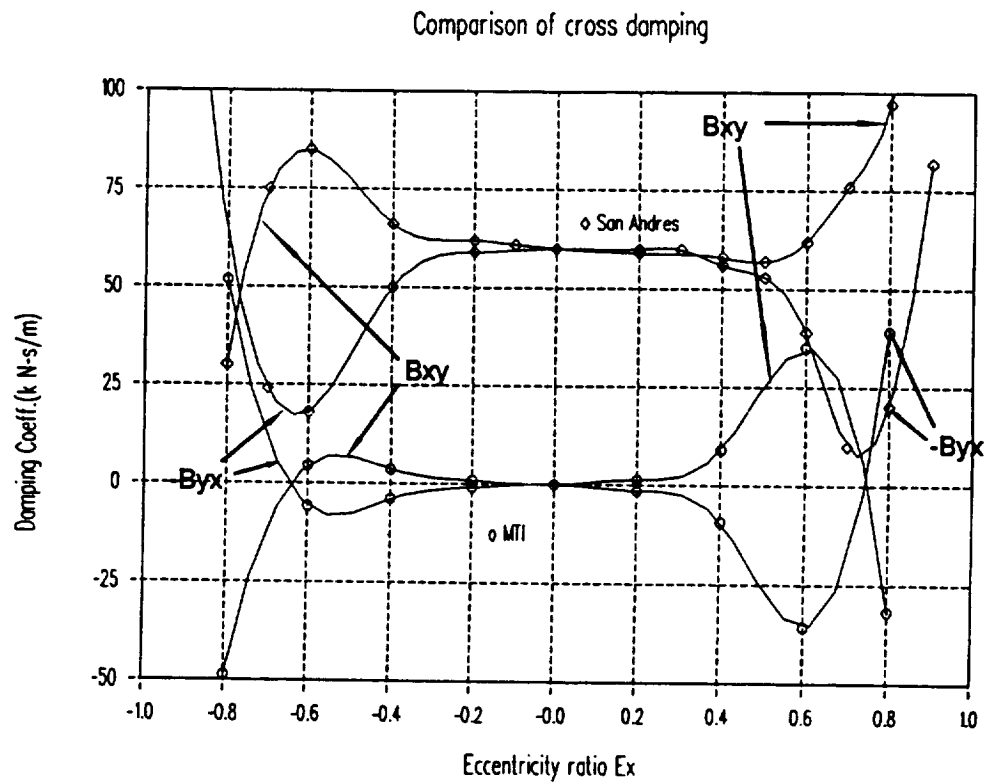
2.   Bou-Said, B., Chaomleffel, J.P., *Hybrid Journal Bearings: Theoretical and Experimental Results*, Trans ASME, **Journal of Tribology**, Apr. 1989, pp.265-269.

3.   Castelli, V., Pirvics, J., *Review of Methods in Gas Bearing Film Analysis*, **Trans. ASME**, (1968), pp.777-792.

4.   Castelli, V., *Design of Gas Bearings - Volume 1, Part 4: Numerical Methods*, **Gas Bearing Course Notes**, Mechanical Technology Incorporated, Latham, NY, (1971)

5.   Elrod, H.G., Ng ,C.W., *A Theory for Turbulent Fluid Films and its Application to Bearings*, Trans ASME, **Journal of Lubrication Technology**, July 1967, pp.346-362.

6.   Elrod, H.G., *A Cavitation Algorithm*, Trans ASME, **Journal of Lubrication Technology**, July 1981, pp.350-354.

7.   Hirs, G. G.,*A Bulk-Flow Theory for Turbulence in Lubricant Films*, Trans ASME, **Journal of Lubrication Technology** April 1973, pp.137-146.

8.   Hirs, G. G.,*Fundamentals of a Bulk-Flow Theory for Turbulent Lubricant Films*, **Doctoral Thesis**, University of Technology Delft, June 1970, available from T.N.O., P.O. Box 29, Delft, The Netherlands.

9.   Ho, Y. S., Chen, N.N.S., *Pressure distribution in a six-pocket hydrostatic journal bearing*, **Wear**, 98 (1984)89-100.

10. Launder, B.E., Leschziner, M., *Flow in Finite-Width Thrust Bearings Including Inertia Effects I--Laminar Flow*, Trans ASME, **Journal of Lubrication Technology**, July 1978, pp.330-338.

C-3

11. Launder, B.E., Leschziner, M., *Flow in Finite-Width Thrust Bearings Including Inertia Effects II--Turbulent Flow,* Trans ASME, **Journal of Lubrication Technology**, July 1978, pp.339-345.

12. Nelson, C.C., Ngyyen,D.T., *Comparison of Hir's Equation with Moody's Equation for Determining Rotordynamic Coefficients of Annular Pressure Seals,* Trans ASME, **Journal of Tribology,** Jan. 1987, pp.144-148.

13. Ng, Chung-Wah, Pan, C.H.T., *A Linearized Turbulent Lubrication Theory,* Trans ASME, **Journal of Basic Engineering,** Sept. 1965, pp.675-688.

14. Press, W.H., Flannery, B.P., Teukolsky, S.A. and Vetterling, W.T., *Numerical Recipes,* Cambridge University Press, (1986)

15. San Andrés, Luis A., *Turbulent Hybrid Bearings with Fluid Inertia Effects Part I: Analysis,* Submitted for publication at the ASME/ASLE Joint Tribology Conference, Toronto, Canada, Oct. 1990.

16. San Andrés, Luis, A., *Effect of Eccentricity on the Force Response of Hybrid Bearing,* submitted to STLE for publication, (1990).

17. Schlichting, Herman, *Chapter X, Turbulent Flow Through Pipes,* **Boundary Layer Theory,** McGrawHill Book Co., 1979, pp.596-634.

4.5 NOMENCLATURE

A, B	misalignment of rotor about the x and y axes, respectively. [radians]
$b_{ij} = B_{ij} (C^3/12\mu R^4)$	dimensionless damping coefficient matrix, where $i,j = x, y, \alpha, \beta$.
C	nominal clearance. [L]
e_b, e_j	roughness of the housing and journal surfaces. [L]
e_x, e_y	components of rotor eccentricity at Z=0. [L]
e	rotor eccentricity at Z=0. [L]
F_x, F_y	components of fluid film force about x and y axes. [F]
$f = F/(P_o R^2)$	dimensionless fluid film force.
H	local film thickness. [L]
H_o	local film thickness for the concentric aligned rotor (i.e., $e_x = e_y = A = B = 0$). [L]
$h = H/C$	dimensionless local film thickness.
K_e	coefficient of pressure drop at inlet to film.
K_{ij}, B_{ij}	Stiffness and damping coefficient matrices, where $i,j = x, y, \alpha, \beta$.
$k_{ij} = K_{ij} (C/P_o R^2)$	dimensionless stiffness coefficient matrix, where $i,j = x, y, \alpha, \beta$.
L	seal length. [L]
M_x, M_y	components of fluid film force about x and y axes. [F-L]
$m = M/(P_o R^3)$	dimensionless fluid film moment.

$\hat{n}$	unit vector normal to fluid film boundary.
P	local pressure. $[F/L^2]$
$p = P/P_o$	dimensionless local pressure.
P_l, P_r	Left and right boundary pressures. $[F/L^2]$
P_p, P_s	Pocket and supply pressures. $[F/L^2]$
P_o	Reference pressure, used for scaling the pressure field, which is normally set equal to P_s, P_p, P_l or P_r. $[F/L^2]$
Q_r	flow from pocket or recess. $[L^3/T]$
$q_r = Q_r (12\mu/P_oC^3)$	dimensionless flow from pocket or recess.
R	seal radius. $[L]$
$Re^* = \rho h^3 \nabla p/\mu^2$	local Reynolds number based on pressure-driven flow.
$Re_o^* = \rho C^3 P_o/(R\mu^2)$	refernce Reynolds number based on pressure-driven flow.
t	time. $[T]$
$u = U (12\mu R/C^2 P_o)$	dimensionless circumferential component of fluid velocity.
$v = V (12\mu R/C^2 P_o)$	dimensionless axial component of fluid velocity.
U, V	circumferential and axial fluid velocity components, averaged across the film. $[L/T]$
U_b, U_j	linear velocity of housing and journal surfaces (equal to $R\omega_b$, $R\omega_j$, respectively). $[L/T]$
X, Y, Z	cartesian coordinates. $[L]$
$z = Z/R$	dimensionless axial coordiante.
$\alpha = A (2L/C)$	misalignment ratio about the x-axis.

$\beta = B\,(2L/C)$ misalignment ratio about the y-axis.

ϵ_x, ϵ_y components of rotor eccentricity ratio.

$\epsilon = e/C$ rotor eccentricity ratio.

θ circumferential coordinate. [radians]

$\Lambda_b = 6\mu U_b R/(C^2 P_o)$ dimensionless velocity of housing surface.

$\Lambda_j = 6\mu U_j R/(C^2 P_o)$ dimensionless velocity of rotor surface.

$\Lambda_r = \rho C^6 P_o/(288\,A_o^2 C_d^2 \mu^2)$ coefficient of orifice restriction.

$\Lambda_e = K_e\,(Re_o^* C/288\,R)$ coefficient of pressure drop at inlet to film.

μ fluid dynamic viscosity. [F-S/L^2]

ρ fluid density. [F-T^{2}L^{-4}]

ω_b, ω_j angular velocity of housing and journal surfaces. [rad/T]

$\tau = t\,(C^2 P_o/12\mu R^2)$ dimensionless time.

4-60

5.0 INDUSTRIAL COMPRESSIBLE CYLINDRICAL CODE, GCYL

The program GCYL (acronym for gas lubricated cylindrical) is used for analyzing a variety of seals that can be defined in a cylindrical coordinate reference frame. Figure 5-1 shows solid ring configurations and Figure 5-2 shows typical sectored ring configurations that the program analyzes. The capabilities of the program include the following:

- Varying geometries, as indicated on Figures 5-1 and 5-2.

- Variable or constant grid representation. Maximum grid size is 30 grid points in the axial direction and 74 grid points in the circumferential direction. Figure 5-3 shows a typical grid network. The circumferential parameter is θ, and the axial parameter is Z. The grid points are identified in the axial direction as I and in the circumferential direction as J. The extent of I is 1→M, and the extent of J is 1→N.

- Specified boundary pressures or periodic boundary conditions in the circumferential direction.

- Axial symmetry option

- Four degrees of freedom, x and y translations of rotor origin and angular displacements about the x and y axes through the rotor origin

- Determining load as a function of shaft position or determining shaft position to satisfy a given load.

- External Pressurization (Hydrostatic) of inherently compensated orifices, spot recesses or full recesses.

- Choice of English or SI units

The output of the program includes:

- Clearance distribution

- Pressure distribution

- Leakage along specified flow paths

Self-Energized —
Hydrostatic

Tapered In Flow
Direction

Rayleigh Step in
Direction of Flow

Circumferential
Multilobe

Circumferential
Rayleigh Step
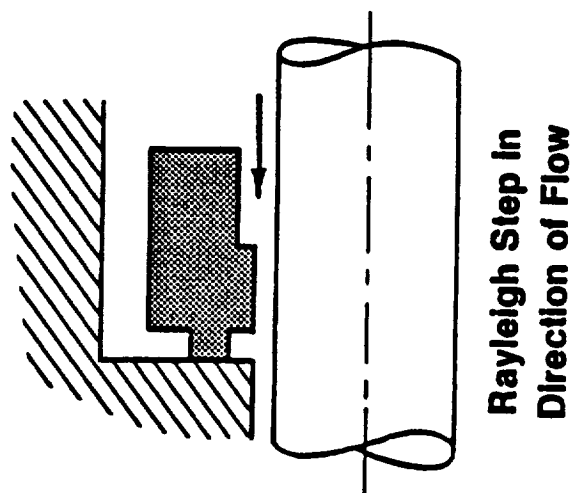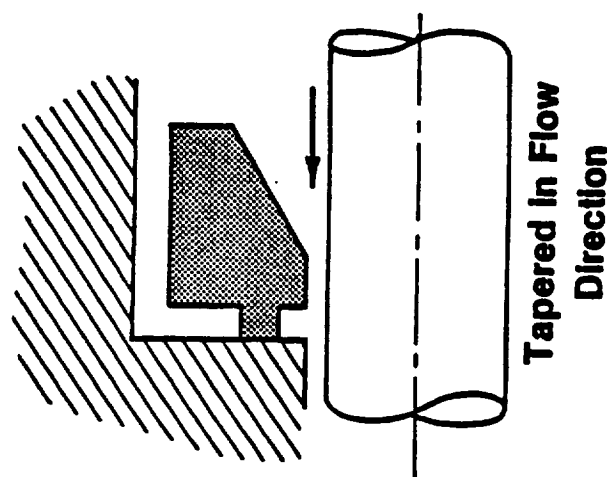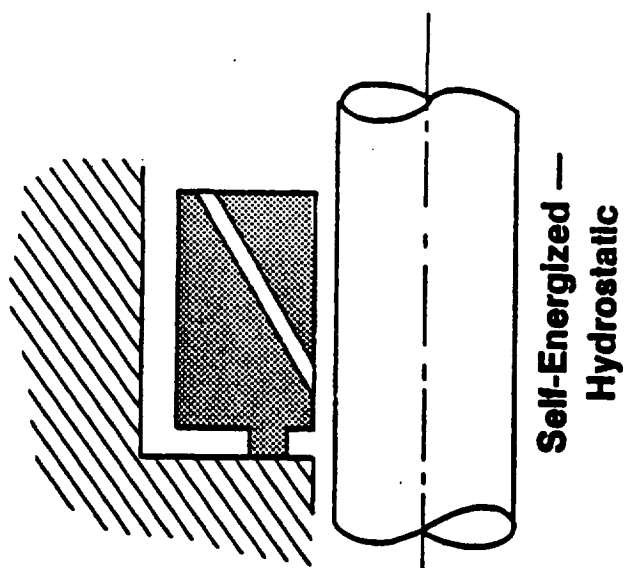
Figure 5-1   Leakage Path Geometries (Floating Ring)

852165
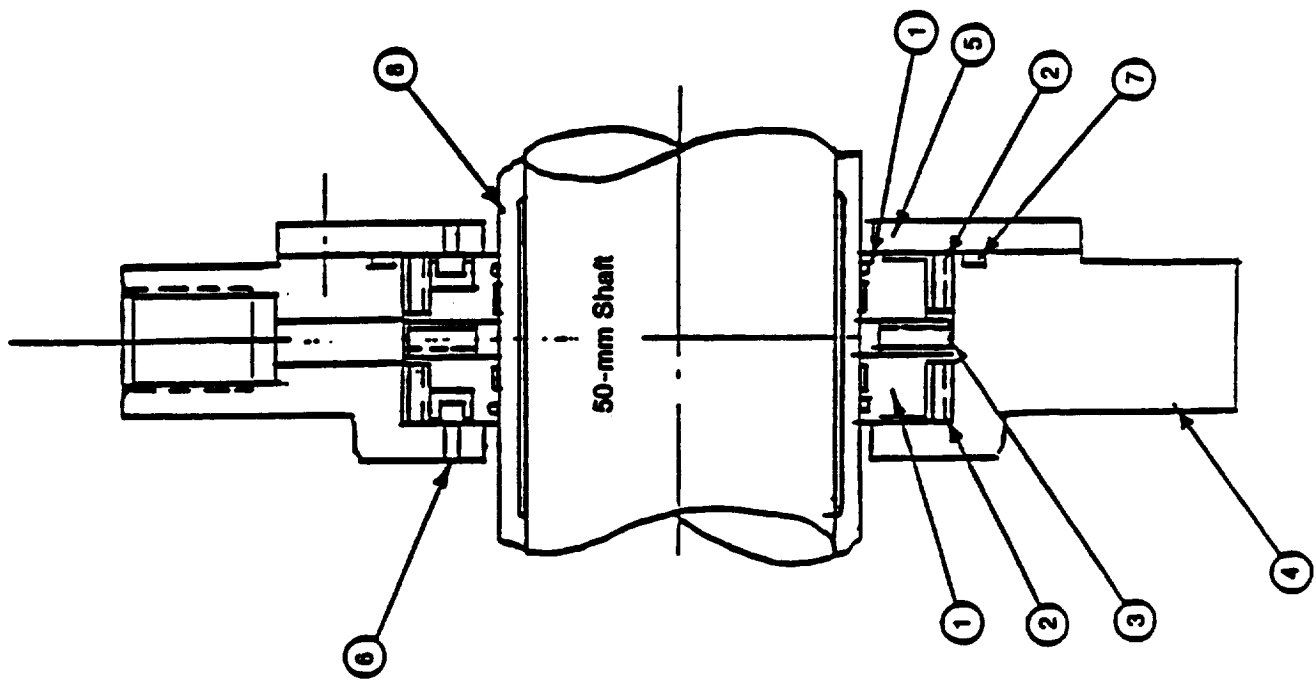
Item	Description	Material
1	Segmented Ring Rayleigh Step	Carbon
2	Spring-Radial	Inconel X-750
3	Spring-Axial	Inconel X-750
4	Housing	Stainless Steel 17-4 PH
5	Cover	Stainless Steel 17-4 PH
6	Stop Pin	Stainless Steel 17-4 PH
7	Seal	Teflon
8	Sleeve	Inconel 718 Hard Chromium Plated
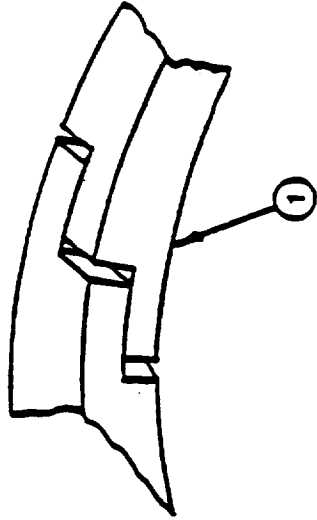
Figure 5-2   Floating Ring Concept with Jointed Segmented Rings

5-3
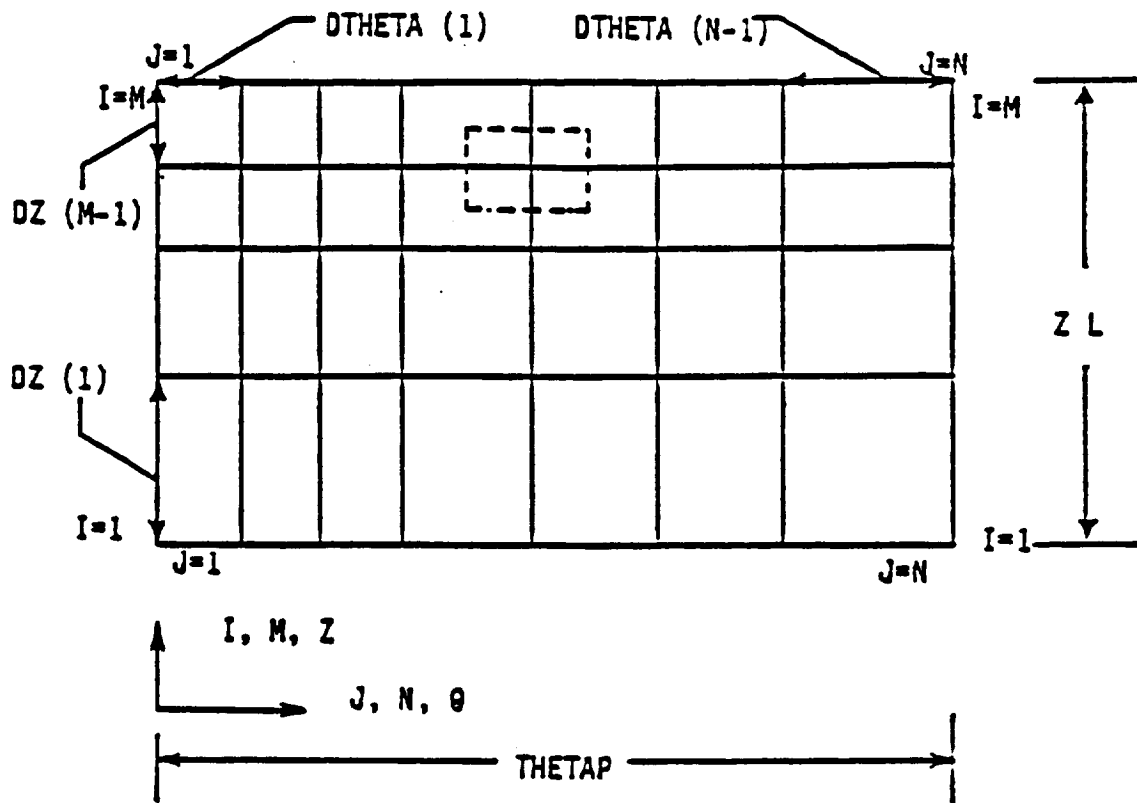
Figure 5-3   Unwrapped Seal Surface

- Load and Load angle

- Righting Moments

- Viscous dissipation

- Cross-coupled, frequency-dependent, stiffness and damping coefficients

- Plotting routines for the pressure and clearance distribution

The program has been written for a PC environment using OS/2 as an operating system. Relatively large dimensions have been utilized which would exceed the memory limitations of a DOS environment. The FORTRAN code however, would be amenable to other systems that employ FORTRAN 77 as long as memory is sufficient.

5.1 THEORETICAL DESCRIPTION AND NUMERICAL METHODS

General Theory

Reynolds' equation for compressible flow for a cylindrical geometry* is as follows:

$$\frac{1}{R^2} \frac{\partial}{\partial \theta} \left(ph^3 \frac{\partial p}{\partial \theta} \right) + \frac{\partial}{\partial z} \left(ph^3 \frac{\partial p}{\partial z} \right) = 6\mu\omega \frac{\partial(ph)}{\partial \theta} \qquad (5-1)$$

$$+ 12\mu \frac{\partial(ph)}{\partial t}$$

The equation is made dimensionless with the following definitions. (Upper case variables are dimensionless).

$$Z = z/R, \quad H = h/C_o, \quad T = t/t_o, \quad P = p/p_o,$$

$$\Lambda = \frac{6\mu\omega R^2}{P_o C_o^2}, \quad t_o = \frac{12\mu R^2}{P_o C_o^2}$$

Substituting the dimensionless variables into Reynolds' equation produces a dimensionless Reynolds' equation.

$$\frac{\partial}{\partial \theta} \left(PH^3 \frac{\partial P}{\partial \theta} \right) + \frac{\partial}{\partial Z} \left(PH^3 \frac{\partial P}{\partial Z} \right) = \Lambda \frac{\partial(PH)}{\partial \theta} + \frac{\partial(PH)}{\partial T} \qquad (5-2)$$

For steady-state solutions, the time dependent term on the right hand side is eliminated except for the computation of spring and damping coefficients.

In the solution methods subsequently described, the Reynolds' equation is not applied directly. The Reynolds' equation represents the divergence of the mass flow at any grid point. The more convenient cell method is to conduct a mass balance directly, and not the divergence of the mass flow at each point.

Formation of Equations for Determining Pressure Distribution

---

*Nomenclature is included in Section 5-5

The general method of solving for the pressure distribution is the cell method[1]**, whereby a flow balance through a cell volume is accomplished. The perimeter of the cell extends halfway between the grid point and its four neighboring points. A typical cell is shown by the dashed lines on Figure 5-4. The principal grid point is at Row i (length direction) and Column j (circumferential direction). For convenience of programming the grid points are numbered for each cell sequentially from 1 to 9 with grid point 5 being the principal point. The corners of the cell boundaries are also numbered from 1 to 4.

Figure 5-5 shows the flow balance through the cell. There are eight flows across the cell boundaries, and there can also be a source (or sink) flow into or out of the cell control volume. The reason eight flows are used in lieu of four is that it permits discontinuous clearance boundaries at grid lines (such as Rayleigh steps) without taking derivatives across a discontinuous boundary.

The net flow through a cell can be expressed as:

$$Q_{12}^{+} \frac{\Delta Z_i}{2} + Q_{12}^{-} \frac{\Delta Z_{i-1}}{2} + Q_{14}^{+} \frac{\Delta \theta_j}{2} + Q_{14}^{-} \frac{\Delta \theta_{j-1}}{2}$$
$$-Q_{34}^{+} \frac{\Delta Z_i}{2} - Q_{34}^{-} \frac{\Delta Z_{i-1}}{2} - Q_{23}^{+} \frac{\Delta \theta_j}{2} - Q_{23}^{-} \frac{\Delta \theta_{j-1}}{2} = Q_{in} \tag{5-3}$$

Q_{12}^{+} means the mass flow per unit length across the plus side of cell boundary 1-2, etc.

The Q's are dimensionless mass flows per unit length, except for Q_{in} which is a dimensionless source inlet flow.

In the θ direction

$$Q = -\bar{P}\bar{H}^3 \frac{\partial P}{\partial \theta} \frac{\Delta Z}{2} + \Lambda \bar{P}\bar{H} \frac{\Delta Z}{2} \tag{5-4}$$

In the length or Z direction

$$Q = -\bar{P}\bar{H}^3 \frac{\partial P}{\partial Z} \frac{\Delta \theta}{2} \tag{5-5}$$

———————————————

**References are identified in Section 5-4
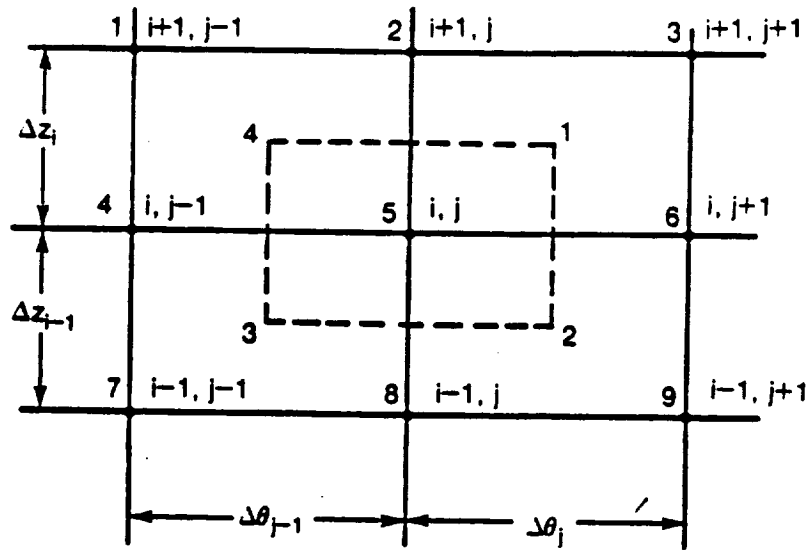
861588

Figure 5-4   Flow-Balance Cell and Associated Grid Network
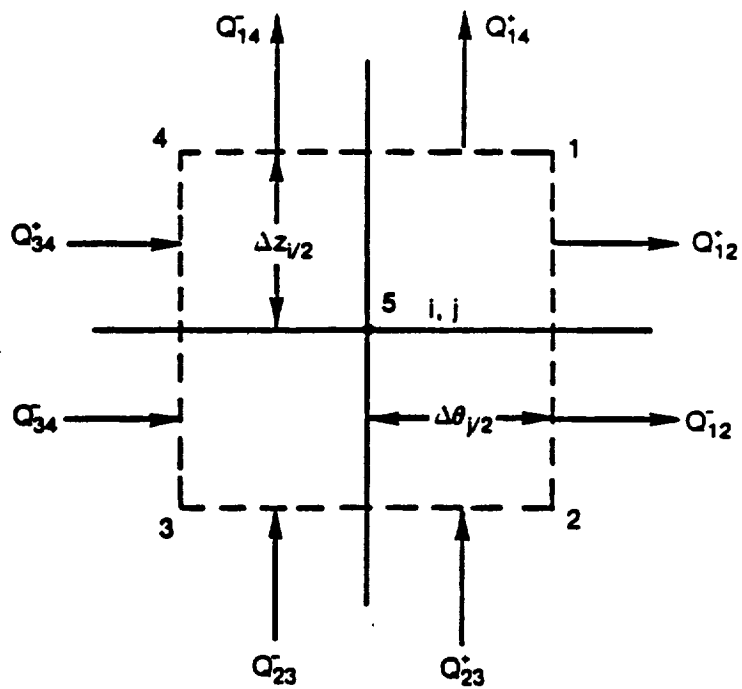
861587

Figure 5-5   Flow-Balance Across Cell

5-8

where Q is defined as

$$Q = \frac{12 \mu G_c T_a \, q}{P_o^2 C_o^3} \qquad (5\text{-}6)$$

(Primed values of P are absolute pressures; unprimed values are gage pressures).

An optional flow can enter the cell from an external source, which can be treated as an inherently compensated orifice, or a conventional orifice restriction. Inherent compensation presumes the orifice area is the surface area of a cylinder circumvented by the hole size and length equal to the clearance under the inlet hole. The conventional orifice area is the area of the hole. The conventional orifice generally discharges into a recess that allows the flow velocity to dissipate into a region of constant pressure. Two types of recesses are permitted; a spot recess which is treated as a source at one grid point, or a recess of finite length in the axial and circumferential directions, which is fed by an inlet orifice.

Pressures are taken as the average pressure across the boundary. For example:

$$P_{12} = \frac{P_{i,j} + P_{i,j+1}}{2} \qquad \text{and} \qquad (5\text{-}7)$$

$$\left.\frac{\partial P}{\partial \theta}\right|_{12} = \frac{P_{i,j+1} - P_{i,j}}{\Delta \theta_j} \qquad (5\text{-}8)$$

etc.

By substituting the pressures and pressure derivatives (equations 5-7 and 5-8) into the mass flow balance equations (equation 5-3 and 5-4), an equation is derived that is a function of the five pressures, P_2, P_4, P_5, P_6 and P_8, and the clearances taken at the cell corner points H_1 -- H_4. Each cell corner point film thickness is computed in the clearance routine by appropriate values of Z and θ and is designated as as HC_i, $i = 1, 4$. For example, HC_1 is the clearance at the cell corner point 1.

An optional flow can enter the cell from an external source, which is treated as an inherently compensated orifice or the usual hole size orifice restriction. Point sources pose numerical instability problems, which are circumvented by applying fine grids surrounding the source points. Flow through the orifice is given as:

$$Q_{in} = OFC \times AO \times P_S' \left\{ \left(\frac{P_R'}{P_S'} \right)^{2/\gamma} \left[1 - \left(\frac{P_R'}{P_S'} \right)^{\frac{\gamma-1}{\gamma}} \right] \right\}^{1/2} \tag{5-9}$$

where,
$$OFC = \frac{12\mu C_d}{P_o C_o^2} \sqrt{\frac{2\gamma G_c T_a}{\gamma - 1}} \tag{5-10}$$

$$A_o = \begin{cases} \pi do H_5 & \text{for Inherent Compensation} \\ \dfrac{\pi do^2}{4} & \text{for orifice compensation} \\ & \text{(spot recess or full recess)} \end{cases} \tag{5-11}$$

$$\text{If } \left(\frac{P_R'}{P_S'} \right) \leq P_{CR} \quad \text{then} \left(\frac{P_R'}{P_S'} \right) = P_{CR} \tag{5-12}$$

$$\text{where } P_{CR} = \left[\frac{2.0}{(\gamma+1)} \right] \left(\frac{\gamma}{\gamma-1} \right) \tag{5-13}$$

$$\text{Also, if } \frac{P_R'}{P_S'} > 1.0, \quad \frac{P_R'}{P_S'} = \frac{1}{P_R'/P_S'} \quad \text{and } P_S' = P_R' \tag{5-14}$$

This condition implies backflow through the orifice.

The primed values indicate absolute pressures (i.e., $P'_R = P_R+1$).

Thus, a system of numerical equations can be derived as a function of five pressures. There is an equation for every grid point.

$$f\ (P_1,\ P_2,\ \ldots\ P_5)\ i,j\ =\ 0 \tag{5-15}$$

The system is non-linear since it is dependent upon multiples of P and its derivatives.

The solution process starts by assuming a pressure distribution, and using Newton-Raphson iteration until the functions f converge to zero within a prespecified truncation error. In equation form, the iteration process is:

$$f_{i,j}^{(old)} + \sum_{k=1}^{5} \frac{\partial f_{i,j}^{(old)}}{\partial P_K} \left(P_K^{(new)} - P_K^{(old)} \right) = 0 \tag{5-16}$$

where the partial derivatives are explicitly determined, e.g.

$$\frac{\partial f_{i,j}}{\partial P_K} = \frac{f(P_1,\ P_2,\ \ldots\ P_K + \epsilon/2 \ldots P_5\ _{i,j}) - f\ (P_1,\ P_2,\ \ldots\ P_K - \epsilon/2,\ \ldots\ P_5)_{i,j}}{\epsilon} \tag{5-17}$$

The actual convergence is not on f, but on $P_K^{(new)} - P_K^{(old)}$, for when the difference vanishes, the condition that f=0 is satisfied.

The Column Method Solution of Newton-Raphson Equations

The column method[2] is used to solve the new pressures in the set of mxn equations defined by equation 5-16. The advantage of the column matrix method is that its inversions are M x M rather than M x N so that its use saves computational time.

The linearized N-R equations may be written in the form:

$$C_j \; P_j + E_j \; P_{j-1} + D_j \; P_{j+1} = R_j \tag{5-18}$$

For each value of j, P_j is a vector containing the jth column of new pressures, R_j is the right hand side column vector and C_j, E_j and D_j are in general tri-diagonal matrices.

Case 1 – Pressure Prescribed at Start and End of Pads

Equations of form 5-18 are written at all points in the grid corresponding to i = 1, 2, →M and j = 2, 3, →N-1 with boundary column vectors P_1 and P_N prescribed. Look for a solution in the form:

$$P_{j-1} = A_j \; P_j + B_j \tag{5-19}$$

Where A_j is an M x M matrix and B_j is a vector. Use equation 5-19 to eliminate P_{j-1} appearing in equation 5-18.

$$(C_j + E_j \; A_j) \; P_j + E_j \; B_j + D_j \; P_{j+1} = R_j \tag{5-20}$$

Solve equation 5-20 for P_j to obtain:

$$P_j = -I_j \; D_j \; P_{j+1} + I_j(R_j - E_j \; B_j) \tag{5-21}$$

Where $I_j = (C_j + E_j A_j)^{-1}$ (M x M matrix)

Set $j = j+1$ in equation 5-19 to obtain

$$P_j = A_{j+1} P_{j+1} + B_{j+1}$$ (5-22)

Compare coefficients in equation 5-21 and 5-22.

$$A_{j+1} = -I_j P_j, \quad B_{j+1} = I_j (R_j - E_j B_j)$$ (5-23)

Set $A_2 = 0$, $B_2 = P_1$

Use equation 5-23 to compute A_3, A_4, $--$, A_N and B_3, B_4 $--$ B_N.

Since P_N is given and all A_j and B_j are computed, we may use equation 5-19 to compute P_{N-1}, P_{N-2}, P_{N-3}, $----$, P_2.

Review of General Procedure for Non-Periodic Boundaries

1) Set $A_2 = 0$
      $B_2 = P_1$

2) Compute A_{j+1}, B_{j+1}
      $A_{j+1} = -I_J D_j$
      $B_{j+1} = I_j (R_j - E_j B_j)$ $j \to 2, N-1$

      where $I_j = (C_j + E_j A_j)^{-1}$

3) Compute P_j
      $P_{j-1} = A_j P_j + B_j$ $j = N, 2$

Case 2 – Column Method for Periodic Boundaries

P_j, B_j, R_j, Z_j are vectors. $N' = N - 1$

5-13

For periodic boundaries, the condition is that $P_1 = P_N$. At the boundary, $j=1$, the general equation is:

$$C_1 P_1 + E_1 P_N' + D_1 P_2 = R_1 \qquad (5-24)$$

At column N', the equation becomes

$$C_{N'} P_{N'} + E_{N'} P_{N'-1} + D_{N'} P_1 = R_{N'} \qquad (5-25)$$

To satisfy the boundary conditions, a solution is assumed of the form:

$$P_{j-1} = A_j P_j + B_j + F_j P_N' \qquad (5-26)$$

$$A_1 = 0, \ B_1 = 0, \ F_1 = \delta \ \text{(Kronocker delta matrix)} \qquad (5-27)$$

Returning to the general equation:

$$C_j P_j + E_j P_{j-1} + D_j P_{j+1} = R_j \qquad (5-28)$$

Substituting for P_{j-1} from equation 5-26, the following results:

$$(C_j + E_j A_j) P_j + E_j B_j + E_j F_j P_N' + D_j P_{j+1} = R_j \qquad (5-29)$$

$$I_j = (C_j + E_j A_j)^{-1} \qquad (5-30)$$

Then,

$$P_j = -I_j D_j P_{j+1} + I_j (R_j - E_j B_j) - I_j E_j F_j P_N' \qquad (5-31)$$

From equation 5-26:

$$P_j = A_{j+1} P_{j+1} + B_{j+1} + F_{j+1} P_N' \qquad (5-32)$$

Comparing equations 5-31 and 5-32:

$$A_{j+1} = -I_j D_j, \ B_{j+1} = I_j (R_j - E_j B_j), \ F_{j+1} = -I_j E_j F_j \quad j=1, 2, \text{--}, N-1 \qquad (5-33)$$

For $P_N = P_1$, we obtain from equation 5-26:

$$P_N' = A_{N'+1} P_1 + B_{N'+1} + F_{N'+1} P_N' \qquad (5\text{-}34)$$

After rearranging:

$$P_N' = (\delta - F_{N'+1})^{-1} (A_{N'+1} P_1 + B_{N'+1}) \qquad (5\text{-}35)$$

or $\qquad P_N' = Y_N' P_1 + Z_N' \qquad\qquad\qquad\qquad (5\text{-}36)$

where

$$Y_N' = (\delta - F_{N'+1})^{-1} A_{N'+1}, \; Z_N' = (\delta - F_{N'+1})^{-1} B_{N'+1} \quad (5\text{-}37)$$

Substituting equation 5-36 into 5-26 we obtain:

$$P_{N'-1} = A_{N'} (Y_N' P_1 + Z_N') + B_{N'} + F_{N'} (Y_N' P_1 + Z_N')$$

$$= (A_{N'} Y_N' + F_{N'} Y_N') P_1 + A_{N'} Z_N' + B_{N'} + F_{N'} Z_N' \qquad (5\text{-}38)$$

$$= Y_{N'-1} P_1 + Z_{N'-1}$$

where

$$Y_{N'-1} = A_{N'} Y_N' + F_{N'} Y_N', \; Z_{N'-1} = A_{N'} Z_N' + B_{N'} + F_{N'} Z_N' \qquad (5\text{-}39)$$

Similarly,

$$P_{N'-2} = A_{N'-1} (Y_{N'-1} P_1 + Z_{N'-1}) + B_{N'-1} + F_{N'-1} (Y_N' P_1 + Z_N') \quad (5\text{-}40)$$

$$= (A_{N'-1} Y_{N'-1} + F_{N'-1} Y_N') P_1 + A_{N'-1} Z_{N'-1} + B_{N'-1} + F_{N'-1} Z_N'$$

$$\qquad\qquad\qquad\qquad\qquad (5\text{-}41)$$

$$= Y_{N'-2} P_1 + Z_{N'-2}$$

$$Y_{j-1} = A_j Y_j + F_j Y_N'$$
$$Z_{j-1} = A_j Z_j + B_j + F_j Z_N' \qquad\qquad (5\text{-}42)$$

Therefore, in general:

$$P_{j-1} = Y_{j-1} P_1 + Z_{j-1} \text{ or } P_j = Y_j P_1 + Z_j \tag{5-43}$$

$$P_1 = (\delta - Y_1)^{-1} Z_1 \tag{5-44}$$

Review of General Procedure for Joined or Periodic Boundaries

1) Compute A_{j+1}, B_{j+1}, F_{j+1}

$$A_{j+1} = -I_j D_j$$
$$B_{j+1} = I_j (R_j - E_j B_j) \qquad j=1, N-1$$
$$F_{j+1} = -I_j E_j F_j$$

$$A_1 = 0 \qquad I_j = (C_j + E_j A_j)^{-1}$$
$$B_1 = 0$$
$$F_1 = \delta$$

2) Compute $Y_N{}'$, $Z_N{}'$

$$Y_N{}' = (\delta - F_N)^{-1} A_N$$
$$Z_N{}' = (\delta - F_N)^{-1} B_N$$

3) Compute

$$Y_{j-1} = A_j Y_j + F_j Y_N{}' \qquad j = N' \to 2$$
$$Z_{j-1} = A_j Z_j + B_j + F_j Z_N{}'$$

4) Compute $P_1 = (\delta - Y_1)^{-1} Z_1$

5) Compute $P_j = Y_j P_1 + Z_j \qquad j = 2 \to N'$

The coefficient matrices C_j, E_j and D_j, and the right hand side vector R_j, are easily formulated. C_j contains all the coefficients multiplied by P_j. By examining equation 5-16, it is seen that for any row i and column j that values of C are:

$$C_{i, i-1, j} = \frac{\partial f_5}{\partial P_8}$$

$$C_{i, i, j} = \frac{\partial f_5}{\partial P_5} \tag{5-45}$$

$$C_{i, i+1, j} = \frac{\partial f_5}{\partial P_2}$$

Similarly the coefficient matrix E_j contains the elements:

$$E_{i, i, j} = \frac{\partial f_5}{\partial P_4} \tag{5-46}$$

and

$$D_{i, i, j} = \frac{\partial f_5}{\partial P_6} \tag{5-47}$$

R_j contains all elements not multiplied by the pressure

$$R_j = -f_{1j}^{(old)} + \sum_1^5 \frac{\partial f_{1j}}{\partial P_K} P_K^{(old)} \tag{5-48}$$

Separate subroutines are used depending upon the pressure boundary conditions. The subroutine COLP implements the column method for prescribed boundary conditions while COLJ does it for periodic or joined boundaries. The subroutine COEFC forms the C matrix coefficients while COEFF forms the coefficient matrices and right hand side vector D, E, R respectively.

Film Thickness Distribution (see Figure 5-6) Eccentricity and Misalignment

In vector format, the clearance due to eccentricity and misalignment at any angle θ and at distance z' from the mid-plane is:

$$\bar{h} = \left(C_o \bar{e}_r - e_x \hat{i} - e_y \hat{j} - \alpha \hat{i} \times z' \hat{k} - \beta \hat{j} \times z' \hat{k} \right) \cdot \hat{e}_r \tag{5-49}$$

$$h = C_o - e_x \cos\theta - e_y \sin\theta + \alpha z' \sin\theta - \beta z' \cos\theta$$

$$= C_o - (e_x + \beta z') \cos\theta - (e_y - \alpha z') \sin\theta \tag{5-50}$$
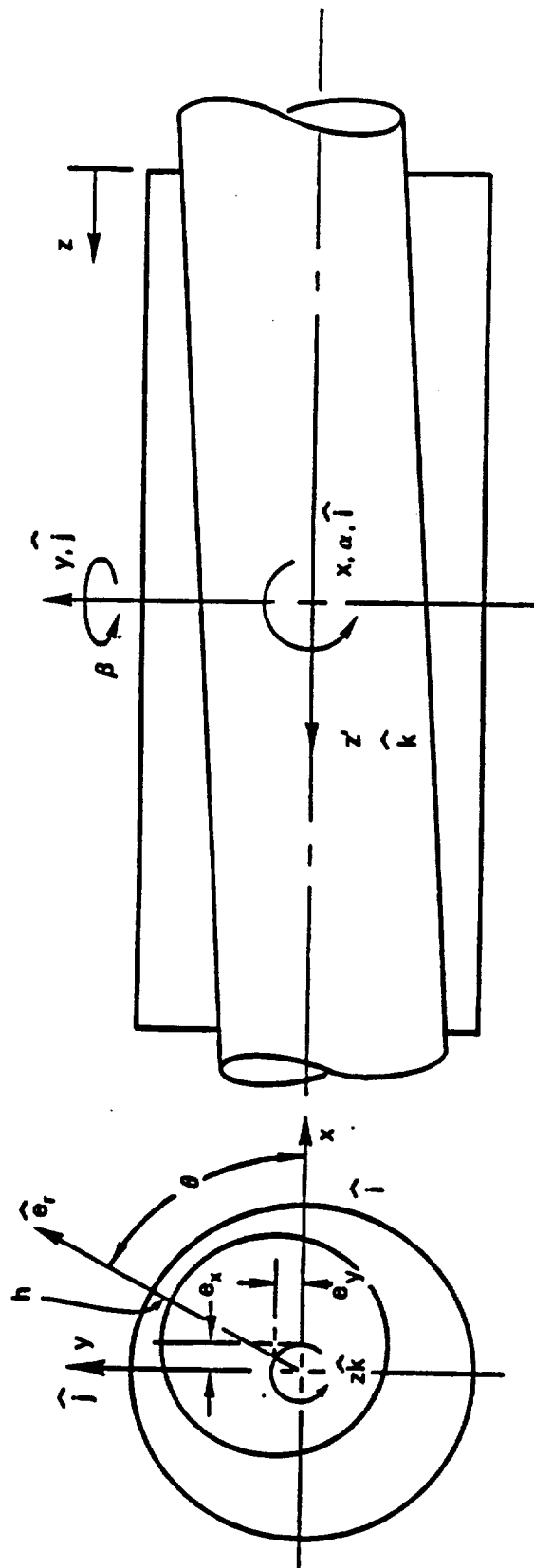
Figure 5-6   Film Thickness Parameters

Using dimensionless variables, equation (5-50) becomes:

$$H = 1 - \left(\varepsilon_x + \beta \frac{(Z - L/2)R}{C_o} \right) \cos\theta$$

$$- \left(\varepsilon_y - \alpha \frac{(Z-L/2)R}{C_o} \right) \sin\theta \qquad (5\text{-}51)$$

which is set equal to:

$$H = 1 - (\varepsilon_x + \varepsilon_\beta) \cos\theta - (\varepsilon_y + \varepsilon_\alpha) \sin\theta \qquad (5\text{-}52)$$

where

$$\varepsilon_\beta = \beta \frac{(Z - L/2)R}{C_o}$$

$$\varepsilon_\alpha = \alpha \frac{(Z - L/2)R}{C_o} \qquad (5\text{-}53)$$

Preloaded Seals

Preloaded seals (see Figure 5-7) can be modeled by adding an additional eccentricity in the x and y directions.

$$\varepsilon_{PR}^{x} = \varepsilon_{PR} \cos\theta_p$$

$$\varepsilon_{PR}^{y} = \varepsilon_{PR} \sin\theta_p \qquad (5\text{-}54)$$

where

$$\varepsilon_{PR}^{x} = \text{x eccentricity due to preload}$$

$$\varepsilon_{PR}^{y} = \text{y eccentricity due to preload}$$

$$\theta_p = \text{preload angle}$$

Rayleigh Step

The grid network for the Rayleigh step is shown on Figure 5-8. The boundaries of the step are defined by the lower left and upper right corners of the depressed region. Interior grid points include the step height in the clearance distribution.
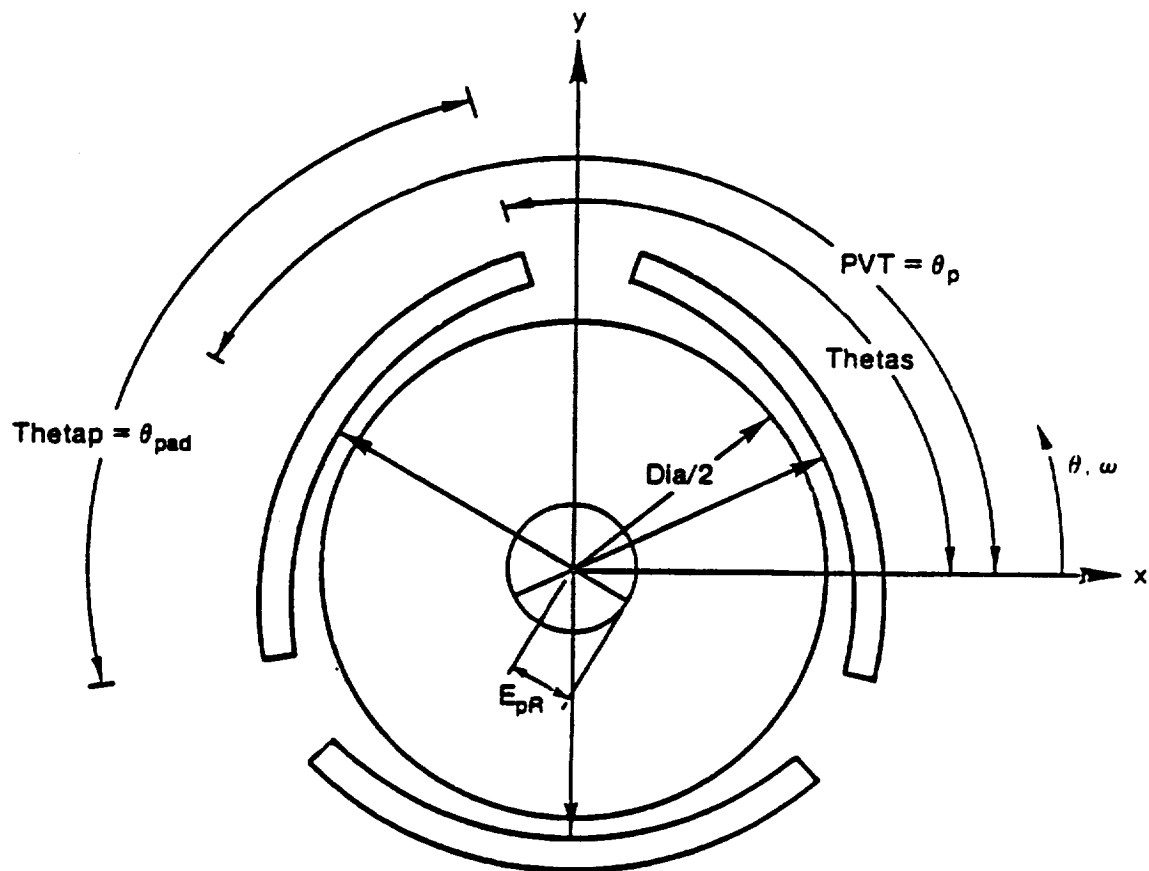
Keyword	Variable	Description
START	THETAS	Pad Start Angle
PADANGLE	THETAP	Pad Angle
PIVOT	PVT	Pivot Angle
PRELOAD	EPR	Offset/Clearance

Figure 5-7   Preloaded Seal

861601

M, 1   M, N

I_2, J_2

A   A

Step Region

I_1, J_1

1, 1   1, N

Step Height
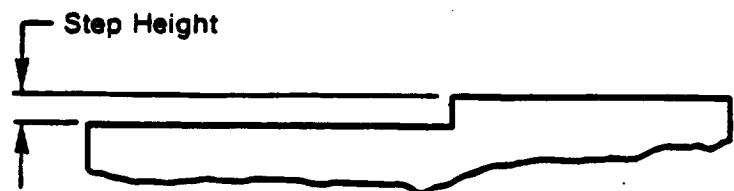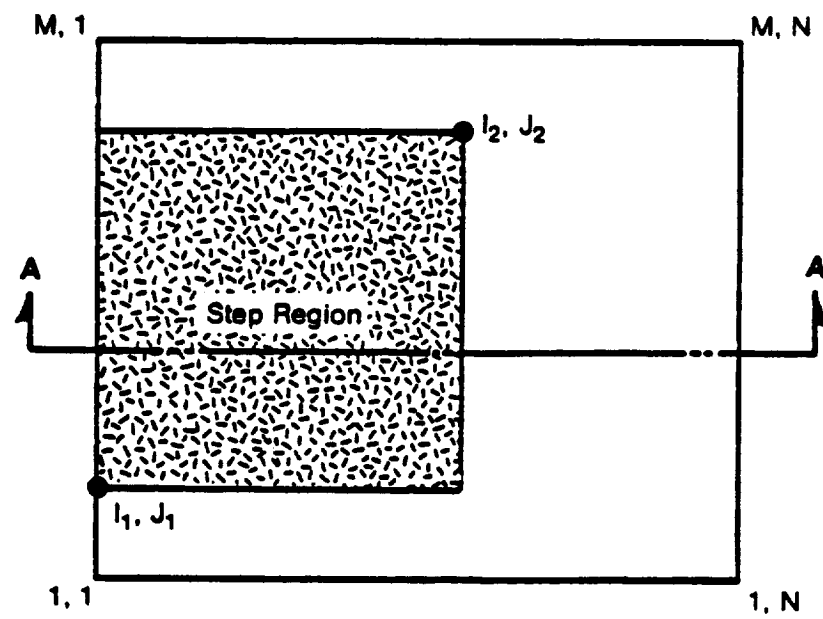
Figure 5-8   Rayleigh-Step

Axial Taper

An axial taper is indicated as Figure 5-9. If $Z \geq Z_t$ then

$$H = H + \delta(Z-Z_t) \tag{5-55}$$
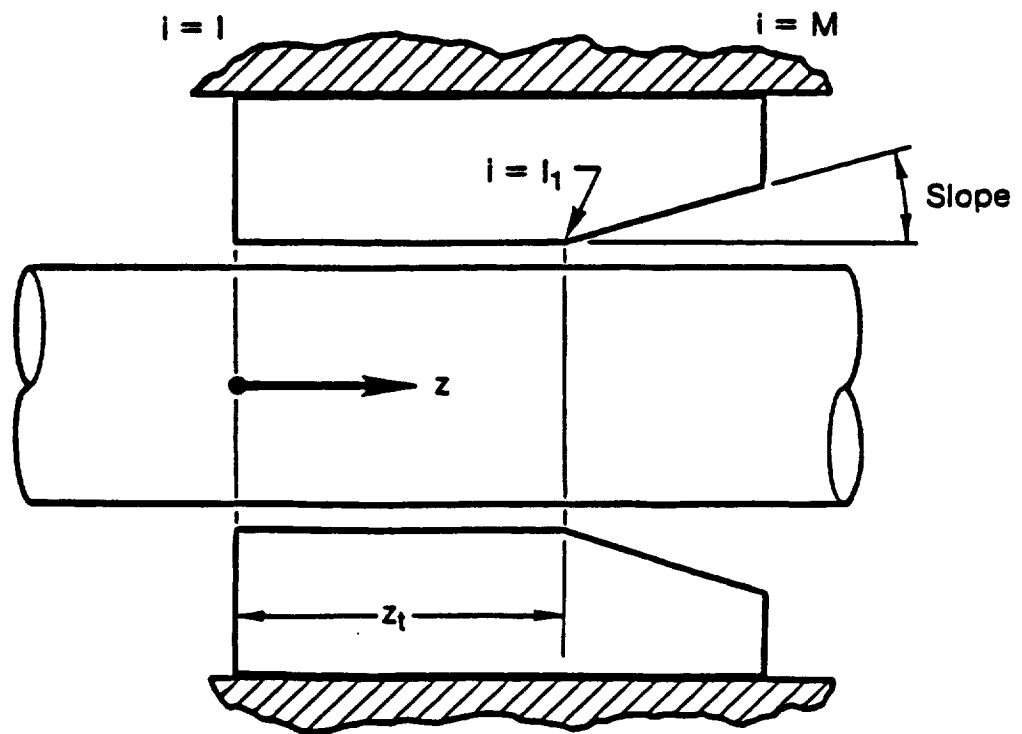
Figure 5-9 Axial Taper

86257

Power Loss (Torque)

Power loss is obtained by integrating the viscous shear forces across the film.

From Figure 5-10, a force balance on an element produces:

$$\frac{\partial p}{\partial x} = \frac{\partial \tau}{\partial z} \quad , \tag{5-56}$$

but

$$\tau = \mu \frac{\partial U}{\partial z} \tag{5-57}$$

Therefore,

$$\frac{\partial p}{\partial x} = \mu \frac{\partial U^2}{\partial z^2} \tag{5-58}$$

Integrating,

$$\frac{\partial U}{\partial z} = \frac{1}{\mu} \frac{\partial p}{\partial x} \ z + C_1 \tag{5-59}$$

$$U = \frac{1}{\mu} \frac{\partial p}{\partial x} \ \frac{z^2}{2} + C_1 z + C_2 \tag{5-60}$$

The boundary conditions are:

$$U = 0 \quad z = 0 \quad \therefore \quad C_2 = 0$$

$$\tag{5-61}$$

$$U = U \text{ when } z = h$$

Substituting:

$$U = \frac{1}{\mu} \frac{\partial p}{\partial x} \ \frac{h^2}{2} + C_1 h \tag{5-62}$$

5-24
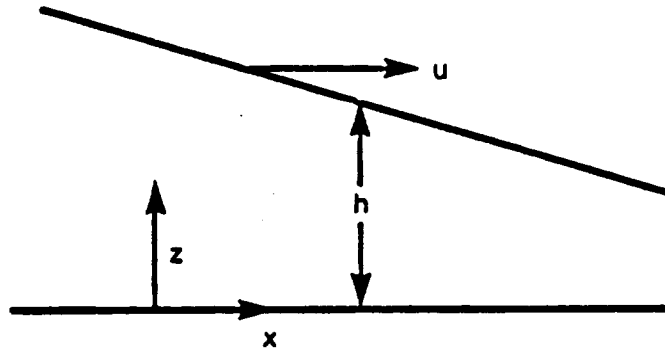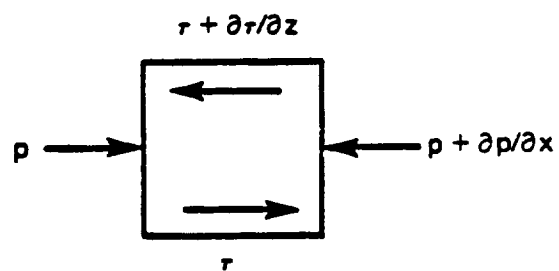
861595

861594

Figure 5-10 Viscous Power Loss

Therefore,

$$C_1 = U/h - \frac{1}{\mu} \frac{\partial p}{\partial x} \ h/2 \tag{5-63}$$

and

$$U = \frac{1}{\mu} \frac{\partial p}{\partial x} \left[\frac{z^2}{2} - \frac{h}{2} z \right] + \frac{U}{h} z \tag{5-64}$$

$$\frac{\partial u}{\partial z} = \frac{1}{\mu} \frac{\partial p}{\partial x} \left[z - \frac{h}{2} \right] + \frac{U}{h} \tag{5-65}$$

$$\tau = \mu \frac{\partial u}{\partial z} = \frac{\partial p}{\partial x} \left[z - \frac{h}{2} \right] + \frac{U}{h} \mu \tag{5-66}$$

$$\tau \ (\text{at } z=h) = \frac{\partial p}{\partial x} \ \frac{h}{2} + \mu \frac{U}{h} \tag{5-67}$$

$$F_f = \text{friction force} = \iint \tau dA$$

$$= \iint \left[\frac{\partial P}{R \partial \theta} \ \frac{h}{2} + \mu \frac{R\omega}{h} \right] R d\theta dz$$

$$= \iint \left[\frac{P_o C_o}{2R} H \frac{\partial P}{\partial \theta} + \frac{\mu}{C_o} \frac{R\omega}{H} \right] R^2 d\theta dZ \tag{5-68}$$

$$= \iint \left[P_o CR \frac{H}{2} \frac{\partial P}{\partial \theta} + \frac{\mu \ \omega R^3}{C_o H} \right] d\theta dZ$$

$$FF = \iint \left[P_o C_o \ \frac{H}{2} \ \frac{\partial P}{\partial \theta} + \frac{\Lambda C_o P_o}{6} \ R \frac{1}{H} \right] d\theta dZ \tag{5-69}$$

$$FF = \iint \left[\frac{H}{2} \ \frac{\partial P}{\partial \theta} + \frac{\Lambda}{6H} \right] d\theta dZ$$

$$TF = \iint \left[\frac{H}{2} \ \frac{\partial P}{\partial \theta} + \frac{\Lambda}{6H} \right] d\theta dZ \tag{5-70}$$

Computation of Seal Flows

The program computes the flow across specified axial and circumferential grid lines. A total of four grid lines can be prespecified. The subroutine FLOCIR determines flow across a circumferential line and the subroutine FLOAXL computes the flow across an axial grid line.

Circumferential Flow Line (see Figure 5-11)

There are three types of points to consider. A point on a grid boundary $J = 1$ or $J = N$, and an interior point. Also, a flow line on $I = M$ requires special consideration. For each point, a flow balance is accomplished through the cell surrounding the point as depicted on Figure 5-11. Consider an interior grid point on an interior grid line ($I = M$).

$$Q_C(I,J) = Q_{14}^- + Q_{14}^+ + Q_{12}^+ - Q_{34}^+ \tag{5-71}$$

where

$$Q_{12}^+ = \left(\left(H_1^3 \frac{\partial P}{\partial \theta} \right)_{12} P_{12} + \Lambda\, H_1\, P_{12} \right) DZ_i / Z \tag{5-72}$$

$$\left. \frac{\partial P}{\partial \theta} \right|_{12} = \left(P_{i,j+1} - P_{ij} \right) / \Delta \theta_j \tag{5-73}$$

$$P_{12} = \left(P_{ij} + P_{i,j+1} \right) / 2.0 \tag{5-74}$$

The remaining flow components are similarly computed and $Q_C(I,J)$ determined.

At $J = 1$, $\left. \frac{\partial P}{\partial \theta} \right|_{34}$ is computed by forward difference and is equal to $\left. \frac{\partial P}{\partial \theta} \right|_{12}$. The pressure $P_{34}^+ = P_{12}^+$.

The clearance H_4 is not a regular grid point clearance and thus is not included in the grid clearance array. H_4 is computed as the average of H_{ij} and $H_{i+1,j}$.

The grid line mass flows are accumulated to obtain the total flow across the grid line.
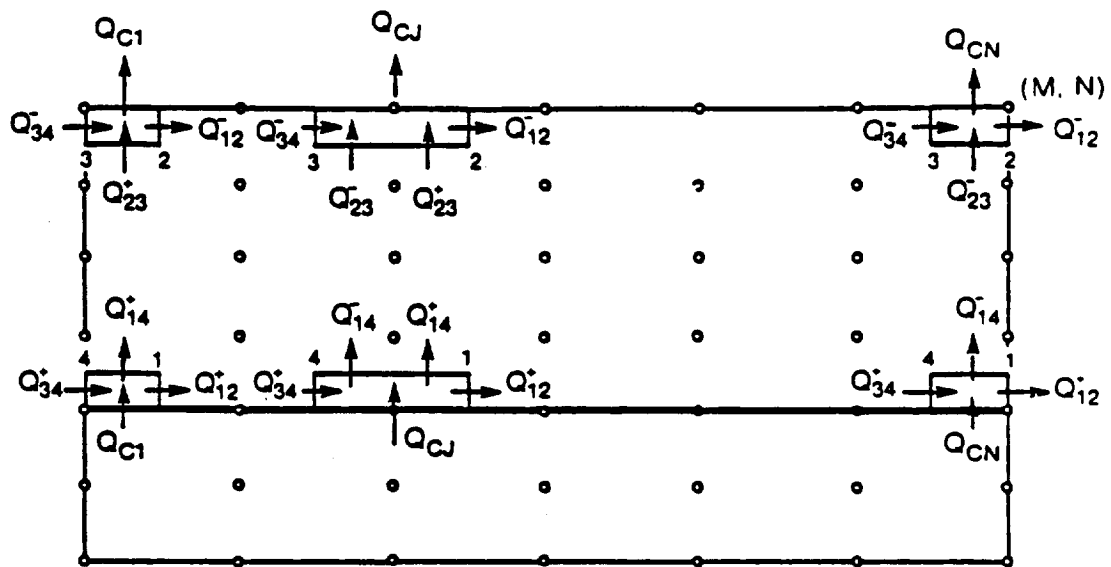
Figure 5-11 Flow Across Circumferential Line

Similar procedures are employed for computing flows across axial lines (see Figure 5-12).
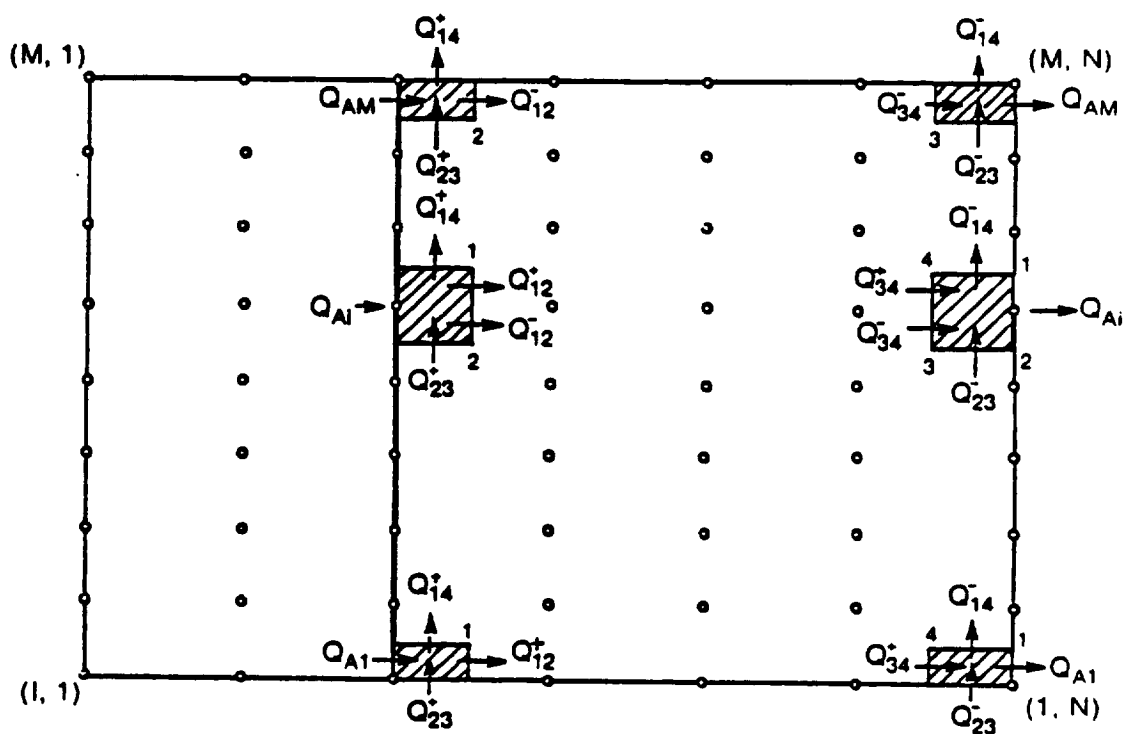
Figure 5-12 Flow Across Axial Line

861602

FREQUENCY DEPENDENT SPRING AND DAMPING COEFFICIENTS

Discretization has been carried out with the use of the cell method [1], which involves a flow balance about each grid point.

$$\int \nabla \cdot \vec{Q} \, dA = \oint \vec{Q} \cdot \vec{n} \, dS = -\frac{\partial}{\partial T} \int (1+P) \, H dA \qquad (5\text{-}75)$$

where $\vec{Q}$ — the mass flow vector per unit length.

The equality of the first two terms comes from the divergence theorem.

In numerical format the right hand side becomes

$$-\frac{\partial}{\partial T}[(1+P_{ij}) \, H_{ij}A_{ij}] \qquad (5\text{-}76)$$

where,

$$A_{ij} = \frac{1}{4} (\Delta\theta_j + \Delta\theta_{j-1})(\Delta Z_i + \Delta Z_{i-1}) \qquad (5\text{-}77)$$

Generally, a small perturbation analysis is used for determining frequency dependent spring and damping coefficients and solving the complete equation (5-75). A small perturbation analysis, however, is generally limited to concentric operation and produces complex expressions for the perturbation coefficients. Identical results can be achieved by direct numerical perturbation of the difference equations used in the column matrix solution approach. This method, which is described below, avoids algebraic error in determining the perturbation coefficients and may be used in complex situations where analytical determination of the perturbation coefficients is not feasible.

After desired convergence of the Newton-Raphson process has been achieved under steady (unperturbed) conditions, the resulting steady state pressure vectors are denoted as $\{\hat{P}\}$ and the coefficient matrices as $[\hat{C}^j]$, etc. and as before the steady state equation becomes:

$$[\hat{C}^j]\{\hat{P}_j\} + [\hat{E}^j]\{\hat{P}_{j-1}\} + [\hat{D}^j]\{\hat{P}_{j+1}\} = \{\hat{R}^j\} \qquad (5\text{-}78)$$

The eccentricity components can be perturbed individually by an amount η, and the matrix $[\hat{C}^j]$ recalculated at the new film thickness (but old pressure

distribution, $\hat{P}$); then subtract $[\hat{C}^J]$ at the old film thickness and divide the difference by η to numerically obtain the partial derivative of $[\hat{C}^J]$ with respect to the eccentricity perturbation. This partial derivative will be denoted by $[\hat{C}^{J,k}]$. Thus,

$$[\hat{C}^{J,k}] = \frac{[\hat{C}^J]|_{\epsilon_k+\eta} - [\hat{C}^J]|_{\epsilon_k}}{\eta} \tag{5-79}$$

The matrices $[\hat{E}^{J,k}]$, $[\hat{D}^{J,k}]$ and $\{\hat{R}^{J,k}\}$ are obtained in a similar manner. Equation (5-78) may now formally be differentiated with respect to ϵ_k to obtain the expression:

$$[\hat{C}^J]\{\hat{P}_j^k\} + [\hat{E}^J]\{\hat{P}_{j-1}^k\} + [\hat{D}^J]\{\hat{P}_{j+1}^k\} = \{\hat{R}^{J,k}\} - [\hat{C}^{J,k}]\{\hat{P}_j\} - [\hat{E}^{J,k}]\{\hat{P}_{j-1}\} - [\hat{D}^{J,k}]\{\hat{P}_{j+1}\}$$

$$\tag{5-80}$$

where $\{\hat{P}^k_j\} = \partial\{\hat{P}_j\}/\partial\epsilon_k$ is the zero frequency stiffness pressure. This expression does not yet contain the time dependent terms found on the right hand side of equation (5-75). It is assumed that a sinusoidal disturbance is applied to the shaft, such that the clearance and pressure derivatives are affected as follows:

$$H = e^{i\sigma t} \; ; \; \hat{P}_j^k = P_j^k e^{i\sigma t} \tag{5-81}$$

To complete the process the right hand side of equation (5-75) is differentiated with respect to ϵ_k and the results added to the right hand side of equation (5-80) with $\partial/\partial t$ replaced by $i\sigma$. The terms to be added to the right hand side of equation (5-80) in this manner are $-i\sigma[\bar{C}^J]\{\hat{P}_j^{,k}\} - i\sigma\{\bar{R}^{J,k}\}$ where $[\bar{C}^J]$ are diagonal matrices whose components are

$$\bar{C}^J_{ii} = H_{ij}A_{ij} \tag{5-82}$$

Because a cell can have clearance discontinuities, such as a step, it is advantageous to partition the cell into 4 components as indicated on Figure 5-2, and then sum the components to obtain $[\bar{C}^J]$. Thus equation (5-82) becomes:

$$\bar{C}^J_{ii} = HC_1A_1 + HC_2A_2 + HC_3A_3 + HC_4A_4 \tag{5-83}$$

where; HC_1 is the clearance at the corner point 1 of the cell and

$$A_1 = \frac{(\Delta \theta_j)(\Delta Z_i)}{4}$$

$$A_2 = \frac{(\Delta \theta_j)(\Delta Z_{i-1})}{4} \; ; \; etc. \tag{5-84}$$

and $\{\bar{R}^{j,k}\}$ are column vectors whose components are

$$\bar{R}_i^{j,k} = A_{ij} \frac{\partial H_{ij}}{\partial \epsilon_k}(1 + P_{ij}) \tag{5-85}$$

By combining terms, the final set of linear difference equations for the complex stiffness pressure derivatives $\{P'^k_j\}$ are obtained

$$[C^{*j}]\{P_j^{,k}\} + [\hat{E}^j]\{P_{j-1}^{,k}\} + [\hat{D}^j]\{P_{j+1}^{,k}\} = \{R^{j,k}\} - [\hat{C}^{j,k}]\{\hat{P}_j\} - [\hat{E}^{j,k}]\{\hat{P}_{j-1}\} - [\hat{D}^{j,k}]\{\hat{P}_{j+1}\}$$

$$\tag{5-86}$$

where,

$$[C^{*j}] = [\hat{C}^j] + i\sigma[\overline{C}^j] \; ; \quad \{R^{j,k}\} = \{\hat{R}^{j,k}\} - i\sigma\{\overline{R}^{j,k}\} \tag{5-87}$$

The system of equations given by equation (5-86) is solved by the column method in a directly analogous manner to that used in solving the steady state equation. The principal difference is that all the matrix operations are performed using complex arithmetic. Integration of the real part of the pressure derivatives yields the stiffness while the complex parts when integrated and divided by σ yields the damping.

5.2 SAMPLE PROBLEMS

5.2.1 Rayleigh-Step Seal

The first sample problem is a four pad Rayleigh-step seal (refer to Figure 5-8).
The geometry and operating conditions are as follows:

- Number of pads = 4

- OPTION = 1, which means the position of the seal will be pre-specified.

- Seal length = 3.852 in. and the symmetry option will be used.

- Variable grid will be used in the axial and circumferential directions.
Since symmetry has been applied in the axial direction, the variable grid
length equals half the actual length, and is equal to 1.926 in.

- The grid will be made finer at the step boundaries where sharp pressure
gradients are expected to occur.

- Seal diameter = 1.9685 in.

- The step height is 0.00165 in. deep and is located at the leading edge
of the pad, 5 degrees from the x axis and the lower left corner of the
step is 0.655 in from the inside radius. The end of the step is 70.6
degrees from the x axis, and since symmetry has been invoked the axial end
of the step as represented on the grid is 1.926 in from the inlet end, or
at the end of the grid.

- The specific heat ratio of the lubricant is 1.4.

- The gas constant is 250,000 $in^2/(s^2\text{-}^{\circ}R)$

- The absolute temperature is 530°R

- The absolute viscosity is 3.0 x 10^{-9} lb-s/in^2

- The eccentricity ratio = 0.2

- The eccentricity angle is 270°

- The shaft speed is 70,000 rpm

● The reference pressure is 200 psig

● The boundary pressures are all 0 psig, or 200 psia.

Results of the problem are indicated on Table 5-1.

Figures 5-13 and 5-14 show the clearance distribution and the pressure distribution produced by the plotting programs. These plots clearly show the highly loaded pad, which is pad number 3 (highest pressure level and lowest film thickness level).

TABLE 5-1

Summary of Results

Sample Problem 1

```
-JOURNAL & LOAD POSITION
   ECCENTRICITY              =        .40000
   ECCENTRICITY ANGLE        =       -90.00 DEG
   MINIMUM FILM              =        .0006015 IN
   LOAD                      =     27.54    LB
   LOAD ANGLE                =        61.44 DEG

   POWER LOSS                =     .4555    HP

   LEAKAGE AT I = 1          = -.44783E-03 LB/S
```

Figure 5-13 Rayleigh Step Seal - Clearance Distribution

GCYL

SAMPLE CASE 1: RAYLEIGH STEP SEAL

DIAMETER = 1.969 IN

LENGTH = 3.852 IN

CLEARANCE = .001000 IN

PRESSURE DISTRIBUTION

SPEED = 70000.00 RPM

.174E+02

3.92

.00 5

92

180

267

355

ANGULAR DEGREES
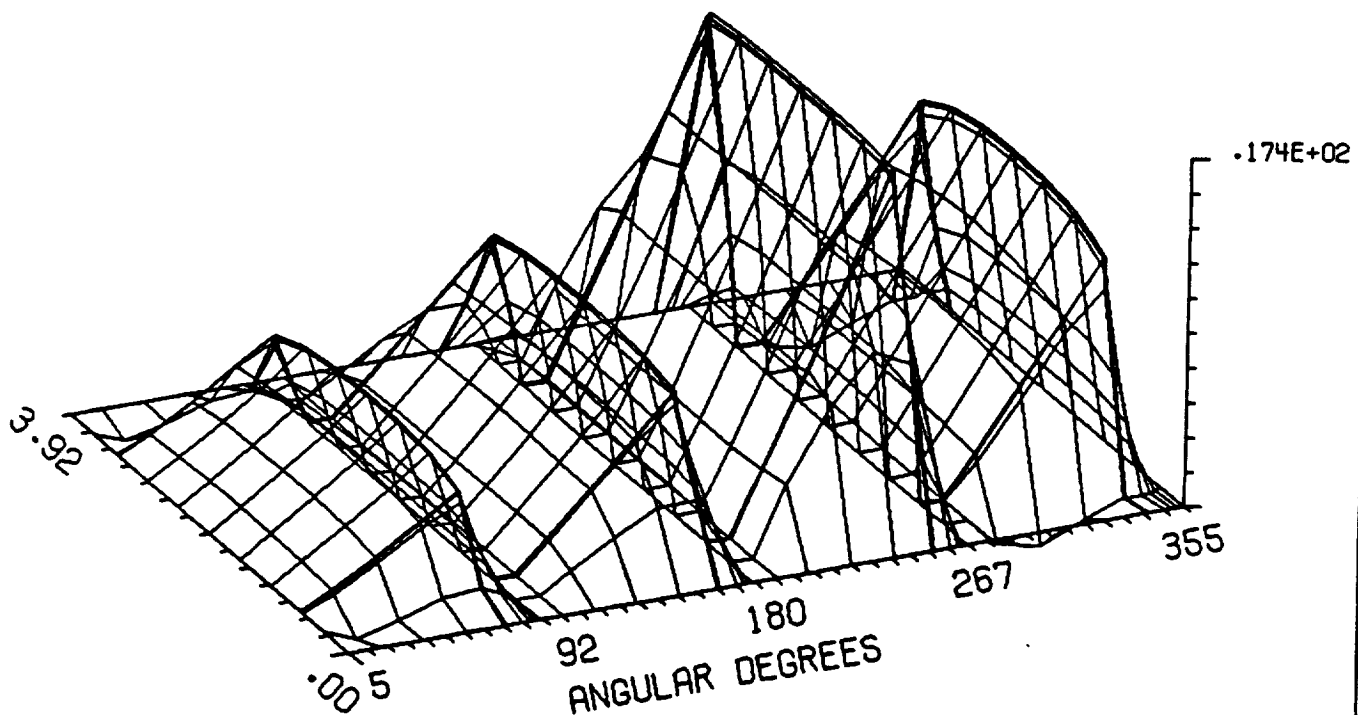
Figure 5-14   Rayleigh Step Seal Pressure Distribution

5.2.2 Sample Problem 2 - Non-grooved Lobe Seal

The non-grooved lobe seal is characterized by offset lobes that are joined at their apexes in a continuous fashion as opposed to a lobe seal where the lobes are separated by axial grooves. Such a seal is depicted on Figure 5-15; it would be manufactured by a broaching process. To analyze this type of seal with the GCYL code the key word SECTOR must be invoked followed by the number of sectors, the lobe preload and preload position within the lobe (see Figure 5-7 for definition of preload). For this example, a lobe hydrodynamic geometry was combined with a external pressurization through source points at the midplane of the seal. The geometry and operating conditions are as follows:

- Seal Diameter - 2.25 in.

- Seal Length - 1.625 in.

- Seal reference clearance - 0.0005 in. The reference clearance is the clearance prior to preload.

- Number of pads - 1. A sectored seal is always considered as a continuous seal although discontinuities exist in the clearance distribution. Thus, the number of pads are always unity and the JOINED option is always applied.

- The preload on each lobe is 0.5 which means at the pivot position the lobe is eccentric toward the shaft one half of the reference clearance (see Figure 5-7).

- The pivot angle of the first sector is 150° from the x axis, and since the first lobe is 90° from the x axis the pivot position is located at the mid angle of each lobe.

- The viscosity of the gas is 3×10^{-9} lb-s/in^2

- The gas constant is 2.5×10^5 in^2/(s^2-°R)

- The ambient temperature is 510°R

- The total number of orifices is 27, 9 in each sector, located at the midplane of each sector. One orifice is located at each interior grid point at the mid plane of the bearing.
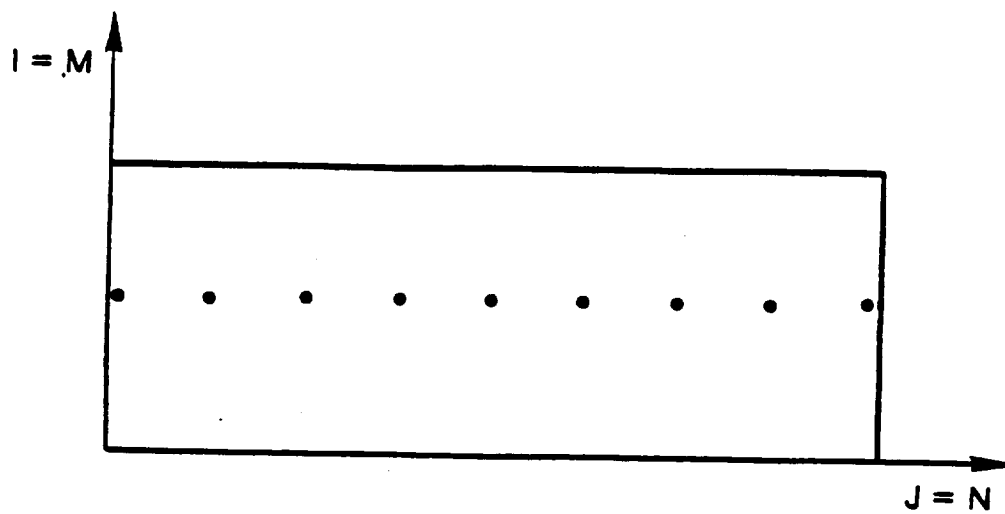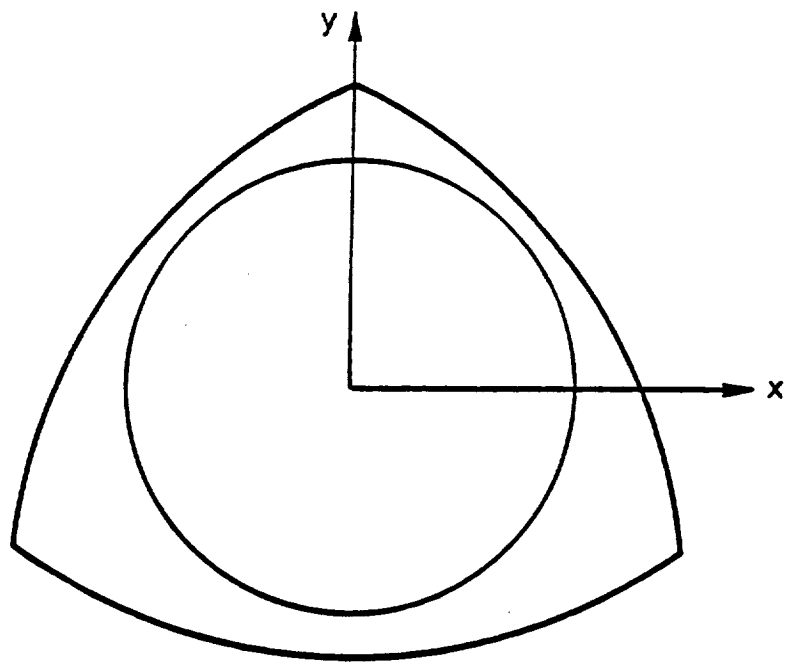
Figure 5-15 Sectored Lobe Seal, Sample Problem No. 2

86260

- The orifice diameter is 0.015 in.

- The coefficient of discharge of each orifice = 0.9

- The supply pressure to the source orifices is 120 psig

- The operating speed = 70,000 rpm

- The reference pressure is 14.7 psig

- The pressure along the boundaries is 0 psig

Table 5-2 summarizes output data. Since the shaft is concentric within the seal, total load capacity is zero. The most important information is the leakage flow.

The clearance and pressure distribution are shown on Figures 5-16 and 5-17 respectively. Notice the discontinuities in the clearance distribution because of the lobed geometry. The proximity of the source points to each other makes the pressure distribution appear as a line source.

TABLE 5-2

Summary of Performance

Sample Problem 2

```
-JOURNAL & LOAD POSITION
  ECCENTRICITY          =      .00000
  ECCENTRICITY ANGLE    =         .00 DEG
  MINIMUM FILM          =    .0002500 IN
  LOAD                  =   .9904E-12 LB
  LOAD ANGLE            =      -53.73 DEG

  POWER LOSS            =    1.233      HP

  LEAKAGE AT I = 1      = -.14924E-03 LB/S

  LEAKAGE AT I = M      =  .14924E-03 LB/S

-RIGHTING MOMENT
  ABOUT X-X        MX =  -.2814E-13 LB-IN
  ABOUT Y-Y        MY =   .1784E-14 LB-IN
```
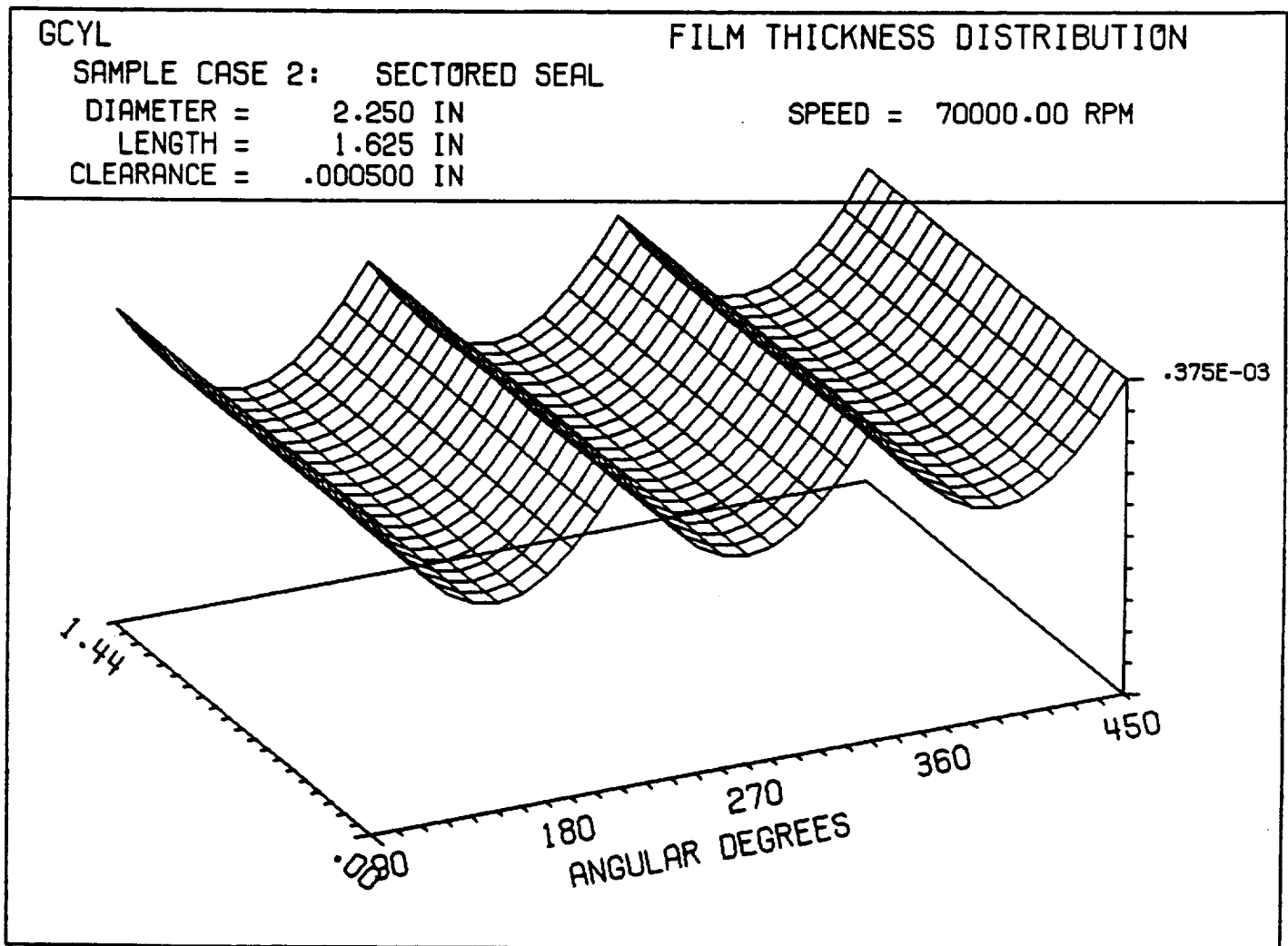
Figure 5-16 Clearance Distribution, Sectored Lobe Seal

SAMPLE CASE 2:   SECTORED SEAL
DIAMETER =   2.250 IN
LENGTH =   1.625 IN
CLEARANCE =   .000500 IN

PRESSURE DISTRIBUTION

SPEED =   70000.00 RPM

.120E+03

450

360

270

180

90

ANGULAR DEGREES
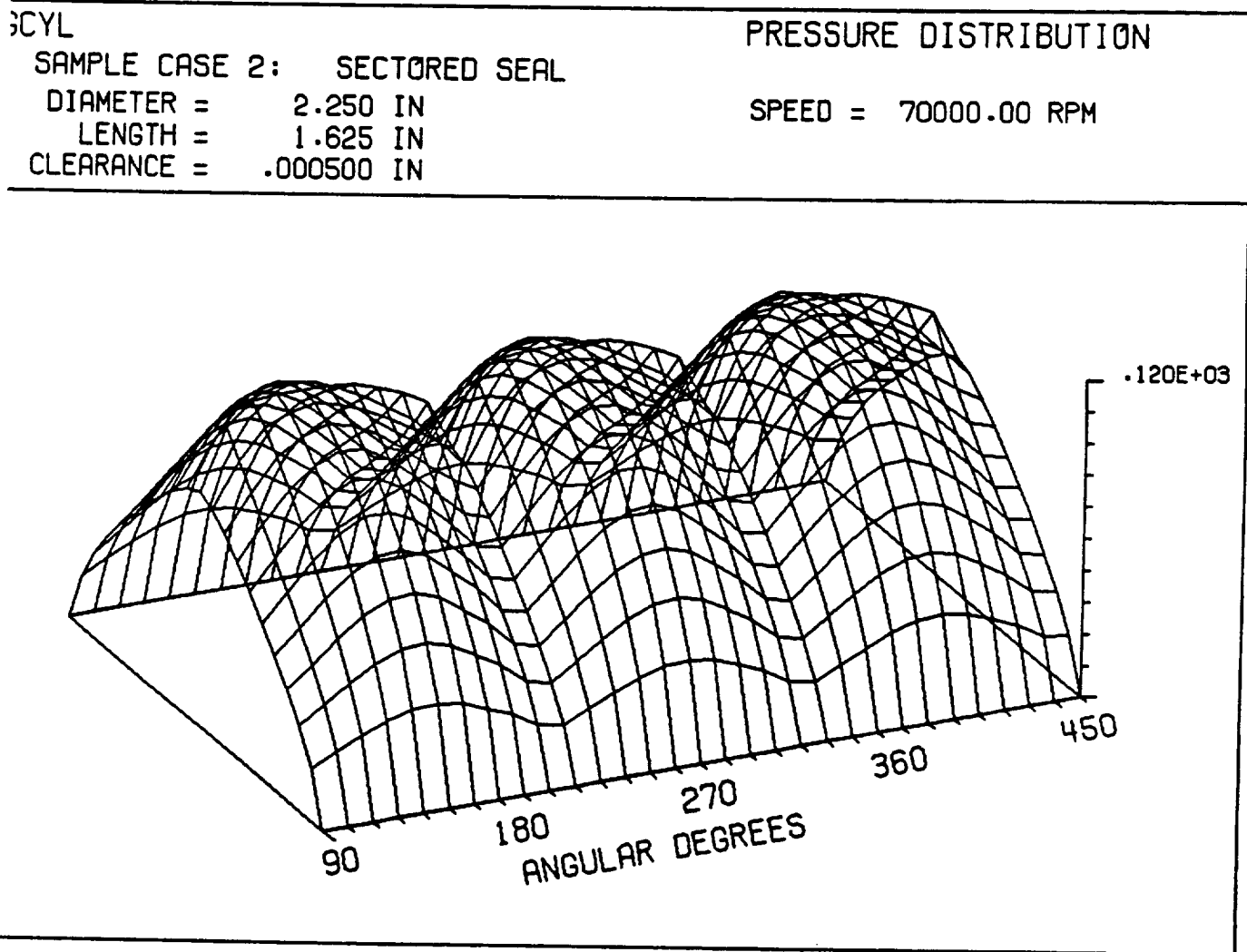
Figure 5-17 Pressure Distribution, Sectored-Lobe Seal

5.2.3 Sample Problem 3 - Three Lobe Seal

This problem deals with the hydrodynamic portion of a 3-Lobe seal where the lobes are separated by axial grooves. Figure 5-7 shows the general geometry and key parameters. The principal parameters are the preload and pivot angle. The following are geometry and operating conditions:

- OPTION =2 which means the position of the seal to satisfy a given load will be determined.

- International units apply; parameter SI invoked.

- Stiffness and damping are to be calculated in two degrees of freedom, x and y, at an imposed frequency equal to running speed of 50,000 rpm.

- The number of pads =3

- The start of the first pad is at 100°, and the pad extent is 100°

- The pad preload is 50 % of the reference clearance, and the preload for the first pad occurs 150° from the x- axis, which means the preload is in the center of the pad.

- The shaft diameter is 0.0508 m.

- The hydrodynamic length is .0254 m

- The reference clearance is 1.27 x 10^{-5} m.

- The lubricant viscosity is 2.07 x 10^{-5} N-s/m^2

- The absolute temperature is 283°K

- The ratio of specific heats of the gas is 1.4

- The gas constant is 290.32 m^2/(s^2-°R)

- Symmetry is applied in the axial direction

- The load to be supported is 200.16 N

- The angle at which the load is applied is 270° from the x-axis.

- The initial eccentricity guess is 0.2, and the initial guess on the displacement angle is 270° from the x-axis.

- The shaft speed is 50,000 rpm

- The reference pressure is 8.274 x 10^5 Pa.

- The boundary pressures are all 0 gage.

Table 5-3 indicates the steady-state performance and stiffness and damping coefficients.

Graphical representations of clearance and pressure distributions are shown on Figures 5-18 and 5-19 respectively.

TABLE 5-3

Summary of Performance

Sample Problem 3

```
-JOURNAL & LOAD POSITION
   ECCENTRICITY           =        .22103
   ECCENTRICITY ANGLE     =       129.38 DEG
   MINIMUM FILM           =      .0000037 M
   LOAD                   =      200.2    N
   LOAD ANGLE             =       -90.00 DEG

   POWER LOSS             =       186.1    W

   LEAKAGE AT I = 1       = -.12875E-04 KG/S

-STIFFNESS COEFFICIENTS
   PRINCIPAL  X    KXX =    .1460E+09 N/M
   CROSS-COUPLED   KXY = -.2379E+08 N/M
   CROSS-COUPLED   KXA =    .0000    N/RAD
   CROSS-COUPLED   KXB =    .0000    N/RAD
   CROSS-COUPLED   KYX = -.3890E+08 N/M
   PRINCIPAL  Y    KYY =    .1002E+09 N/M
   CROSS-COUPLED   KYA =    .0000    N/RAD
   CROSS-COUPLED   KYB =    .0000    N/RAD
   CROSS-COUPLED   KAX =    .0000    N-M/M
   CROSS-COUPLED   KAY =    .0000    N-M/M
   PRINCIPAL  A    KAA =    .0000    N-M/RAD
   CROSS-COUPLED   KAB =    .0000    N-M/RAD
   CROSS-COUPLED   KBX =    .0000    N-M/M
   CROSS-COUPLED   KBY =    .0000    N-M/M
   CROSS-COUPLED   KBA =    .0000    N-M/RAD
   PRINCIPAL  B    KBB =    .0000    N-M/RAD

-DAMPING COEFFICIENTS
   PRINCIPAL  X    DXX =     9939.    N-S/M
   CROSS-COUPLED   DXY = -.1089E+05 N-S/M
   CROSS-COUPLED   DXA =    .0000    N-S/M
   CROSS-COUPLED   DXB =    .0000    N-S/RAD
   CROSS-COUPLED   DYX =     5140.    N-S/M
   PRINCIPAL  Y    DYY =    .1393E+05 N-S/M
   CROSS-COUPLED   DYA =    .0000    N-S/RAD
   CROSS-COUPLED   DYB =    .0000    N-S/RAD
   CROSS-COUPLED   DAX =    .0000    N-M-S/M
   CROSS-COUPLED   DAY =    .0000    N-M-S/M
   PRINCIPAL  A    DAA =    .0000    N-M-S/RAD
   CROSS-COUPLED   DAB =    .0000    N-M-S/RAD
   CROSS-COUPLED   DBX =    .0000    N-M-S/M
   CROSS-COUPLED   DBY =    .0000    N-M-S/M
   CROSS-COUPLED   DBA =    .0000    N-M-S/RAD
   PRINCIPAL  B    DBB =    .0000    N-M-S/RAD
```

CYL
SAMPLE CASE 3:   3-LOBE GAS SEAL
    DIAMETER =   .051   M
      LENGTH =   .025   M
    CLEARANCE =   .000013   M

FILM THICKNESS DISTRIBUTION

SPEED = 50000.00 RPM

.114E-04

1.00

.000

185   270   355   440

ANGULAR DEGREES
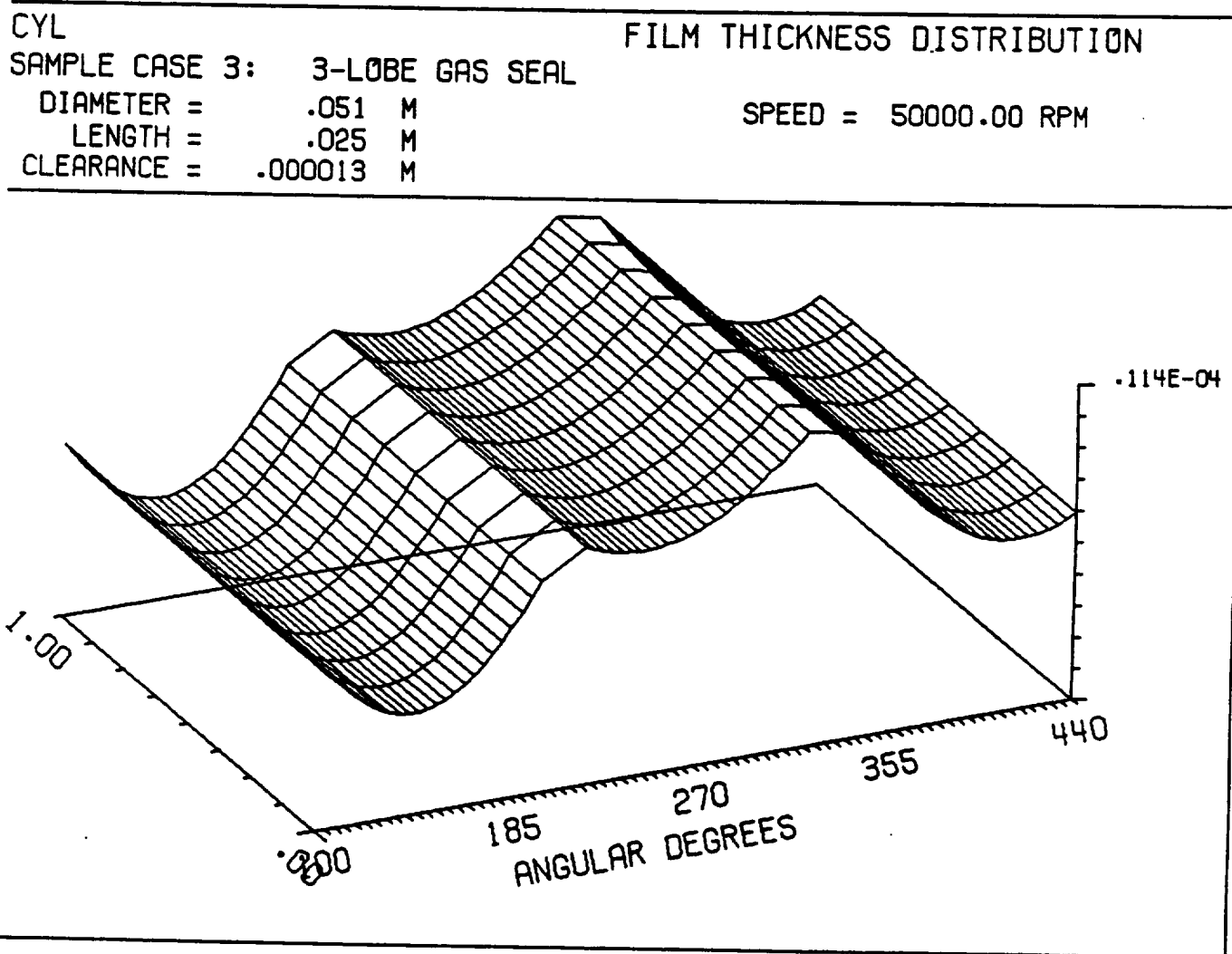
Figure 5-18   Clearance Distribution - Three-Lobe Seal

GCYL   PRESSURE DISTRIBUTION
  SAMPLE CASE 3:   3-LOBE GAS SEAL
     DIAMETER =   .051 M   SPEED = 50000.00 RPM
       LENGTH =   .025 M
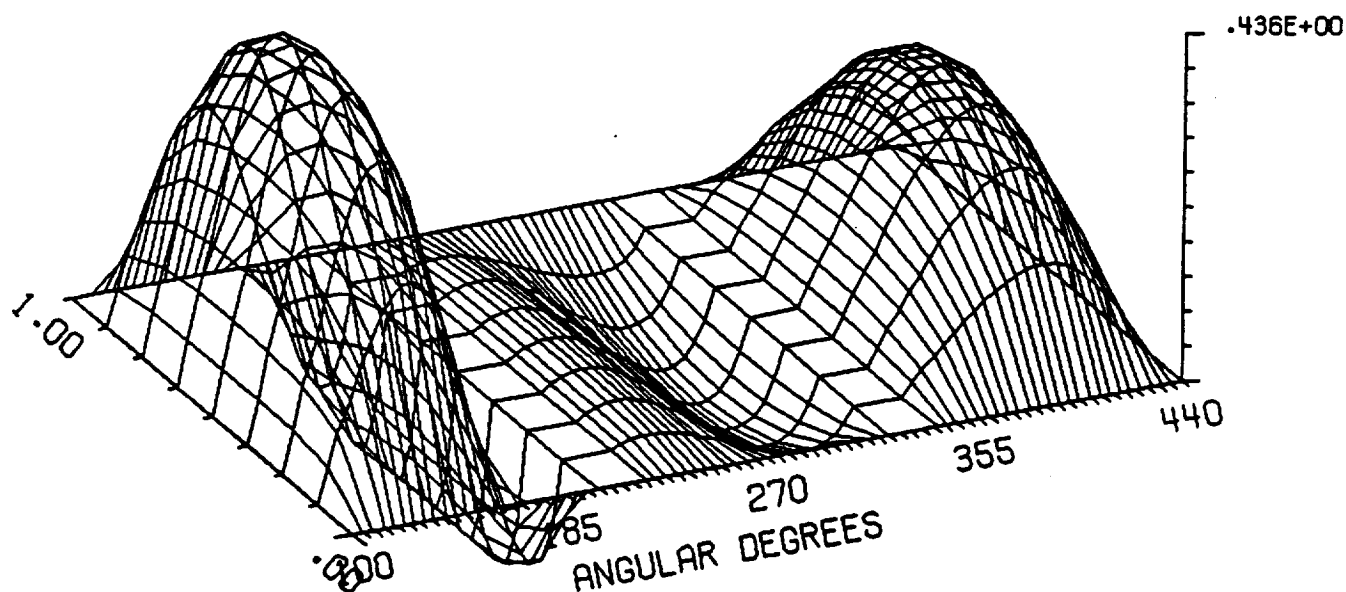   CLEARANCE =   .000013 M

Figure 5-19 Pressure Distribution - Three-Lobe Gas Seal

5.2.4 Sample Problem 4 - T-Shaped Sectored Seal

This problem deals with an actual helium buffered seal analysis and design (for SSME) that was accomplished for NASA. A design that incorporates a self - adjusting clearance that can accommodate thermal and centrifugal distortions and shaft dynamic excursions avoids many of the problems associated with captured clearance designs. The sectored ring seal provides the desired self adjusting clearance features. The general configuration of the sectored seal is shown on Figure 5-20. The sectors consist of T-shaped sections mated to each other at each end with sealed joints. The sectors can move relative to each other circumferentially and that is how the seal accommodates variations in the sleeve dimensions due to thermal expansions and contractions and centrifugal growths. The T-shaped sector was chosen because it is a symmetrical shape and the various fluid and friction forces can be designed to avoid upsetting moments on the individual sectors. An overlapping V joint prevents a direct clearance path between the hydrogen and oxygen ends of the seal. Each sector is supported by a hydrostatic fluid-film on its inner circumference and along the side walls which forms a friction free secondary seal to permit free radial motion of the sectors in response to sleeve movements. The fluid-films are predominantly hydrostatic to avoid any pitching tendencies introduced by the hydrodynamic effects. The hydrostatic bearings are fed by the buffer pressure on the outside diameter of the seal. Figure 5-21 shows the pressure distribution and force balance on the individual sectors.

This sample problem describes one case conducted in the analysis of the circumferential hydrostatic seal on one of the sectors. The geometry and operating conditions are as follows:

- The number of pads to be analyzed is 1.

- OPTION - 2, which means the position of the sector to satisfy a given load will be determined.

- The load applied is 370 lbs.

- The load angle from the x -axis is 270°

- The initial guess on the eccentricity of the seal is 0.5

- The initial guess on the eccentricity angle is 90°

- Variable grids are used in both the axial and circumferential direction. The grid is made very fine around the source points. The starting angle of

the sector is 30° from the x-axis and its angular extent is 120°. the axial length of the seal is 1.627 in.

● The shaft diameter is 2.6798 in.

● The reference clearance is 0.001 in.

● The ratio of specific heats of the gas is 1.66

● The gas constant is 1,790,000 $in^2/(s^2\text{-}°R)$

● The absolute temperature is 528°R

● The gas viscosity is 2.9 x 10^{-9} lb-s/in^2

● The shaft speed is 0 rpm

● The reference pressure is 14.7 psig

● The boundary pressures surrounding the seal are 50 psig

● Cross-coupled stiffness and damping are to be computed at an excitation frequency of 0 rpm

● There are 6 discrete inherently compensated source points in the sector of diameter — 0.020 in. The location of these orifices was determined from the design layout of the sector. The coefficient of discharge of each orifice is unity.

● The buffer pressure is 200 psig

● Flow is to be determined along four paths that make up the periphery of the seal.

● The FILE option was exercised. A previous pressure distribution was read as the initial pressure distribution for this case. Convergence of the pressure is often difficult when solving source problems, whether they be inherently compensated sources or spot recesses. Convergence difficulties occur because sources present spikes in the pressure distribution and pressure gradients become very large. There are two methods for handling these problems which can be applied independently or jointly. The first is to use variable grid and fine grid spacing around the orifice holes. Each grid line around the hole should be at a distance of one to two orifice

5-51

SECTOR SEAL CROSS SECTION

View of Joint

Gas Vent

Helium Gas Inlet

T-Shaped Sector

Secondary Face Seal

V-Joint

Antirotation Pin

Shaft Sleeve

Hydrostatic Feed

Closing Spring

Garter Spring

Secondary Seal Recess

Sector Joint
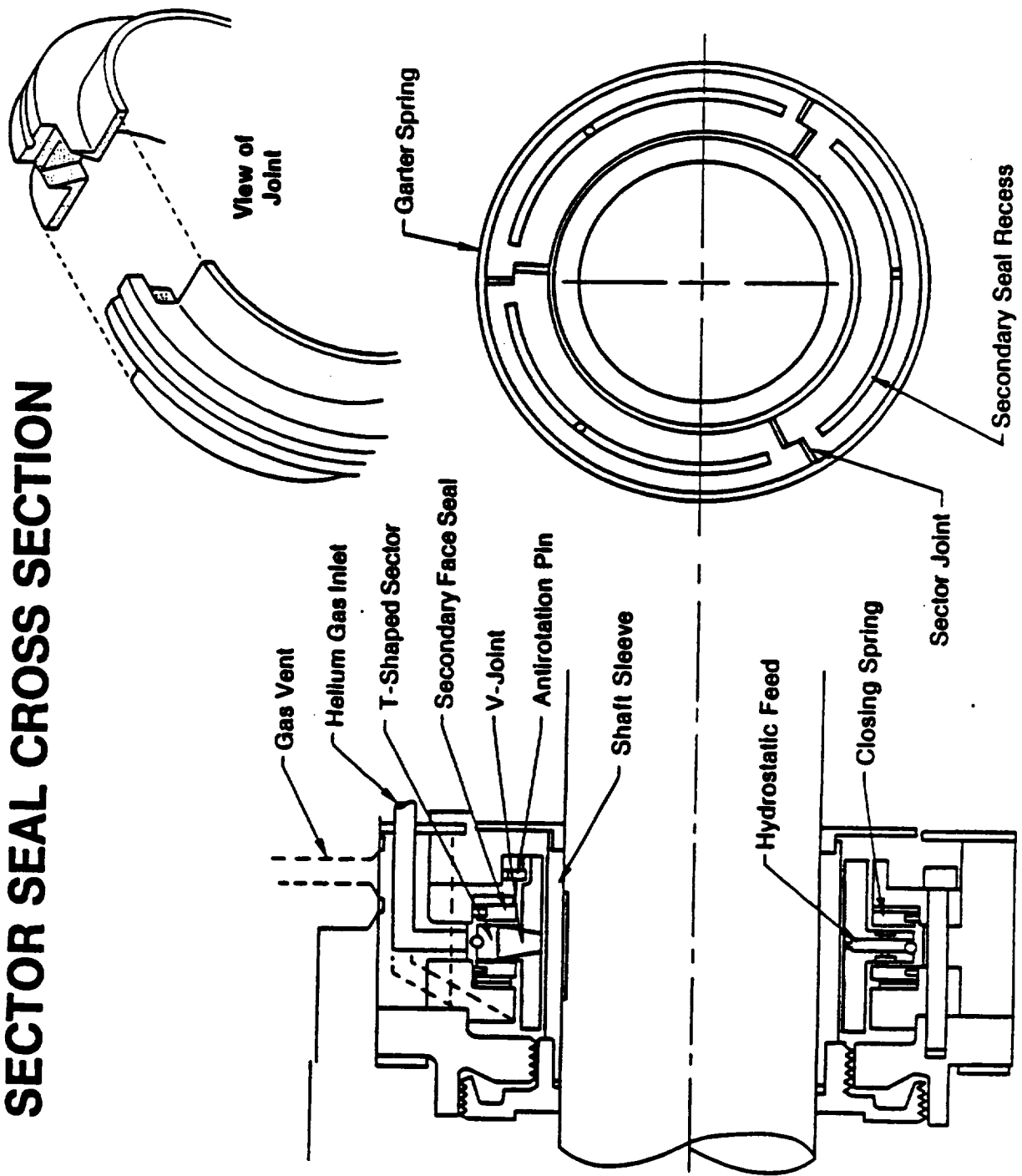
Figure 5-20   T-Shaped Sectored Ring Seal

871514

5-52
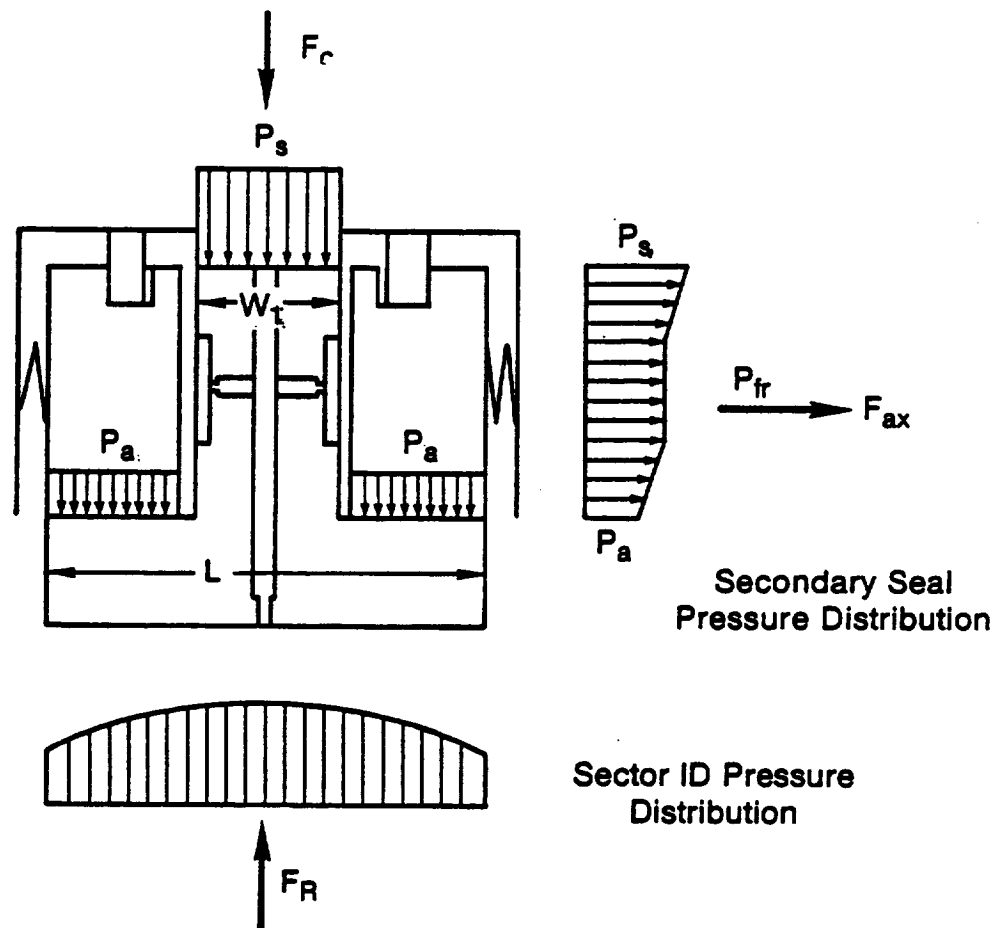
$$F_c = P_s\, A_s + P_a\, A_a$$

Radial Force Balance
$$F_R - F_c \pm F_f \pm F_r = 0$$

Axial Force Balance
$$F_{ax} - F_p - k_a\, \delta_a = 0$$

Figure 5-21 Pressure Distribution and Force Balance T-Sectored Seal

871511

diameters in both the axial and circumferential direction. The other mechanism is to start the problem at low eccentricity and use the pressure distribution as an initial guess to get to the next eccentricity. Continue the process until the desired eccentricity is attained.

As indicated on Table 5-4, the eccentricity of the sector to support the load is 0.55609 and the eccentricity angle is 90°. Figures 5-22 and 5-23 show the clearance and pressure distributions. Note on the plots the dense grid work surrounding the orifice locations.

TABLE 5-4

Summary of Performance of T-Shaped Sectored Seal

Sample Problem 4

```
-JOURNAL & LOAD POSITION
   ECCENTRICITY            =      .55609
   ECCENTRICITY ANGLE      =       90.00 DEG
   MINIMUM FILM            =      .0004446 IN
   LOAD                    =     369.5     LB
   LOAD ANGLE              =      -90.00 DEG

   POWER LOSS            . =      .0000     HP

   LEAKAGE AT I = 1        =  -.40231E-04 LB/S

   LEAKAGE AT I = M        =   .40231E-04 LB/S

-STIFFNESS COEFFICIENTS
   PRINCIPAL  X       KXX =   .4316E+05 LB/IN
   CROSS-COUPLED      KXY =   .6956E-08 LB/IN
   CROSS-COUPLED      KXA =   .1299E-08 LB/RAD
   CROSS-COUPLED      KXB =   .2104E-02 LB/RAD
   CROSS-COUPLED      KYX =  -126.8      LB/IN
   PRINCIPAL  Y       KYY =   .4982E+05 LB/IN
   CROSS-COUPLED      KYA =  -295.4      LB/RAD
   CROSS-COUPLED      KYB =  -59.46      LB/RAD
   CROSS-COUPLED      KAX =   .3522E-06 IN-LB/IN
   CROSS-COUPLED      KAY =  -.3701E-02 IN-LB/IN
   PRINCIPAL  A       KAA =   .4361E+05 IN-LB/RAD
   CROSS-COUPLED      KAB =  -.3030E-06 IN-LB/RAD
   CROSS-COUPLED      KBX =   .1380E-02 IN-LB/IN
   CROSS-COUPLED      KBY =  -.9135E-10 IN-LB/IN
   CROSS-COUPLED      KBA =   .2327E-08 IN-LB/RAD
   PRINCIPAL  B       KBB =  9965.       IN-LB/RAD

-DAMPING COEFFICIENTS
   PRINCIPAL  X       DXX =   10.82      LB-S/IN
   CROSS-COUPLED      DXY =  -.7990E-11 LB-S/IN
   CROSS-COUPLED      DXA =  -.2932E-12 LB-S/RAD
   CROSS-COUPLED      DXB =   .3324E-06 LB-S/RAD
   CROSS-COUPLED      DYX =   .1418E-01 LB-S/IN
   PRINCIPAL  Y       DYY =   80.23      LB-S/IN
   CROSS-COUPLED      DYA =   .3588E-01 LB-S/RAD
   CROSS-COUPLED      DYB =   .6553E-02 LB-S/RAD
   CROSS-COUPLED      DAX =   .6908E-10 IN-LB-S/IN
   CROSS-COUPLED      DAY =   .8762E-06 IN-LB-S/IN
   PRINCIPAL  A       DAA =  4.516       IN-LB-S/RAD
   CROSS-COUPLED      DAB =  -.3370E-09 IN-LB-S/RAD
   CROSS-COUPLED      DBX =  -.2926E-06 IN-LB-S/IN
   CROSS-COUPLED      DBY =   .6752E-14 IN-LB-S/IN
   CROSS-COUPLED      DBA =   .4698E-12 IN-LB-S/RAD
   PRINCIPAL  B       DBB =   .9017      IN-LB-S/RAD

-RIGHTING MOMENT
   ABOUT X-X          MX  =   .2753E-05 LB-IN
   ABOUT Y-Y          MY  =  -.6058E-14 LB-IN


-FLOW THRU SPECIFIED GRID LINE
   FROM   1   1 TO  27   1    FLOW=  -.5908E-04 LB/S


-FLOW THRU SPECIFIED GRID LINE
   FROM   1  34 TO  27  34    FLOW=   .5908E-04 LB/S


-FLOW THRU SPECIFIED GRID LINE
   FROM   1   1 TO   1  34    FLOW=  -.4023E-04 LB/S


-FLOW THRU SPECIFIED GRID LINE
   FROM  27   1 TO  27  34    FLOW=   .4023E-04 LB/S
```

;CYL FILM THICKNESS DISTRIBUTION
NASA SECTORED SEAL INHERENT COMPENSATION.DRAWING DIMEN
DIAMETER =   2.680 IN   SPEED =   .00 RPM
LENGTH =   1.627 IN
CLEARANCE =   .001000 IN

.722E-03

1.21

150

120

90

60

.030

ANGULAR DEGREES

Figure 5-22 Clearance Distribution – T–Sectored Seal
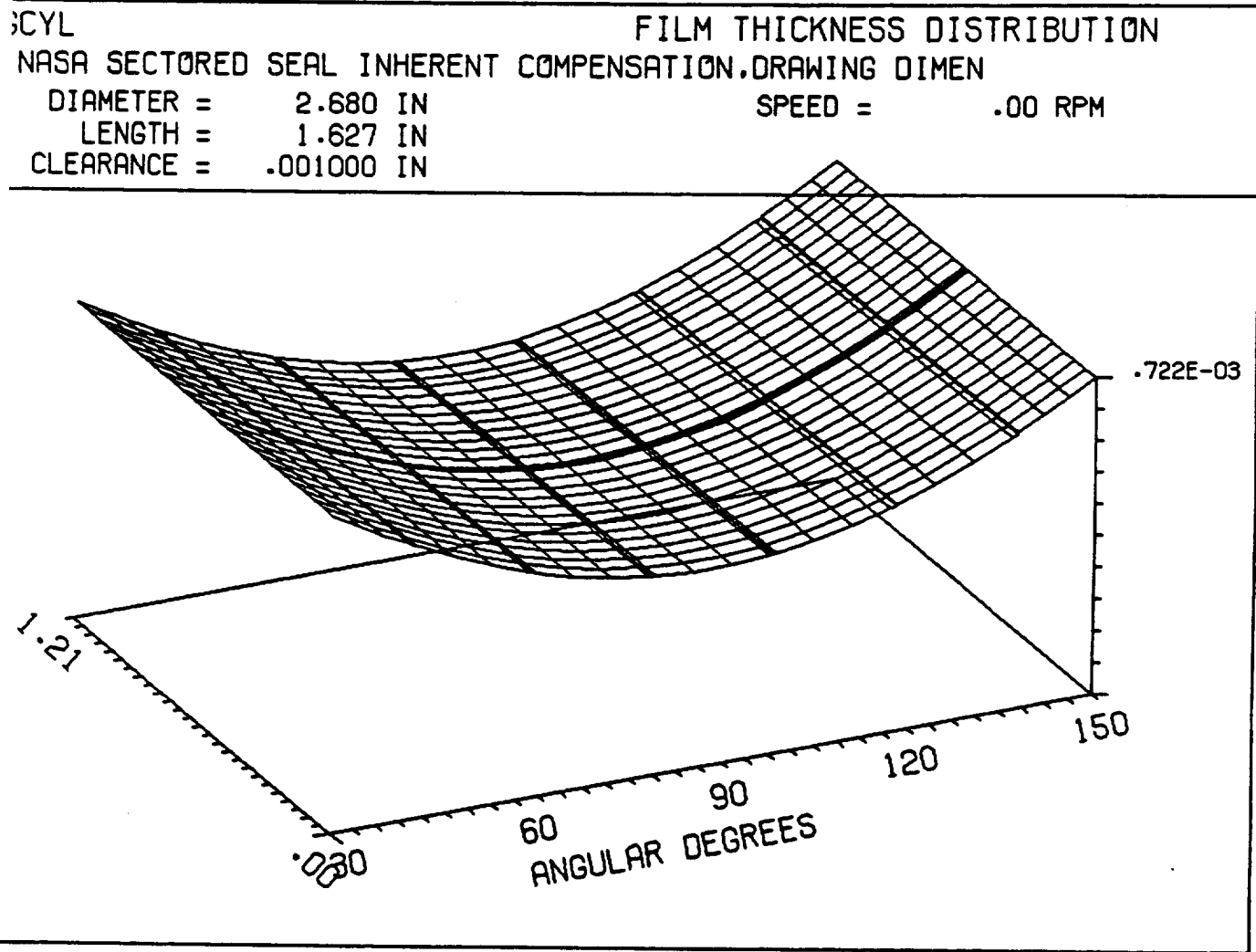
GCYL   PRESSURE DISTRIBUTION
 NASA SECTORED SEAL INHERENT COMPENSATION,DRAWING DIMEN
    DIAMETER =   2.680 IN   SPEED =   .00 RPM
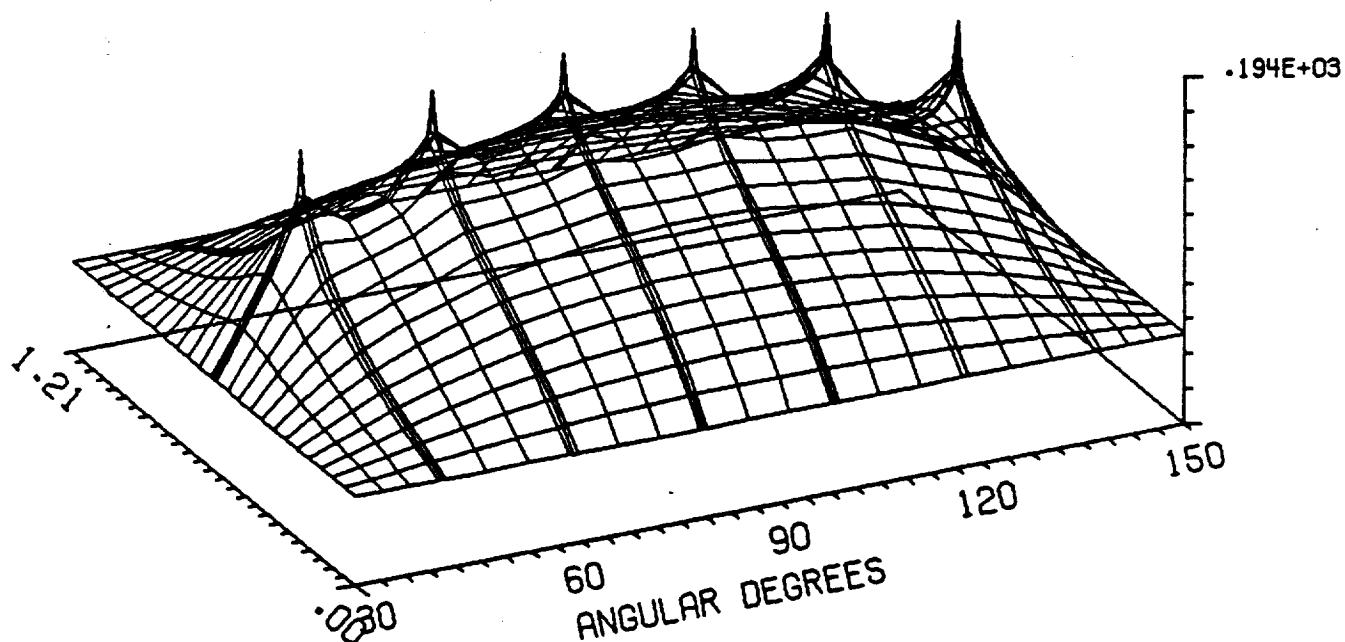   LENGTH =   1.627 IN
  CLEARANCE =   .001000 IN

.194E+03

1.21

.030

ANGULAR DEGREES

30   60   90   120   150

Figure 5-23 Pressure Distribution – T-Sectored Seal

5-57

5.2.5 Sample Problem 5. Rayleigh-step, Floating-Ring Seal

This example represents another buffer fluid seal that was designed for use in the SSME. The principal of operation of a hydrodynamic, lift-pad, floating-ring seal is illustrated on Figure 5-24. The seal consists of two rings that are mounted back-to-back. The buffer fluid enters between the rings and forces the rings up against the stationary housing. The buffer fluid leaks in the clearance annulus between the shaft and the seal and prevents ingress of exterior fluid on either side of the floating-ring assembly. The rings are held in equilibrium by a number of forces as shown on Figure 5-24. F_C is a pressure force from the inlet buffer fluid that forces the rings up against the housings. This pressure force is partially balanced on the housing sides of the rings by undercutting and exposing the housing sides of the rings to buffer pressure. This balance force is identified as F_B. F_H represents a hydrodynamic force that is generated by rotation between the shaft and ring. The net hydrodynamic force is zero when the shaft and rings are in the concentric position. However, when the ring becomes eccentric with respect to the shaft, a hydrodynamic force is built up that opposes the eccentricity. There is also a normal force, F_N, acting on the ring at the contact area between the ring and the housing. In addition to the equilibrium forces mentioned above, there is a friction force, F_f, between the seal ring and housing.

Figure 5-25 shows the hydrodynamic geometry that is incorporated into the bore of the seal rings. A portion of the length of the bore is segregated into sectors, and these sectors are separated from one another by axial grooves. A circumferential groove that goes completely around the bore is installed upstream of the final seal dam region. At the interior of the sectors, Rayleigh-step pockets are machined. The velocity direction of the shaft is such that it produces hydrodynamic pressures due to pumping of the fluid over the Rayleigh-step. The sealing occurs across the dam which is a narrow annulus of low clearance exposed to high pressure at its interior circumferential groove and to lower pressure at its outboard end. The shaded regions on Figure 5-25 indicate depressions from grooves and Rayleigh-step pockets.

In this example one pad of the Rayleigh-step interface was examined from the high pressure interior end to the low pressure exterior end. The high pressure end is at the bottom end of the grid (I = 1). Geometric and operating parameters are as follows:

- International units are to be employed

- NPAD -1, because we are examining the performance of one pad only which is represented on the grid as a 90° arc from the center of one axial groove

Helium Buffer Fluid

F_C

F_H

F_f

F_B

F_N

F_B = Pressure Balance Force
F_N = Normal Contact Force
F_f = Friction Force
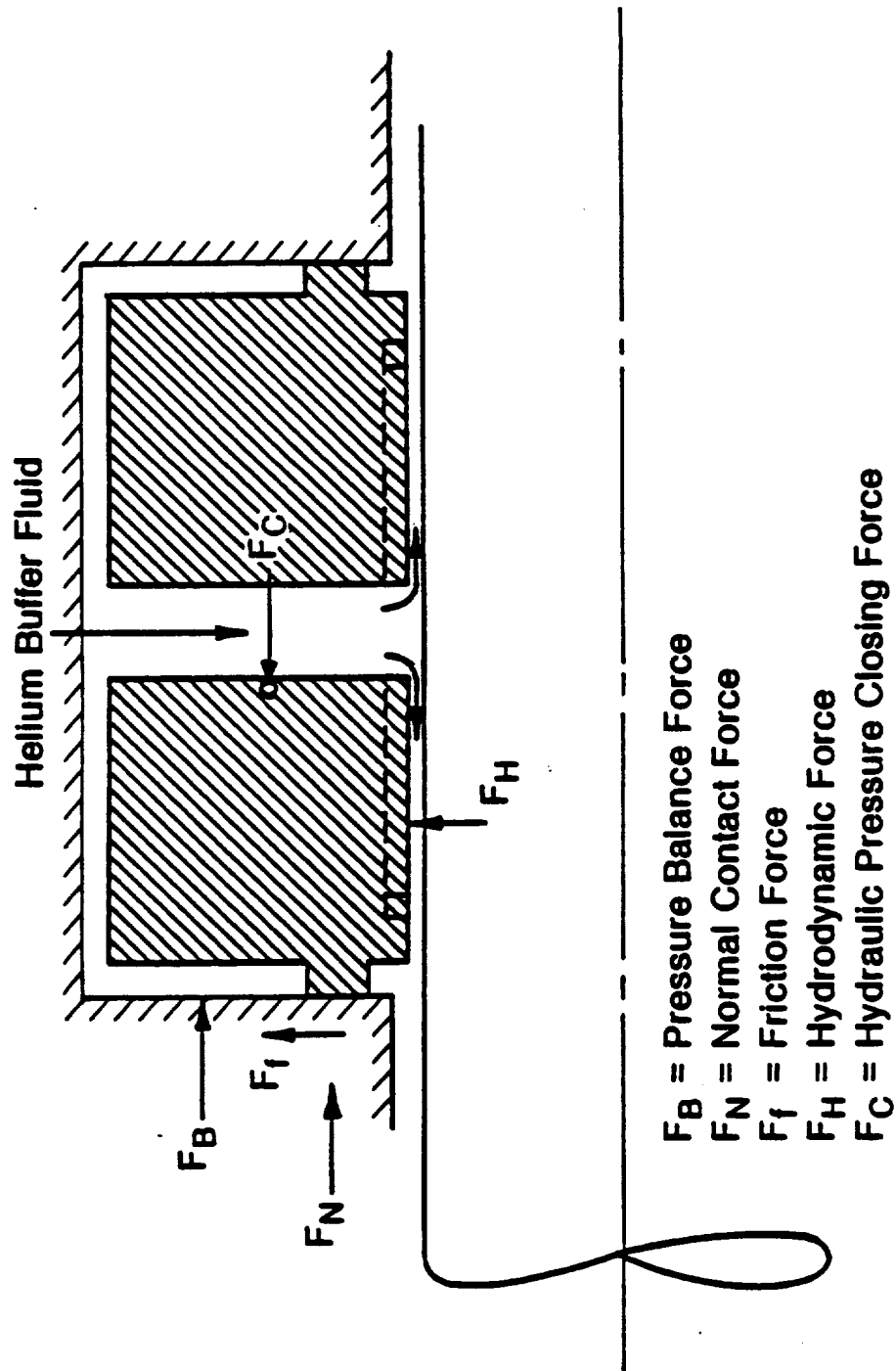F_H = Hydrodynamic Force
F_C = Hydraulic Pressure Closing Force
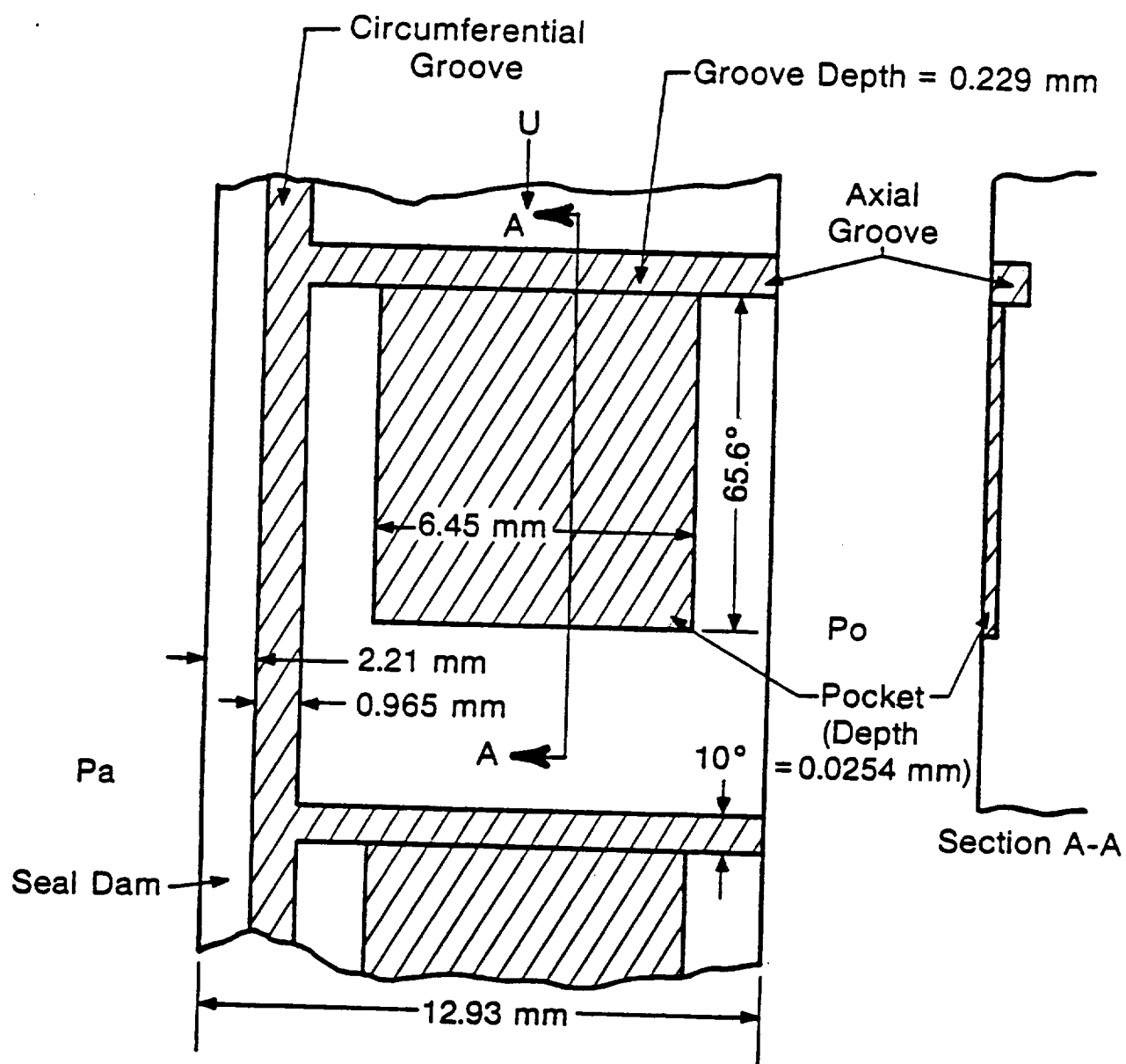
Figure 5-24 Floating Ring, Rayleigh-Step Seal

Figure 5-25 Developed View of 50-mm Rayleigh-Step Pad

832437

to the next. Thus the pad angle is 90°. The pad starts at 0°. Also, the boundary conditions at the circumferential ends of the single pad must be periodic, i.e. all pads will act identically, which will occur when the shaft is in the concentric position. Periodicity is invoked by applying the JOINED parameter.

- The shaft diameter is .05 m

- The total seal length is 0.0123 m

- The seal clearance is 1.27×10^{-5} m

- The step height is 2.54×10^{-5} m

- The gas viscosity is 2.19×10^{-5} N-s/m^2

- The absolute temperature is 338.6°K

- The ratio of specific heats is 1.66

- The gas constant is 1154.8364 m^2/(s^2-°K)

- The shaft speed is 70,000 rpm

- The reference pressure is 101,352.93 Pa

- The high pressure to be sealed is 1.37895×10^6 Pa which would be at the bottom of the grid. The remaining boundaries are at 0 psig

Table 5-5 shows performance of the sector examined. Since only one quarter of the seal is being examined, the leakages at the axial inlet (I=1) and outlet (I=M) would be multiplied by 4 to get total leakage. The leakage at the outlet is greater than the leakage at the inlet end because of the added flow contribution from the axial groove. The 3-D plots of the clearance and pressure distributions are shown on Figures 5-26 and 5-27 respectively. Note on Figure 5-27 that the high ambient pressures in the grooves overshadows the increased pressure from the Rayleigh-step.

TABLE 5-5

Performance Results

Sample Problem 5

```
-JOURNAL & LOAD POSITION
   ECCENTRICITY            =         .00000
   ECCENTRICITY ANGLE      =             .00 DEG
   MINIMUM FILM            =         .0000127 M
   LOAD                    =      571.0       N
   LOAD ANGLE              =        -134.78 DEG

   POWER LOSS              =       21.79      W

   LEAKAGE AT I = 1        = -.21681E-04 KG/S

   LEAKAGE AT I = M        =   .40252E-03 KG/S

-RIGHTING MOMENT
   ABOUT X-X          MX =  -.1596      N-M
   ABOUT Y-Y          MY =   .1551      N-M
```

GCYL   FILM THICKNESS DISTRIBUTION
  RAYLEIGH - STEP SEAL PROBLEM
    DIAMETER =   .050 M   SPEED =   70000.00 RPM
      LENGTH =   .012 M
   CLEARANCE =   .000013 M

.381E-04

0
22
45
ANGULAR DEGREES
67
90

Figure 5-26   Clearance Distribution - Rayleigh-Step Pad

5-63

GCYL   PRESSURE DISTRIBUTION
 RAYLEIGH – STEP SEAL PROBLEM
    DIAMETER =   .050   M   SPEED =   70000.00 RPM
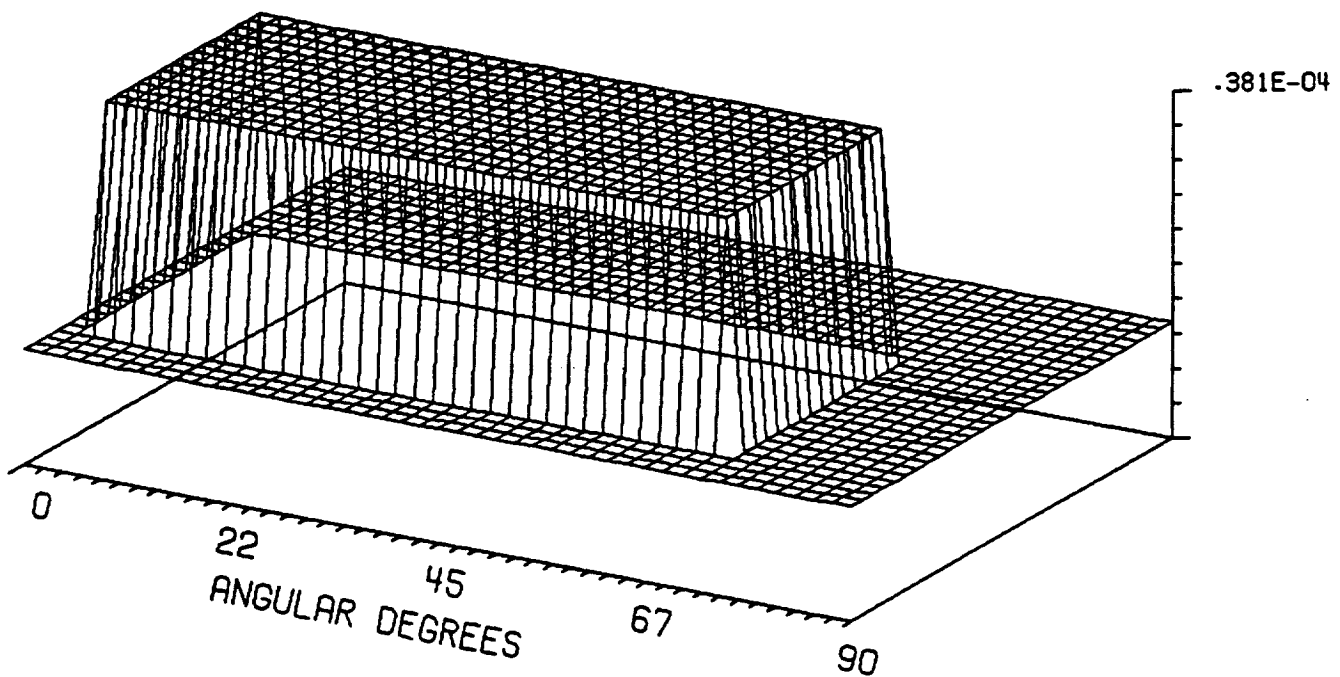   LENGTH =   .012   M
  CLEARANCE =   .000013   M

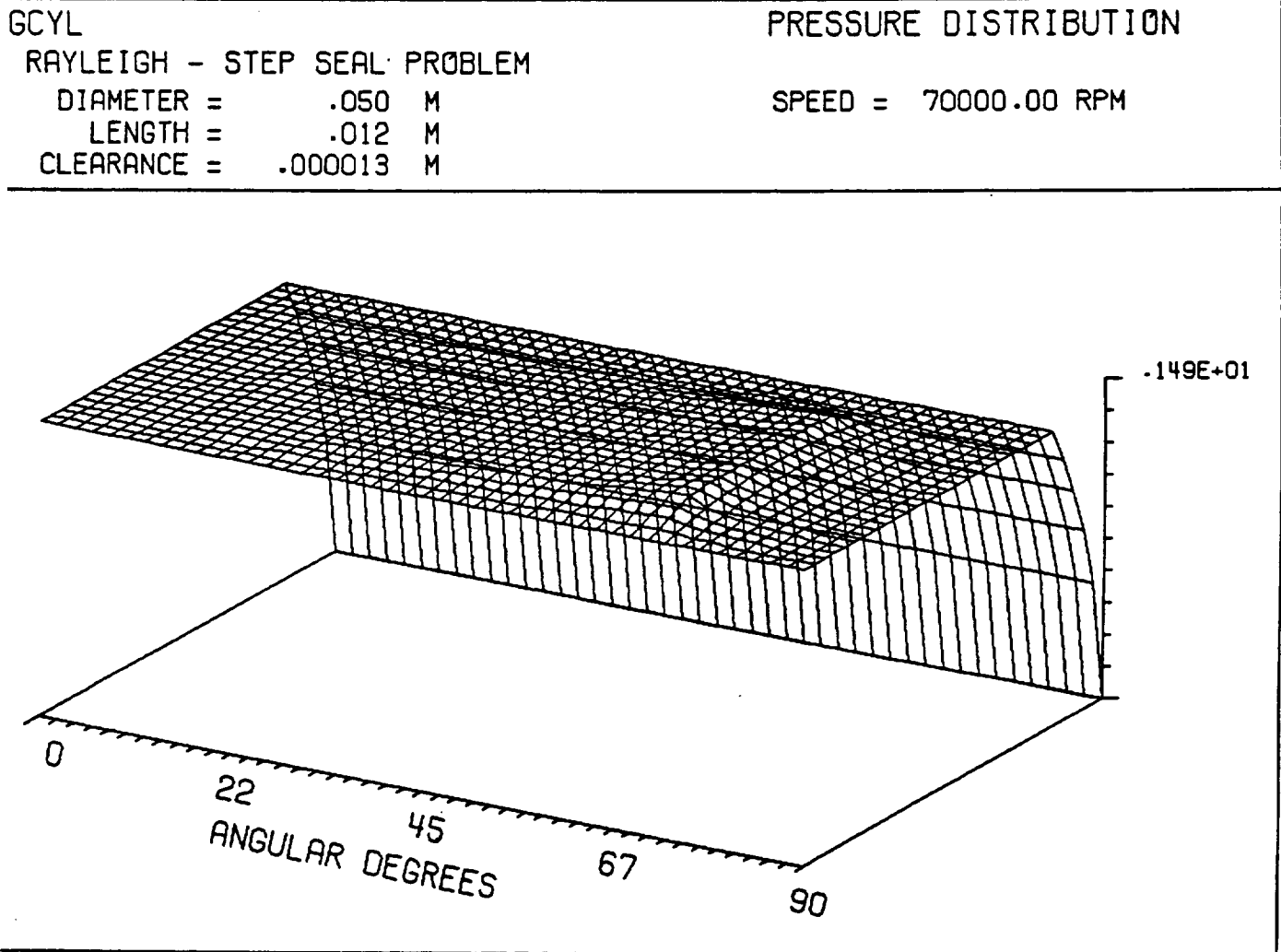.149E+01

0
22
45
67
90
ANGULAR DEGREES

Figure 5-27 Pressure Distribution – Rayleigh-Step Pad

5-64

5.2.6 Sample Problem 6. Rayleigh-step Seal with Eccentricity

This problem will be similar to problem 5 except the shaft is to be eccentric with respect to the seal ring. In this case periodic boundary conditions cannot be used, and to conserve grid space one hydrodynamic pad will be modeled and the number of pads will be four. To model separate pads however requires that the boundary conditions be known on all extremities of the pad. The seal dam region is not a separate pad problem but is a single 360° pad. Thus the problem resolves into two problems; one that treats the separate Rayleigh pads and one that treats the seal dam. For this particular example, only the Rayleigh-step hydrodynamic region is considered. The following geometric and operating parameters have been applied:

- International units are invoked

- OPTION -1, the shaft position relative to the seal ring is specified

- Stiffness is to be calculated in four degrees of freedom at an excitation frequency of 70,000 rpm.

- The number of pads is 4 and each pad has an extent of 90°

- The shaft diameter is 0.05 m

- The shaft length is 0.0123 m

- The reference clearance is 1.27×10^{-5} m

- The gas viscosity is 2.19×10^{-5} N-s/m^2

- The absolute temperature is 338.6°K

- The ratio of specific heats is 1.66

- The gas constant is 1154.84 m^2/(s^2-°K)

- The shaft eccentricity ratio is 0.5

- The eccentricity angle is 270°

- The shaft speed is 70,000 rpm

- The reference pressure is 1.01353×10^5 Pa

• The pad boundary pressures are 1.37895×10^6 Pa

As shown on Table 5-6, at the specified position, the load capacity of the seal is 52.96 N and the load angle is 71.63° from the x-axis. The minimum film thickness is 6.4×10^{-6} m. The clearance and pressure distributions are shown on Figures 5-28 and 5-29 respectively.

TABLE 5-6

Summary of Results

Sample Problem 6

```
-JOURNAL & LOAD POSITION
  ECCENTRICITY           =      .50000
  ECCENTRICITY ANGLE     =     -90.00 DEG
  MINIMUM FILM           =     .0000064 M
  LOAD                   =    52.96     N
  LOAD ANGLE             =      71.63 DEG

  POWER LOSS             =    95.08     W

  LEAKAGE AT I = 1       = -.88483E-04 KG/S

  LEAKAGE AT I = M       =  .88483E-04 KG/S

-STIFFNESS COEFFICIENTS
  PRINCIPAL   X    KXX =    .1016E+08 N/M
  CROSS-COUPLED    KXY =    .3371E+07 N/M
  CROSS-COUPLED    KXA =    14.33     N/RAD
  CROSS-COUPLED    KXB =   -.3404     N/RAD
  CROSS-COUPLED    KYX =   -.6161E+06 N/M
  PRINCIPAL   Y    KYY =    .1169E+08 N/M
  CROSS-COUPLED    KYA =    37.51     N/RAD
  CROSS-COUPLED    KYB =    20.59     N/RAD
  CROSS-COUPLED    KAX =   -.8526E-10 N-M/M
  CROSS-COUPLED    KAY =   -.5781E-10 N-M/M
  PRINCIPAL   A    KAA =    27.53     N-M/RAD
  CROSS-COUPLED    KAB =    1.657     N-M/RAD
  CROSS-COUPLED    KBX =    .1284E-09 N-M/M
  CROSS-COUPLED    KBY =   -.8787E-11 N-M/M
  CROSS-COUPLED    KBA =   -10.32     N-M/RAD
  PRINCIPAL   B    KBB =    14.46     N-M/RAD

-DAMPING COEFFICIENTS
  PRINCIPAL   X    DXX =    786.4     N-S/M
  CROSS-COUPLED    DXY =   -216.6     N-S/M
  CROSS-COUPLED    DXA =   -.4094E-03 N-S/M
  CROSS-COUPLED    DXB =    .8221E-04 N-S/RAD
  CROSS-COUPLED    DYX =    192.7     N-S/M
  PRINCIPAL   Y    DYY =    901.7     N-S/M
  CROSS-COUPLED    DYA =   -.1011E-02 N-S/RAD
  CROSS-COUPLED    DYB =   -.6955E-03 N-S/RAD
  CROSS-COUPLED    DAX =    .4642E-15 N-M-S/M
  CROSS-COUPLED    DAY =    .5113E-15 N-M-S/M
  PRINCIPAL   A    DAA =    .3572E-02 N-M-S/RAD
  CROSS-COUPLED    DAB =   -.1573E-03 N-M-S/RAD
  CROSS-COUPLED    DBX =   -.9665E-15 N-M-S/M
  CROSS-COUPLED    DBY =    .2712E-15 N-M-S/M
  CROSS-COUPLED    DBA =   -.5069E-04 N-M-S/RAD
  PRINCIPAL   B    DBB =    .2612E-02 N-M-S/RAD

-RIGHTING MOMENT
  ABOUT X-X        MX  =    .7687E-15 N-M
  ABOUT Y-Y        MY  =    .4289E-15 N-M
```

SCYL   FILM THICKNESS DISTRIBUTION
RAYLEIGH - STEP SEAL PROBLEM
   DIAMETER =   .050 M   SPEED =   70000.00 RPM
     LENGTH =   .012 M
  CLEARANCE =   .000013 M

.445E-04

0

90

180

ANGULAR DEGREES

270

360
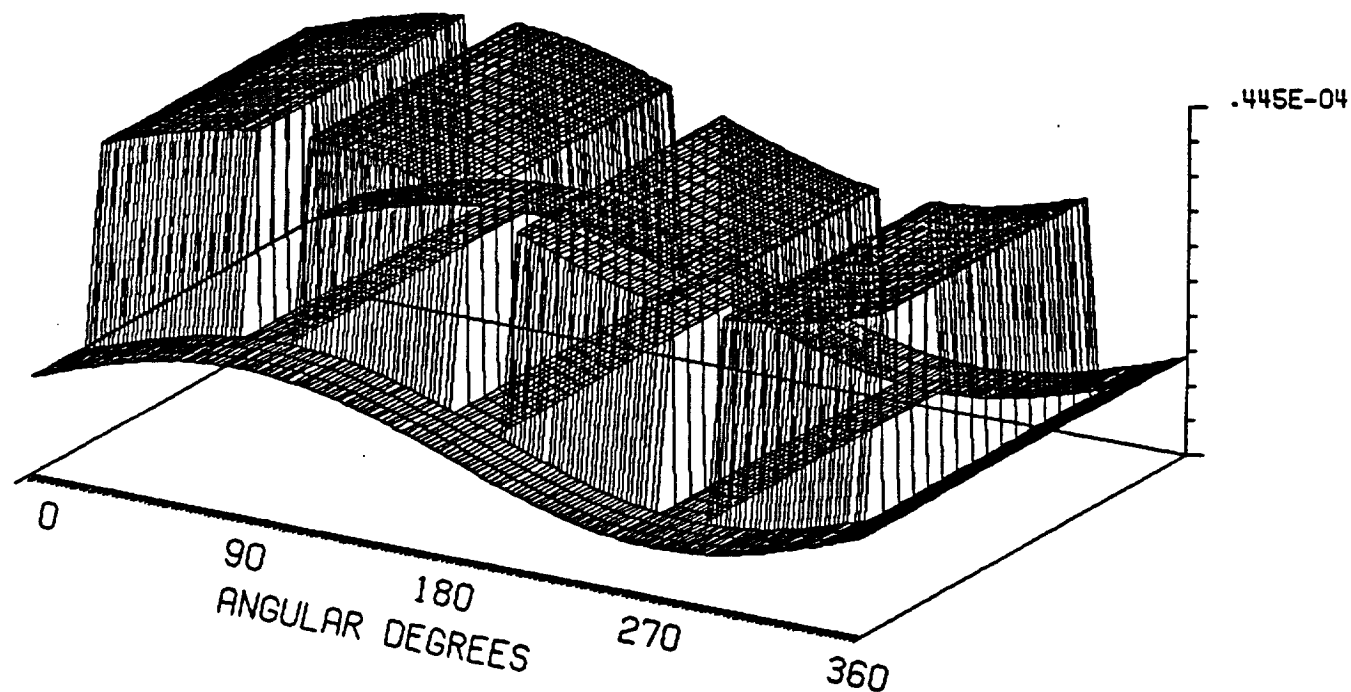
Figure 5-28 Clearance Distribution - Rayleigh-Step Seal with Eccentricity

GCYL   PRESSURE DISTRIBUTION
  RAYLEIGH - STEP SEAL PROBLEM
    DIAMETER =   .050 M   SPEED = 70000.00 RPM
      LENGTH =   .012 M
  CLEARANCE =   .000013 M

.174E+01

360
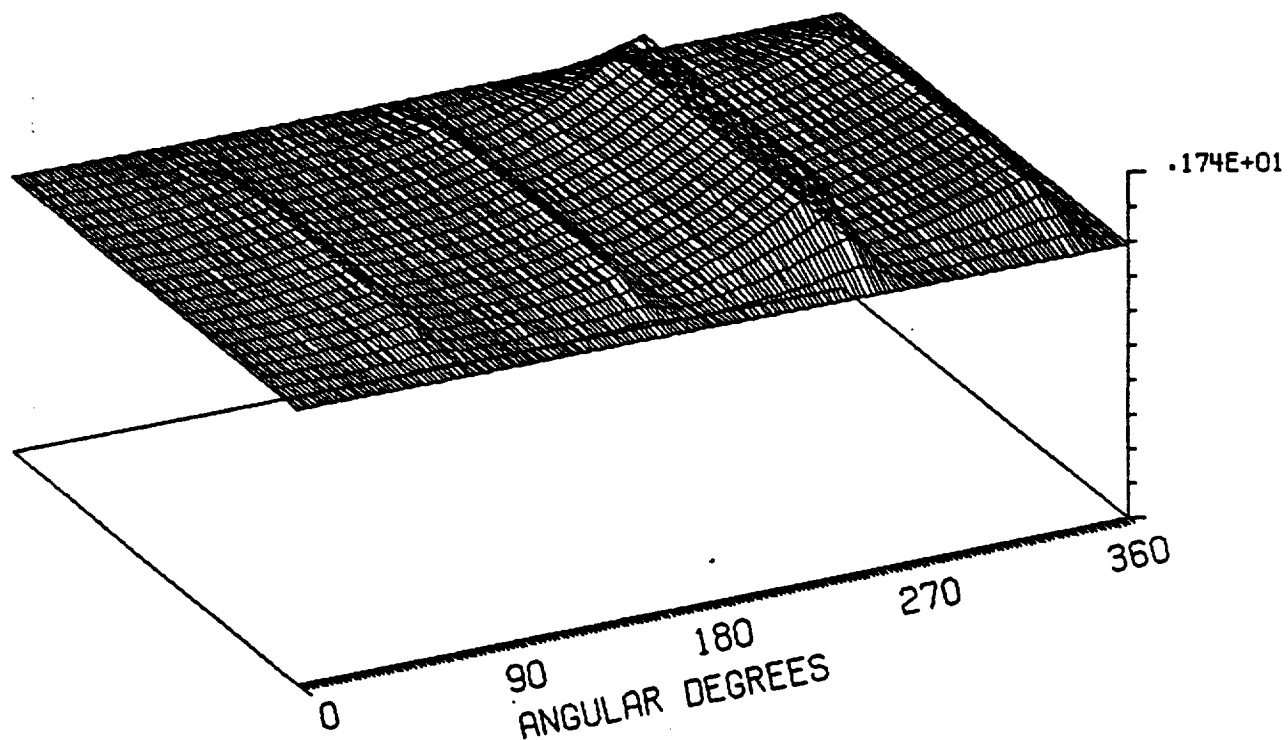
270

180

90

0

ANGULAR DEGREES

Figure 5-29   Pressure Distribution - Rayleigh-Step Seal with Eccentricity

5.3 Verification of GCYL

Several mechanisms were used to conduct verification of the code. For the most part the results of the code were compared against information in the public domain literature, and in some instances, comparisons were made against the results of other codes and against manual computations.

The first case is the pressure distribution of an infinitely long slider. The results are compared at several values of Λ as shown on Figure 5-30.

Further comparisons were made for a plain cylindrical seal with an L/D ratio of 1 with information from reference 3. Computations were made at two different eccentricity ratios, $\epsilon = 0.6$ and 0.8. Non dimensional load capacity and attitude angles are shown on Figures 5-31 and 5-32 respectively. Excellent correlation is demonstrated.

A significant feature of the GCYL code is the computation of frequency dependent stiffness and damping coefficients. The method was first implemented in the compressible Spiral-Groove computer code SPIRALG. These stiffness and damping coefficients are important because they are used to represent the fluid film characteristics in dynamic analysis. Their computation embodies many features of the code including steady state performance. Table 5-7 shows comparisons for three codes for an excitation frequency of zero, and for a 360° cylindrical seal in the concentric position. The first column represents the code GCYL as previously modified with only the capability to compute zero excitation frequencies. The second column represents the latest version of the code with the frequency dependent stiffness and damping routines. The third column are the results produced by the Spiral Groove code with zero groove depth, so that the geometry of the three cases are equivalent.

Table 5-7
Comparison of Spring and Damping Coefficients

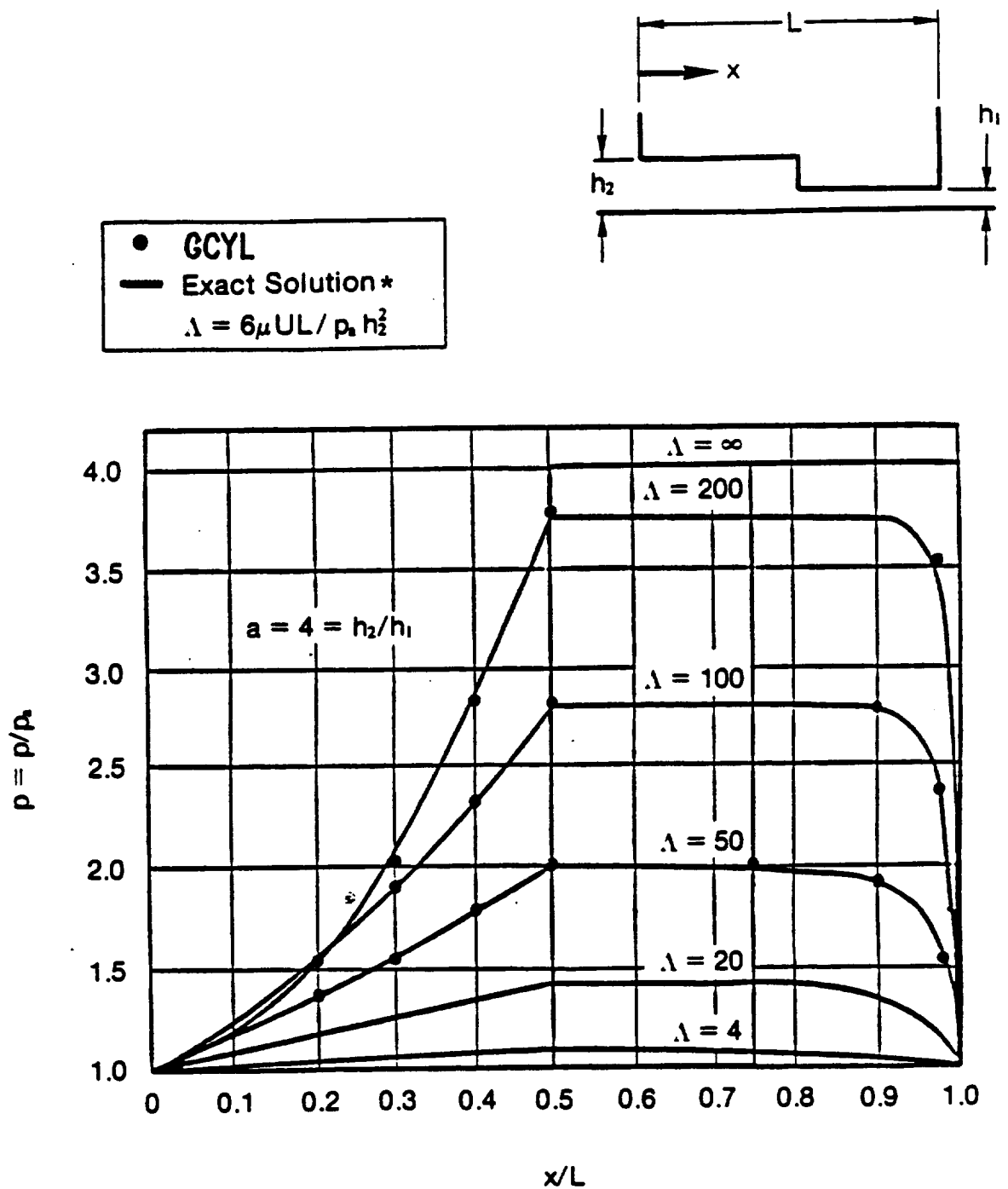| Coefficient	Unit	GCYL (Previous)	GCYL (New)	SPIRALG
K_{xx}	lbs/in	5,715	5,719	5,715
K_{xy}	lbs/in	7,301	7,301	7,363
K_{yx}	lbs/in	-7,107	-7,092	-7,140
K_{yy}	lbs/in	12,550	12,590	12,752
K_{aa}	in-lbs/rad	384.2	384.2	395

Figure 5-30 Rayleigh-Step, Program Verification

*"Theory of Hydrodynamic Lubrication", O. Pinkus, B. Sternlicht,
McGraw-Hill, New York, 1961
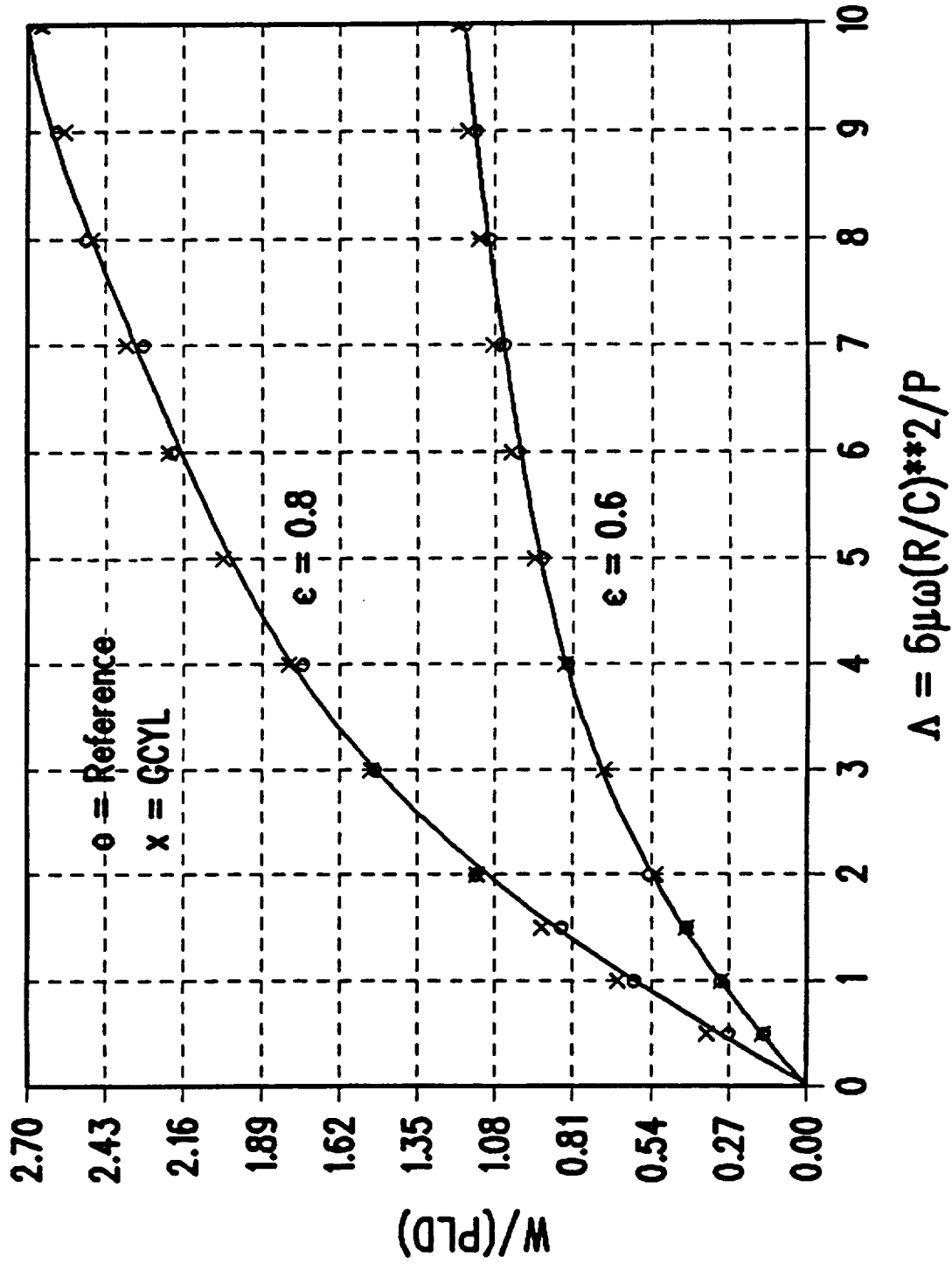
5-71

Plain Cylindrical Seal, L/D = 1

$$\Lambda = 6\mu\omega(R/C)\ast\ast2/P$$

Figure 5-31 Dimensionless Load Capacity vs. Λ

- "Design of Gas Bearings", Published by Mechanical Technology Inc., 1969

Plain Cylindrical Seal, L/D = 1

o = Reference
x = GCYL

ε = 0.6

ε = 0.8

Attitude Angle, φ

$\Lambda = 6\mu\omega(R/C)**2/P$
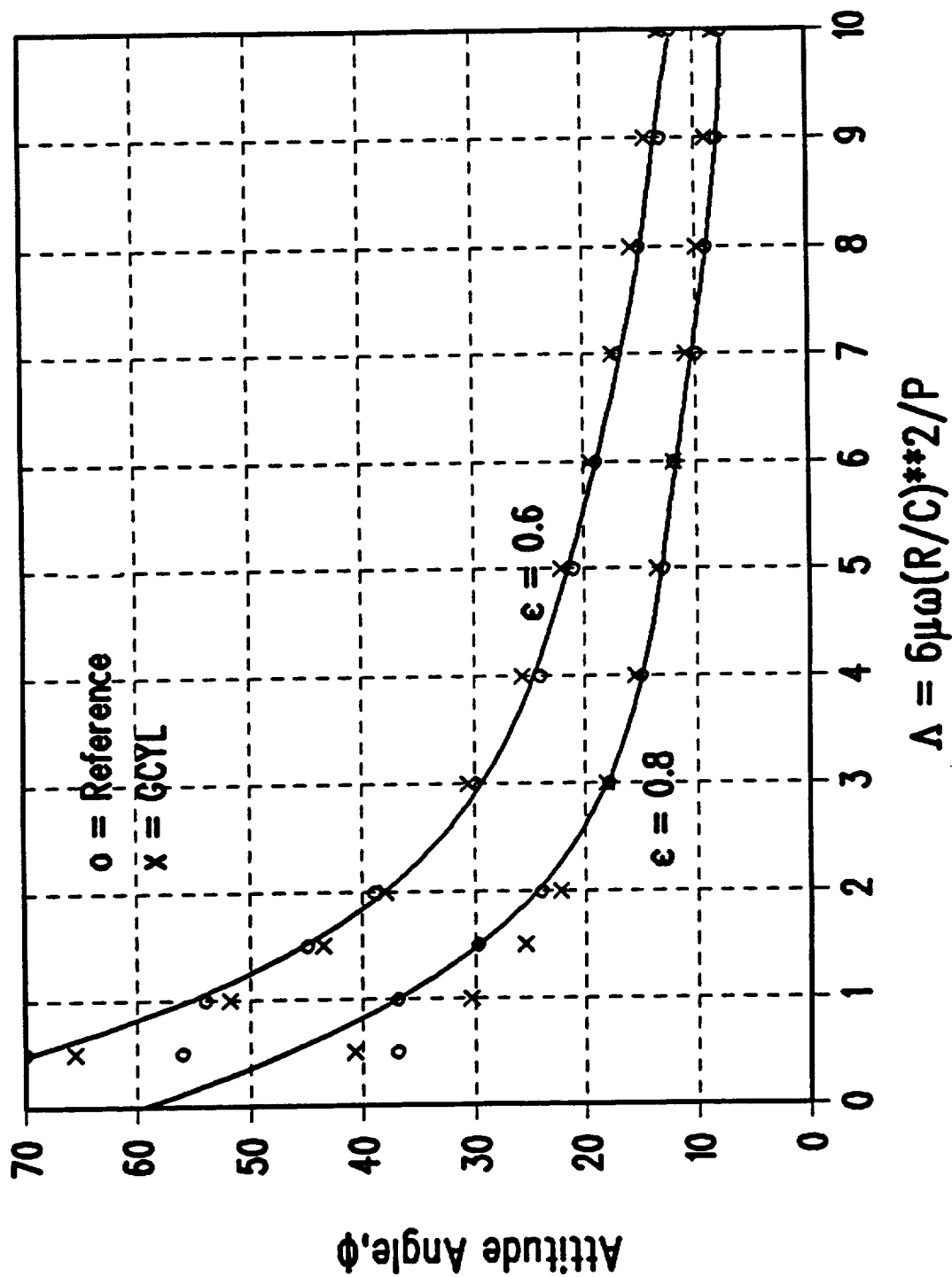
Figure 5-32 Attitude Angle vs., Λ

o "Design of Gas Bearings", Published by Mechanical Technology Inc., 1969

5-73

Table 5-7
Comparison of Spring and Damping Coefficients

Coefficient	Unit	GCYL (Previous)	GCYL (New)	SPIRALG
K_{ab}	in-lbs/rad	181.6	181.6	194
K_{ba}	in-lbs/rad	-277.2	-277.2	-300
K_{bb}	in-lbs/rad	122.6	122.6	124
Damping Constants				
D_{xx}	lb-s/in	1.402	1.387	1.403
D_{xy}	lb-s/in	-1.888	-1.870	-1.855
D_{yx}	lb-s/in	2.992	2.999	3.019
D_{yy}	lb-s/in	1.957	1.897	1.901
D_{aa}	in-lb-s/rad	0.1088	0.1079	0.1148
D_{ab}	in-lb-s/rad	-.0447	-.0450	-.046
D_{ba}	in-lb-s/rad	0.0377	0.0377	0.0385
D_{bb}	in-lb-s/rad	0.0662	0.0659	0.0695

L - 1 in., D - 1 in., C - .001 in., μ - $3\text{x}10^{-9}$ lb-s/in^2, N - 48,000 rpm
ϵ_y- 0.5, excitation frequency - 0

K_{ij} is the stiffness in the i direction due to a j displacement
D_{ij} is the damping in the i direction due to a j velocity
x and y are translations and a and b are rotations.

Table 5-8 shows a comparison for a synchronous excitation (excitation frequency that is equal to the shaft speed). For both situations, the correlation is very good.

Table 5-8
Stiffness and Damping Comparison at Synchronous Frequency

Coefficient	Unit	GCYL	SPIRALG
K_{xx}	lbs/in	7,498	7,467
K_{xy}	lbs/in	1,122	1,203
K_{yx}	lbs/in	-1,122	-1,203
K_{yy}	lbs/in	-7,498	-7,467
K_{aa}	in-lbs/rad	100.1	99
K_{ab}	in-lbs/rad	127.7	134
K_{ba}	in-lbs/rad	-127.7	-134
K_{bb}	in-lbs/rad	100.1	99
Damping Constants			
D_{xx}	lb-s/in	1.603	1.603
D_{xy}	lb-s/in	-0.8657	-0.8613
D_{yx}	lb-s/in	0.8657	0.8613
D_{yy}	lb-s/in	1.603	1.603
D_{aa}	in-lb-s/rad	0.0578	0.0596
D_{ab}	in-lb-s/rad	-0.01518	-0.0146
D_{ba}	in-lb-s/rad	0.01518	0.0146
D_{bb}	in-lb-s/rad	0.0578	0.0596

L = 1 in, D = 1 in, C = .001 in, μ = 3 x 10^{-9}lb- s/in^2,
ϵ = 0.0, N = 48,000 rpm

Table 5-9 shows the variations in stiffness and damping for a 360° cylindrical seal with an excitation frequency equal to operating speed as compared to an excitation frequency of zero.

Table 5-9
Stiffness and Damping Coefficients at
Two Excitations

Operating Speed	rpm	48,000	48,000
Excitation Frequency	rpm	48,000	0
K_{xx}	lbs/in	9,648	5,885
K_{xy}	lbs/in	1,942	7,267
K_{xa}	lb/rad	0.7303	-0.2391
K_{xb}	lb/rad	1.291	1.298
K_{yx}	lb/in	1,040	-7,116
K_{yy}	lb/in	17,670	13,050
K_{ya}	lb/rad	1.451	3.258
K_{yb}	lb/rad	0.4477	1.877
K_{aa}	in-lb/rad	639.4	420.6
K_{ab}	in-lb/rad	71.58	192
K_{ba}	in-lb/rad	-193.8	-293.8
K_{bb}	in-lb/rad	221.1	133.7

Damping Coefficients

D_{xx}	lb-s/in	1.658	1.406
D_{xy}	lb-s/in	-0.7059	-1.859
D_{yx}	lb-s/in	0.9180	3.012
D_{yy}	lb-s/in	1.521	1.897
D_{aa}	in-lb-s/rad	0.090	0.113
D_{ab}	in-lb-s/rad	-0.0311	-0.0473
D_{ba}	in-lb-s/rad	0.0256	0.0393
D_{bb}	in-lb-s/rad	0.0666	0.069

360° Cylindrical Seal, L = 1 in, D = 1 in, C = .001 in,
μ = 3 x 10^{-9} lb-s/in^2, 0 gage pressure at both ends

Substantial differences are noted, which demonstrates the significance of applying proper frequencies when computing stiffness and damping.

An internal check of the code can be made by analyzing a recessed hydrostatic bearing. With the flow path option, the net flow around the periphery of a hydrostatic pad can be determined and compared against the inflow to the recess. For flow continuity, the sum of the peripheral flows should equal the inlet flow. The following geometry and operating parameters were considered.

- A single pad with grid dimensions of 15 x 37 (M x N).
- The pad diameter is 2 inches
- The pad length is 2 inches
- The pad clearance is 0.001 in.
- The pad angle is 180° and the starting angle is at 180°
- There is one recess located in the pad, and the grid corner points are as follows: Left bottom corner, M = 3, N = 22
  Right Top corner, M = 13, N = 27
- The specific heat of the gas is 1.4
- The gas constant is 250,000 in²/(s²-°R)
- The absolute temperature is 530° R
- The absolute viscosity is 3 x 10⁻⁹ lb-s/in²
- The inlet orifice diameter to the recess is 0.020 in and the coefficient of discharge is 1.0. The orifice is located in the grid at M = 8, N = 24.
- The supply pressure to the orifice is 150 psig. The pressure surrounding the pad is at 0 psig. The reference ambient pressure is 14.7 psia.
- Several eccentricities and speeds were examined and are defined in the subsequent discussions.

The output from the code supplies the total flow from the peripheral flow path and the pressure in the recess. A manual computation can then be made for calculating the inlet flow through the orifice using the following equation:

$$f_0 = 386.4 \; A_0 C_D G_1 P_s \left\{ \left(\frac{P_r}{P_s}\right)^{\frac{2}{\gamma}} \left[1 - \left(\frac{P_r}{P_s}\right)^{\frac{\gamma-1}{\gamma}}\right] \right\}^{\frac{1}{2}} \qquad (5\text{-}88)$$

where,

$$G_1 = \sqrt{\frac{2\gamma}{G_c \theta (\gamma - 1)}} \qquad (5\text{-}89)$$

5-77

f_o — inlet flow, lb/s

A_o — orifice area. in^2

C_D — discharge coefficient

p_s — supply pressure, psia

p_r — recess pressure, psia

γ — ratio of specific heats

G_c — gas constant, in^2/(s^2-°R)

θ — absolute temperature, °R

Table 5-10 provides the results of several cases

Table 5-10 Recessed Pad Flow Comparisons

ϵ	N	Q_p	p_r	Q_o	Δ
	rpm	lbs/s	psig	lbs/s	%
0.0	0.0	0.001188	43.2*	0.001189	0.08
0.4	0.0	0.001174	84.4	0.001176	0.17
0.0	70,000	0.001188	36.1*	0.001189	0.08

* Choked Flow

ϵ — Eccentricity ratio

N — Shaft speed

Q_p — Peripheral flow

p_r — Recess pressure

Q_o —Orifice flow

Δ — percent variation

Note that the peripheral and orifice flows differ by less than 0.2%.

When using the source points or spot recess options of the code, it is important to surround the source point with a fine grid to obtain an accurate result and a computation in which pressures will converge. Studies were made of varying grid sizes for a source problem. The variable grid option was applied and varied. A single pad with a central row of orifices were analyzed (see sample problem Number 4). The following information is pertinent:

- Number of pads — 1
- Pad angle — 120°
- Start angle — 30°
- Number of grid points in circumferential direction — 37
- Number of grid points in axial direction — 15

- Diameter — 2.6798 in.
- Length — 1.627 in.
- Specific Heat Ratio — 1.66
- Gas constant — 1,790,000 $in^2/(s^2\text{-}°R)$
- Absolute Temperature — 528°R
- Viscosity — 2.9 x 10^{-9} lb -s/in^2
- Shaft Speed — 0 rpm
- Reference pressure — 14.7 psia
- Boundary pressures — 60 psig
- Supply pressure to inherently compensated orifices
- Preload — 20% located at the center of the pad
- Stiffness is to be determined
- Six source points are located along a circumferential line in the axial center of the pad at circumferential grid locations 5, 10, 15, 20, 25, 30.

The hole diameter is 0.015, and the coefficient of discharge is 1.0. Tables 5-11 and 5-12 indicate the effect of grid width around the source point in both the axial and circumferential directions. Table 5-11 indicates the source pressures as the grid width is changed. They are relatively unaffected until the grid width is 8x the orifice hole size. A similar conclusion can be drawn for the other performance parameters of load, flow, stiffness and damping as indicated by Table 5-12. The recommended grid width from the source point to a neighboring grid line is twice the orifice diameter.

Table 5-11
Comparative Studies - Discrete Orifices Vs. Grid Size
Orifice Size — 0.015 in.

A — Grid width around orifice in both circumferential and axial directions

Comparison of Source Pressures

A in	P_1 psig	P_2 psig	P_3 psig	P_4 psig	P_5 psig	P_6 psig
0.015	129	144	151	151	145	129
0.030	128	144	151	151	144	128
0.060	126	143	149	149	143	126
0.120	122	140	147	136	140	122

Table 5-12, Comparison of Performance

A in.	W lbs	Q_1 lbs/s	Q_M lbs/s	K_{xx} Lbs/in x 10^{-6}	K_{yy} lbs/in x 10^{-6}	Dxx (lbs-s)/in	Dyy (lbs-s)/in
0.015	314.9	0.11338	0.11338	0.0419	0.1320	2.945	16.43
0.030	315.4	0.11393	0.11393	0.424	0.1338	2.933	16.33
0.060	316.4	0.11496	0.11496	0.0432	0.1371	2.911	15.83
0.120	319.3	0.1186	0.1186	0.0446	0.1480	2.866	11.75

A — grid width
W — load capacity
Q_1 — flow out of grid line M-1
Q_M — flow out of grid line M-M
K_{xx} and K_{yy} — Stiffness in x and y directions, respectively
D_{xx} and D_{yy} — Damping in x and y directions, respectively

5.4 REFERENCES

1. Castelli, V. and Pirvics, J., "Review of Methods in Gas Bearing Film Analysis", Trans. ASME, J. Lubrication Technology, October 1968, pp 777-792.

2. Castelli, V. and Shapiro, W., "Improved Method of Numerical Solution of the General Incompressible Fluid-Film Lubrication Problem", Trans. ASME, J. Lubrication Technology, April 1967, pp 211-218.

3. "Design of Gas Bearings", published by Mechanical Technology Inc., 1969.

5.5 NOMENCLATURE

C_d = inherently compensated orifice coefficient of discharge

C_O = reference clearance (concentric clearance)

d_O = orifice diameter

e = shaft displacement from concentric position

F_f = viscous friction force

FF = dimensionless viscous friction force = $F_f/(p_O C_O R)$

G_C = universal gas constant

h = local film thickness

H = dimensionless film thickness = h/C_O

l = bearing length

L = dimensionless length = l/R

N = number of orifices in a row

p = pressure

p_O = reference pressure

P = dimensionless pressure = p/p_O

P_{CR} = critical pressure ratio

P_R = orifice downstream pressure

P_S = supply pressure upstream of orifice

q = mass flow

R = journal radius

r = orifice hole radius

S_c = source correction factor

t = time

t_O = reference time = $\dfrac{12\mu R^2}{p_O C_O^2}$

T = dimensionless time = t/t_O

T_a = absolute temperature

T_f = viscous friction torque

TF = dimensionless viscous friction torque = $T_f/(p_O C_O R^2)$

U = journal surface velocity

z = axial direction coordinate

Z = dimensionless axial coordinate = z/R

α = misalignment angle about x-x axis

β = misalignment angle about y-y axis

γ = ratio of specific heats

ϵ = eccentricity ratio = e/C_o

θ = angular direction (direction of sliding)

θ_p = angular extent of pad

Λ = compressibility parameter = $\dfrac{6\mu\omega R^2}{p_o C_o^2}$

μ = absolute viscosity

ω = rotating speed

6.0 Knowledge Base System Development

One of the significant aspects of the overall program is the generation of a Knowledge Based System (KBS) having the following objectives:

1) To integrate the scientific and industrial codes into a package that will provide access to important technical data and information to facilitate generation of optimum seal configurations.

2) To provide a user friendly graphical user interface with context sensitive help.

3) To provide Expert systems to help select the type of seal best suited for the intended application, analyze user input and output of analysis codes to guide the seal design optimization process.

This report describes the architecture of the KBS and the development of the user interface elements during the first year of the program.

6.1 KBS COMPONENTS

A schematic of the KBS is shown in Figure 6-1. Functions of the various components are described below.

6.1.1 Executive Program

The executive shell integrates all the components of the KBS and provides the user with a single point of access for all the resources in the KBS. Features of the executive are:

■ Access to scientific and industrial codes.

■ Access to the expert systems for seal type selection and seal design guidance.

■ Utility functions including browsing and printing output files created by the analysis programs, plotting routines to display the results in a graphical form, and procedures for the users to add their own programs to the KBS.

■ Network communications with the Cray X-MP computer used for running the scientific codes. The communication procedures will be made as transparent as possible.

NASA Workstation
Functional Block Diagram
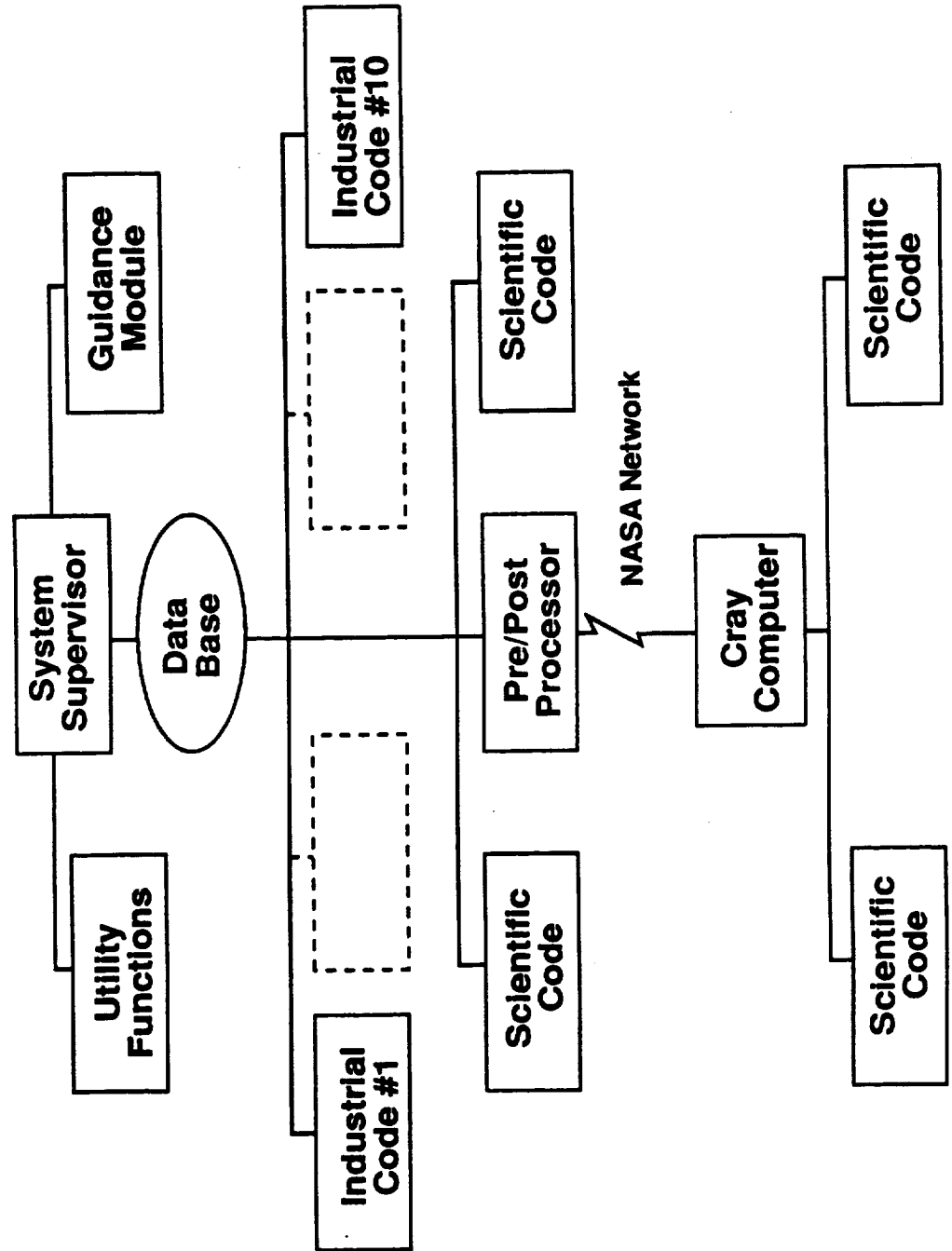
■ Database services to access the databases used to store input and output data sets for the analytical codes. The access will be controlled using passwords to prevent unauthorized access.

6.1.2 Scientific Codes

Scientific seal analysis codes will provide steady-state and transient analysis capability based on full three-dimensional Navier-Stokes equations. Other characteristics of these codes include the following:

■ Cylindrical, polar, and non-orthogonal body-fitted coordinates

■ Stationary and rotating coordinate systems

■ Advanced turbulence models suitable for high-shear rotating flows

■ Incompressible and compressible flows

■ Cavitation or liquid film rupture

■ Energy conservation equation with viscous heating and phase changes

■ Provisions for additional field equations such as electromagnetic and electrostatic forces

The seal analysis will encompass a number of generic seal categories including Cylindrical, Labyrinth, Damper, Honeycomb, Face, Noncontinuous, Wave, Grooved, Tip, Contact, and Brush seals. The models for these seals will be very extensive and detailed, requiring a Cray X-MP class computer for execution in a reasonable time.

The KBS will be used to prepare the input data and the input files sent to the Cray using a network. After execution, the output files will be downloaded from the Cray computer and post-processed on the KBS. The users of the scientific codes are expected to be high-level research personnel familiar with the fundamental theories used in the codes, the mathematical underpinnings and the basic structure of the code, and the types of seals being analyzed. The assistance provided to these users will focus on the mechanics of defining the analytical model during input. An extensible database of typical models will be provided as a starting point for user input. The final user input will be checked using expert systems to ensure that all the necessary input has been supplied and that there are no obvious errors in grid specification, boundary conditions, material characteristics, etc. This function is essential given the expense of running these codes on a Cray computer. Expert systems and conventional data reduction software will be provided to assist the user in interpreting the outputdata.

6.1.3 Industrial Codes

The industrial codes are simpler two- and three-dimensional codes for several different types of seals. Some of the codes included in the package are:

- Bushing and Ring Seals
    - Uniform
    - Axial Step and Taper
    - Hydrodynamic Step and Taper
    - Self Energized Hydrostatic
    - Segmented
- Face Seals
    - Contact Face Seals
    - Radial Step and Taper
    - Hydrodynamic Step and Taper
    - Hydrostatic
    - Spiral Groove
    - Multi-pad
- Labyrinth Seals
    - Straight
    - Stepped
    - Abradable
    - Angled
- Tip Seals
- Damping Seals
- Brush Seals
- Electro-fluid Seals
- Smart Seals

The anticipated users of the industrial codes include seal design and application engineers, seal users such as rotating machinery designers, and analysts performing seal design audits and failure analysis. These users may not be familiar with all of the seal analysis capability incorporated into these codes or with all of the design and analysis options available for a specific application. The assistance provided to these users will include extensive on-line, context-sensitive help for each code, and error trapping to ensure that input values are within admissible limits. A graphical user interface using windows and drop-down menus will be provided for each code to ensure a uniform look and feel. The names of menu items and seal variables will be standardized to reduce the learning curve. Expert systems will be provided as needed to guide the user in setting up an optimum analytical model and to interpret the output data.

Seal design optimization is an iterative process involving seal interfacial analysis, rotordynamic analysis, and thermo-elastic analysis. Expert systems will be provided to guide the user through this process by helping the user to select the analyses to be performed and to decide when to terminate the iterative process.

6.1.4 Databases

Databases will be included to store input and output data sets for example problems and for problems used for analytical code validation. The databases will also enable users to develop a library of analytical models tailored for their individual needs and to maintain a history of analyses performed using the codes. The analytical codes will access their databases directly to store and retrieve data. Users may also access the databases using database services provided through the executive.

6.2 HARDWARE AND SOFTWARE SYSTEM SELECTION

6.2.1 Initial System Selection

The hardware and software system selection were driven by the need for a graphical user interface and the computational requirements for the analysis codes. The choice was complicated by having to anticipate the hardware and software availability six years down the road, by a wide variation in the computing power available to the anticipated users, and by the wide range of computational requirements for the individual analysis codes.

After a review of KBS requirements, an Intel 80386 and 80486 based IBM PC compatible hardware platform running OS/2 with the Presentation Manager interface was selected. FORTRAN 77 was selected for implementing the analytical codes and C as the primary language for user interface development. Developing graphical user interfaces is a time consuming process. The Toolbook authoring system was selected to explore alternatives to

developing the user interfaces in C. NEXPERT Object was selected as the expert system shell. NEXPERT is available for several operating environments and provides portable knowledge bases. Other options considered included UNIX on RISC workstations and Windows 3.0. The reasons for selecting OS/2 were as follows:

■ The ease-of-use features planned for the KBS provide the most benefit for projected users of the industrial codes who may not be intimately familiar with the content of the codes and may not be comfortable using computers. These users are in organizations that typically use Intel based, IBM PC compatible machines. Therefore, Intel 80386 or 80486 based machines were selected to enable users to use existing hardware.

■ Windows environment was not acceptable because of its DOS based limitations on memory, networking support, etc. Most of the analytical codes require more resources than provided by DOS. While it was possible to provide a collection of utilities to overcome these shortcomings, the cost of maintaining and developing a large software package like the KBS with such makeshift arrangements would be prohibitive in the long run.

■ UNIX is a complex multi-user, multitasking operating system. It requires considerable expertise to install and manage UNIX systems. The expected users of the industrial codes are used to simple DOS systems and usually do not have the expertise or the support staff to manage UNIX systems. The multi-user capabilities provided by UNIX do not add enough value to offset the added complexity and cost of development.

■ OS/2 combines the best features of UNIX and Windows environments.

■ OS/2 is a single-user system. This reduces the complexity of the operating environment and the time required to learn it. However, the system security features such as log in control provided by UNIX and needed for a multi-user system are not available in OS/2.

■ Like UNIX, OS/2 is a robust multitasking system designed for use over networks. In addition, it has features such as Multi-threading, Dynamic Data Exchange (DDE), Dynamic Link Libraries (DLLs), and Installable File System (IFS) which are not yet available in UNIX. These features implement operating system concepts developed in recent years and provide a flexible, extensible operating environment. Multi-threading is essential for support of multi-processor hardware platforms. DDE allows for data links between programs that are more flexible than traditional inter-process communication method. DLLs allow development of code modules shared by several programs and easy upgrade of software already in use.

■ The cost of third party software for OS/2 is comparable to DOS and Windows environments, and is much cheaper than similar UNIX software. The ability of OS/2 to run current DOS software in the DOS compatibility

mode and the use of the DOS file system makes for an easy transition for expected users of the industrial codes.

■ OS/2 Extended Edition is the most comprehensive software development environment available today. The Application Programming Interfaces (API) for the base operating system, the database manager, and the communications manager provide a rich, robust, and well integrated environment to develop applications with seamless access to databases and networking capabilities. On any other platform these capabilities would have to be duplicated with tools from several different vendors which do not always work together cleanly. That is why OS/2 is becoming the platform of choice for mission critical applications and for downsizing mainframe or minicomputer applications using a client-server architecture.

■ OS/2 Version 2.0, due before the end of 1991, will be a 32-bit operating system with an API that is portable to non-Intel hardware platforms.

Based on comments by the peer review panel after the first workshop at NASA Lewis research Center, development of the KBS was interrupted to re-evaluate the harware and software system selection. A segment of the attendees at the annual workshop and members of the Peer Review Panel appointed by NASA favored the UNIX operating system. NASA did not want to deny UNIX users access to the KBS by limiting the development to OS/2.

6.2.2 *Hardware and Software System Re-evaluation*

Issues of software portability, cost of a delivery system, availability of adequate software development and maintenance tools, cost of software development, and expected evolution in operating system environments are under evaluation.

6.2.2.1 *Hardware Platforms*

The hardware choices being evaluated are Intel 80386 or 80486 based IBM PC compatibles and RISC workstations. The advantages of an Intel-based platform are wide availability and low cost. Most of the anticipated industrial users are already using Intel-based machines. The major advantage of RISC machines is better floating-point performance. There are, however, several competing RISC platforms. This makes it necessary to commit to one hardware vendor or bear the additional costs of supporting all the different platforms used by the anticipated users of the analysis codes. It is anticipated that the performance of high-end PCs and low-end workstations will converge over the next few years. Therefore, the hardware platform should not be a decisive factor in the final system selection process.

6.2.2.2 Operating Systems

The two operating systems being evaluated are a flavor of UNIX with OSF/MOTIF user interface, and OS/2 with the Presentation Manager interface. Both these systems offer a multi-tasking environment which is a must for a system that has analytical codes that take a long time to execute. The user must have access to other functions on the machine while analysis proceeds in the background.

The advantages of UNIX are portability between Intel-based and RISC platforms running the same version of UNIX. Major disadvantages of UNIX are the number of different versions available from different vendors and the high cost of third-party software. UNIX vendors seem to be converging on two versions: System V Release 4 from Unix International with the Open Look Interface and OSF Unix with the Motif interface. Porting software between versions is not a trivial task. Additional disadvantages of UNIX on Intel-based machines are slow speed, large memory and disc size requirements.

The advantages of OS/2 are a modern, integrated design that provides all the facilities needed for developing applications with graphical user interfaces, ability to run thousands of existing PC-DOS applications, lower cost third party software, and lower memory and disc size requirements. Currently, the major disadvantage is lack of portability to non-Intel hardware. However, a portable version of OS/2 that uses the same programming model as OS/2 version 2.0 is expected to be available in the 1992-93 time frame.

Apple Computer and IBM recently signed a letter of intent to jointly develop a new object-oriented, portable operating system. A new object-oriented operating system that will run on Intel x86, Motorola 680x0, and IBM RS/6000 based computers and which will run existing AIX, Macintosh, and OS/2 applications. The new platform will be developed by a new company jointly owned by Apple and IBM. An industry standards group will be formed to set standards for the emerging software architecture and act as a clearinghouse for information about the project. The operating system will be available in two to three years and will be made available to other hardware platform vendors. The operating system will be based on reusable software components easily portable to various systems. The object oriented nature of the system will allow vendors to differentiate their version of the enviroments by adding features such as portions of Macintosh and OS/2 operating systems or other applications. The level of customization will be greater than that provided in the current NextStep environment on NEXT machines, which is the only object-based operating environment currently available. Object oriented technologies developed by the joint company will be incorporated into OS/2 and the Macintosh operating systems as it becomes available to facilitate their integration into the jointly developed operating system. Apple and IBM will provide application programming interfaces (API) for the older operating systems like OS/2 and Macintosh to allow them to run new object-oriented applications. For IBM,

OS/2 will evolve to be a migration path to the new operating system in the late 1990's. An encapsulation technology will be provided to allow older applications to run on the new hardware/software platforms. This may include providing full binary compatibility so that the older applications do not have to be recompiled.

6.2.2.3 Portability Issues

Software portability was considered at three different levels:

1. The analysis codes are being developed using ANSI standard FORTRAN 77 for portability. The codes are currently being designed to read input from a file and write output to a file. These codes need only to be recompiled for use on any system.

2. Input and output post-processing programs with an easy-to-use graphical user interface. These programs will create the input files needed by an analysis code and read the output files for post-processing, viewing results, etc. This portion of the code is usually operating system dependent. Software tools that provide portable code for porting graphical user interfaces between UNIX and OS/2 are now becoming available. These are being considered.

3. Advanced, interactive two- and three-dimensional graphics capability. This capability is envisioned for future versions of the analysis codes as low-cost, portable software tools become available for developing interactive graphics applications. The current graphical user interfaces are being designed to enable future incorporation of these capabilities.

6.2.2.3 Software Development Tools

MTI experience with developing the user interface for the industrial codes showed that conventional approaches to developing software are not cost effective when developing software with graphical user interfaces. A number of tools are becoming available that significantly reduce the cost of developing a graphical user interface and, in some cases, provide means to port the interface between different operating environments such as OS/2 and UNIX with OSF/Motif interface. These packages usualy allow porting of user interface elements such as windows, menus, dialog boxes, scroll bars, and buttons. The code for other graphics elements drawn using graphics primitives such as lines, areas, curves, and special features such as detectable, dynamic segments for interactive graphics is not ported. These elements can be implemented using function libraries that provide support for standards like PHIGS and GKS. However, these libraries usually require a run-time license for each workstation that runs code using the library. Some of the available tools for developing graphical user interfaces are described below.

Open Interface from Neuron Data. Open Interface is a software development environment that allows the development of portable code for a graphical user interface for DOS/Windows, OS/2 Presentation Manager, Unix with Motif and Open Look, Macintosh, and VAX VMS DEC Windows environments. The interface code is developed using a graphical screen layout tool which generates codes using generic C function calls designed by Neuron Data. This code is then compiled and linked with libraries for the environment to which the code is being ported. Cost of the development system is $9,000 for OS/2 and $12,000 for Unix. Run-time systems are $350 and $500 for OS/2 and Unix, respectively. The Open Interface environment was used by Neuron Data to develop the NEXPERT Object expert system shell that is availble for all of the above environments.

CaseWorks. CaseWorks is a software development environment for developing a graphical user interface for Windows 3.0, OS/2 Presentation Manager and Unix Motif environments. The development system generates C code for an interface defined using CaseWorks tools. The Unix Motif product has been developed but is not shipping at this time because of a lack of demand for it. The company claims it is ready to ship it if there is sufficient demand for it. The cost of the OS/2 version is $2,000. There are no run-time fees.

Extensible Virtual Toolkit (XVT). XVT is a set of libraries that support the Macintosh, Windows, OS/2 Presentation Manager, Open Look, and Motif environments. The user interface is developed using XVT function calls, and the resulting code is copiled and linked using an XVT library for the environment in which the application is going to run. The cost of XVT is $800 for DOS, Macintosh and OS/2 environments and $3,500 for UNIX environments.

Information Engineering Facility (IEF) from Texas Instruments. IEF is a DOS and OS/2 based CASE tool. The current version supports software development for OS/2 Presentation Manager and Windows graphical user interfaces. A new version due out at the end of the year will let the developers distribute applications developed with IEF on HP 9000 and IBM RS/6000 running UNIX with the MOTIF GUI. This facility is geared towards developing business software that uses a mainframe database as a central source of data, with software running on DOS and OS/2 workstations. Prices vary depending on the configuration but are in the $6,000 to $10,000 range.

Gpf - GUI Programming Facility from Microformatic. Gpf is a software development environment for developing a graphical user interface for the OS/2 Presentation Manager. The development system generates C code for an interface defined using Gpf tools. Gpf is a sophisticated tool that includes tools for reading data from the OS/2 Database Manager databases. Gpf generates the code with the SQL commands and the C function calls required to open and read data from the databases. The cost of Gpf is $3,500 with no run-time fees.

Gpf is not available for any other platform at this time. It would be the tool to use if we stay with OS/2 as the operating system.

Expert System Shells. The CLIPS library of C routines available from COSMIC is currently limited to a forward-chaining reasoning capability. An object-oriented version is being developed. However, CLIPS is best suited for embedded expert systems and may not be convinient for this project if expert system capabilities are to be integrated with advanced 3-D interactive graphics in future versions of the codes. We need an object oriented expert system shell that is potable across several operating environments. NEXPERT Object seems to be the best compromise based on capabilities, portability, and cost. Third party tools are available for developing interactive graphics applications using NEXPERT. The selection of an expert system shell can be put off until early 1992.

Database Management Systems. The cost of OS/2 Extended Services (this includes the Database Manager, the Communications Manager and the OS/2 LAN Requester) is about $600. IBM has announced that the OS/2 Database Manager is being ported to AIX and will be available in the second or third quarter of 1992. The price for the AIX version has not been announced. Third party relational database management systems such as Oracle and Informix are available for both OS/2 and UNIX. Cost of a single user version of Oracle is $2,000 for UNIX and $1,500 for OS/2. A C language interface is included in the price. The run-time version of Oracle for OS/2 costs $200; The price for a UNIX run-time version was not available. The cost for the required tools for a development system (1-2 users) for Informix is $3,800 for Unix and $995 for OS/2. Run-time prices are $1,540 for UNIX and $295 for OS/2. The costs for Informix include the 4GL compiler.

Object-Oriented Programming (OOP). Graphical user interface are composed of objects such as windows, buttons, etc. and are, therefore, a natural application for OOP techniques. Programming using objects allows the developer to work with objects such as windows while hiding the details of how the object works. This saves development and maintenance costs and facilitates portability between operating environments. The details of how an object works are buried in the definition of an object, not in the application that uses the object. Only the object library needs to be changed when porting between environments. The two OOP languages suited for this project are Smalltalk and C++. Smalltalk is a pure OOP environment while C++ is a hybrid language consisting of OOP extensions to C. Smalltalk V from Digitalk is available for Macintosh, Windows, and OS/2 environments. A UNIX version is planned. While Smalltalk is the best choice based on technical reasons, C++ is better for this project given the preference for C expressed by the peer review panel. The best C++ environment that is available on both UNIX and OS/2 is Glockenspiel C++ with the CommonView2 class library. The cost is $900 for OS/2 and $5,500 for IBM RS/6000 series machines.

Other Tools. There are several other tools available that generate executable files that require runtime licences. These tools are not discussed given the preference for C expressed by the peer review panel.

6.3 RECOMMENDATIONS

MTI recommends that we persue a two track development plan:

- Develop the scientific codes on a UNIX platform used by a majority of the large aerospace companies. IBM AIX can be used if eventual migration to the new IBM-Apple operating system is desired.

- Continue development of Industrial codes on an OS/2 platform with eventual migration to the new IBM-Apple operating system.

- Integrate the two systems using network communications. The integration task will be quite simple once DCE protocols are available for UNIX and OS/2.

Object oriented tools such as Glockenspiel C++ and CommonView 2 class libraries which are portable between OS/2 and UNIX should be used to develop all the user interface code. This approach will leave open the option of using only one development platform and then porting to other platforms by recompiling the code on those platforms. In that case, MTI recommends that OS/2 be the development platform given the reduced cost of development tools and lower development costs because of a simpler operating environment.

ANSI standard FORTRAN77 should be used to develop the analytical codes. The codes should be designed such that they can also be used without the graphical user interfaces developed for the KBS. This will permit their distribution to customers using hardware and software platforms not supported by the KBS.

Use a portable shell such as NEXPERT to develop the larger expert systems. Smaller embedded systems can be developed using CLIPS or other C libraries.

6.4 IMPLEMENTATION OF THE SEAL ANALYSIS KBS

The work done during this period focused on the development of a graphical user interface for some of the industrial seal codes and the executive program. OS/2 Presentation Manager (PM) and other system facilities were used to provide an interface with windows, drop-down menus, context sensitive help, dialog boxes for program input, and interactive graphics to

reduce the amount of numeric input where it was feasible to do so. The user interface was implemented for the following codes:

- The executive program that is used to control access to all the analysis codes and provide utility services such as printing and browsing text files.

- Spiral Groove Gas Seals Analysis (SPIRALG)

- Cylindrical Gas Seals Analysis (GCYL)

- Incompressible Cylindrical Seals Analysis (ICYL)

- Fluid Properties Calculations (FLUIDPROPS)

- Spiral Groove Face Seals Optimization Program (SPIRALP)

6.4.1 Description of User Interface

The opening screen for the executive program is shown in Figure 6-2. Each program has its own button displaying the icon for the program. The user only has to click on the program button with a mouse to start a program. User options are selected from drop-down menus accessed from the action bar using either a mouse or a keyboard. For example, the FILE menu has options for printing and browsing text files such as output files created by the analysis programs. Figure 6-3 shows the output file from an analysis program being viewed in the browse window. Figure 6-4 shows the file selection screen for selecting input and output files. Plotting capability is currently provided using existing PC-DOS programs. A fully integrated OS/2 capability will be added in the future.

Multitasking features of OS/2 are used to allow the user to have several codes running at the same time. The number of codes active at any time is limited only by memory available on the computer. Figure 6-3 shows the executive program and a Cylindrical Gas Seals analysis code (GCYL) active at the same time. The analysis code has been reduced to an icon (the same icon that is used in the button) to reduce screen clutter. Within each program, input and analysis are run as separate processes. This allows the user to start analyzing a data set and then prepare the input for the next analysis while the current analysis is in progress.

Names of menu items are kept consistent between programs. For example, seal analysis variables are categorized according to function such as defining the scope of the analysis, specifying seal geometry, operating conditions and lubricant properties, etc. These functional groups are the same for most types of seals but the variables in each group change depending on the type of seal. The INPUT menu shown in Figure 6-5 lists the functional groups applicable for GCYL. Selecting a group from the list opens up a dialog box for entering values for variables in the group. All industrial codes have the same input menu list
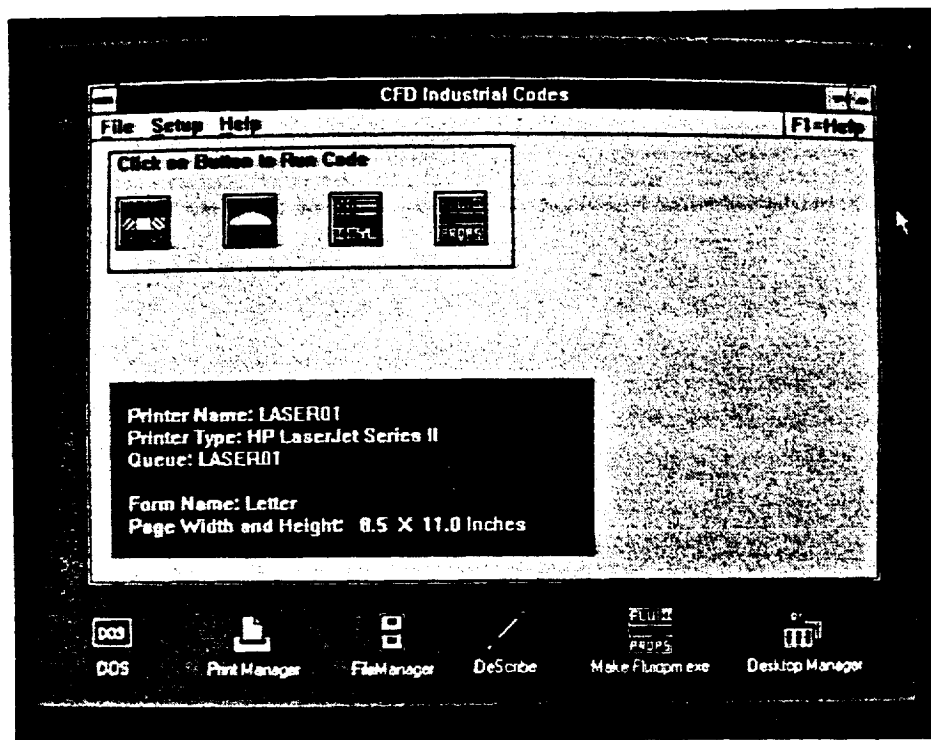
FIGURE 6-2 Executive Program Main Window
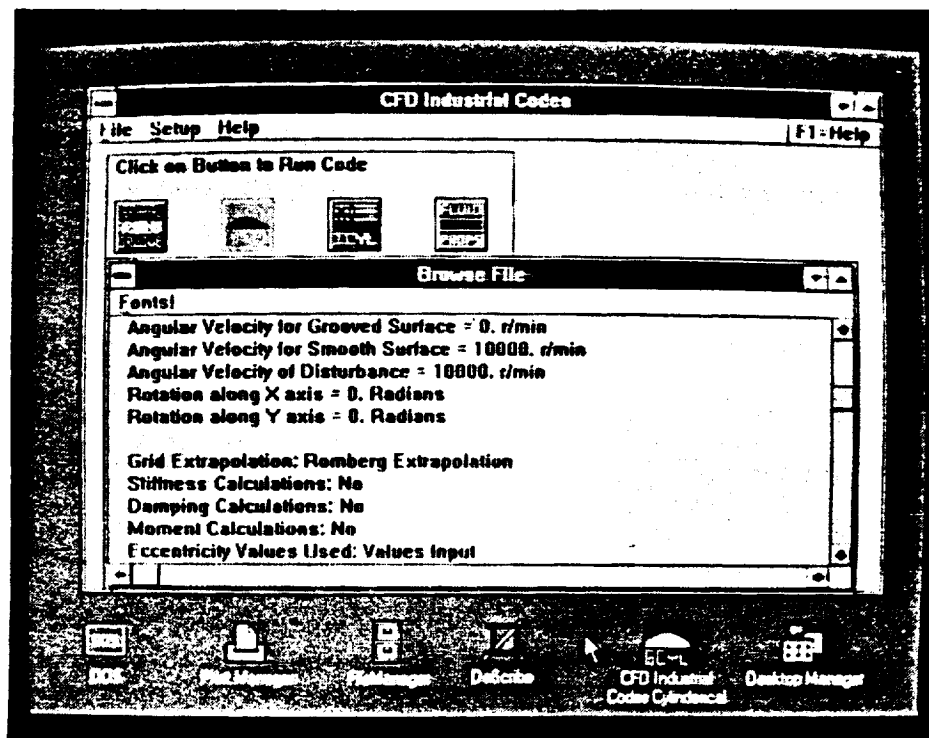
FIGURE 6-3 Browsing Output File
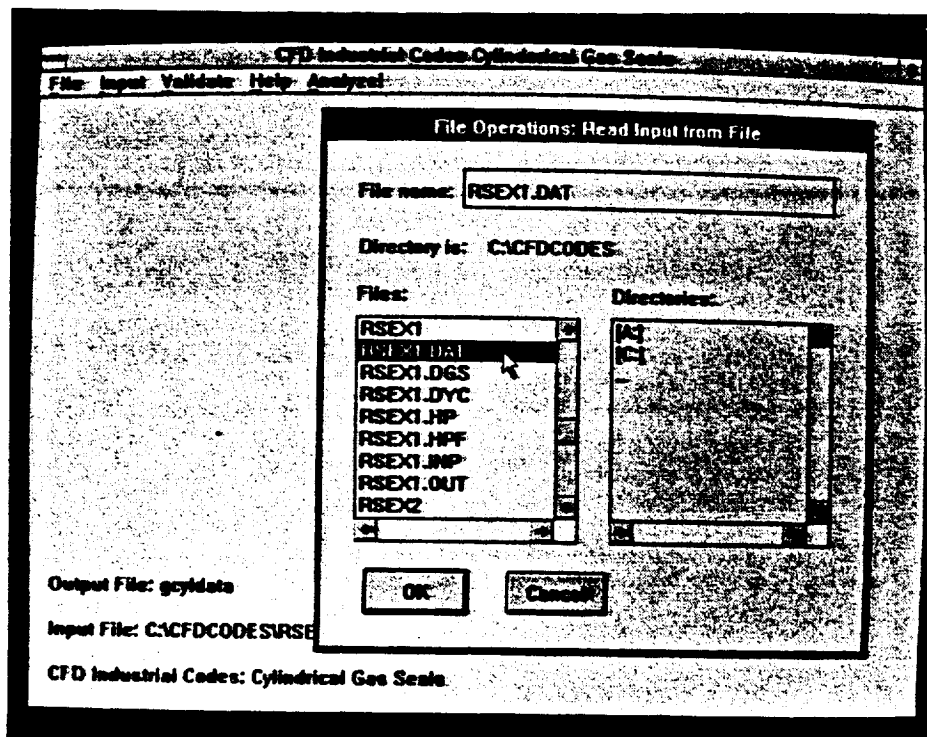
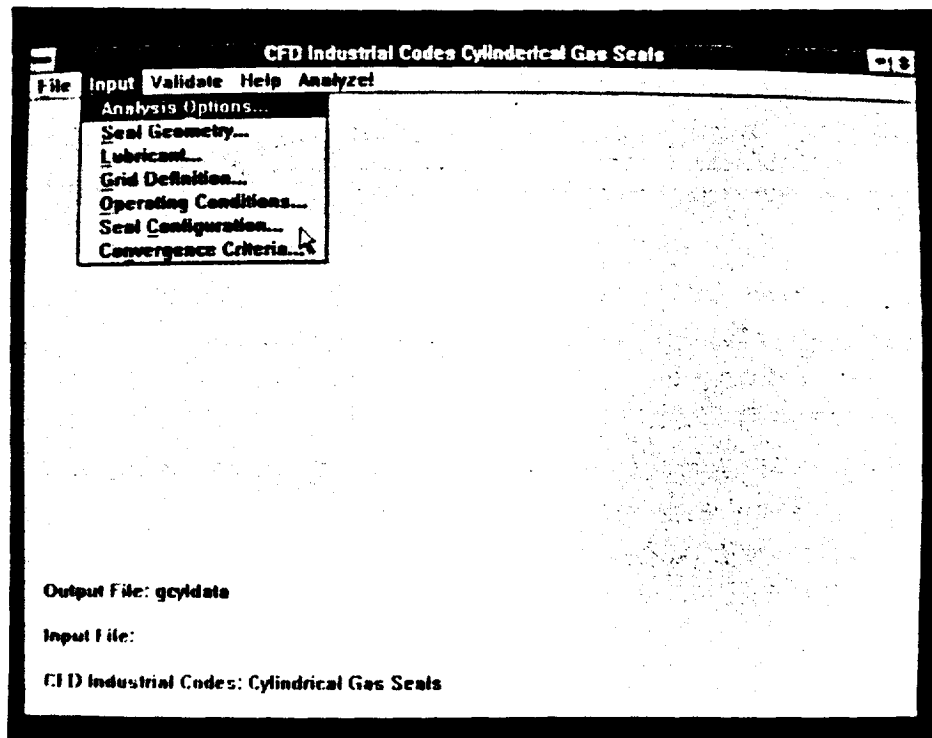FIGURE 6-4 File Selection Screen Input and Output

FIGURE 6-5 Standardized Input Menu Items

6-17

V91-239

but the contents of the dialog boxes change depending on the seal type being analyzed. Examples of dialog boxes for the Analysis Options and Grid Definition menu items are shown in Figures 6-6 and 6-7, respectively. This consistency allows the user to quickly locate the variables to be input in any of the codes. Within each functional group, the names of variables have been made consistent across programs. Variable and user interface consistency should reduce learning time and make the codes easy to use by reducing the volume of information the user has to learn to master the interface. The user is left free to concentrate on the technical content of the codes.

User input for analysis programs is done using dialog boxes containing entry fields for numeric data, radio buttons for selecting mutually exclusive options, and check boxes for selecting other optional features. The choices are presented in simple language avoiding computer jargon. Default values are provided for all variables. The user can move between fields using the mouse or the keyboard. Figure 6-8 shows a data entry screen from a code to calculate fluid properties. The input options are restricted to admissible values. For example, when the user selects fluid property calculations for specified temperatures and density, only the temperature and density entry field are displayed. The values entered in the fields are checked against acceptable limits. The limits are dynamic, and may change depending on the values of related variables. When the user switches the types of units used in the input, the values displayed in the entry fields and the unit labels are changed to reflect the choice of the user. The output is displayed using the same units as the input. The input values are saved by clicking on the ACCEPT button. Clicking on the DISCARD button discards the changes.

Interactive graphics capability is provided where needed to reduce the amount of numeric input and to make the input more intuitive. For example, seal pads in padded seals analyzed by the GCYL code have several features on them such as recesses, Rayleigh steps, and fluid sources. In the original program, the user had to input the grid coordinates for the location and extent of all these features. An interactive capability is provided to enable the user to lay out the features on the grid using the mouse. Figure 6-9 shows a seal pad with a Rayleigh step and several constant pressure points. The user can add or delete the features shown in the features palette by using the mouse. The user first selects a feature from the palette by clicking on the appropriate radio button. The mouse pointer changes its shape to reflect user selection. The pointer is then moved to the grid window and the feature is placed on the grid by clicking the mouse at the appropriate grid location. Grid coordinates of the mouse pointer are displayed in the lower left corner of the grid display window. If additional information such as step height for a Rayleigh step is required for a given feature, entry fields are displayed above the features palette. The user interface code handles the details of generating the correct input statements for the GCYL code.

Help is available at any time through the HELP menu or by pressing the F1 function key. The F1 key help is context sensitive. For example, if the user is entering data in an entry field and
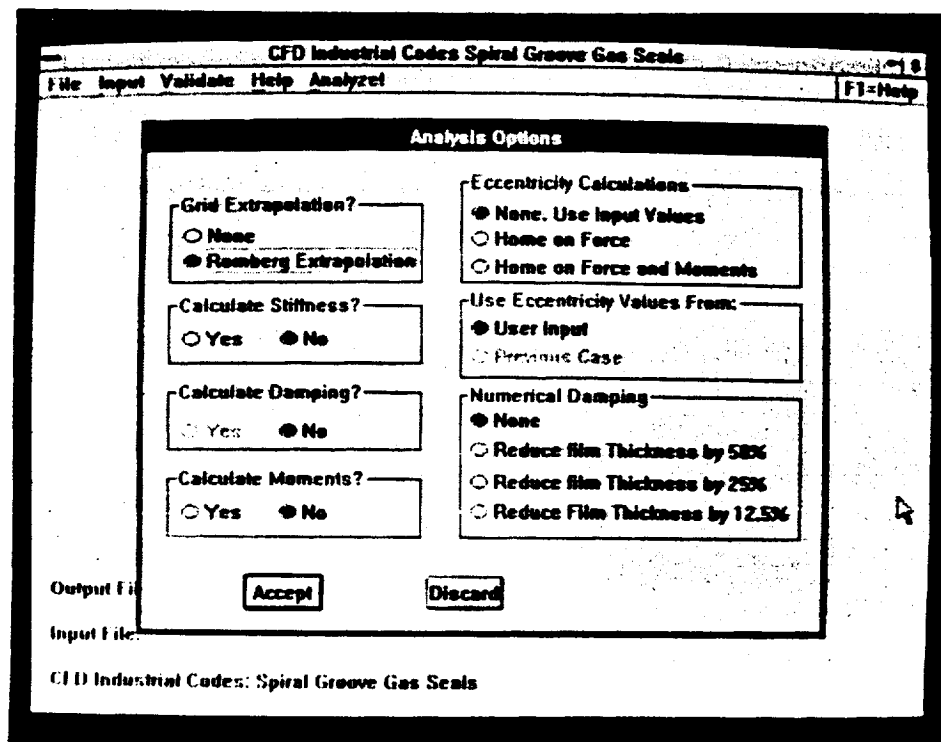
FIGURE 6-6 Analysis Options Screen for Spiral
Groove Gas Seals Program.

FIGURE 6-7 Grid Definition Screen for Spiral
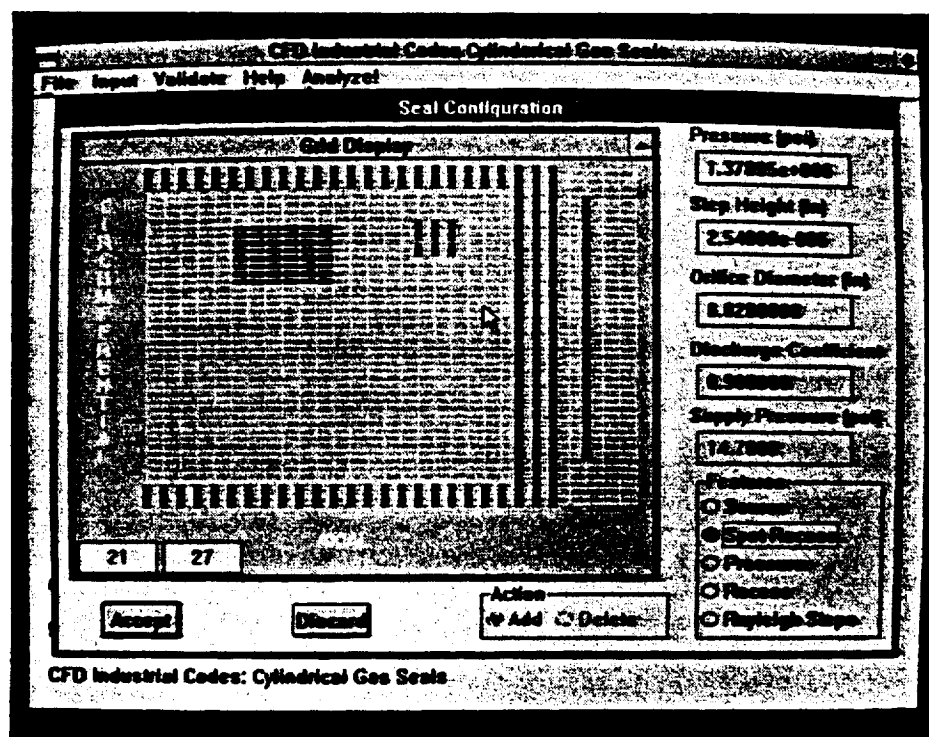Groove Gas Seals Program.

FIGURE 6-8 Data Input Methods

FIGURE 6-9 Interactive Specification of Seal Features

presses the F1 key, the help information for that field is displayed. Figure 6-10 shows the help window that pops up when the F1 key is pressed while entering data in the "Groove Angle" field in GCYL. Figures from manuals are included in the help system. Once the help window is displayed, the user is free to browse through any portion of the help system for that code and has access to all the help utilities such as searching, printing, etc. provided by the Information Presentation Facility (IPF) in OS/2. Hypertext links are used as needed to provide explanations for technical terms used in the help information. The help for each program includes the following information:

- The purpose of the program

- Its capabilities and limitations

- References for additional information

- Code validation.

- Description of input and output parameters

- Examples describing the problem and showing typical input and output data sets

- Description of procedures for the user interface

6.4.2 Current Status of KBS Components

This section describes the status of the various components of the seal analysis KBS.

6.4.2.1 Executive Program

The structure of the executive program is shown in Figure 6-11. The main program is designed to use separate threads for utility functions such as printing files and plotting data. This allows the user to have access to other program functions while these functions are being performed. When the user clicks on a program button, the analysis program is launched as a separate process. The button is disabled to prevent the use of multiple instances of the same program. The utility functions are available through the File menu. Utilities to print and browse output files have been implemented. Plotting capability will be added later.

Help is available from the Help menu or by using the F1 function key. The help information needs to be updated.
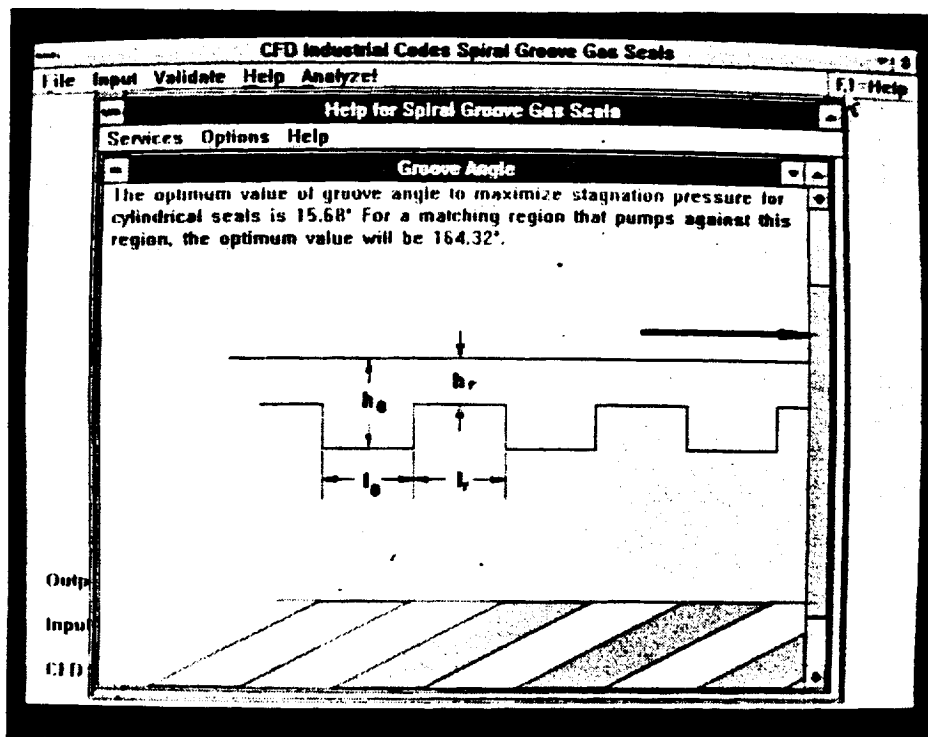
FIGURE 6-10 Context Sensitive Help Facility

EXECUTIVE PROCESS

USER
INTERFACE
PROCESS

PRINTING
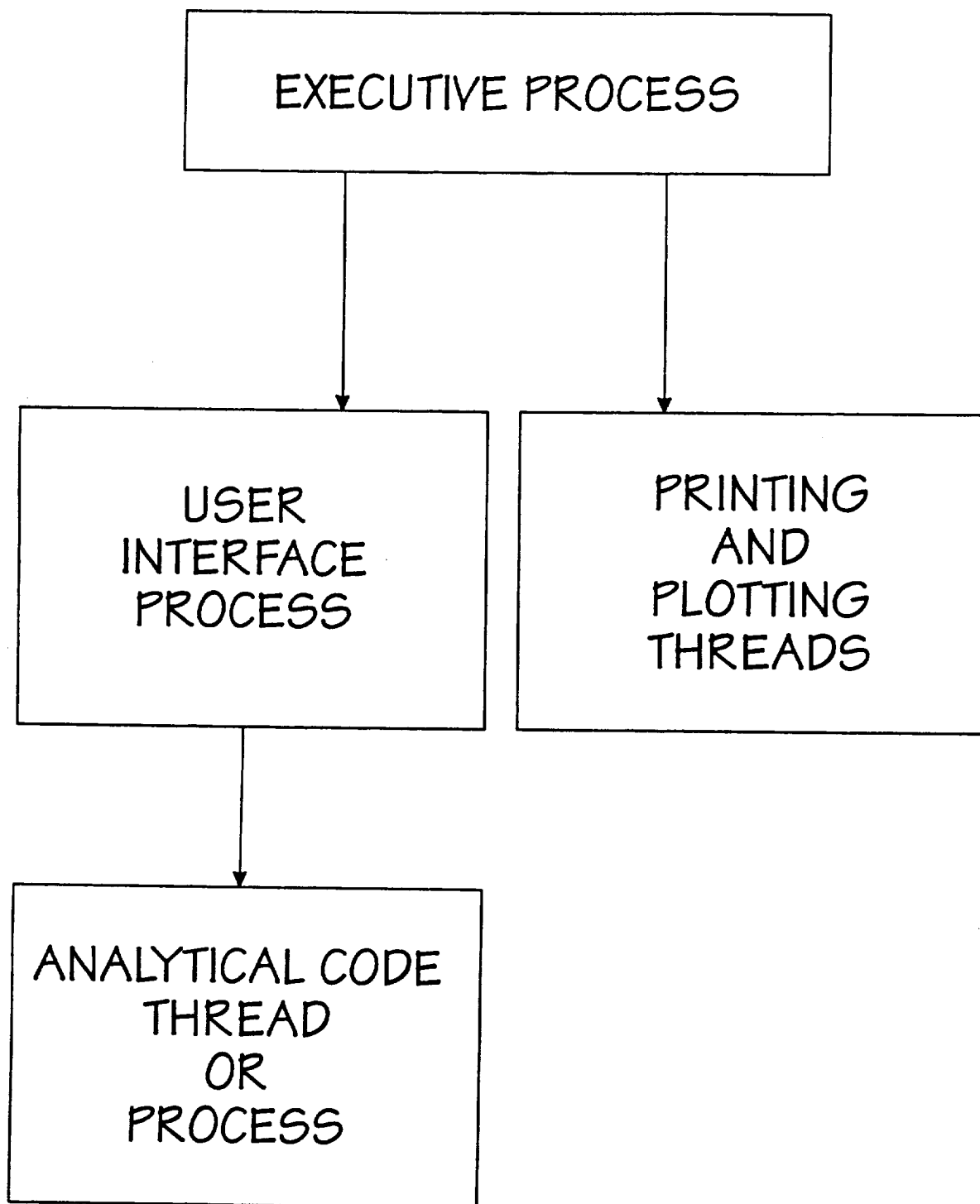AND
PLOTTING
THREADS

ANALYTICAL CODE
THREAD
OR
PROCESS

FIGURE 6-11: STRUCTURE OF THE EXECUTIVE PROGRAM

The name of the printer designated as the default printer during OS/2 setup is displayed in the main window. If the printer setup is changed, the display can be updated using the Printer Setup option in the Setup menu. Printer interface was designed for compatibility with OS/2 version 1.2. It needs to be updated to version 1.3 to provide additional capabilities that will make printing more flexible. The code to do so is already available but needs to be incorporated into the program.

When the user selects the Print... option in the File menu, a file selection dialog box pops up to select the name of the file to be printed. Clicking on the Cancel button in the dialog box will cancel the printing procedure. After a file has been selected, a dialog box listing all available printer fonts is displayed to select the font to be used for printing.

When the user selects the Browse... option in the File menu, a file selection dialog box pops up to select the name of the file to be browsed. Clicking on the Cancel button in the dialog box will cancel the browsing procedure. After a file has been selected, it is displayed in a separate window. The Fonts! menu item in the browse window lets the user select any of the available screen fonts. The window is closed using the system menu bar in the browse window. Only one browse window is allowed.

The font support for browsing and printing needs to be improved. File opening and saving dialog boxes also need improvement. This work was postponed until OS/2 version 2 becomes available because these dialog boxes have been standardized in that version. These changes are quite simple and will be implemented for all the codes.

6.4.2.2 Spiral Groove Gas Seals Analysis (SPIRALG)

This code is complete. Enhancements made to the analysis codes after the user interface was developed may require some changes to the code.

6.4.2.3 Cylindrical Gas Seals Analysis (GCYL)

The help information in the code needs to be expanded.

The user interface needs to support input for variable grids and to build in checks in the interactive seal layout portion of the code to prevent the user from specifying invalid seal configurations. The code was structured to support such checks but they need to be implemented.

6.4.2.4 Incompressible Cylindrical Gas Seals Analysis (ICYL)

ICYL user interface was implemented using Toolbook. It is an alternate way of designing user interfaces for OS/2 applications. The menu options are displayed in the main window as shown in Figure 6-12 and are selected using a mouse or typing the number assigned to the item. Cascading menus shown in Figure 6-13 are used to display options available for each of the main menu items in a manner similar to drop down menus used in the presentation manager. An Input screen for menu item 5a is shown in Figure 6-14. Input elements such as radio buttons and entry fields are the same as for presentation manager applications. The user can go directly to any input screen using buttons in the upper right corner of the screen. Our work revealed some important shortcomings in Toolbook when used for engineering applications. The major difficulty was in the handling of large arrays. These can, however, be overcome by developing C functions which Toolbook can call.

If NASA decides to stay with OS/2 for the CFD contract, the ICYL interface will be implemented using the presentation manager format because several prospective users at the last workshop at NASA wanted to stay with C.

6.4.2.5 Fluid Properties Calculations (FLUIDPROPS)

This code was obtained from NASA. The user interface is complete.

Help information needs to be added to the program.

The analytical portion of the program received from NASA is prone to crashes and was not changed in any way. Error trapping needs to be improved to facilitate graceful recovery from errors.

6.4.2.6 Spiral Groove Face Seals Optimization Program (SPIRALP)

The user interface is complete.

Help information needs to be added to the program.

The analytical portion of the program is prone to crashes and was not changed in any way. Error trapping needs to be improved to facilitate graceful recovery from errors.
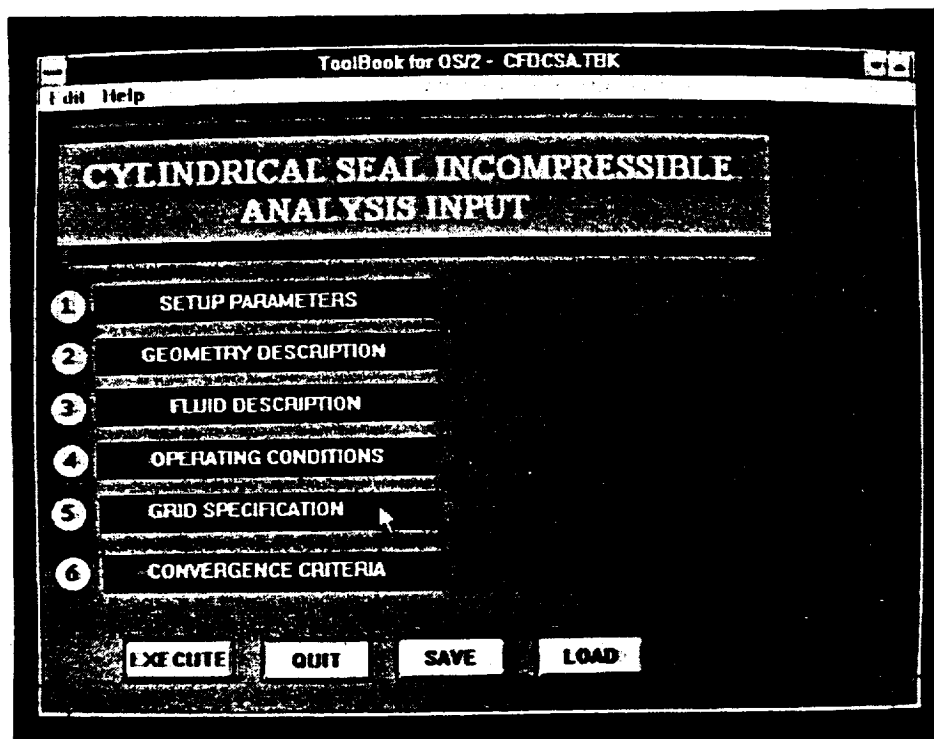
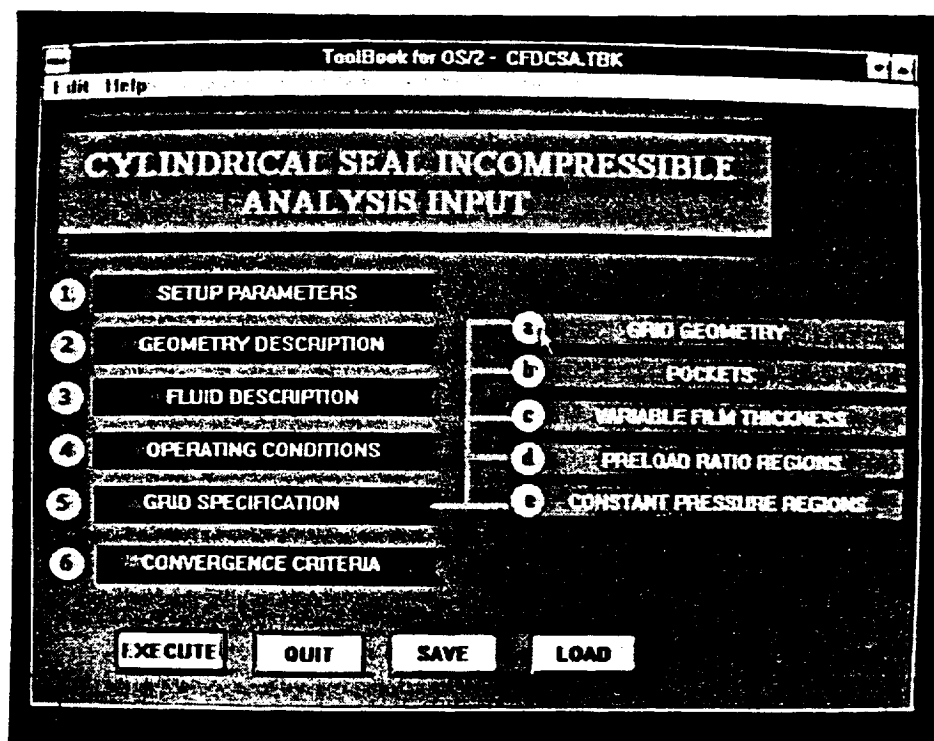FIGURE 6-12 User Interface for ICYL designed
using Toolbook.

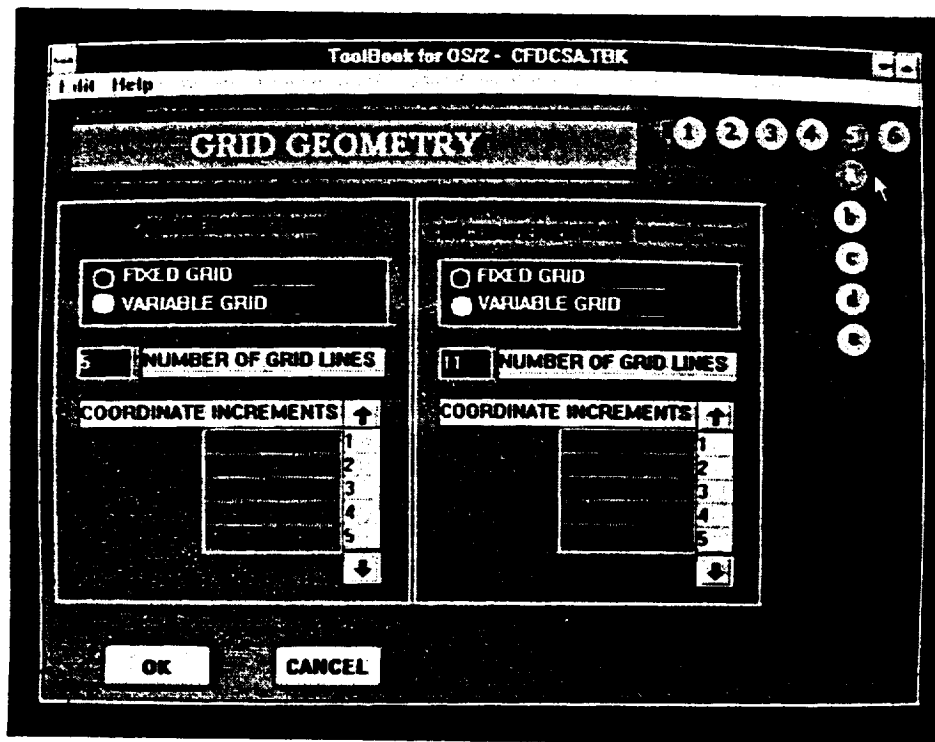FIGURE 6-13 Cascading Menus in the ICYL Interface

V91-242

FIGURE 6-14 Input Screen in the ICYL Interface.

6.5 FUTURE PLANS

Additional analysis codes are currently being developed. The development of the user interface has been postponed pending final selection of an operating system. The decision is expected in October 1991. The development of expert system components will begin when the first scientific code is available in 1992.

REPORT DOCUMENTATION PAGE

1. AGENCY USE ONLY (Leave blank)	2. REPORT DATE	3. REPORT TYPE AND DATES COVERED
	April 1992	Final Contractor Report

4. TITLE AND SUBTITLE

Numerical, Analytical, Experimental Study of Fluid
Dynamic Forces in Seals

Interim Report No. 1

5. FUNDING NUMBERS

WU–590–21–11
C–NAS3–25644

6. AUTHOR(S)

William Shapiro, Antonio Artiles, Bharat Aggarwal, Jed Walowit,
Mahesh M. Athavale, and Andrzej J. Preskwas

7. PERFORMING ORGANIZATION NAME(S) AND ADDRESS(ES)

Mechanical Technology, Inc.
968 Albany Shaker Road
Latham, New York   12110

8. PERFORMING ORGANIZATION REPORT NUMBER

None

9. SPONSORING/MONITORING AGENCY NAMES(S) AND ADDRESS(ES)

National Aeronautics and Space Administration
Lewis Research Center
Cleveland, Ohio 44135–3191

10. SPONSORING/MONITORING AGENCY REPORT NUMBER

NASA CR–189113

11. SUPPLEMENTARY NOTES

Project Manager, Anita D. Liang, Space Propulsion Technology Division, NASA Lewis Research Center, 977–7439. Wilbur Shapiro, Antonio Artiles, and Bharat Aggarwal, Mechanical Technology Inc.; Jed Walowit, Jed A. Walowit, Inc., Clifton Park, New York; Mahesh M. Athavale and Andrzej J. Przekwas, Computational Fluid Dynamics Research Corp., Huntsville, Alabama.

12a. DISTRIBUTION/AVAILABILITY STATEMENT

Unclassified - Unlimited
Subject Category 20

12b. DISTRIBUTION CODE

13. ABSTRACT (Maximum 200 words)

NASA/Lewis Research Center is sponsoring a program for providing computer codes for analyzing and designing turbomachinery seals for future aerospace and engine systems. The program is made up of three principal components: 1) the development of advanced 3-D Computational Fluid dynamics codes, 2) the production of simpler 2-D industrial codes, and 3) the development of a Knowledge Based System (KBS) that contains an expert system to assist in seal selection and design. The 3-D code is being produced by a major subcontractor, Computational Fluid Dynamics Research Corporation (CFDRC) of Huntsville, AL, who are enhancing an existing CFD code, REFLEQS. The first task of CFDRC has been to concentrate on cylindrical geometries with straight, tapered and stepped bores. Improvements have been made by adoption of a colocated grid formulation, incorporation of higher-order, time-accurate schemes for transient analysis and high-order discretization schemes for spatial derivatives. This report describes the mathematical formulations and presents a variety of 2-D results, including labyrinth and brush seal flows. Extensions to 3-D are presently in progress.

14. SUBJECT TERMS

Turbomachinery; Sealing; CFD; Models; Codes; Dynamics;
Design; Analysis; Expert system

15. NUMBER OF PAGES

312

16. PRICE CODE

A14

17. SECURITY CLASSIFICATION OF REPORT	18. SECURITY CLASSIFICATION OF THIS PAGE	19. SECURITY CLASSIFICATION OF ABSTRACT	20. LIMITATION OF ABSTRAC
Unclassified	Unclassified	Unclassified	

National Aeronautics and
Space Administration

Lewis Research Center
Cleveland, Ohio 44135

FOURTH CLASS MAIL

ADDRESS CORRECTION REQUESTED

NASA